CO_2 Utilization with Complexation of Polyelectrolyte Complex Nanoparticles and Surfactants for Environmentally Friendly Unconventional Oil Recovery: Mechanistic Study, Recovery and Multiscale Visualization

By

Hooman Hosseini
B.Sc. Polymer Engineering, Tehran Polytechnic, Tehran, Iran, 2010
M.Sc. Polymer Engineering, Tehran Polytechnic, Tehran, Iran, 2013
M.Sc. Chemical Engineering, University of Missouri, Columbia, US, 2015

Submitted to the graduate degree program in Department of Chemical and Petroleum Engineering and the Graduate Faculty of the University of Kansas in partial fulfillment of the requirements for the degree of Doctor of Philosophy.
Committee members:

Reza Barati Ghahfarokhi

(Chairperson)

Jyun-Syung Tsau

Edward Peltier

Stephen J. Randtke

Shapour Vossoughi

Russell Dean Ostermann

Date defended: 12/15/2020

The Dissertation Committee for Hooman Hosseini certifies that this is the approved version of the following dissertation:

CO_2 Utilization with Complexation of Polyelectrolyte Complex Nanoparticles and Surfactants for Environmentally Friendly Unconventional Oil Recovery: Mechanistic Study, Recovery and Multiscale Visualization

Reza Barati Ghahfarokhi

(Chairperson)

Date defended 12/15/2020

Abstract

Despite the imbalance in supply and demand of energy, due to the pandemic caused by the spread of coronavirus, the energy sector is experiencing a historic boost in oil and natural gas production thanks to development of hydraulic fracturing for unconventional recovery from tight shale formations. However, the process suffers from large dependency on water resources with reported negative environmental impacts. Reduction of freshwater use in hydraulic fracturing via high internal phase emulsions (foams) is a promising approach help to protect the quantity and quality of drinking water resources, to reduce the volume of water requiring disposal and, where deep well injection is the means of disposal, to reduce the risk of causing seismic activity. A sustainable approach for reduction of freshwater consumption and produced water disposal is to inject fracturing fluid with minimum aqueous phase volumes prepared using water obtained from the production cycle itself. The main objective of this work is to generate a stabilized supercritical CO_2 ($scCO_2$) foam using produced water and to study its texture, investigate its interactions with oil, and to use multiscale observation techniques to correlate foam microstructure with its stability and oil recovery performance in an environmentally friendly unconventional oil recovery process.

Application of compressed CO_2 foam provides enough viscosity for hydraulic fracturing and improves oil production while also serving as a promising CO_2 storage and sequestration method in shale formations. The mixture of produced water and compressed CO_2 in supercritical state was stabilized to form homogenous $scCO_2$ foam. Two oppositely charged polyelectrolytes were dissolved and mixed in produced water to generate Polyelectrolyte Complex Nanoparticle (PECNP) that in turn helped form a stable lamella between the aqueous phase and the $scCO_2$ while degrading in the presence of crude oil. The foam system improved fracture propagation, proppant transport, and fracture cleanup compared to the base case foam system with no PECNP.

Enhanced bulk viscosity and improved foam quality as a result of complexation at the interface was identified with rheometry in addition to sandpack experiments with PECNP-surfactant ratios of 1:9 and 4:6, in 33.3 kppm and 66.7 kppm salinity brine systems, respectively. Formation damage was controlled by the newly introduced mixtures as fluid loss volume decreased across the tight Kentucky sandstone cores by up to 78% and 35% for $scCO_2$ foams made with PECNP-WLMs in 33.3 and 66.7 kppm salinity brine, respectively. The formation of PEC-surfactant nanoparticles was verified via dynamic light scattering and transmission electron microscopy (TEM). A Raman spectroscopic model was developed to realize the structural changes

associated with complexation. The possibility of molecular complexation for lamella stabilization was also explored for EOR application. Molecular complex containing PECNP and N-120 ethoxylated surfactant was employed to enhance $scCO_2$ foams made with the thin film of high salinity brine formed between $scCO_2$ bubbles and the formation of molecular complex improved DLVO forces in aqueous polyelectrolytes for carbonate surfaces.

Millimetric view cell visualization was coupled with micrometric fluidic visualization to facilitate multi-scale observation of physical structure, geometry, dynamics and stability of electrostatically enhanced $scCO_2$ foam. Multiphase flow in fractured medium was emulated using glass micromodels. Wet etching technique on glass was performed via UV photolithography and thermal bonding, whereas dry etching was conducted with selective laser etching (SLE) inside the bulk glass. Lamella stability as a result of complexation of two oppositely charged polyelectrolytes with zwitterionic surfactant was investigated and compared in the view cell and glass microchips.

To my family: Father, Mother & Brother

Acknowledgment

I would like to express my sincere gratitude to my PhD adviser, Prof. Reza Barati Ghahfarokhi, for giving me the privilege of performing research in Unconventional Resource Lab at University of Kansas. I appreciate his diligence and confidence in teaching his students to understand scientific matters fundamentally and efficiently. He changed my career, directing it toward a clear scientific path to follow in the future, and he taught me how to take responsibility and be diligent in my scientific approach. Without his insight and financial support, none of this research would have been possible. I could not have imagined having a better advisor and mentor for my PhD study.

I would like to acknowledge my committee members, Professor Shapour Vossoughi, Professor Edward Peltier, Professor Stephen J. Randtke, Professor Russell Dean Ostermann and Dr. Jyun-Syung Tsau for evaluating my dissertation defense, for agreeing to review this thesis, and for providing constructive feedback and suggestions to improve this work. I would like to specially thank Dr. Jyun-Syung Tsau for encouragement, insightful comments, constructive discussions during the project.

My sincere thanks also go to Professor Saman A. Aryana from Department of Chemical Engineering, University of Wyoming for generously providing me with instrument and resources needed for micro visualization project.

I would like to acknowledge the National Science Foundation EPSCoR Research Infrastructure Improvement Program: Track -2 Focused EPSCoR Collaboration award (OIA-1632892) for financial support of this project.

I also like to recognize Dr. Karen Shafer-Peltier, Professor Craig Marshall and Dr. Qiang Ye who have generously helped me with interpretation of Raman Spectroscopy results, Dr. Ye for MicroCT training and analysis and John Wasserbauer from microGlass, LLC for support and useful discussions regarding the SLE technique.

I also like to extend my appreciation to Rudhra Anandan for professional trainings of high-pressure CO_2 foam generators in the beginning of this project (year 2017) and Zach Kessler, Scott Ramskill and Jeff Worth from Chemical and Petroleum Engineering Department and Tertiary Oil Recovery Program (TORP) at the University of Kansas for technical support.

Surely, this would have not been possible without my parents' help, support, and everlasting kindness. I would like to thank my father (Mohammad Rasool Hosseini), my mother (Nasrin Khanbabaei) and my brother (Farid Hosseini) for being my beloved family and my greatest supporters in life.

Table of Contents

List of Figures

List of Tables

List of Equations

Author's note

The presented thesis contains a collection of the contents borrowed from following publications by author during his PhD study at the University of Kansas (2017-2020). It also includes additional content from author's PhD proposal and comprehensive exam. The following are publications and submitted or prepared manuscripts for journal submission which were originally authored by Hooman Hosseini and then the content, pictures and tables were borrowed with copy right permission and proper citations to prepare this thesis:

- Visualization and Stability Measurement for 3D-Bulk Supercritical CO_2 foams: Effect of Ionic Complexation on Tubular and Diverging Flow, Hooman Hosseini, Jyun-Syung Tsau, Reza Barati, Prepared Manuscript for submission, 2021
- Synergistic Foam Stabilization and Transport Improvement in Simulated Fractures with Polyelectrolyte Complex Nanoparticles: Microscale Observation using SLE Fabricated Glass Micromodels, Hooman Hosseini, Jyun-Syung Tsau, John Wasserbauer, Saman A. Aryana, Reza Barati, Submitted manuscript to Journal of FUEL, February 2021
- Microfluidic Fabrication Techniques for High-Pressure Testing of Microscale Supercritical CO_2 Foam Transport in Fractured Unconventional Reservoirs, Hooman Hosseini, Feng Guo, Reza Barati, Saman A. Aryana. Protocol and Video Article, Journal of Visualized Experiments (JoVE), July 2020
- Multi Scale Flow Observation and Stability Measurement for Environmentally Friendly Waterless Fracturing Using Supercritical CO_2 Foam, Hooman Hosseini, Jyun-Syung Tsau, Saman A. Aryana, Reza Barati, 20th Annual meeting of American Institute of Chemical Engineers, AIChE, San Francisco, November 2020
- Development of Highly Stable Lamella Using Polyelectrolyte Complex Nanoparticles: An Environmentally Friendly scCO_2 Foam Injection Method for Greenhouse Gas Management Using EOR. Negar Nazari, Hooman Hosseini, Jyun-Syung Tsau, Karen Shafer- Peltier, Craig Marshall, Qiang Ye, and Reza Barati. Journal of Fuel, October 2019

- Experimental and Mechanistic Study of Stabilized Dry CO_2 Foam Using Polyelectrolyte Complex Nanoparticles Compatible with Produced Water to Improve Hydraulic Fracturing Performance, Hooman Hosseini, Jyun-Syung Tsau, Karen Shafer- Peltier, Craig Marshall, Qiang Ye, and Reza Barati. ACS Industrial & Engineering Chemistry Research, May 2019
- Assessing the Effect of Polyelectrolyte Complex Nanoparticles on Foam Film Stabilization and Oil Recovery in Carbonate Reservoir. Negar Nazari, Hooman Hosseini, Jyun-Syung Tsau, Karen Shafer-Peltier, Craig Marshall, Qiang Ye, and Reza Barati. Applied Energy Symposium, MIT A+B (AEAB2019), May 2019.
- Lowering Fresh Water Usage in Hydraulic Fracturing by Stabilizing $scCO_2$ Foam with Polyelectrolyte Complex Nanoparticles Prepared in High Salinity Produced Water, Hooman Hosseini, Jyun-Syung Tsau, and Reza Barati. SPE International Conference and Exhibition on Formation Damage Control, Lafayette Louisiana, February 2018
- Environmentally friendly waterless fracturing with supercritical CO_2 foam prepared in produced water: Mechanistic study, Hooman Hosseini, Jyun-Syung Tsau, Karen Shafer- Peltier, Craig Marshall, Qiang Ye, and Reza Barati. ACS National Meeting & Exposition, San Diego, California, August 2019
- Highly stable $scCO_2$-high salinity brine interface for waterless fracturing using polyelectrolyte complex nanoparticles, Hooman Hosseini, Jyun-Syung Tsau, and Reza Barati. 256th ACS National Meeting & Exposition, Boston, Massachusetts, August 2018
- CO_2 Foam Fracturing Fluids Stabilized in High Salinity Environment Using Polyelectrolyte Complex Nanoparticles, Hooman Hosseini, Jyun-Syung Tsau, Edward Peltier and Reza Barati, Kansas Governor's Water Conference, October 2017"

Chapter 1: Introduction

1.1. Prologue

In spite of advent of renewable energy and significant demand for solar, wind, hydropower and biomass, fossil fuel production still plays a dominant role in global energy sector as global oil production has increased to more than 2.5-fold over the last 50 years and crude oil has become the largest energy source on planet earth as in 2019 it was reported about 84% of global primary energy originated from coal, oil and gas [1]. This growth occurs despite the development of clean and renewable energies [2,3] as well as growing air pollution concerns associated with fossil fuels, CO_2 emission and generation of other greenhouse gases [1] into atmosphere which are mitigated by newly developed technologies in carbon capture, utilization, and storage (CCUS) sector [4]. Accordingly, the progress in oil and gas conformance improvements is accompanied by advances in CCUS [5].

Tight shale reservoirs contribute to 75% of natural gas and 50% of total petroleum liquids in United States [6]. The permeability and porosity of which, less than 1 mD (milli Darcy) and 15 %, respectively highlights the tight shale physical characteristics. Hydraulic fracturing is an essential technique for stimulation of hydrocarbon production from low permeability formations that were previously inaccessible [7].

To stimulate the tight shales where oil is trapped in rock formations and cannot be extracted in traditional ways, hydraulic fracturing is employed. High pressure water and chemicals break up rock formations, releasing the oil from tight formation and forcing it to the surface [8]. Nearly 70 years old, hydraulic fracturing is an essential technique for stimulating hydrocarbon production from low permeability formations [7]. Figure 1 represents the process of hydraulic fracturing.

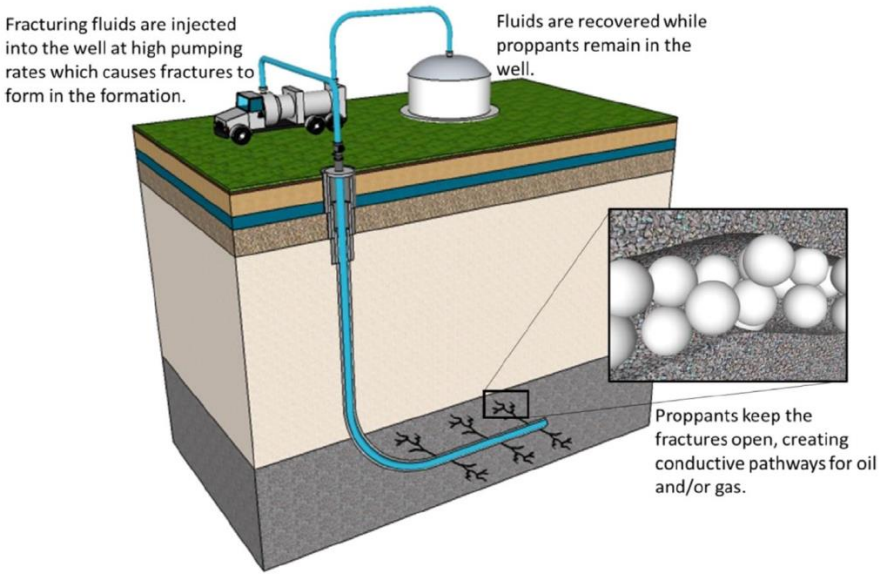

Figure 1. The schematic of hydraulic fracturing process, reprinted with permission from [9], Copy right Elsevier 2016

The process consists of high pressure pumping of fluid to initiate the fracture networks vertical to horizontal wells followed by pumping a particle-laden fluid to leave the fracture open [10]. The technology is now very well developed in a way that more than 60% of all the drilled wells are fractured to increase the production rate with stimulation. From the early development of hydraulic fracturing process in the 20th century, chemical fluids were used to open/propagate the fractures and to carry the proppants to the fracture [11,12]. Ideal fracturing fluid needs to offer high apparent viscosity to ensure efficient proppant transportation, compatibility with formation, efficient clean-up after treatment, excellent proppant settling and placement and low formation damage [13].

Water based fracturing has been commonly used in commercial shale gas and shale oil production due to its low cost, availability and efficiency [14,15], however, the excessive use of water led to water-scarcity related to drought as a typical well injects 2 to 4 million gallons of water to

reservoirs for fracturing [14]. Partial volumes of injected water (known as flow back) are recovered in early stages of fracturing process. Flow back and produced water need to be treated before re-injection or disposal to prevent the damage to ecosystem and to preserve the stability of injection fluid. Needless to mention, deep injection or excessive disposal of the wastewaters trigger seismicity that results in low-degree earthquakes [16]. To minimize the use of fresh water in the beginning of the fracturing and produced water disposal to the surface at the end and also deep injections to subsurface, waterless fracturing methods are employed [17]. Demand for foam based fracturing fluids is on the rise due to unique properties such as reduction of water usage, compatibility with water sensitive formations, no pore plugging in the formation, high apparent viscosity, recyclability, clean-up properties and proppant carrying capability [5].

The success of foam flooding in reservoirs largely depends on foam stability and foam-oil interactions responsible for flow resistance in porous media [18]. Foam stability is crucial for shear resistive capability about the wellbore and fracture, proppant carrying and in coordination with rheological properties, it ensures the fracture propagation and proppant settlements [5]. For a responsive foam in hydraulic fracturing application, lamella film stability at initial stages is required, however, the generated foam needs to be decomposable upon meeting the oil, and also foam needs to break as fast during the flow back and proppant release to maintain the fracture opening and conductivity [17]. Therefore, an unstable lamella is required upon introduction of oil to foaming system. Hydraulic fracturing fluids experience high shear since fluid flows through the wellbore tubular and the shear rate drops significantly as the fluid enters the fracture [19]. Therefore, shear rate sweep and static measurement studies help with understanding of the fluid behavior as it is mainly affected by flow geometry, time scale and foam microstructure and stability [20]. The rheology of dry CO_2 foam is widely regarded as non-Newtonian [20,21].

Highly viscous, dry foam capable of using produced water as its external phase needs to be developed. The foam system needs to have positive impact on fracture propagation, proppant transport and fracture clean up compared to the base case foam system with minimum chemical stabilizers. The formation of molecular complexes needs to be validated with light scattering techniques at the molecular level and the chemical conjugation mechanism for this complexation needs to be evaluated. Formation damage to tight shale formations need to be studied for waterless fluid mixture to assess the environmental impact. The produced water compatibility and reduction of water disposal are important factors to consider for introducing an environmentally friendly $scCO_2$ foams for hydraulic fracturing of unconventional reservoirs.

Macroscale observation of $scCO_2$ foam generation and stability in view cell enables the access to complex fluid macroscale topographic features, quantification of bubble frequency and measurement of hydrodynamic parameters which are influencing the underground fluid transport and stability. Instability mechanism such as coarsening rate, coalescence, and bubble drainage need to be evaluated. Foam- oil interactions and instability through oil lamella spreading, bridging mechanism and lamella rupture are critical factors for oil recovery which need to be evaluated in macroscale, however, the detailed fracture transport and microcrack stability requires microscale investigation. Visualization of multiphase flow in convergence/divergence, constrictions and channels with variable dimensions can also be useful for evaluation of foam stability for wellbore injections and subsurface transport in fracture/microcracks. Impact of chemical ingredients residing in CO_2-water lamella on bubble geometry and dimensions in constrictions can be investigated.

As there is numerous research conducted on different scales from flooding on cores to rocks and sand-pack systems, less was known in pore scale transport [22]. Before the oil reaches the surface, it travels through the channels of fractures, microcracks and to the network of porous rocks [3,14]. Since fluid flow and transport processes in reservoir occur within the rock micro scale pores and low matrix permeability affect the long-term production, after demonstration of performance a downscaling in observations is required to highlight the relative importance of pore-scale and matrix fluid transport. The significance of visualization in microfluidic is due to real time analysis of fluid flow and stability in fracture and micro-cracks in a way that was never seen before in at the laboratory scale because of typical high Reynolds number and convection forces associated to macro scale phenomena. Microfluidic platforms enable direct visualization and quantification of the relevant microscale processes. These platforms provide real-time control of the hydrodynamics and chemical reactions to study pore-scale phenomena alongside recovery considerations[7].

Foam generation, propagation, transport, and dynamics needs to be visualized in microfluidic devices emulating microcrack-matrix conductive pathways relevant to oil recovery from tight formations. Fluid exchange between fracture and matrix is directly expressed in accordance with the geometry[23], thereby highlighting the importance of simplistic and realistic representations. Several relevant microfluidic platforms have been developed over the years to study various processes.

The aim of microscale visualization research is to present a microfluidic platform that enables the study of $scCO_2$ foam topographic features such as bubble shapes, sizes and distribution, lamella stability in the fracture for hydraulic fracturing. Additionally, fracture patterns that are

intended to simulate the transport of fluids in fractured tight formations need to be described. There is a need to design the fracture pattern on glass chip that resembles the confinement and geometries of real fracture pathways for subsurface applications. Simulated pathways may range from simplified patterns to complex microcracks based on tomography data or other methods that provide information regarding realistic fracture geometries. As an alternative to traditional etching techniques such as photolithography/wet-etching, cutting edge techniques need to be explored to create a pressure resistive microfluidic device for subsurface oil recovery and a comparative analysis of the platforms is needed to identify the desired fabrication technique.

The main objective of microfluidics study is to answer the urgent industry need to study the inaccessible microscale foamability, fracture transport, stability, and fluid loss behavior of waterless fracturing fluids. The multiphase flow of waterless fluids such as $scCO_2$ foam containing chemical stabilizers such as polyelectrolyte complex nanoparticle and ionic surfactants needs to be studied in order to correlate the physio-chemical characteristics of micro to macro scale in unconventional oil recovery. Such study in subsurface emulated condition requires development of pressure-resistive micromodels with simplified 2D fractured patterns of glass micro models. After development of pressure resistive micromodels with state-of-the-art techniques of micromodel fabrication, the $scCO_2$ foam fracture flow and stability and fluid loss properties for variety of ionic stabilizers is CO_2-Water lamella needs to be investigated.

1.2. Objectives

The present study focuses on foamability, fracture transport, stability, fluid loss behavior, fracture conductivity and cleanup properties of $scCO_2$ in highly concentrated electrolytes (highly saline brine with sea-level salt concentration) containing ionic

stabilizers such as Zwitterionic Surfactant (ZS) and complexes of ZS and PECNP in macroscale and pressure resistive and simplified 2D fractured patterns of glass micro models. The performance of dry foams stabilized with 1 wt% ZS can be compared to ZS-PECNP enhanced $scCO_2$ foams in view cell, fluid loss module and sand-pack and the results can be coupled with microscale observation on glass microfluidics to correlate the physio-chemical characteristics of micro to macro scale in unconventional oil recovery.

The project seeks to tackle the water-less fluid multiscale stability and instability problems in hydraulic fracturing with visualization techniques. The multiscale observation will lead to development of topography quantification techniques for foam analysis in confined mediums. The project aims at comprehensive multiphase flow study for sustainable oil recovery with environmentally beneficial process (produced water reinjection, minimal freshwater use and produced water disposal) and biofriendly-compounds (Dextran Sulfate, PECNPs; see section 2.4) for ultimate decline in freshwater consumption and produced water disposal at surface. This sustainable and recyclable approach will be economically beneficial for oil industry and water resource management (e.g. lowering the cost of water lifting, handling, treating and disposal and increasing the oil production). The produced water compatibility with $scCO_2$ offers a promising approach for CO_2 storage in underground formations. The findings of this study are valuable for other applications across the spectrum of chemical and petroleum engineering dealing with microscale transport/isolation of $scCO_2$ in confined mediums.

1.3. Dissertation outline

The research performed in this proposal involves two major parts: (i) development of water-less fracturing fluid and investigation of its physiochemical properties and oil recovery

performance; (ii) development of visualization techniques, macro and micro scale observations and quantification of complex fluid morphology in view cell and microfluidic chips to enable study of multiphase flow stabilized in produced water for sustainable oil recovery.

In the first part of this work $scCO_2$ foam chemical composition, generation, stability, rheology, interfacial properties, and hydraulic fracturing performance (recovery) were investigated. Figure 2 exhibits the roadmap to establish a correlation between foam physiochemical and morphological properties to unconventional oil recovery performance.

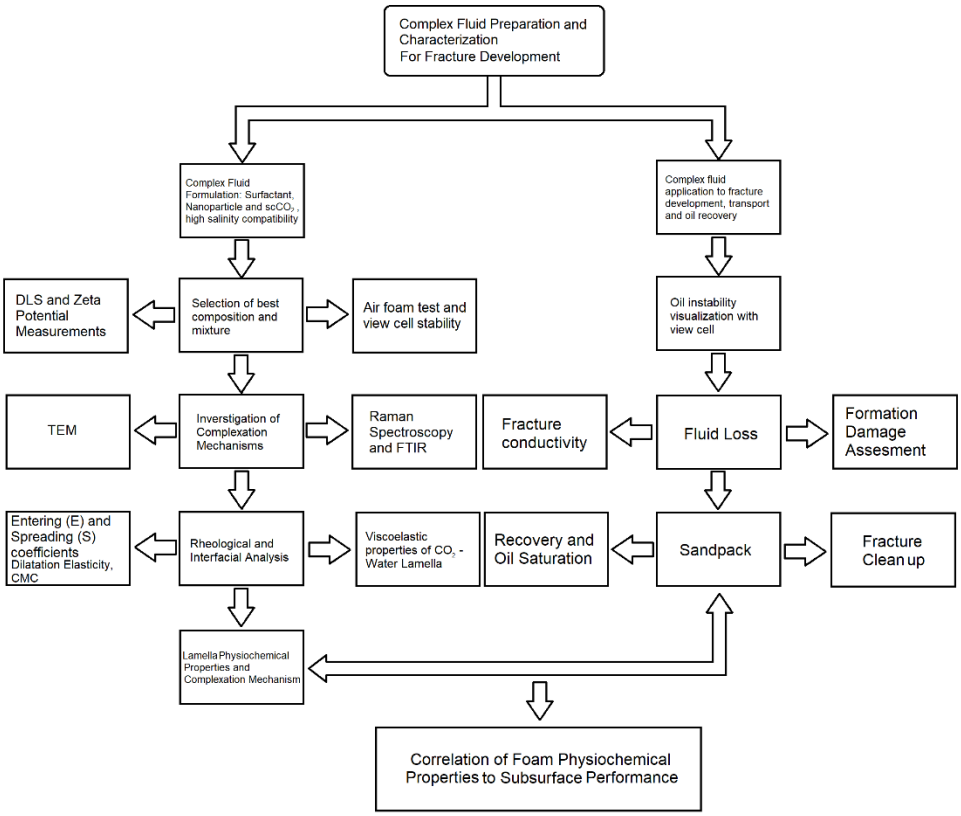

Figure 2. A roadmap for first part of this thesis including complex fluid preparation and characterization for fracture development

First, complex fluid is developed by selection of chemical components compatible with high salinity produced water and $scCO_2$. The compatibility is evaluated with air foam test, $scCO_2$ foam stability in view cell, zeta potential and particle size analysis (sections 4.1 and 4.3 in chapter 4).

The best performing mixtures are selected for mechanistic study and oil recovery performance. Electrostatic interaction between polyelectrolyte complex nanoparticles with entangled wormlike micelles (WLM) of viscoelastic surfactant (VES) is investigated through zeta potential, particle size analysis, and transmission electron microscopy (TEM) and Raman spectroscopy. Rheological and interfacial properties are employed to explore the viscoelastic properties and CO_2 -water lamella, lamella entering and spreading coefficient for oil instability analysis and dilatation elasticity for elastic response of lamella interface to external perturbations. The developed and optimized complex fluid (dry $scCO_2$ foam) is then generated in view cell and oil instability is evaluated. Subsequently, fluid loss and sandpack are performed to evaluate formation damage, fracture conductivity and clean-up and oil recovery performance.

In the second part of this thesis, the complex fluid comprising $scCO_2$ foam generated with optimized ratio of variety of foam stabilizers is employed for high pressure injection into view cell and microfluidic chip and the multiscale visualization is carried out. The macro scale visualization approach includes employment of monocular digital microscope camera with defined working distance to the view cell and employing specified illumination source and light adjustments to determine the stability, foam morphology features and instability of foam to resemble the foam capability for proppant settlement and oil recovery in the fracture. The dual stability behavior of waterless fluid for hydraulic fracturing is verified with this approach where the initial film stability at initial stages is necessary; however, the generated foam needs to degrade when it comes in contact with oil and needs to break rapidly during the flow back, leaving behind a fracture with effective conductivity. The microscale visualization is performed to evaluate the microstructural transport, stability, and fluid loss behavior of $scCO_2$ foam in a fracture/matrix medium resembling tight shale formation.

The micro scale visualization approach includes development of pressure resistive microchips and microchip holders and employment of high-resolution camera to study the multiphase flow in microscale and in a timely manner. The development of pressure resistive microchip requires comparative study between traditional glass microfabrication techniques such as photolithography to recently developed selective induced laser etching (SLE) to find the optimum resistance to harsh reservoir condition for LOC studies of multiphase flow. A systematic method of morphology quantification is developed to quantify the bubble geometry, size, distribution, and morphology for the images obtained from macro and micro scale observations. The method will couple the ability of MATLAB image processing tool to enhance the pictures with binarized capability from ImageJ and recently developed watershed – segmentation strategies (section 3.11). Accordingly, hydrodynamic flow properties such as dimensionless parameters and magnitude of capillary forces can be derived from quantification of foam topography. Multiscale complex fluid morphology and stability performance need to be correlated to chemical composition of CO_2 – water lamella where the interface is enhanced with variety of ionic stabilizers. Topography, stability and fluid loss performance of scCO_2 foams enhanced with zwitterionic surfactant and PECNP-Surfactants is compared to evaluate the impact of ionic complexation on physicochemical properties of scCO_2 foam in subsurface formation physical properties such geometrical constraints, permeability and pressure drop gradients in fracture, microcrack and tight shale matrix. The workflow diagram of the proposed endeavor is shown in Figure 3.

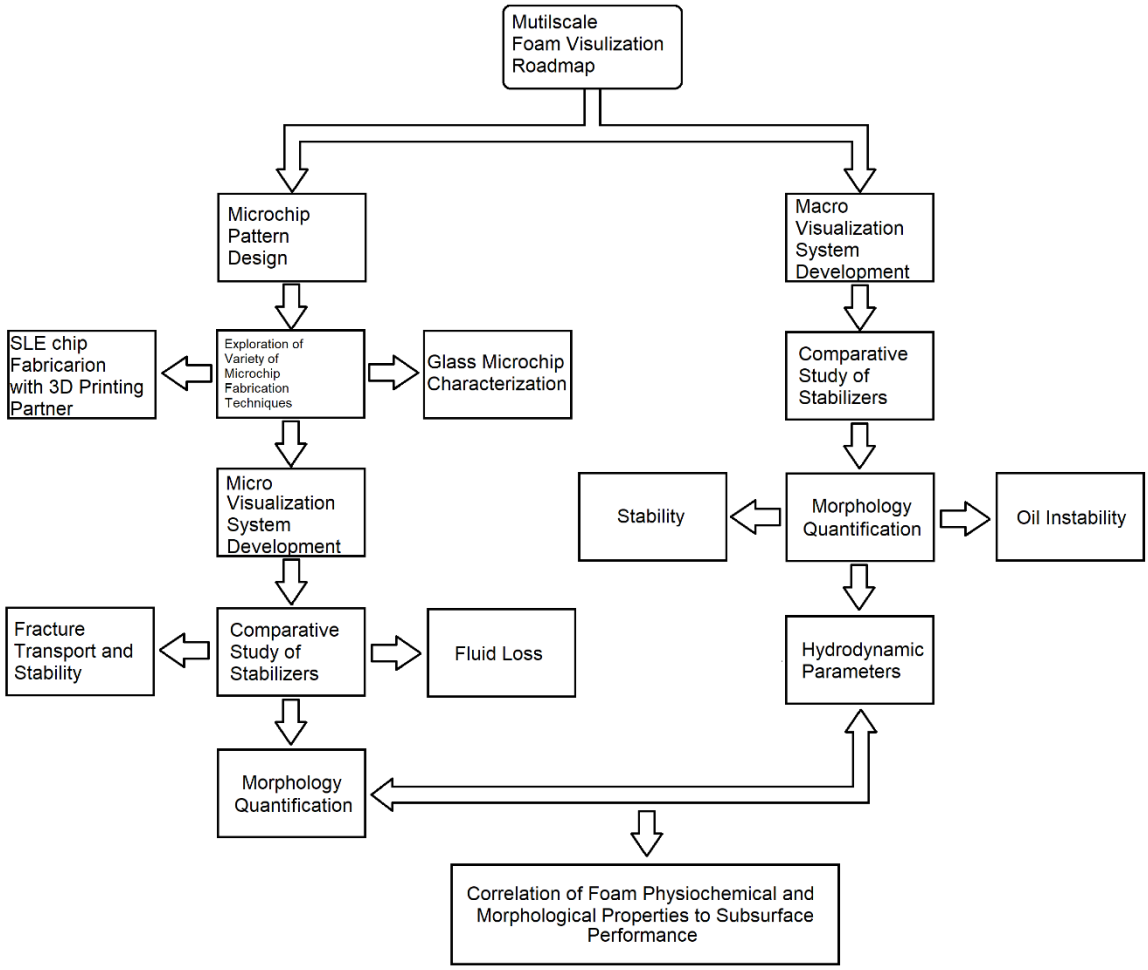

Figure 3. Multiscale foam visualization roadmap leading to correlation of foam physiochemical and topological properties to subsurface performance

Foam texture and individual lamella resistance in different fracture geometries are deemed to be influenced by steric disjoining pressure enhancement originated from electrostatic complexation of surfactant oligomers and ionomers in nanoparticle. The fracture patterns are designed in a way to simulate the physical appearance of the pathway for fracturing fluid transport in the fractured reservoir. The simulation of this pathway could be in simplified form of laboratorial patterns of fracture and micro cracks or in the form of realistic depictions obtained on micro-CT. AutoCAD is employed to design the fracture

pattern and laser etching, or photolithography are used to etch and transfer the fracture pattern on glass chip in a manner that resembles the confinement and geometries of real fracture pathways for subsurface applications. In this work, using glass micromodel engraved with pseudo fracture pattern, dry $scCO_2$ foam in-situ generation, transport, stability and fluid loss are visually examined via high resolution camera imaging and the pictures are processed and statistically quantified to make a physiochemical correlation between micro facture/matrix transport and stability behavior of $scCO_2$ bubbles with foam microstructural properties, additionally, the ability of different ionic stabilizers (ZS and ZS-PECNP) are assessed in a comparative study.

Chapter 2: Literature Review

2.1. Waterless processes: toward protecting the environment

Water based or gas based fracturing fluids have historically been among the popular methods to conduct the fracturing job [24]. Some water based fluids comprise lower concentration of other ingredients such as polymers and guars to increase the viscosity of fluid and assist proppant suspension and transportation to the fracture [25]. Slickwater (fracturing fluid with friction reducer additive) was also reported to improve the fracture length [26]. Currently, alternatives to water-based fluids are being investigated due to large amounts of water usage, formation damage, process expense and environmental issues [24]. Also, low viscosity of slick water weakens the ability of fluid to suspend, place and carry the proppants and viscosifying agents used to increase the viscosity of fluid might be plugging the pore throats and cause the formation damage [17]. Gas based fracturing fluids were traditionally CO_2 and N_2 gases and they are applied to water sensitive reservoirs and improvement of clean up, proppant transportation and placement and increase of up to five fold was reported in production using these mixtures as well as formation damage control [24]; however, the low viscosity and density of the gas molecule overshadows the process scale up and environmental benefits [24].

2.2. Foam: environmentally friendly approach to waterless fluid

Foam and energized fluids are composed of one compressible component such as carbon dioxide or nitrogen that are considered to overcome the formation damage, low viscosity and clean-up efficiency of conventional fracturing fluids in tight and ultra-tight unconventional formations [27]. Ultra-low water content and high apparent viscosity are exceptional properties of foam fracturing fluids [24]. Figure 4 represents the combination of dry foams with produced water recycled in the field for environmentally friendly oil recovery [28].

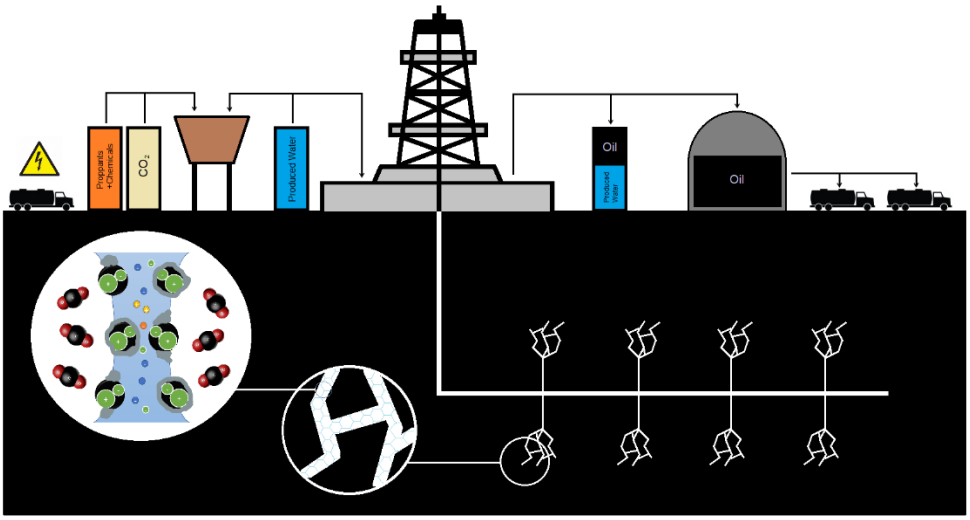

Figure 4. Dry foams as efficient water-less fluids for environmentally friendly unconventional oil recovery.

Reprinted with permission from [28] ACS 2019.

High apparent viscosity helps to increase the proppant capability and to ensure the required fracture width and height, [29]. Moreover, foams are known for their interfacial film elasticity and the capability to reduce the formation damage [30].

2.3. CO_2 for subsurface oil recovery

Better fracture stimulation was reported using CO_2-based energized fluids [31]. CO_2 is mixed with fluids injected to deeper wells to form a low water content fracturing fluid [32]. Despite the environmental concerns about CO_2 pollution in atmosphere [33] and heavy emphasis on its capture [4,34], storage [35,36] and sequestration [36,37], if properly managed, CO_2 is abundant, nonflammable, essentially non-toxic for variety of applications such as refrigeration [38], material synthesis and processing [37,39], medicine [40], chemical industry [41] and of course, oil industry for oil recovery enhancements [42]. CO_2 foam has been under consideration as a prominent fracturing fluid capable of being stored and sequestered in the formation while increasing the effectiveness of shale oil and gas production and reducing environmental impacts [5,43]. Due to discrepancies in cohesive energy

density of oil and CO_2 and having lower density than oil and water, the affinity of CO_2/water has been subject of variety of studies to stabilize the gas/liquid mixture while flowing through low permeable formations [44]. Low density and viscosity of CO_2 enhances the propagation in low permeability reservoirs, however, there exist issues reported with ice formation [45], challenges in storage [46] and filtration of liquid CO_2-based fracturing fluid [24].

Supercritical fluids have attracted considerable attention owning to liquid-gas properties from low viscosity, rapid diffusivity and wettability to low surface tension properties [47]. Pressurized CO_2 as supercritical CO_2 foam ($scCO_2$ foam) is a notable non-aqueous fracturing fluid which offers more miscibility with hydrocarbons to prevent flow blocking in small pores [48]. $scCO_2$ with operational critical point (31.1 °C, 73.8 bar) exhibits gas-like diffusivity and liquid like density [47]. $scCO_2$ offers promise to effectively fracture the rock due to coupled-compressibility-thermal shock effects [43] as CO_2 expands to the new fracture volume. Potential drawbacks of $scCO_2$ injection are increased expenses of capturing, pressurizing and transporting and lack of enough viscosity to carry the proppants if degraded under shear [43].

$scCO_2$ in water (C/W) foams are stabilized with nanoparticles or surfactants through CO_2-water interfacial adhesion [49]. Surfactants, in general, form protective layers at gas/liquid interface to prevent the coalescence between the bubbles (uniform dispersion) and to make gas and liquid phase compatible in the mixture [50]. Some issues with surfactants such as imbalanced head/tail solubility in CO_2/aqueous phase impacts the resulting emulsion stability [51]. Foamed liquids with CO_2 compatible viscoelastic surfactants (VES) offer stable fracturing fluids with viscous behavior under shear which helps to degrade in the fracture in addition to leaving no residue behind [45].

2.4. $scCO_2$ foam stabilization: ionic approach

To enhance the compatibility of $scCO_2$ with water phase variety of methods were proposed. The presence of adsorbed surfactant layers stabilize the lamellae between the $scCO_2$ and the aqueous phase [52] taking advantage of electrostatic repulsion between the two faces of lamellae [53]. Similarly, increasing the surfactant concentration under the influence of electrolyte concentration would help with forming long-range electrostatically ordered microstructures on the thin liquid films and the bulk of the lamellae to inhibit foam film drainage (stratification) [54] Formation of viscoelastic lamella stabilizes the gas-in-water foams by suppressing the gravity drainage, lamella thinning and eventually Ostwald ripening [55]. Figure 5 illustrates the positive effect of molecular synergy for stabilization of dry foams in hydraulic fracturing [31].

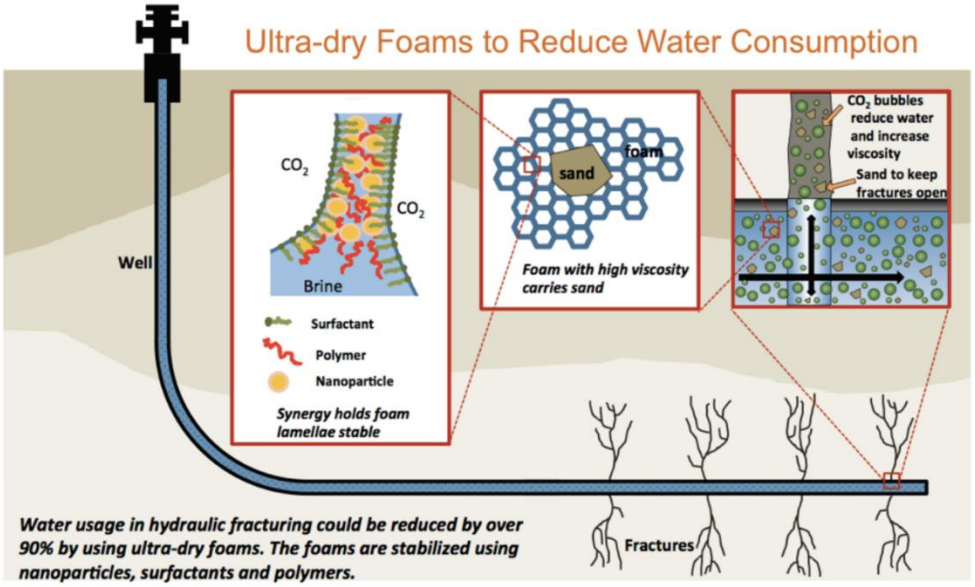

Figure 5. Overview of required synergy for stabilization of dry foams in hydraulic fracturing, employing nanoparticles, polymers and surfactants [31], open access content on web

Nanoparticles with large surface area [56] were found to overcome the challenges associated with surfactant adsorption on reservoir rocks [24], thermal conductivity [57], fluid loss [58], water invasion [59],

fluid propagation in porous media [56,60] and pore throat plugging [61] to achieve proper fracture width and height [24]. Nanoparticle stabilized high quality CO_2 foams were found to generate wider fracture with smaller fracture half-length due to high viscosity of dry fracturing fluid [31]. Figure 6 reveals the effect of variety of fracturing fluids to create desired fracture volume [31].

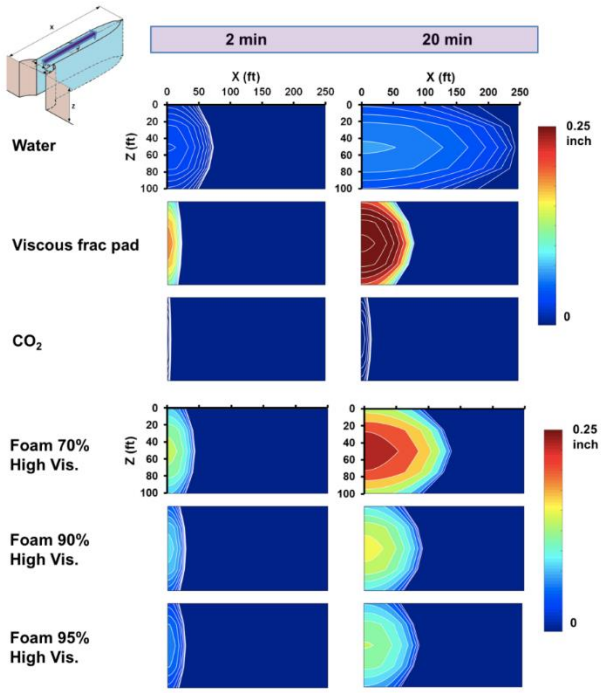

Figure 6. Simulated effect of variety of fracturing fluids to create desired fracture volume [31,62], Reprinted with permission from [62] Elsevier 2016.

Further simulation results confirmed the efficiency of cleanup in 10 days as opposed to that of viscous fracpad which could take up to 1000 days [31]. Figure 7 represents the efficient cleanup properties for dry CO_2 foams enhanced with nanoparticles [31].

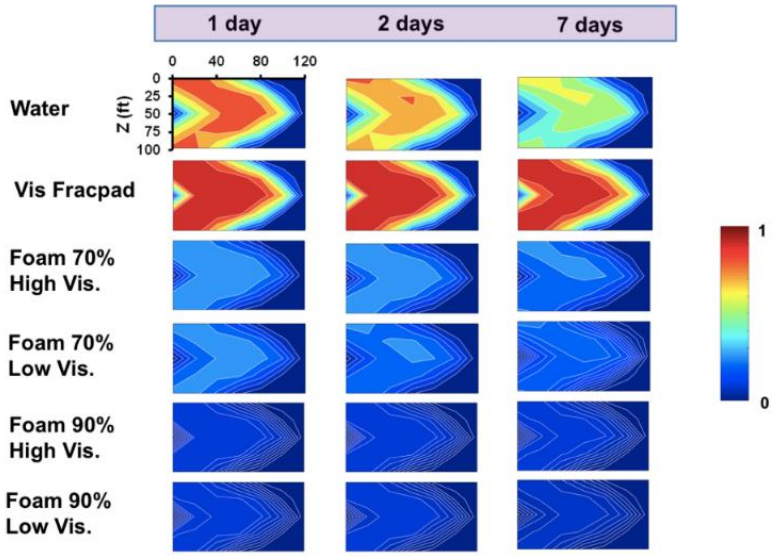

Figure 7. Water saturation map obtained different fracturing fluids resembles the fracturing cleanup efficiency for high viscosity dry foams enhanced with nanoparticles [31,62], , Reprinted with permission from [62] Elsevier 2016.

Electrostatic interaction between polyelectrolyte complex nanoparticles with entangled wormlike micelles (WLM) of viscoelastic surfactant (VES) is investigated to eliminate fluid loss issues, improve the viscosity of VES-based fluids, to enhance the proppant suspension capabilities to tailor ionic activity of surfactants and to reduce the surfactant adsorption to reservoir rocks with addition of ionic hindrances. Polyelectrolyte complex nanoparticles were developed by our group for both Enhanced Oil Recovery (EOR), reservoir treatment and hydraulic fracturing applications [17,32,63–66].

Polyelectrolytes are widely used charged polymers compatible with aqueous solutions useful for adsorption [67], ionic conduction [68] and controlled release [66]. Branched Polyethyleneimine (PEI) with different types of cationic amine functionality is capable of polyelectrolyte complex nanoparticles (PECNP) formation in electrostatic complexation with Dextran Sulfate (DS: Sodium Salt) comprising anionic sulfonate functionality in adjusted pH medium [17]. Figure 8 illustrates a

cartoon for molecular complexation of PECNP and Zwitterionic Surfactants (ZS) which is verified by TEM and Raman Spectroscopy in Chapter 4.1.

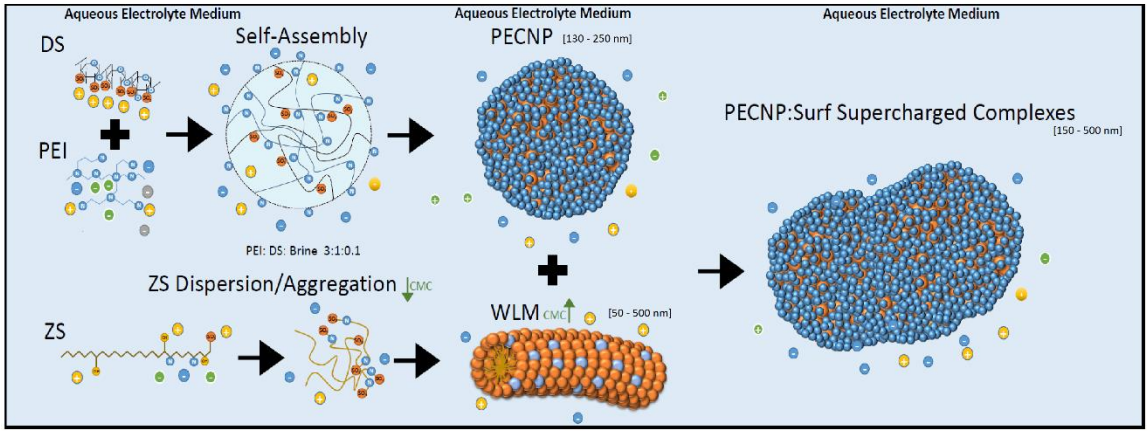

Figure 8. Illustration of molecular complexation of PECNP and zwitterionic surfactant (ZS) explored in this work (chapter 4.1)

Interactions between the polyelectrolytes and oppositely charged surfactant creates a variety of different colloidal systems with liquid crystalline-like mesostructured and long-range order on nanometer scale.

PEI and DS are both biodegradable and biocompatible polyelectrolytes [5,69]. In preparation of nanoparticle, PEI and DS are combined with fixed proportions to obtain electrostatically stable ionic super complex to improve the disjoining pressure in the lamella. PECNPs were originally developed for drug delivery applications [70] and due to biocompatibility to organisms were adapted to oil field applications [71,72]. Polyethyleneimine is a water soluble, non-viral gene delivery polymer that offers high transfection efficiency both in vitro and in vivo [73]. To decrease the toxicity due to polycationic activity of PEI, a degradable polyanionic Dextran sulfate (DS) is added to decrease the cytotoxicity of DNA-incorporated nano-gel [73]. Dextran sulfate is a biodegradable polymer containing a branched chain of anhydroglucose units with 2.3 sulfate groups per glucosyl residue

frequently used on pharmaceutical applications with proven biocompatibility [73]. DS chemical structure is illustrated in Figure 9.

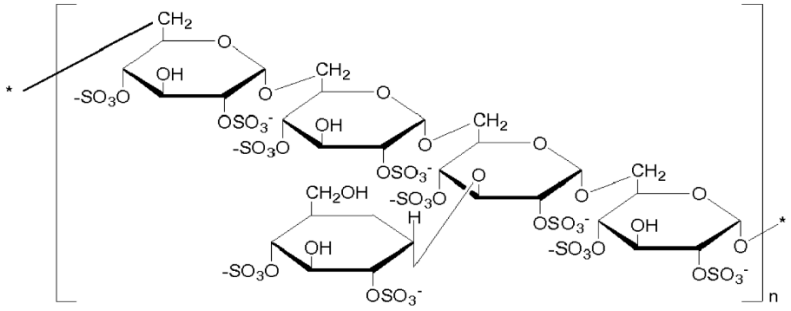

Figure 9. Dextran Sulphate (DS) chemical structure [5], open access content on the web

In terms of functional properties to protect the ecosystem in oil and gas industry, Polyethyleneimine-dextran sulfate polyelectrolyte complexes are used to protect the enzymes from harsh conditions and their vesicle loaded with enzymes helps to degrade the guar gels, HPG solutions and borate-cross-linked gels at variety of pH and temperature and also to degrade the filter cake therefore preventing the fluid loss in hydraulic fracturing [74]. The similar bio/organism-compatibility is expected in EOR application.

The formation of complexes of nanoparticle and surfactant is shown in Figure 8. Branched Polyethyleneimine (PEI) contains 25% primary amines, 50% of secondary amines and 25% tertiary amines [17]. PEIs are low molecular weight compounds with the general formula –[CH_2-CH_2-NH_2]-, made by ring opening polymerization of aziridine. The polymer of this type, can be linear (primary amine in the backbone), partly branched or repetitively branched polymer also known as dendrimer (with secondary and tertiary amines). All three foams are soluble in water [5,75]. The main variants of PEIs are linear and branched as shown in Figure 10.

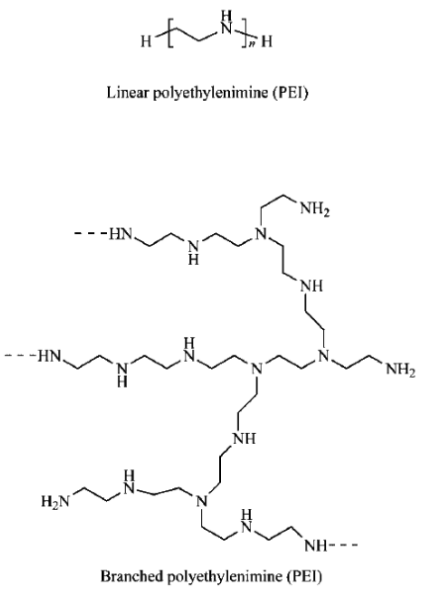

Figure 10. Structures of different types of polyethyleneimines [75], open access chemical structures on web

For primary amines, the nitrogen is bound to one carbon, and substitution of more hydrogen for carbon turns the amide group to secondary and tertiary amides. Figure 11 reveals all types of major amine groups [76].

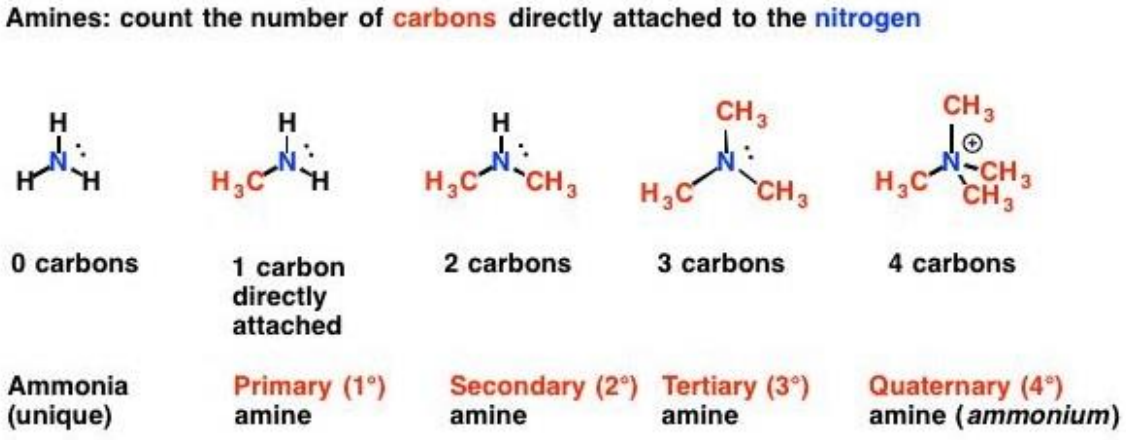

Figure 11. All types of major amine groups in amide for depending on neighbor carbon bonding [76], open access content on web

From Figure 11, one can notice the chemical reactivity of ammonia and primary amine are larger than other types due to availability of N-H bonds with lower energy of dissociation [76]. Amines can react as either nucleophiles or bases and removal of proton generates the amide ion. The electrostatic activity of amines originates from high electron density of nitrogen atom when paired with adjacent hydrogens, however, when protonation occurs the activity of protonated amides declines due to lowering the density of electrons on Nitrogen [77], therefore, it can be concluded more positive amide nuclei in protonated primary amines (in aqueous solution) will form stronger electrostatic bond with sulfate in DS as a result of higher electron density difference between the pairs, so more stable PECNP is formed employing linear PEI which is also achieved by pH adjustment for aqueous PEI solution containing branched configuration of polymer. Also, more open sites will be available for interactions with oppositely charged sulfonate in surfactants. The hypothesis is the number of PEI cationic moieties affects the DS-PEI interaction, stability and electrostatic stabilization of CO_2-water lamella as it has strong effect on the PEI-DNA interactions is biomedical applications [75].

The aggregation of PEI chains is more likely to happen in branched PEI and binding with DS is negatively affected, however, the densely populated amine sites are found on branched PEI. Studies showed the free energy of amine hydration is increased in the order, primary, secondary, and tertiary, indicating that molecules become compact with branching the PEI [78] and subsequently, electrostatic complexation is negatively affected due to conformational and reactivity hindrances. The solution stability is also dependent on PEI polymer structure and PEI/DS charge ratio. The linearity of the PEI chains would decorate the resulting polyplex with more ionic active sites for electrostatic interactions with surfactant. Moreover, Zeta potential and

particle size of as obtained PECNP nanoparticle is altered by linear and branched chain conformations of PEIs.

2.5. Foam Stability in Formations: Geothermal and Geophysical Influence

Foam stability in porous media is characterized based on three flow regimes with three different flow behaviors and foam generation mechanisms. Firstly, surface facilities and the pore wall, where flow may create bulk foam. Secondly at near-wellbore region where the flow rate and pressure are high and thirdly, formation which is far away from the injection well, where pressure gradient and flow rate are much lower [79]. The additional regime in fractured reservoirs would be flow in fracture and micro crack pathways in which the shear and pressure gradient would even drop to lower values [5]. Foam stability in general can be evaluated through bulk stability or lamella stability. Bulk stability is affected by permeability of porous medium, injection rate, pressure, reservoir temperature, brine salinity, foaming agents and oil [79]. Lamella stability in porous media originates from mechanisms of foam creations in porous media. Leave behind, lamella division and snap-off mechanisms are common mechanisms of lamella stability dealing with gas invasion of pore bodies through other throats, creation of two lamella from single one in pore space movement and drop of local capillary entry pressure in the throat [79].

Foam stability in the fracture is affected by high temperature conditions, high shear rate while pumping and low shear rates while fracture is closing [80]. Failure to maintain the foam stability results in proppant inhomogeneous distribution in the fracture closure [80]. The stability in the fracture can be evaluated by liquid drainage rate and foam collapsing time of sample which are also obtained by dynamic foam rheology and view cell measurements, however, microscale observation in microfluidics will be performed to correlate the results of micro to macro scale.

2.6. Microstructural studies: Topography and Stability in millimetric scale

The foam stability and rheology can be studied in accordance to microstructural change with time. Qichao and coworkers studied the bubble shape and size with time [81] as bubble coalescence with adjacent small bubbles increases the size of bubbles and thickness of bubble films changes from 10 to 2 μm during 7 h as a result of lamella drainage. Figure 12 represents the different microstructures of the films formed with SiO_2 and SiO_2/SDBS enhanced N_2 foams during 7h periods and corresponding bubble size distribution. One concludes the ability of bubbles to preserve their shapes depends on adsorption of organic/inorganic ionic complexes to the lamella and to enhance the dilatational elasticity of interface and resistance to morphological deformations [81].

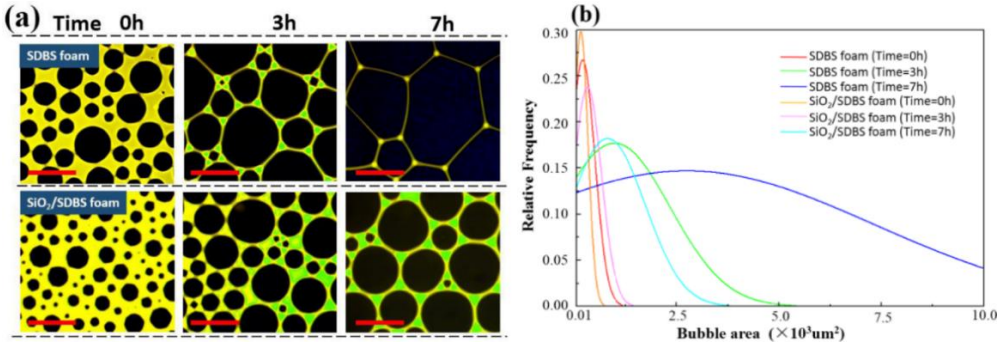

Figure 12. (a) Microscopic analysis of SiO_2 and SiO_2/SDBS enhanced N_2 foams during 7 h periods and (b) corresponding bubble size distribution [81], reprinted with permission from [81], ACS 2015

The changes in microstructural bubble morphologies can be eventually attributed to foam viscosity, interfacial tension and even proppant suspension capability from near-well-bore to far-well-bore and from the main fractures to micro fractures. Higher interfacial elasticity leads to more resistance to proppant settling deformations and helps to carry the proppant along the lamella borders with longer film stability [81]. Interactions between proppant and bubble lamella in nanoparticle (SiO_2) and nanoparticle/surfactant (SiO_2/SDBS) was enhanced in N_2 foams according

to Qichao and coworkers [81]. The proppant is suspended in a more confined medium of bubble lamellas in case of SiO_2/SDBS enhanced foam with narrower distribution bubbles and lower bubble sizes which, gives rise to longer lamella surface interaction with proppant area. The microstructural changes were not studied for high pressure systems at confined mediums such as fractures and microcracks.

Foam drainage has been more accurately observed with Hele-Shaw cells in the literature [82]. Microstructural analysis is also conducted through 2-D hele-shaw cells and microfluidic devices. Previously, rheology and micro structure of foams are correlated through Hele-Shaw cell observations [83]. Tong and coworkers produced a 2D foam in a vertical Hele-Shaw (HS) cell in order to measure the bubble size distribution at steady state with image analysis and they used integrated numerical model to evaluate the agreement of numerical and experimental results on spatial and temporal evaluation of bubbles while liquid drainage occurred [82]. Foaming dynamics in Hele-Shaw cells was subject of comprehensive study by Caps and co-workers with simple water and soap foam in the cell [84]. Thin film liquids are created during each flip of Hele-Shaw cell and flipping the cell with upside-down directions accelerates the liquid drainage toward the bottom of the cell. Figure 13 represents the formation of foam in Hele-Shaw cell with different consecutive flips to reach different bubble sizes [84].

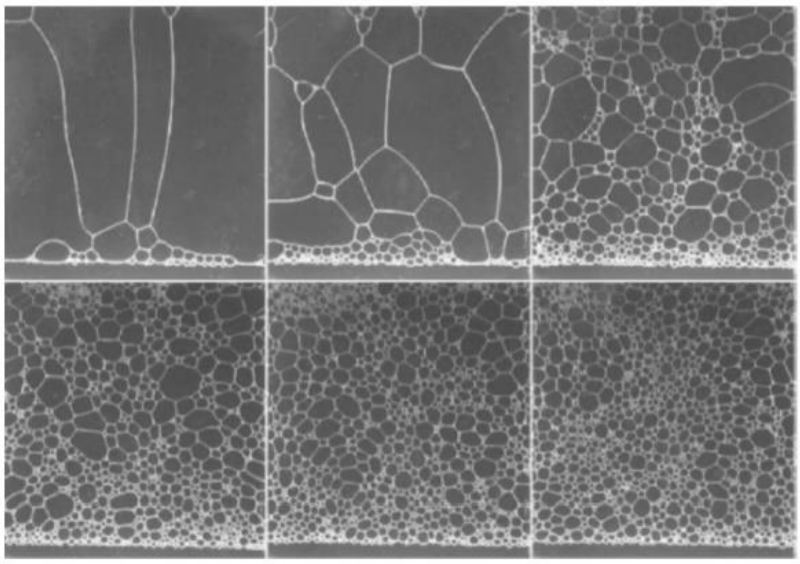

Figure 13. Six consecutive images of the foam with different flipping cycles of HS cell reported by Caps and co-workers [84] (open access content on web)

Accordingly, bubble size, cumulative probability distributions of the bubble size with number of flips, ratios between the standard deviation of the bubble size distribution and the mean bubble size with number of flips were determined [84]. The bubble breakup process was studied with the help of high-speed camera and breaking bubble was drawn in the gray scale for clear analysis. It was reported that transport of small bubbles into the fluid flow is responsible for primary bubble segregation as it's shown in Figure 14 [84]. Such morphologies are observed in thin film layers of foams generated at low pressure, whereas, in practical subsurface application foam is generated with unknown frequency and dense population of bubbles and the fluid is hindered by pore or fracture walls affecting the microstructural stability and proppant carrying capability of foam.

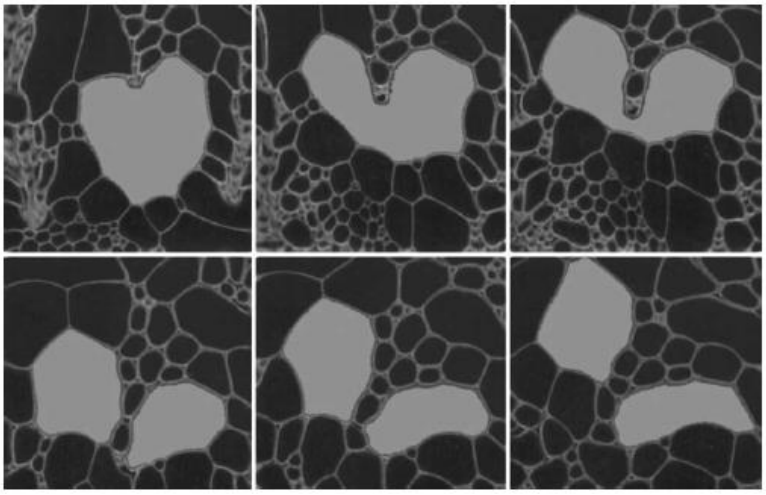

Figure 14. Bubble split sequence recorded at a time frame rate of 100 frames/s showing the bubble breakage by the falling liquid reported by Caps and coworkers [84] (open access content on web)

Szabries et al introduced an analyzed systems for foam structural analysis for EOR [85]. Figure 15 reveals the figure of (a) experimental setup, (b) illumination and light adjustments to determine the stability and foam structure and (c) schematic of high pressure foam analyzer used by Szabris and coworkers [85].

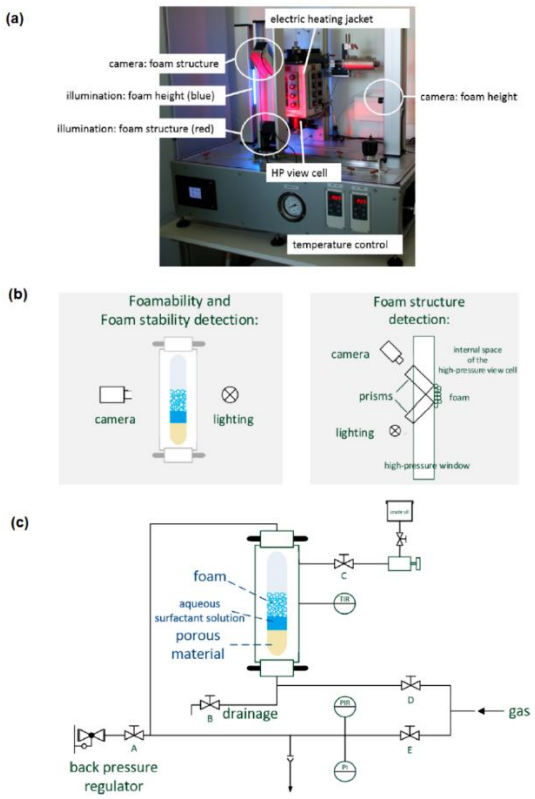

Figure 15. Schematic reveals the figure of (a) experimental setup, (b) illumination and light adjustments to determine the stability and foam structure and (c) schematic of high pressure foam analyzer [85], reprinted with permission from [85], ACS 2019

The foam height and structure were detected simultaneously as a function of foam age with apparatus illustrated in Figure 15. The apparatus offers an extended optical access by means of three high pressure tongue-shaped windows (Figure 15a). Special arrangement of prism allows for bubble morphology observations whether shape or size distribution for high pressure generated CO_2 and N_2 foams (Figure 15b). The schematic of foam analyzer system is shown in Figure 15c. The result of foam imaging is illustrated in Figure 16.

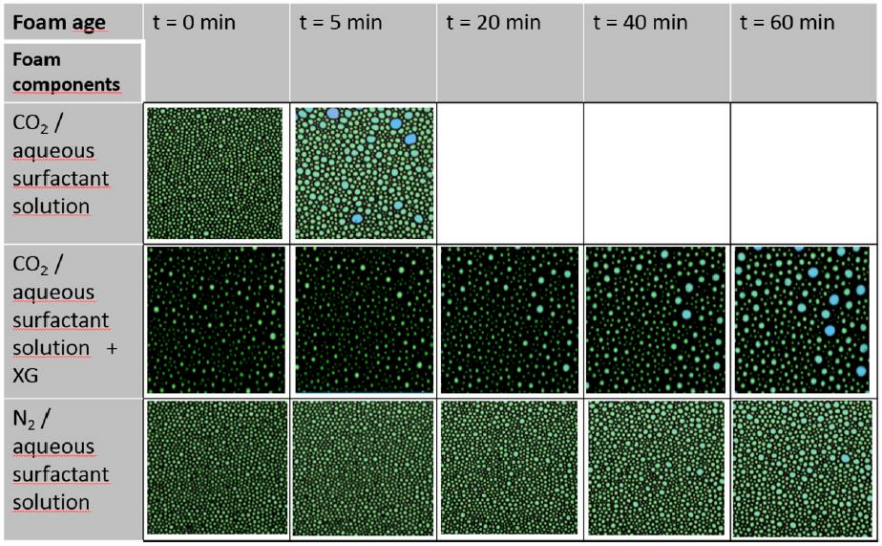

Figure 16. Microstructure of foams generated at 5 MPa and 45 °C [85], reprinted with permission from [85], ACS 2019

With these new imaging and illumination systems, the authors of this work were able to quantify mean bubble area (MBA) and the MBA variation with time and also relative foam height and long term stability pressurized CO_2 and N_2 foams with different stabilizers were evaluated [85]. The work presented a new way to analyze the 3D foam microstructures at high pressures within the context of EOR. The methodology for optically transmitted light to receive visible foam height (Figure 15b) is adapted to our system for foam macrostructure analysis in hydraulic fracturing.

2.7. Multiscale Observations

As there are numerous researches conducted on different scales from flooding on cores to rocks and sandpack systems, less was known in pore scale transport [22]. Before the oil reaches the surface, it travels through the channels of fractures, microcracks and to the network of porous rocks [3,14]. Since fluid flow and transport processes in reservoir occur within the rock nonometric to milimeteric cracks, pores and low matrix permeability affects the long-term production, a

downscaling in observations is required to highlight the relative importance of pore-scale and matrix processes.

2.8. Microscale observations: downscaling to study pore-scale

Lab on the chip (LOC) is used in oil and gas industry as visualization tools for fluid propagation, flooding, fracturing, and emulsification in recovery processes [86]. Microfluidics is a promising approach to quantify the micro scale processes and the real time control of hydrodynamics and chemical reactions to make a link between pore scale phenomena and production [7]. Current and envisioned energy applications of microfluidics address subsurface and surface operations (Figure 17) [7].

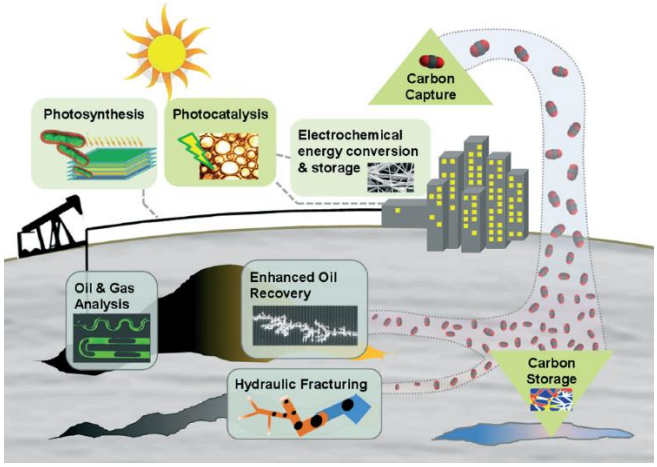

Figure 17. Illustration of applications of microfluidics for surface and subsurface operations and correlation to environmentally friendly processes. Reprinted with permission from [86], RSC 2014

Therefore, the microscale flow study is critical, and it is mainly performed via visualization techniques such as optical microscopy and high-speed visualization offering pore scale vision. The significance of visualization in microfluidic is due to real time analysis of mixing and chemical reactions, alteration in wettability, production of new phases, dynamic, kinematic and mass transport studies in a way that was never seen before in a laboratorial scale because of high

Reynolds number and convection forces associated to macro scale phenomena. Figure 18 illustrate a simple microfluidic device made of cured PDMS on glass.

Figure 18. Simple cure PDMS microchannels full of different dye fluids representing a micro model, Reprinted with permission from [87], ACS 2013

The material for making the device plays a dominant role in fabrication of microfluidic devices [88]. Surface properties of device materials are greatly amplified in microfluidics due to high surface to volume ratio, laminar flow through the microfluidics and dominancy of capillary effects [88,89]. Therefore, each material requires a certain microfabrication strategy depending on application and properties of the device. Moreover, the microfluidic pattern, size and operational condition vary for different applications. Thus, material, design, structural and operational conditions need to be evaluated to set up a prototype for micro pore dynamics in fractures that reassemble the harsh reservoir condition for $scCO_2$ foam fracturing. Microfluidics offers the possibility to study the coupling of hydrodynamics and mixing and reactive phenomena in such complex systems in hope to improve the $scCO_2$ foam stability and produce water compatibility for environmentally friendly oil production in hydraulic fracturing process.

2.9. Microfluidics in subsurface oil recovery

In hydraulic fracturing, before the recovery to the surface, foam travels through the fracture channel and meets the oil from formation rocks, so the critical processes concerned with oil recovery from tight shales occurs within the micrometric and nanometric scale of the cracks and pores in the rocks [3]. Microfluidic offers a great understanding of micro scale fluid transport and oil recovery to the surface. As early applications of micro-mechanics in energy sector began in the early 90's [3] when early micro models developed for two phase flow and oil-recovery [90] majority of research during this period of discovery was focused on EOR applications, through oil recovery from polymer floods, surfactant/water floods, nano floods using nano particles and foam floods [3]. The focus has been on oil displacement with pumping the liquids and studying the behavior of displacing fluid traveling through the porous medium and facing the oil in terms of compositional and conformational change [91], viscoelastic behavior [92], viscosity characterization, and stability [3]. In hydraulic fracturing simulations with micro models mainly the fluid propagation and hydrodynamic occurs through the fracture and micro cracks of shales, within the rock nanometer to millimeter sized pores of fracture. A discrete fracture network is adapted from characterization of shale reservoirs to stimulate production form hydraulically fractured well through diffusion, desorption, connectivity, and permeability is introduced in recent publications in literature. Figure 19 represents the ever increasing number and subject area for the publications with key word 'Fracture Microfluidics' in the last 10 years according to Scopus search engine [93].

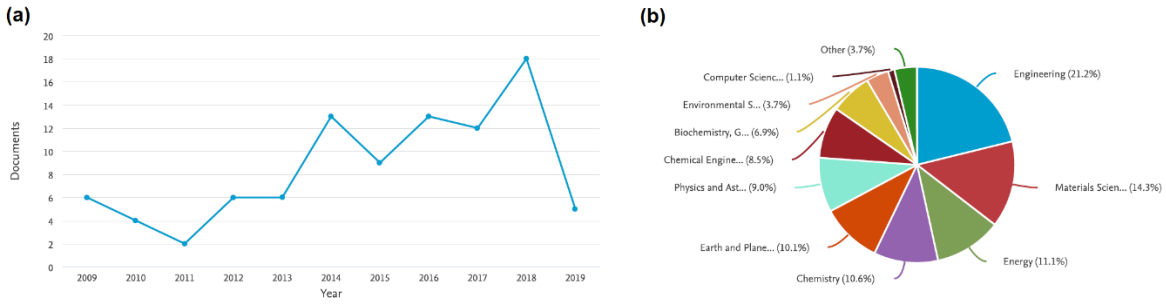

Figure 19. The status of recent publications with key word "Fracture Microfluidic" in Scopus data base (a) number of publications per year (b) publications according to subject area (data generated by Scopus data base) [93]

'Fracture microfluidics' is a general topic that covers variety of two-dimensional matrix-fracture micromodels applicable in EOR and hydraulic. Homogeneous and heterogeneous glass etched micromodels were employed for pore scale investigation of matrix-fracture interaction during CO_2 injection by Vahapcan and coworkers [94]. The authors insist phase behaviors and flow patterns to/from the fracture and from/to the matrix need to be studied to optimize the oil production [94]. Precise placement of proppant packs is critical to assure the conductivity in the fracture and continued flow of hydrocarbons from the formation into the producing well [3,25]. Consequently, optical microscopy emerged as helpful tool to study the pack forms, settlement or disintegration as flow rate and pressure changes in the reservoir [3]. There is an opportunity for design of microfluidic systems with pre-defined proppant particle distribution to optimize the fracture conductivity.

The majority of experimental works on stimulation of hydraulic fracturing with microfluidics were limited on applicability due to ambient operational condition [7]. There have been a few studies for high-pressure and high-temperature microfluidics with direct observation of flow in a medium that mimics the subsurface condition. Jimenez-Martinez and co-workers recently introduced two major studies on critical pore scale flow and transport mechanism in

complex network of fractures and matrix [95,96]. Authors studied three phase microfluidic simulated at reservoir conditions (8.3 MPa and 45°C) for production efficiency assessment of $scCO_2$ for re-stimulation with leftover brine (less miscible fluid)[95]. In their study, direct observation of dynamic evolution of $scCO_2$ restimulation in an oil and brine bearing process with high pressure – temperature microfluidics reveals this fact that presence of residual oil from initial production creates spatiotemporal variability for efficient interaction of $scCO_2$ with hydrocarbon and thus production increases. The study offers no direct observation on multiphase flow in the fracture and oil wet silicone micromodel pattern resembles the EOR application for mixing of oil-brine-$scCO_2$. Figure 20 represents the temporal snapshots of $scCO_2$ displacement process (top t=0s, middle, t=5.7s, bottom t=11.4s).

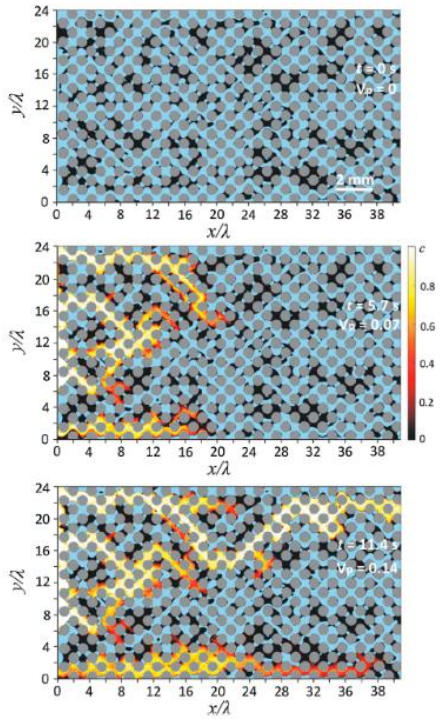

Figure 20. Time laps pore-scale observation of $scCO_2$ normalized concentration field c(x,t) [95]. Open access content on the web [95]

Three dimensional topographies of real fracture can be useful in replicating a realistic pattern on micromodels [7,97]. Carey and coworkers investigated the fracture-permeability behavior of ultra-tight shale using core flood device and X-ray tomography of fractures [98], conducting direct shear experiments the fracture patterns were emulated on shale samples and it is shown in Figure 21.

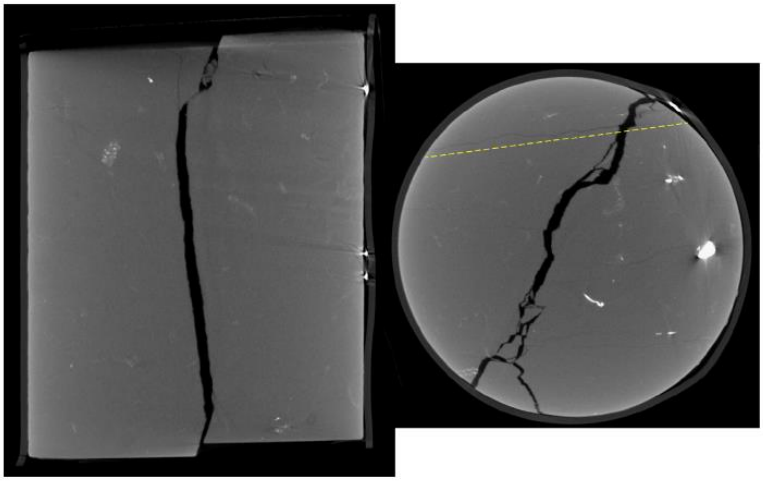

Figure 21. X-ray tomography of fracture patterns developed by shear experiment, reprinted with permission from [98] Elsevier 2015

In recent years, researchers from US Los Alamos National Laboratory have been working on experimental systems that allow direct observation of multiphase transport within geological micromodels with CCUS objective [7]. Porter et al used $scCO_2$ real-rock micromodels with idealized and realistic fracture patterns and the research was focused on water imbibition, hydrocarbon/brine displacement and $scCO_2$-brine-oil flow within the channels [97]. Middleton and co-workers introduced an etched shale micro-model to inject $scCO_2$ into a water saturated fracture to observe different localized flow pattern and dissolution of $scCO_2$ in water [14]. To the best knowledge of this author, the microscale

observation for stabilization of $scCO_2$ bubbles in concentrated electrolytes with confined movement in fractured medium for sustainable and environmentally friendly (waterless) oil recovery processes has not been studied. Pore level dynamic study of nanoparticle stabilized $scCO_2$ in different zones comprising fracture and micro cracks with interconnected or dead end topology requires novel microscale observation on subsurface emulated Lab-on-a-Chip (LOC) devices due to harsh reservoir condition and wide range of length scale involved in shale production [7].

Process selection for micromodel fabrication can be performed based on optical transparency of the glass device using photolithography and wet etching in inorganic acids to create the pattern on the glass followed by adhesive bonding [99]. However, lack of mechanical integrity and non-uniformity of geometry for the chips made by adhesive bonding (e.g. thermal fusion) affect the pressure resistivity and magnitude of light reflections from desired features within the micromodel [100]. Electromagnetic radiation provides a novel way to etch the glass. The invent of femtosecond (fs) infrared laser source shed new light on printing of in depth pattern in glass micro-chips with shorter pulse duration and energy deposition time leading to minimum damage and improved spatial resolution [101]. Femtosecond laser irradiation into the bulk glass entails nonlinear adsorption and modifies the material at focal point, and it is followed by wet etching to create microstructures [102]. The programmed laser path file and a polished fused glass silica substrate (SiO_2) are often loaded to glass 3D etching devices [103]. The predetermined network pattern (designed by CAD) is directly 'laser-written' inside the glass substrate and the entire procedure (prior wet etching) is automated and computer controlled [100] thanks to combination of 3D microscanner (fast writing of micro vectors with micrometric

resolution) and precise micrometric 3-axes system [103]. The process eliminates additional steps for sealing the microchip such as anodic or thermal bonding.

Figure 22 exhibits an amplified femtosecond fiber laser system (IMRA America, FCPA μJewel), operating at a wavelength of 1045 nm with a 450 fs pulse width and 100 kHz repetition [104].

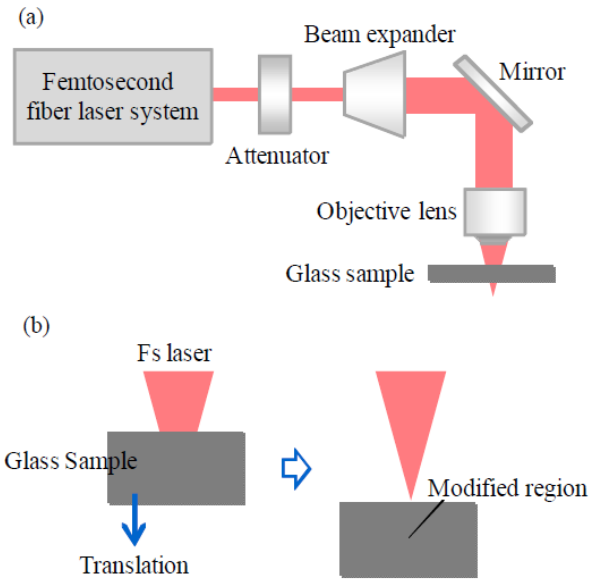

Figure 22. Fs fiber laser system for glass sample modification process (a) laboratorial setup (b) using a motorized stage helps to create a linear modified region [104], open access content on web [104]

A microfluidic setup for high pressure – temperature applications consists of gas cylinder and pumps, fluid mixers, microfluidic chip sealed and contained in stainless steel pressure vessel with sapphire view cell, pressure controllers and transducers and visualization system. When the chip is ready, analysis of real time incidents inside the chip is performed by optical methods. A basic microfluidic setup may include external pump, microfluidic device, pressure controllers and visualization system [105]. Figure 23 depicts a common laboratorial microfluidic setup including external pumps, microfluidic chip, inverted light microscope, camera and image processing computer unit.

Figure 23. A basic microfluidic setup including microfluidic chip, inverted light microscope, camera, and image processing computer unit.

The pump injects the fluid with pre-defined flow rate to chip pattern from the inlet tube and depending on the specific application, it may interact, displace, or saturate the chip with injected fluid. The typical setup utilizes real-time visualization, quantification or control of flow [105]. For visualization system, if the chip is transparent, a transmitted microscope (light source and optical access are at the opposite side of the chip) or a reflected microscope are employed. The example of pressure vessel design for hosting the microchip is shown in Figure 24. In this compartment two sapphire window glass will make a sandwich with glass microfluidic chip in stainless-steel high-pressure housing (pressure vessel) [106].

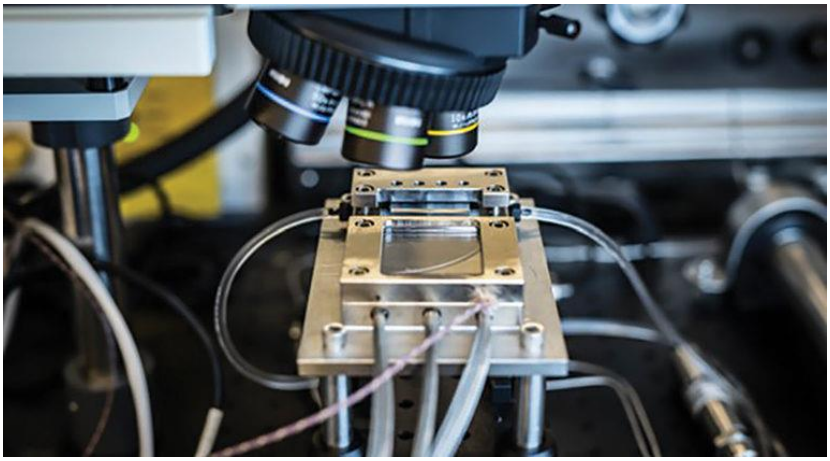

Figure 24. Pressure vessel containing microfluidics in bulky visualization instalment, open access content on web [106]

Accordingly, the illumination system is set on top of the cell camera and objective lens on the bottom part will detect the reflective light from glass microfluidic chip.

The microfluidic fabrication techniques for micromodels tolerable to high pressure were previously explored in the literature. Tigglaar and coworkers discussed fabrication and high-pressure testing of glass microreactor chips through in-plane connection of fibers to chips to test flow through glass capillaries connected to the microreactors[107]. They presented their findings related to bond inspection, pressure tests (up to 69 MPa) and in-situ reaction monitoring by ^{1}H NMR spectroscopy. As such, their platform may not be optimal for relatively large injection rates, pre-generation of multiphase fluid systems for in-situ visualization of complex fluids in permeable media. Paydar and coworkers presented a novel way to prototype modular microfluidics using 3D-printing[108]. This approach does not seem well-suited for high-pressure applications since the microchip material is a photocurable polymer and the chip is able to withstand only up to 0.4 MPa. Most microfluidic experimental studies related to transport in fractured systems reported in the literature focus on ambient temperature and relatively low pressure conditions[7]. There have been several studies with a focus on direct observation of microfluidic systems that mimic subsurface

conditions. For example, Jimenez-Martinez and co-workers introduce two studies on critical pore-scale flow and transport mechanisms in a complex network of fractures and matrix[95,96]. The authors studied three-phase systems using microfluidics under reservoir conditions (8.3 MPa and 45 °C) for production efficiency; they assessed $scCO_2$ usage for re-stimulation where the leftover brine from a prior fracturing is immiscible with CO_2 and the residual hydrocarbon[95]. Oil-wet silicon microfluidic devices have relevance to mixing of oil-brine-$scCO_2$ in Enhanced Oil Recovery (EOR) applications; however, this work does not directly address pore-scale dynamics in fractures. Another example is work by Rognmo et al. who studied an upscaling approach for high-pressure, in-situ CO_2 foam generation[109]. Most of the reports in the literature that leverage microfabrication are concerned with CO_2-EOR and they often do not include important fabrication details. To the best of the authors' knowledge, a systematic protocol for fabrication of high-pressure capable devices for fractured formations is currently missing from the literature.

Chapter 3: Materials and Methods

3.1. Complex fluid development

High salinity brine is synthesized according to procedure introduced by Hosseini et al [17]. The Mississippian Limestone Play (MLP) recipe contains aqueous solution of more than 202,848 ppm total dissolved solids consisting of $CaCl_2.2H_2O$ (Fisher Chemical, Certified ACS), $MgCl_2.6H_2O$ (Fisher Chemical, Certified ACS, Crystalline), $SrCl_2.6H_2O$ (Fisher Science Education, Lab Grade), Na_2SO_4 (Fisher Chemical, Certified ACS, Granular) NaCl (Fisher Chemical, Certified ACS, Crystalline) and KCl (Fisher Chemical, Potassium chloride for calomel cells, Crystalline). The salts were added to reverse osmosis and deionized water (RO- DI- water). The salt type and concentration in MLP brine are shown in Table 1. The highly concentrated brine synthesized according to laboratorial recipe adopted from original MLP recipe (202,848 ppm, ~200,000 ppm) was then diluted to 66,666 ppm (3X) and sea-water level 33,333 ppm (6X) nominal concentrations.

Table 1. Mississippian Limestone Play (MLP) brine composition (original and laboratorial concentrations), reprinted with permission from [28] ACS 2019

MLP	Elements	Ca	Mg	Na	K	Cl	Sr,Fe,Mn,SO_4,etc	Total
Nominal Concentration	Concentration (mg/L)	12,780.4	2,601.1	64,779.4	374.9	120,630	1,482.6	202,648.4
Synthesized MLP	Salt	NaCl	Na_2SO_4	KCl	$MgCl_2.6H_2O$	$SrCl_2.6H_2O$	$CaCl_2.2H_2O$	Total
Lab Concentration	Concentration (mg/L)	163,661	1,224	715	21,759	1,535	46,886	235,782

Zwitterionic surfactant HDP-0761-12-2AM was provided by Harcros Chemicals Inc. The surfactant structure was designed for optimum ionic activity in form of short chain aliphatic molecules with positive amine and negative sulfonate functional groups. The main ingredients in

the form of solvent and additive to the surfactant solutions are listed in Table 2 (provided by Harcros).

Table 2. Solvent and additives in HDP-0761-12-2AM surfactant provided by Harcros, reprinted with permission from [28] ACS 2019

Chemical Name	CAS number	%
Water	7732-18-5	60 -< 70
Sodium Chloride	7647-14-5	5 -< 10
3-chloro-1,2-Propanediol	96-24-2	< 0.2
Other components below reportable levels	-	30 -< 40

The hypothetical structure of Zwitterionic Surfactant (ZS) is shown in Figure 25.

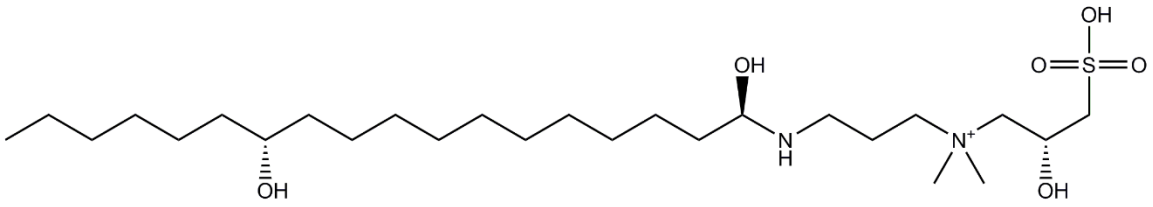

Figure 25. Zwitterionic surfactant hypothetical structure based on the provided structure by Harcros company and FTIR and Raman Spectroscopy analysis

The surfactant was dissolved in 33.3 kppm and 66.7 kppm brines to form 1 w/w% reference solutions. Polyelectrolyte complex nanoparticles (PECNP) are prepared according to the procedure developed by Barati and co-workers [17,63,64]. Branched Polyethyleneimine (PEI) is obtained from Sigma Aldrich with an average molecular weight of 25,000, 1.03 g/mL density at 25 °C and corresponding viscosity ranging between 13,000 cP to 18000 cP at 50 °C. Dextran Sulfate (DS) is provided from Sigma Aldrich with 500,000 molecular weight. PEI and DS are separately dissolved in high salinity brines with 1 w/w% and the pH for PEI solution is lowered to 8.5 by addition of 6 N HCl (up to 1 ml gradual addition of acid to 100-120 ml of PEI solution)

[17,64]. pH calibration curves for HCL 6N amount added to PEI 1 wt% solution in 33.3 kppm and 66.7 kppm are shown in Figure 26.

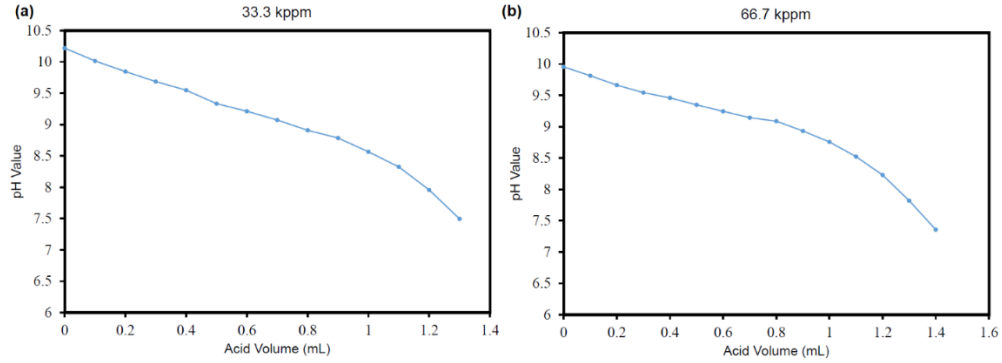

Figure 26. pH calibration curves for HCL 6N amount added to PEI 1 wt% solution in 33.3 kppm and 66.7 kppm brine solutions [28]

In order to tailor the properties of PECNP, linear PEI, poly(allylamine) is purchased from Sigma Aldrich with an average molecular weight of 17,000, 1.02 g/mL density at 25 °C and corresponding viscosity of 50 cP at 50 °C. The poly(allylamine) contains a major portion of primary amine groups and in combination with DS forms a modified PECNP with enhanced ionic properties for CO_2-water lamella stabilization. The solution of 1 w/w% DS in high salinity brine is prepared and PEI and DS solutions are mixed accordingly. The mixing ratio of PEI to DS, to the diluting brine solution (PEI:DS:Brine) is chosen to be 3:1:0.1 to make positively charged nanoparticles. The proportion of mixing linear PEI with DS can be similar or different according to zeta potential and particle size preliminary test results. This ratio is developed based on previous observations with zeta potential and particle size measurements [32,63]. The nanoparticle solution is mixed with surfactant solutions (1 w/w %) in 33.3 kppm brine and 66.7 kppm brine for 20 minutes to form the PECNP-surfactant complexation with different mixing ratios of PECNP:surfactant 0:10, 1:9, 2:8, 3:7, and 4:6. The concentration of the surfactant remains constant in mixing with nanoparticles (1 w/w %). The foaming solution is later mixed with $scCO_2$ (90 v/v %) in inline

mixers at 40 °C to form the actual foam. Figure 27 represents the schematic of colloidal synthesis and foam lamella constituents.

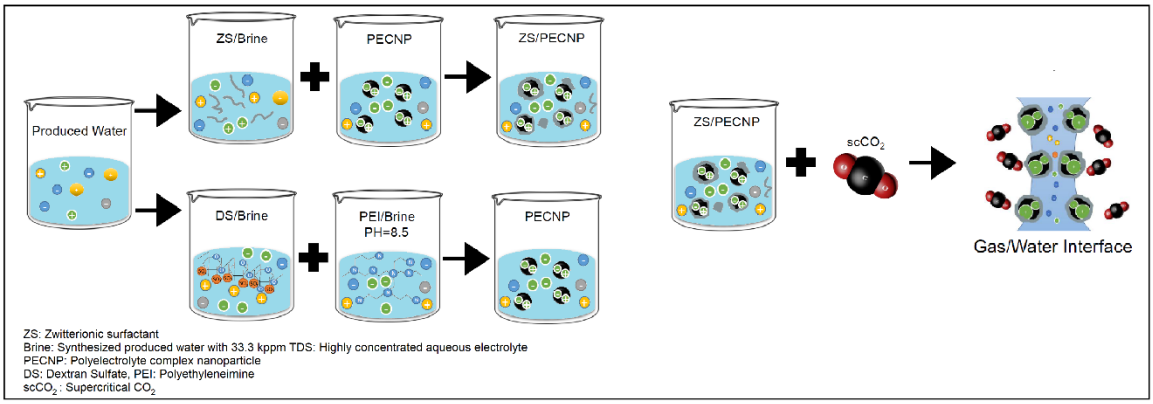

Figure 27. Laboratorial procedure to prepare ZS/PECNP complexes to enhance CO2-high salinity brine interface

To investigate the molecular complexation in EOR application, the choice of surfactant was different. The SURFONIC N-120 used for EOR study belongs to the class of Nonyl phenol ethoxylates with a non-ionic nature (upon aqueous hydration) and 12 Ethylene oxide (EO) groups. Huntsman Chemicals, Woodlands, TX, USA (CAS # 9016-45-9), synthesized the surfactant for improved water compatibility in EOR. Figure 28 exhibits the chemical structure of SURFONIC N-120.

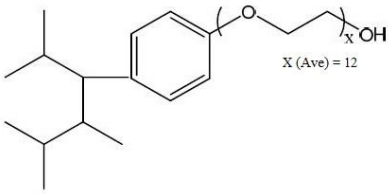

Figure 28. Chemical structure of SURFONIC N-120 surfactant [110,111]

The EO group is a surface-active agent compatible with other nonionic surfactants and with ion active species [112]. The theoretical molecular weight and hydroxyl number of the surfactant are 748 and 75, respectively. The density is 1.066 g/mL at 25°C. The surfactant solution was prepared

in 33,667 and 67,333 ppm salinities. The solution's CMC was obtained as 0.11 wt.% [63]. Therefore, the surfactant concentration in the solution was kept at 0.1 wt.% for all the experiments to preserve the surface activity of the surfactant and to avoid the foam film stratification [113]. Details of core flooding application with complexation PECNP and SURFONIC N-120 can be found in our recent publications for foam flooding in carbonate reservoirs [48,110].

3.2. Fourier Transform-Infrared (FT-IR) spectroscopy

The chemical functional groups on the surfactant molecules were examined with a Spectrum 400 FT-IR spectrometer (Perkin Elmer, Waltham, MA) equipped with two temperature stabilized deuterated triglycine sulphate detectors. A small aliquot of liquid sample was deposited onto the diamond crystal top plate of an attenuated total reflection (ATR) accessory (GladiATR, Pike Technologies, Madision, WI). Sixty scans were co-added over the range of 4000-650 cm^{-1} with a spectral resolution of 4 cm^{-1}. Air was taken as the reference for the background before each sample. After acquisition of each spectrum, the ATR plate was cleaned in situ by cleaning it with ethanol solution three times and allowing it to dry. No residue from the previous sample was observed in subsequent background spectra and when compared it to the previous background spectra. Also, an atmospheric correction routine is performed for CO_2/H_2O suppression by the Spectrum software (PerkinElmer, Waltham, MA).

3.3. Dynamic light scattering

The hydrodynamic diameter of ionic particles was measured by dynamic light scattering measurement, through the average of three readings using a NanoBrook Omni Particle sizer and zeta potential analyzer by Brookhaven Instruments. pH of colloidal solutions, density, and viscosity of each sample as well as mean particle diameter were employed for determining the zeta potential. For the zeta potential measurements, the samples were diluted 20 times in background

electrolyte of 1mM KCl where the average of three readings were considered for analysis on the NanoBrook Omni. The standard 35 mV red diode laser with nominal 640 nm wavelength was employed to detect the size range, size distribution and electrophoretic mobility using the Smoluchowski model.

3.4. The air-foam stability measurements

Experimental setup was designed to quantify bulk foam height as a function of time to determine the aqueous foam stability. The predetermined amount (10 mL) of foaming solution comprising different proportions of PECNP to surfactant (PECNP:Surfactant of 1:9, 2:8, and 3:7) was transferred to 20 mL vials for primary foam decay analysis. The sealed and scaled vial containing the 50 % mixture with air was heavily agitated for 30 times for perfect mixing of air and liquid. The scaled vial was placed and kept in an oven with a constant temperature of 40 ºC (Figure 29). A camera was set inside the oven and the air foam height in the vials was recorded every minute. Figure 29 illustrates the setup for air-foam stability measurements.

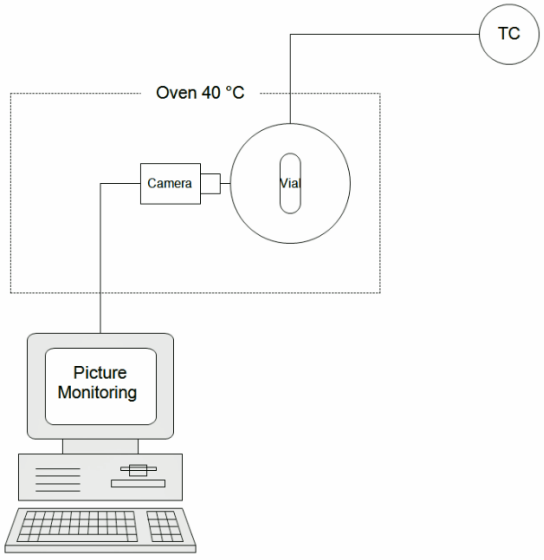

Figure 29. Simple vial test for PECNP/Surfactant mixtures in high salinity brine mixed with air as preliminary test before actual test with $scCO_2$ [17], reprinted with permission from [28] ACS 2019

3.5. Interfacial tension analysis

$scCO_2$ interfacial tension in high salinity brine containing surfactants and PECNP was measured according to axisymmetric drop shape analysis of pendant drop by a tensiometer at pressures and temperatures in which CO_2 is in supercritical conditions. The $scCO_2$ bubble is formed on the tip of stainless-steel capillary in high pressure chamber (1330 psi) filled with PECNP-surfactant solution while isothermal temperature of 40 °C was maintained by applying thermal jackets around the pipes and chamber. The DROPimage software and high-resolution camera were employed to measure the surface tension for each bubble in dynamic mode for 1 h. A minimum of three runs for each sample was recorded. Schematic of the employed tensiometer in this analysis is provided in Figure 30. The droplet area was determined by analyzing the droplet profile using a camera coupled with image analyzer software (DROPimage).

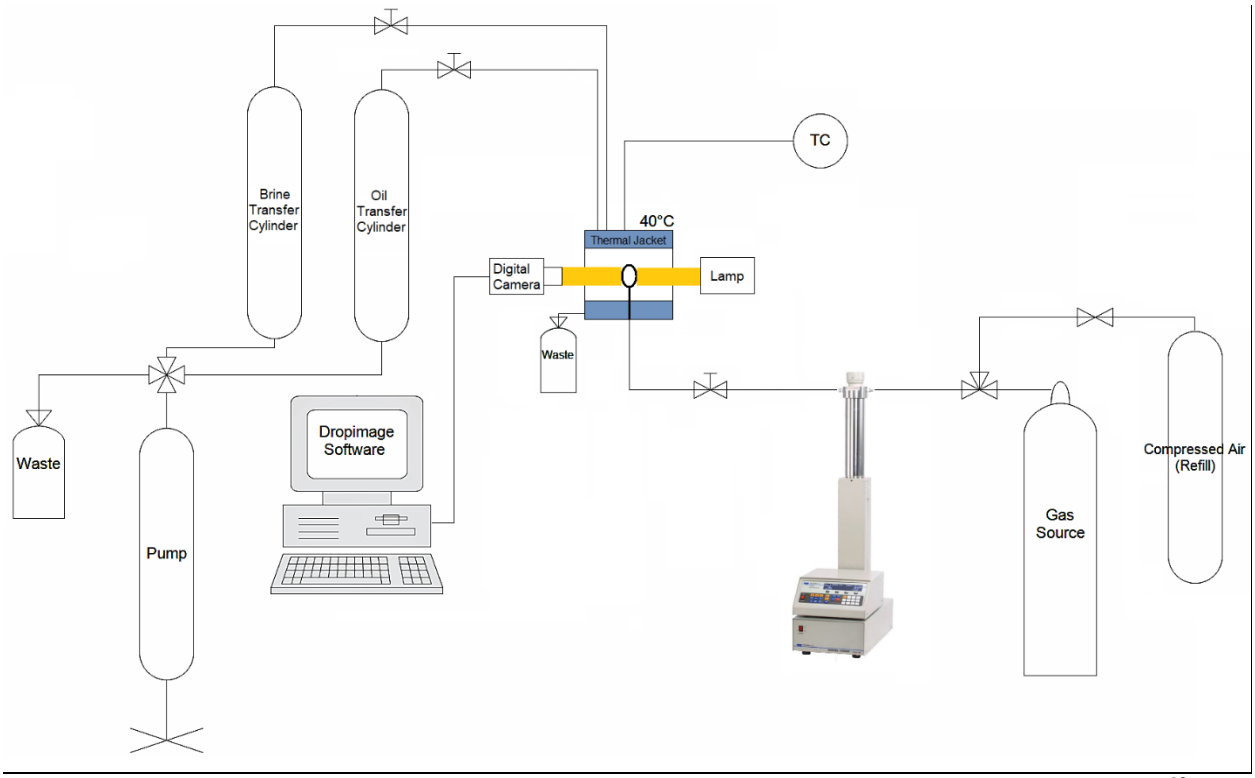

Figure 30. Process flow diagram for interfacial tension analysis setup, reprinted with permission from [28] ACS 2019

Critical micelle concentration (CMC) was determined with different concentrations of surfactant dissolved in high salinity brines and the corresponding interfacial tension was estimated accordingly. Dilatational elasticity was estimated according to a ramp-type perturbation approach previously presented by Tewes and coworkers [114]. The variation of interfacial pressure after compression of equilibrated surface layer of pendant drop ($\Delta\pi_e$) is correlated to surface area variation ($\frac{\Delta A}{A_i} = \frac{U_b t}{A_i}$) as a result of mechanical strain to estimate the equilibrium surface dilatational elasticity [114,115]:

3-1 $$\Delta\pi_e = E_e \frac{U_b t}{A_i}$$

where A_i is surface area prior to applying the mechanical strain, U_b is the constant velocity of compression during the time (t) and E_e is equilibrium surface dilatational elasticity. The non-equilibrium portion of surface pressure variation ($\Delta\pi_{ne}$) is also calculated based upon dissipation of accumulated energy during compression and relaxation [114], where τ stands for relaxation time.

3-2 $$\Delta\pi_{ne} = \frac{E_{ne} U_b t}{A_i}(1 - e^{-\frac{t}{\tau}})$$

Details of calculations are found in our recent publication [28].

3.6. Rheological measurements

Oscillatory shear stability of bulk foam is examined through stress-controlled rotational measurements using an Anton-Paar MCR 302 rheometer. The temperature was controlled by a water-circulating bath (6 to 40 °C). The setup utilized feed cylinders, pumps, circulating coolers and thermal isolators (Figure 31). A Couette geometry module was used in a pressure cell to study the viscoelastic behavior of $scCO_2$ foam. Constant (2000 s^{-1}) and variable shear rates (2000 s^{-1} to

100 s^{-1}) were used for static (stagnant foam in the cell) and dynamic (continues flow of foam in the cell) measurements at 40 °C and 1,350 psi. The detailed procedure is introduced as following:

The rheometer setup consists of feed cylinders, pumps, the main rheometer unit connected to a PC software and a waste pump collector. To maintain isothermal conditions in lines, valves and pumps, a recirculating cooler (ISOTEMP 1016D) and heating tapes were used and the temperature was set to 6˚C. Pump A is refilled with CO_2 and temperature and pressure were set to a supercritical state of 40°C and 1350 psi. Pump B was also filled with the foaming liquid. Lines containing $scCO_2$ and foaming solution were connected, and the produced foam flowed through the rheometer cup and from there to the waste collector pump (Pump C). The proportion of $scCO_2$ to foaming mixture was chosen to be 9 to 1 based on previous observations by our group [32,63]. The measurements were carried out in dynamic (constant flow of foam solution), static (stagnant foam liquid in the cup) and ramp (variable shear rate in static mode). During the static and ramp modes 45 to 120 data points were collected with 30-second time intervals. The Rheoplus software was used to set the rheological adjustments. The main rheometer unit was connected to a PC software and a waste pump collector.

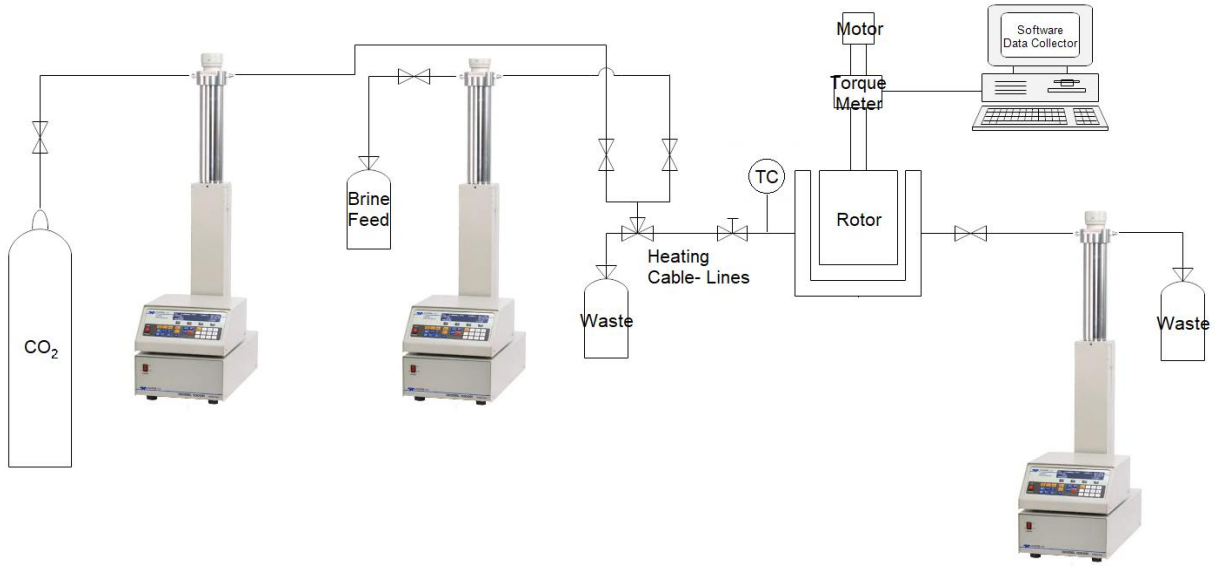

Figure 31. Process flow diagram for rheometer setup, reprinted with permission from [28] ACS 2019

3.7. Raman spectroscopy

Raman spectra of lyophilized powders were determined by using a LabRAM ARAMIS Raman spectrometer (LabRAM HORIBA Jobin Yvon, Edison, NJ) with a HeNe laser (λ = 633 nm, power = 17 mW) as an excitation source. The instrument conditions were: 200 µm confocal hole, 150 µm wide entrance slit, 600 g/mm grating, and 50X long working distance objective Olympus lens. Data acquisition was performed using LabSPEC 5 (HORIBA Jobin Yvon). The samples were mounted in a computer-controlled, high-precision x–y stage. Spectra were acquired over a range of 700–2400 cm^{-1} with 60 s exposure time and 10 times accumulation.

The acquired Raman spectra were processed using Matlab (the MathWorks, Inc. Natick MA, USA) to smooth the curves (through binning adjacent data points), to remove digital noise (through binning adjacent data points) and to remove the fluorescence background (by subtracting a fifth order polynomial fit to the original spectrum). Furthermore, contributions to the spectra from cosmic rays were removed manually when appropriate. The spectra of mixtures of PECNP and surfactant (1:9 ratio) were fit with average surfactant and PECNP spectra using least-squares

fitting in a manner similar to the method described by Shafer-Peltier for modeling of biological Raman spectra [116].

Spectra of dextran sulfate and Polyethyleneimine were also collected in the same manner to aid in data interpretation and peak assignment but were not included in the model. Vectors representing each fit were created using the MATLAB polyval function and residuals of each fit were determined. An average of three to four spectra were then used (except in the case of the PECNP:Surfactant complex spectra) for further analysis.

3.8. Transmission Electron Microscopy (TEM)

5 µl of solutions of PECNP and PECNP-surfactant mixture were placed onto a 300 mesh Lacey carbon copper grid (EMS LC 300 Cu), respectively, for 1 minute and blotted twice with a filter paper. The 300 mesh copper grid with PECNP and PECNP-surfactant mixture was examined using a 200 kV FEI Tecnai F20 XT field emission transmission electron microscope at an electron acceleration voltage of 160 kV. TEM images were captured using a normative and standardized electron dose on eucentric specimen stage and a constant defocus value from the carbon-coated surfaces. Images were randomly acquired in a size of (1024 x1024) pixel resolution at 10 different locations within the grid.

3.9. View cell, dynamic fluid loss and sand pack measurements

The $scCO_2$ foam stability, core fluid loss properties and fracture clean up performance were examined via a high pressure-high temperature foam flooding apparatus utilized with shear loop mixer, sapphire view cell, dynamic fluid loss and sand pack modules. The internal view of foaming flood apparatus is shown in Figure 32. Figure 32a reflects the view cell, vertical core holder and modules for fluid loss and sandpack and Figure 32b represents the close view of sandpack and housing for view cell module.

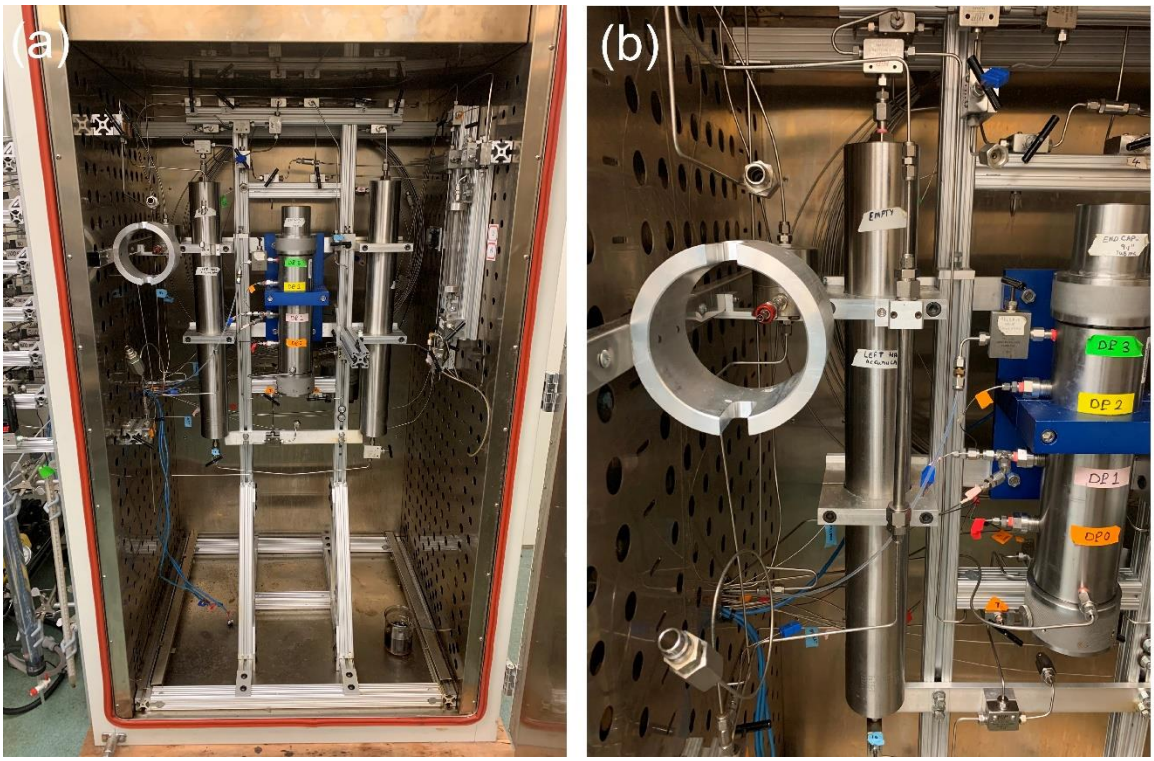

Figure 32. Internal view of high pressure-high temperature foam flooding apparatus (a) view cell, vertical core holder and modules for fluid loss and sandpack (b) the close view of sandpack and housing for view cell module

The foam is generated with in-line mixing of $scCO_2$ foam (40°C, 1350 psi) and the aqueous solution (surfactant or PECNP:Surfactant solutions) prepared in 33.3 kppm and 66.7 kppm high salinity brine with different proportions of PECNP:Surfactant (1:9, 2:8, 3:7, and 6:4, with 0:10 being the surfactant solution itself). The process flow diagram (PFD) of the system is presented in Figure 33.

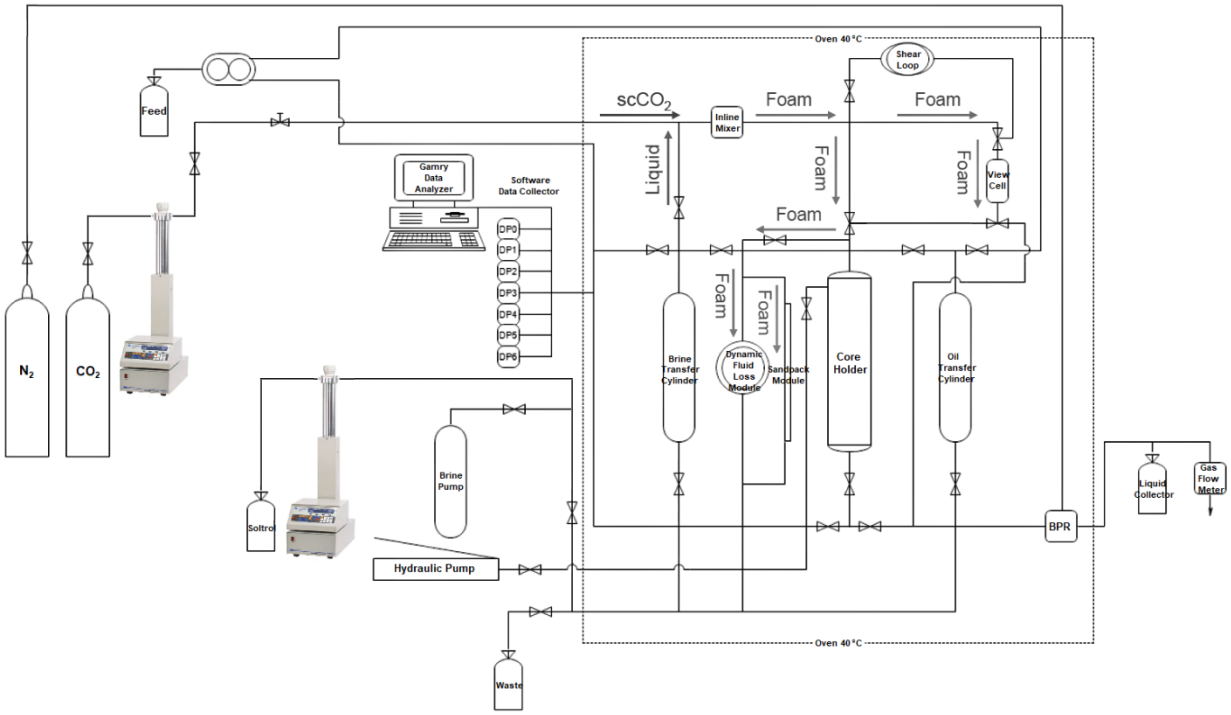

Figure 33. Flow diagram for high pressure, high temperature CO_2 foam flooding setup with view cell foam stability module, fluid loss and sand pack modules. Pathways A, B and C represent the foam flow through view cell, dynamic fluid loss and sand pack modules, reprinted with permission from [28] ACS 2019

The foaming liquid is mixed with $scCO_2$ and the components are directed toward the Swagelok inline mixer with 7 μm pore size. The generated foam is then directed to the view cell to measure the foam stability and foam textural properties. A GoPro camera was set to record the foam height on every minute. Figure 34 illustrates the foam generation and degradation in view cell captured by GoPro camera.

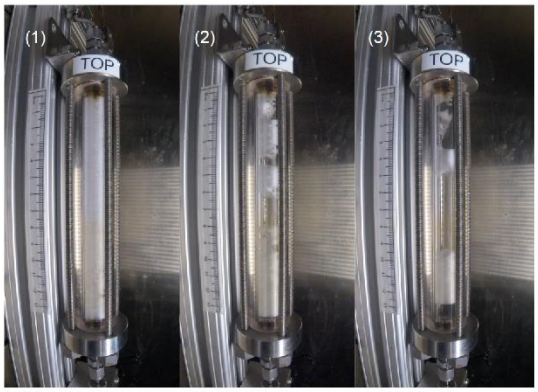

Figure 34. View cell measurements carried out to measure the foam stability in absence of oil, captured by GoPro camera inside the high pressure-high temperature foam flooding apparatus. (a) Foam isolation in the view cell (b) foam degradation (c) fully drained and destabilized foam, reprinted with permission from [28] ACS 2019

After the foam was established in the view cell, oil was immediately introduced to the view cell to evaluate the stability of the of $scCO_2$ foam in the presence of crude oil. Figure 35 depicts the process of foam destabilization in presence of oil captured by GoPro camera.

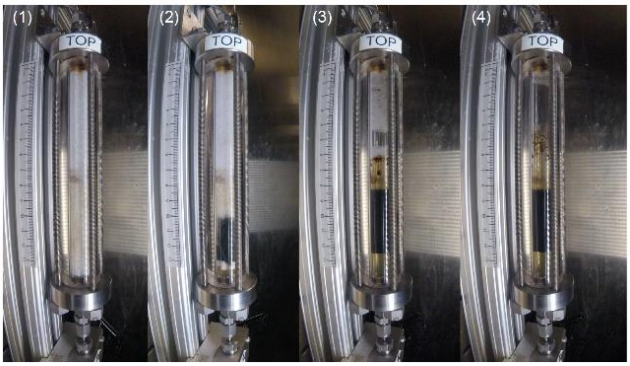

Figure 35. View cell measurements carried out to measure the foam stability in presence of oil, captured by GoPro camera inside the high pressure-high temperature foam flooding apparatus. (a) Foam isolation in the view cell (b) Introduction of the oil (c) Foam drainage in the presence of oil (d) Total foam disappearance and oil dominance, reprinted with permission from [30]. SPE 2018.

The generated foam could also be directed to the fluid loss module embedded low with a permeability Kentucky sandstone (Table 3) sitting perpendicular to fluid flow to measure the ability of fracturing fluid to prevent the leak-off in the tight formation.

Table 3. Physical properties for Kentucky sandstone core, data provided by Kocurek Industries. Reprinted with permission from [17] Copyright SPE 2018.

Core	Gas Permeability	Brine Permeability	Porosity	UCS Strength
Kentucky Sandstone Core	1 to 5 mD	0.18 mD	14%	8000 psi

The fluid loss module is presented in Figure 36 as a core sits adjacent to the fluid flow path and degree of fracturing fluid flow and leak-off in low permeability rocks were measured. The $scCO_2$ foam was generated and directed to the fluid loss setup where the tight core was exposed to foam flow. Two pathways directed the flow through the cell, one was adjacent to the core and the other through the core (fluid loss). The volume of gas and liquid coming out of the core were recorded versus time.

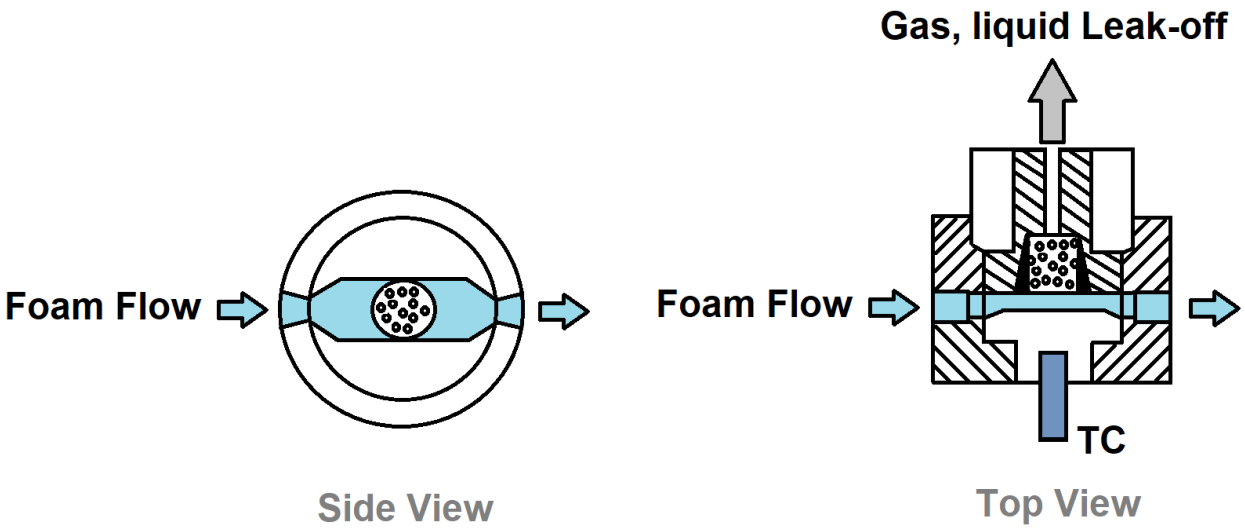

Figure 36. Fluid loss module from different views used in HPHT CO_2 foam apparatus (side and top view) [17] Copyright SPE 2018.

The volume of lost gas and liquid through the core and their corresponding fluid loss coefficient were measured according to equation [117]:

2-3 $$V_L = C_w\sqrt{t} + S_P$$

Where V_L is the total fluid loss volume (gas and liquid), C_w is fluid loss coefficient (wall-building coefficient) and S_p is the volume leaked off before any filtration occurred.

The mixture of $scCO_2$ and foaming solution can also be directed to a pack of low density, 20/40 mesh size, ceramic proppant (CARBOECONOPROP provided by CARBO CERMAICS INC.) [118] Saturated with high salinity brine (predetermined pore volume) and MLP crude oil. The sequence for sand pack experiment includes primary brine flood to measure the initial pack permeability, oil flood for pack saturation, foam flood for pack clean-up and secondary brine flood for final pack permeability after clean-up. The pressure difference across the dynamic fluid loss and sand pack is monitored with Validyne pressure transducers linked to Gamry data analyzer. The system contains the left transfer cylinder filled with foaming solution and right transfer cylinder filled with MLP crude oil with properties provided in Table 4.

Table 4. MLP crude oil physical properties

Oil	Viscosity (40 °C, 1.66 s^{-1})	Density
Mississippian crude oil	3.88 cP	0.83 g/cm^3

3.10. Macro visualization experiments

A novel foam visualizing system is presented in this work to investigate the $scCO_2$ foam structure including bubble shape, size and distribution, lamella stability and instability in the presence of oil for hydraulic fracturing applications, which is also applicable to EOR. The $scCO_2$ foam stability was examined via a high-pressure, high-temperature foam flooding apparatus utilized with transfer cylinders, inline mixer, sapphire view cell and back pressure regulators (BPR). The schematic of the system is presented in Figure 37.

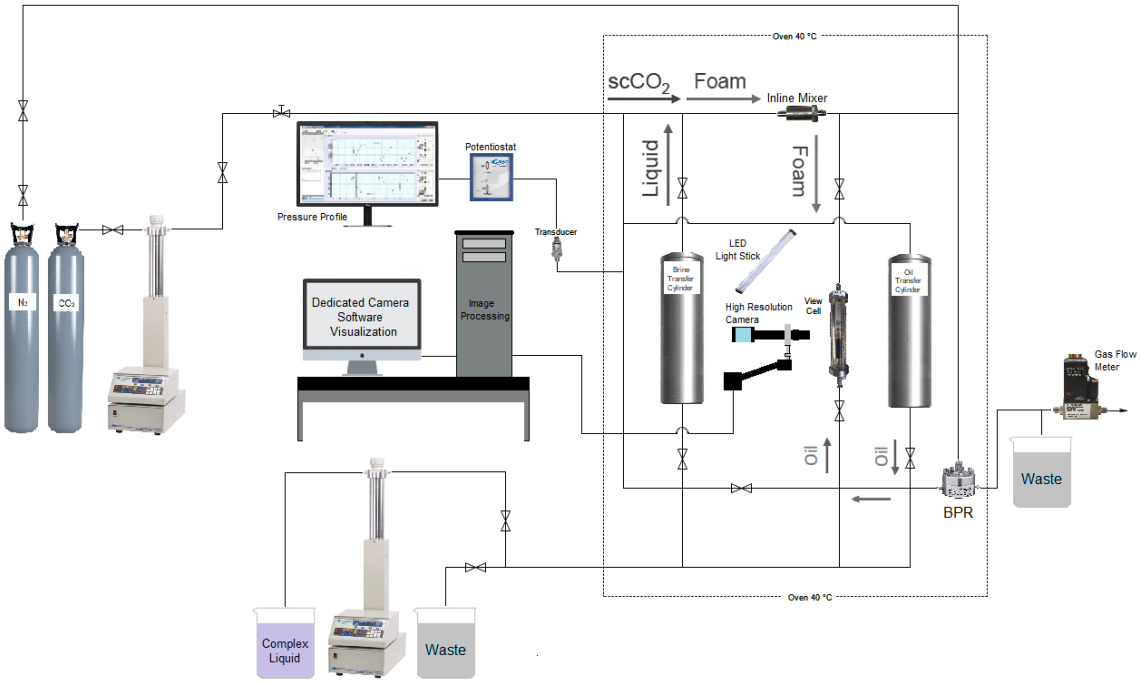

Figure 37. Flow diagram for high-pressure, high-temperature CO_2 foam flooding setup with view cell foam connected to high resolution camera and visualization unit

For more accurate microstructural observations with engineered light source, a 14 MP monocular digital microscope camera from AIHOME with 180X or 300X zoom c-mount lenses was employed to analyze the microstructure and real time bubble dynamics of generated foam in the view cell. An adjustable arm was set on the set-up to alter the horizontal and vertical movement of camera. Pixel size with this camera is 1.43*1.43 μm and 60 fps frame rate. The R/G/B colors are adjustable and five times digital zoom is possible with the software (manual zoom: 180X). Figure 38 reveals the picture of deployed AIHOME monocular microscope camera including the main module and camera lens and c-mount lens dimensions.

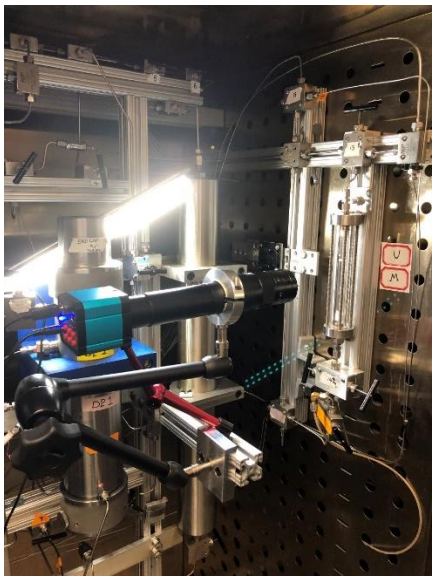

Figure 38. Multiphase visualization with millimetric field of view. The light source location is on top of the camera or on other positions with respect to the camera to adjust light reflection for photography

Working distance and zoom capability are important to adjust a clear view for mechanistic studies and Figures 37, 38 demonstrate the setup utilizing this camera in combination with view cell while illumination source location varies in order to obtain an optimum light in the picture. The light source location can be set direct on the camera or it can be located on other positions with respect to the camera to avoid the blurriness of 3D foam in observation.

3.11. Image processing

The obtained images with AIHOME camera are analyzed with special dedicated software HAYEAR to obtain the bubble size correlated to each picture. The HAYEAR software graphic user interface for image and video capture and analysis. Once the bubble dimension and scale (pixel/distance) is known, a general image analysis tool ImageJ (ImageJ, an open-source Java image-processing program inspired by NIH image) coupled with MATLAB image processing tool (the MathWorks, Inc. Natick MA, USA) are employed to enhance the quality of images including

light, contrast and sharpness and to obtain the average bubble size and bubble size distributions for each foam microstructural image (Figure 39).

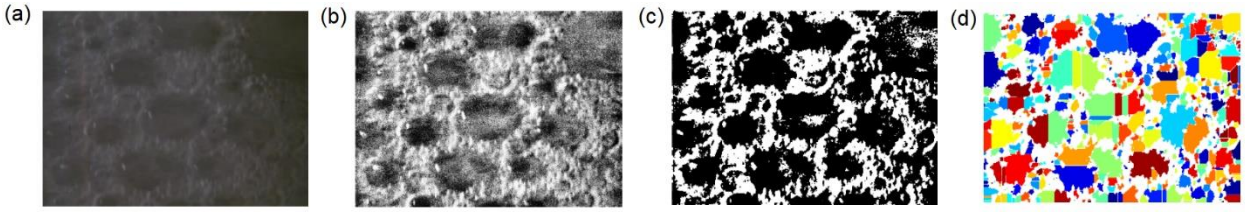

Figure 39. Image processing levels on pictures obtained in field of view (a) original image cropped to find optimum lighting in the area (b) Matlab processed image with corrections of light, contrast and sharpness (c) Image J processed to black and white contrast (d) final processing with water-shed segmentation method to find the pore size and pore size distribution

For higher magnifications, it is possible to observe and quantify the singular bubble phenomena such as lamella drainage, bubble coalescence and disproportionation as well as snap-off, lamella division and leave behind mechanisms [119]. The enhanced image with MATLAB is then processed through ImageJ for pore size distribution analysis. The pore size distribution is obtained with the following protocol. First, the desired area of the picture is selected and duplicated. Then, the image is converted to gray scale (8-bit image type). The known distance obtained from HAYEAR software is entered to ImageJ with 'Set Scale'. FFT Bandpass Filter command filters large structure down to 160 pixels. "Adjust Threshold" is employed to create the black and white contrast between two phases. By checking "over/under" the contrast is varied in a green and black colored background and on B&W, the ultimate black and white contrast is set. Eventually, using analyze particles with setting size range on 5 to infinity and selecting to show overlay, the summary of particles and particle size distribution is obtained. "Analyze particle" in imageJ determines the bubble size distribution. Some larger bubbles with this method are ignored and more accurate analysis is required. More accurate analysis for pore or bubble size distribution of 2D porous media images was introduced by Rabbani and coworkers to detect pore and throats

for analyzing the connectivity and permeability of the network [120]. The method can also be applied to 2-D images. Using the method introduced by this group (online – open access MATLAB code [85]) and input of resolution (micron/pixel) specific to each picture, the bubble size distribution and bubble map area are obtained. Their analysis is deemed to be more accurate due to detection of vast majority of bubble areas in the map compared to original processed photo shown in Figure 39d. The introduced method by Rabbani et al is a new computational algorithm to detect pore (or bubble) network by coupling distance function and watershed segmentation [120]. These results are comparable with commercialized foam analysis systems. Accordingly the remainder of PECNP-surfactant generated $scCO_2$ foams can be analyzed with a combination of three steps: (i) image quality enhancement with MATLAB image processing toolbox (ii) black and white phase differentiation and saturation enhancement with ImageJ (iii) using computational network algorithm introduced by Rabbani et al [85] to detect bubble area and distribution in the corresponding micrograph.

3.12. Microfluidic device fabrication (Photolithography)

2D CAD design is drawn with predetermined size for fracture and micro cracks. Figure 40 represents the 2D CADs for photomask printing alongside the magnified main features.

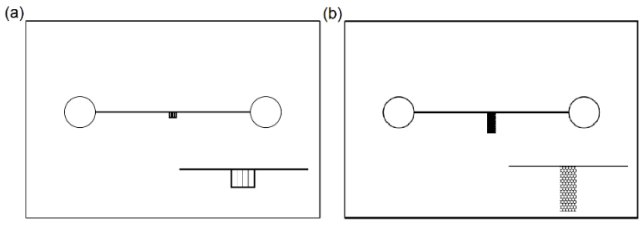

Figure 40. 2D CADs for photomask printing (a) chip #1 and (b) chip #2 (main features are magnified in lower right of each design)

An area of interest is selected as bounding box to confine the dimensions and desired medium. The main channel within the box is 127 μm wide and 2.2 cm long which serves as subsurface fracture. Array of microcracks are all connected to the middle part of main channel and they are distributed with their sequential proportions (1:8, 1:4, 1:2), to the main channel (127 micron) so the order of channel widths in the main module is 127 μm (left), 15.87 μm, 31.75 μm, 63.5 μm and 127 μm (right). The main fracture is linked to circular inlet/outlet ports with 0.04 cm diameters for homogenous dispersion of multiphase fluids upon injection/extraction. The design was submitted to Fine Line Imaging company to print the photomask with resolution of 20,320 DPI (for 12 μm minimum feature size) on high-contrast, polyester-based transparent films. Figure 41 illustrates the printed photomask.

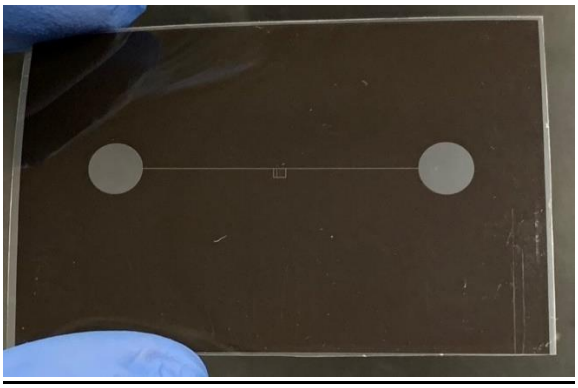

Figure 41. Photomask printed by Fine Line Imaging company on polyester transparent films, reprinted with permission from [121] JOVE 2020

In-house made UV light source is employed to transfer the computer-aided designed CAD patterns from the mask to photoresist layer on borofloat glass substrate (provided by Telic company) coated with chromium and photoresist layers. Figure 41 exhibits the Illustration of in-house collimated UV light source containing LED light sources and a stage.

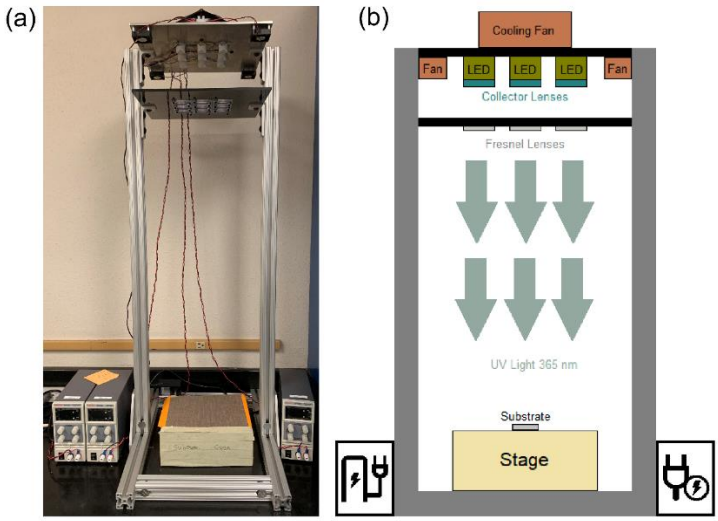

Figure 42. Illustration of in-house collimated UV light source. (a) Photograph and (b) A schematic of laboratory UV light stand containing LED light sources and a stage, reprinted with permission from [121] **JOVE 2020**

The patterns are transferred to the photoresist by altering its solubility as a result of its exposure to UV light. A full-spectrum, mercury-vapor lamp may serve as the UV source. The use of a collimated, narrow-band UV source, however, improves the quality and precision of the fabrication significantly. This work uses a photoresist with peak sensitivity at 365 nm, a collimated UV source consisting of an array of light emitting diodes (LED), and an exposure time of approximately 150 s. This UV source is a developed in-house and offers a low maintenance, low-divergence, collimated UV light source for lithography. The UV source consists of a square array of nine high-power LEDs with a target peak emission wavelength of 365 nm at 25 °C (3.45 mm x 3.45 mm UV LED with Ceramic substrate. A light-collecting UV lens (LED 5 W UV Lens – see Table of Materials) is used on each LED to reduce the divergence from ~70° to ~12°. The divergence is further reduced (~5°) by using a 3 x 3 array of nine converging polyvinylchloride (PVC) Fresnel lenses. The setup produces collimated and uniform UV radiation over a 3.5-inch squared area. The details of

the fabrication of this low-cost light source for UV lithography is adapted from the method presented by Erickstad and co-workers [122] with minor modifications[123],[124]. Figure 41 illustrates the LED UV light source mounted on the celling of UV stand alongside the stage at the bottom for substrate UV exposure (the procedure is performed in a darkroom). The UV stage is placed 82.55 cm from the nine Fresnel lenses that are mounted on a rack 13.46 cm below the rack that houses the LEDs. As seen in Figure 41a, there are four small fans (40 mm x 40 mm x 10 mm 12 V DC Cooling Fan) on the bottom of the plate that houses the LEDs and there is a larger fan (120 mm x 38 mm 24 V DC Cooling Fan) on the top. Three variable DC power supplies are used to power the LEDs. One power supply feeds the center LED at 0.15 A, 3.3 V; one power supply feeds the four corner LEDs at 0.6 A,14.2 V; and one power supply feeds the remaining four LEDs at 0.3 A, 13.7 V. The stage, shown schematically in Figure 41b, is divided into 1 cm^2 sub-areas and the intensity of the UV light is measured in each using a UV power meter (Table of Materials) that is equipped with a 2W 365 nm robe assembly. On average, the UV light has an average strength of 4.95 mW/cm^2 with a variability characterized by a standard deviation of 0.61 mW/cm^2. Figure 42 presents a color-coded plot of UV intensity map for this UV light source. The intensity over the region of 10 cm by 10 cm is relatively uniform with values ranging from 4 to 5 mW/cm^2 in the center of the stage where the substrate is placed and exposed to the light.

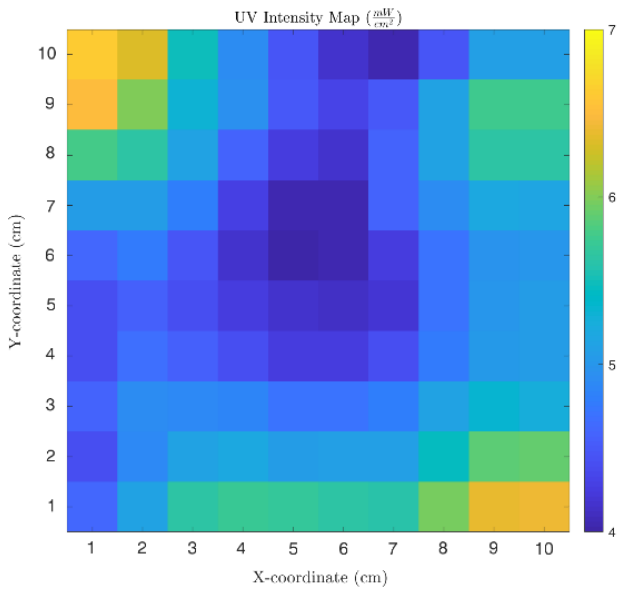

Figure 43. Color-coded plot of UV intensity in a 10 x 10 cm^2 area of the stage where the substrate is placed for UV exposure. UV intensity values range from 4 to 5 mW/cm^2 as recorded using a UV meter, reprinted with permission from [121] JOVE 2020

The use of the UV source may be coupled with UV blocking shields/covers for its safe use. Additional safety measures may include the use of UV safety goggles (Laser Eye Protection Safety Glasses for Red and UV Lasers – (190–400 nm)), face-shields marked with the term Z87 that meets the ANSI standard (ANSI Z87.1-1989 UV certification) to provide basic UV protection, lab coats and gloves to minimize the exposure.

Photo-developer solution is used to dissolve the radiated features in the positive photoresist (40 s). The substrate is submerged in chromium etchant (provided by TRANSENE) at 40 °C for 40 s to transfer the pattern from the photoresist to the chromium layer. The process is shown in Figure 44.

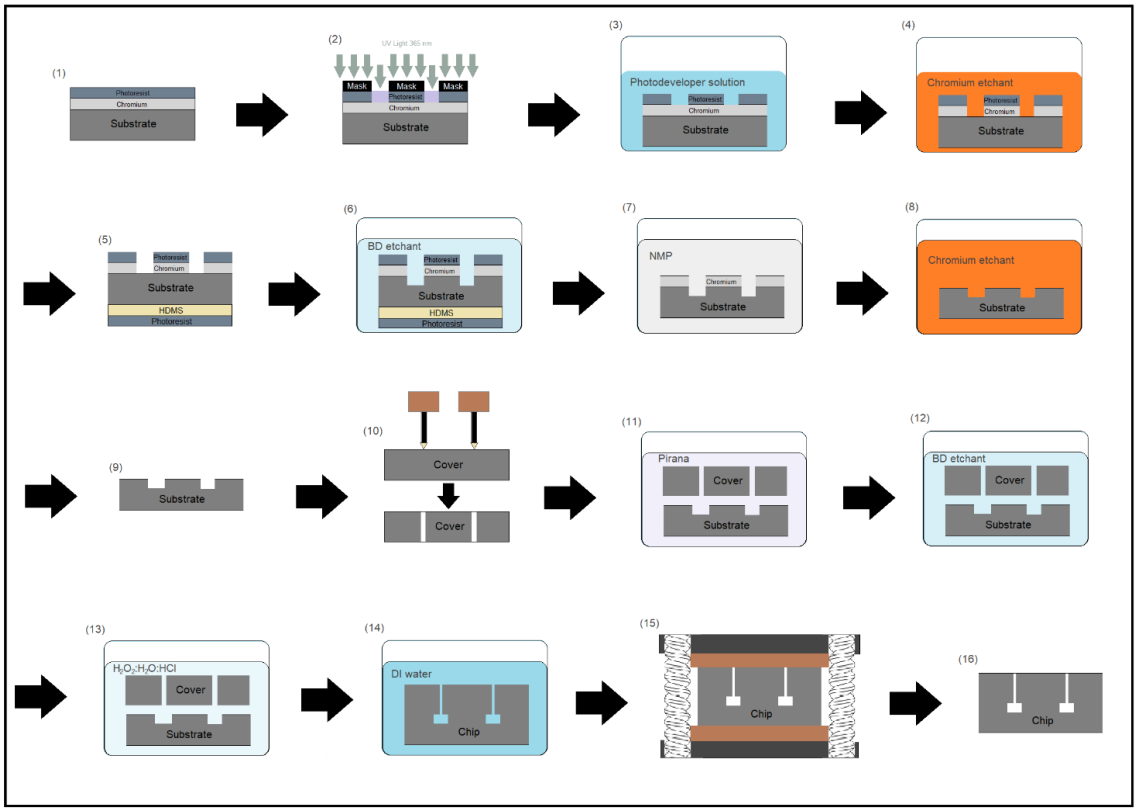

Figure 44. Schematics of photolithography and thermal bonding fabrication process for borosilicate glass substrate in 16 steps, reprinted with permission from [121] JOVE 2020

The backside of the borosilicate glass is coated with Hexamethyldisilazane (HDMS, KMG Electronic Chemicals) and photoresist for protection against BD etchant and then is submerged in BD (buffered) etchant (provided by TRANSENE) for a predetermined amount of time. The channel depth (etched feature) is examined via laser scanning confocal microscopy at this point for dipped substrate in BD etchant (Figure 45). In this work, a 10x magnification is used for data acquisition. Once channel depths are satisfactory, move to the cleaning and bonding stage.

OLYMPUS OLS4000, Lext 3D measuring laser microscope was used to optically examine the pattern on the surface of the glass microchips. The observation was performed to visually examine the top view of pattern, to measure the channel width and to identify

possible flaws. A dedicated software was employed to analyse the dimensions and topography.

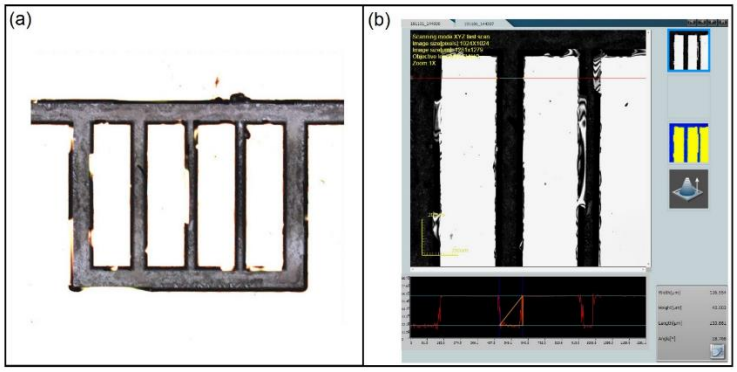

Figure 45. Examination of channel depth via confocal microscopy for substrate dipped in BD-etchant for 136 h (no sonication in this case). (a) channel overview (b) channel depth measurement (~43 µm), reprinted with permission from [121] JOVE 2020

The etched substrate is then pre heated and submerged in N-Methyl-2-pyrrolidone (NMP, Ultra-Pure Solutions, Inc) solvent at 65 °C for 30 min to remove all photoresist. The cleaned substrate is submerged in chromium etchant (40 °C) for 40 s to remove the remaining chromium layer from the substrate and then the channel depths is characterized using laser scanning confocal microscopy. (This work uses a 10x magnification for data acquisition) (Figure 46).

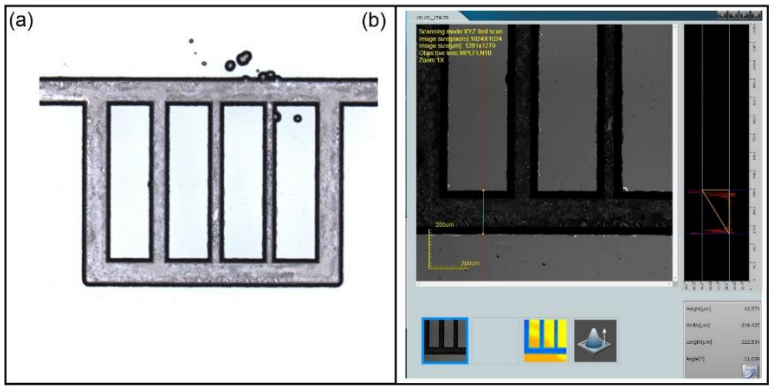

Figure 46. Examination of channel depth via confocal microscopy for a substrate with chrome layer removed after NMP rinsing. (a) Channel overview. (b) Channel depth measurement (~42.5 µm), reprinted with permission from [121] JOVE 2020

The positions of the inlet/out holes are marked on a separate blank borosilicate substrate (cover plate) by aligning the cover plate against the etched substrate. holes are blasted in the marked locations using a micro abrasive sandblaster and 50 µm aluminum-oxide micro sandblasting media. Both the etched substrate and the cover plate are cascade rinsed with DI water. The substrate and cover plate then dried, and RCA wafer cleaning procedure is performed [121]. The substrate is submerged alongside a sand-blasted cover plate with drilled inlet/outlet holes in a boiling Piranha solution for 20 min to remove all the remaining debris. Both glass pieces are submerged in BD etchant for 30 s and to clean the surfaces and then in 6:1:1 volume solution of H_2O: H_2O_2: HCl for 10 min to remove the inorganic impurities (H_2O_2 and HCl from Fisher Chemical). The solution containing the glass pieces are moved to glovebox/clean room. The glass pieces are submerged in DI water and they are pressed by matching the sides firmly against each other to create a stack for bonding process. The stack is placed between the two ceramic plates and it is placed in a vacuum oven (100 °C) for 60 min followed by main thermal bonding process in

temperature-controlled oven (1 °C/min heat up to 660 °C for 6 h). The schematics of thermal bonding processes are illustrated in Figure 47.

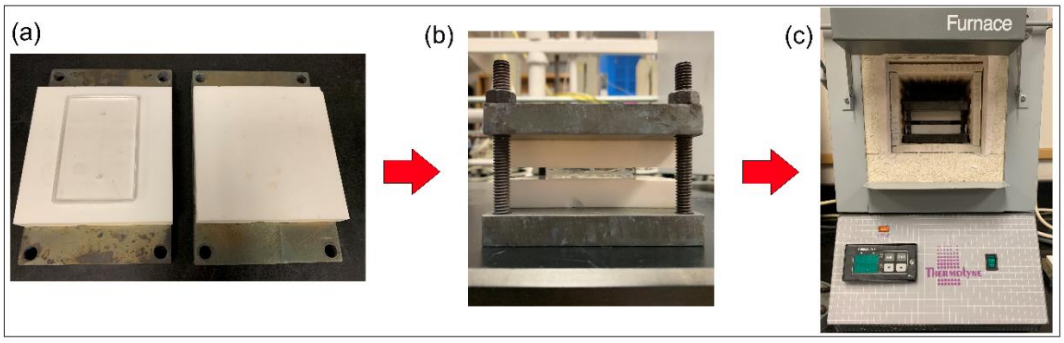

Figure 47. Schematic of thermal bonding process. (a) Placing two glass wafers between two smooth ceramic plates. (b) Placing the ceramicplates between two metallic plates and tightening the bolts. (c) Placing the metallic and ceramic holder containing the substrates inside a programmable furnace to achieve the desired temperatures for thermal bonding, reprinted with permission from [121] JOVE 2020

Figure 48 summarizes the laboratorial steps involved with fabrication and testing of glass microfluidic chip with UV lithography and thermal bonding approach.

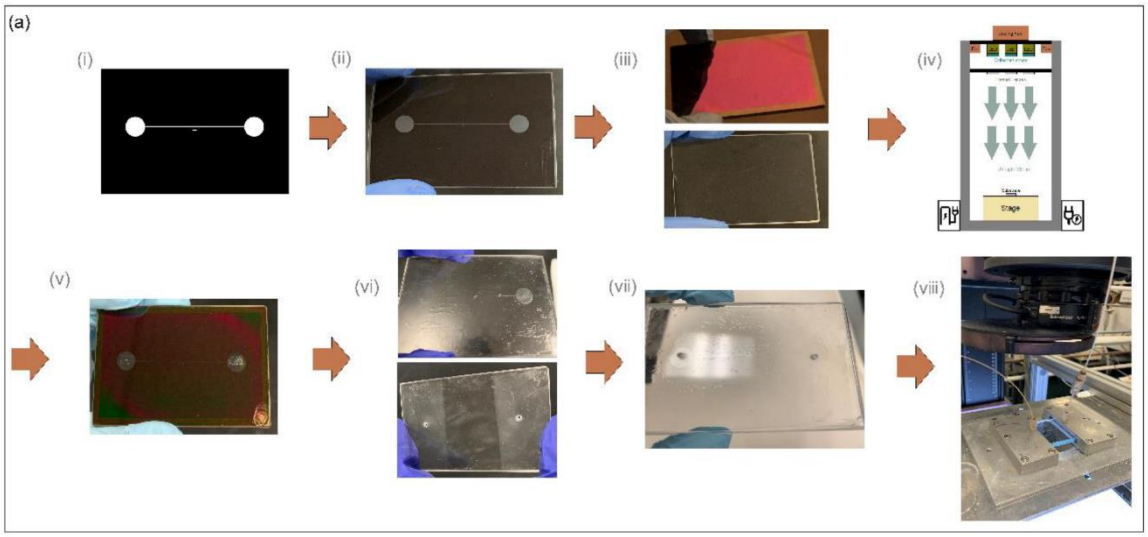

Figure 48. UV lithography and thermal bonding fabrication method of glass microfluidic device. (a) Fabrication process for fractured media microfluidic deviceusing photo-lithography (a.i) design for a positive

photoresist, (a.ii) printed photomask on a polyester-based transparency film, (a.iii) blank andphotoresist/chrome coated glass substrates, (a.iv) transferring the pattern to the substrate via UV radiation, (a.v) etched substrate, (a.vi) etchedsubstrate after chrome layer removal and the blank substrate prepared for thermal bonding, (a.vii) thermally bonded device, and (a.viii) $scCO_2$ injection, reprinted with permission from [121] JOVE 2020

3.13. SLE Microfluidic device fabrication

The design of geometrical patterns for Selective Laser Etching (SLE) requires development of a three-dimensional CAD design inspired by 2D network of fracture/micro channels (Figure 49). A 2D scheme comprising geometrical features and flow patterns Is designed using AutoCAD (Autodesk, San Rafael, CA) with features that are representing microcrack/fractures to study the foam stability and transport (Figure 49).

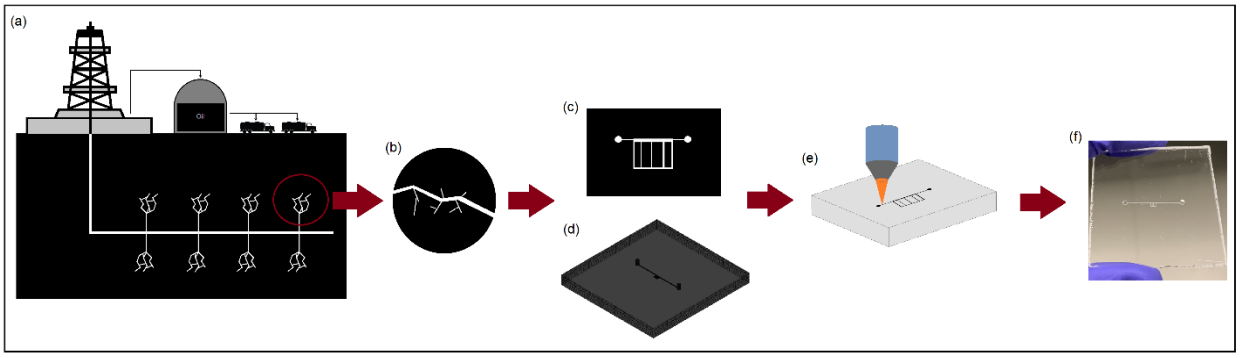

Figure 49. A process of fracture emulation on SLE glass microchip for subsurface oil recovery of tight shale formations (a) hydraulic fracturing of tight shale formations is considered as application model (b) real fracture geometry on rock samples are obtained. (c, d) simplified pseudo fracture network is designed by AutoCAD in 2D and 3D format. (e) Laser printing of pseudo fracture network on fused glass microchip (f) completed SLE chip after post processing, reprinted with permission from [121] JOVE 2020

SLE designs mainly follows 2D design for UV lithography and include the additional step of extruding the two-dimensional design to the third dimensions and

incorporating inlet and outlet ports (Figure 50). In this work, the designs used in SLE fabrication have features that are 254 μm in depth and the flow network design is positioned approximately 1746 μm from one face of a 4.5 mm thick glass chip.

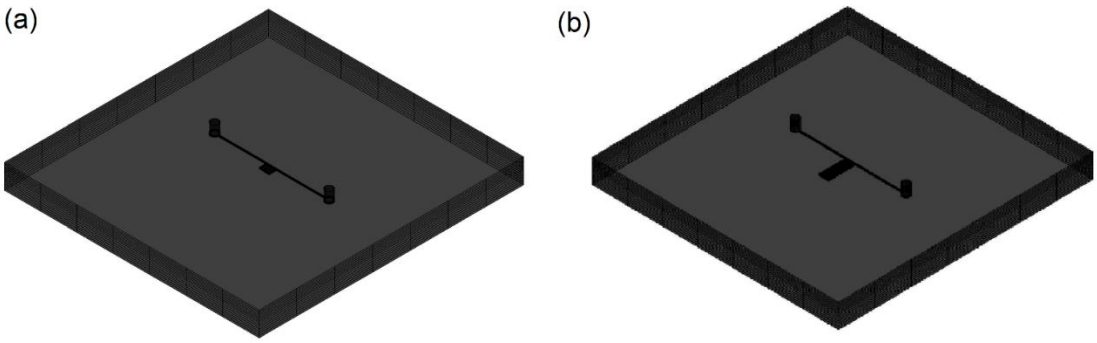

Figure 50. 3**D CAD designs for (a) chip #1 and (b) chip #2, reprinted with permission from** [121] **JOVE 2020**

Following CAD design, the SLE chips are fabricated from Fused silica glass (SIEGERT WAFER GmbH) by LightFab GmbH, Germany to generate the 3D structure in a subtractive 3D printing process. A LightFab 3D printer with scanning focused ultrashort pulsed laser (femtosecond laser) source from Trumpf GmbH, Ditzingen, Germany is used to locally change the glass properties in focal volume with pulse duration of 0.5 ns, a repetition rate of 50 kHz, pulse energy of 400 nJ, and a wavelength of 1.06 μm. The maximum processing area and depth in the glass substrate are 200 x 200 mm^2 and 7 mm, respectively. A microscope with a 20X objective lens (Zeiss) and 10 mm working distance is employed. A linearly polarized laser beam oriented perpendicular to the stage was used to write the pattern in the substrate. The etching rate for treated glass and untreated glass are reported as ~250 μm/hour and ~0.25 μm/hour, respectively. The time of the process for bulk etching is referred to as 'write time' during which the laser obliterates a fraction of the glass substrate and the channels are formed. The write time of 1 month are allocated to

etching process. Chips were manually singulated to an accuracy of ± 1 mm and a channel width tolerance of +/- 5 μm. Accordingly, the desired geometrical pattern is etched inside the glass substrate. The process was followed by a wet etching step to remove the glass debris. KOH 32 wt% at 85˚C with sonication (ultrasound) was used for this purpose. The fabricated chip is pressure resistive and the pressure resistivity up to 9.65 MPa was confirmed during $scCO_2$ foam injection. The summary of this method is depicted in Figure 51.

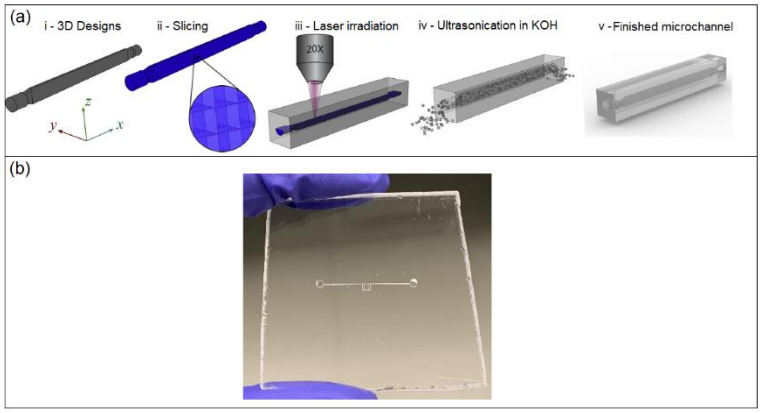

Figure 51. SLE design and fabrication process. (a) Schematic of SLE design and fabrication process (this figure has been reprinted with permission from Elsevier27), and (b) the resulting 3D printed microfluidic device. Design and fabrication steps include (a.i) designing the innervolume of channels, (a.ii) slicing the 3D model to create a z-stack of lines to define the laser path, (a.iii) laser irradiation on the polished fusedsilica substrate, (a.iv) preferential KOH etching of laser etched materials, and (a.v) the finished product, reprinted with permission from [121] JOVE 2020

It is worth noting the dry etching inside the glass silica bulk could be performed via two approach namely (i) channel widening and (ii) welding. The proposed channels were considered long for laser etching, thus, widening towards the entrances for the etching fluids was employed and accordingly time frame of the etch required to clear the smallest channel led to some non-uniformity in the outer channels, nevertheless, the approach is preferred over welding where the

model is sliced into two halves at the top of the channels and the channel is written in one of halves so the narrow inlets are written in other half (lid) and a weld line is written along the edge of each channel. Although, the welding approach reduces the write time and leads to more accurate dimensions, it is expected the pressure resistivity of the chip is affected and thus widening approach was authors' choice to maintain the integrity of the chip for harsh reservoir applications.

3.14. $scCO_2$ foam injection/isolation experiments

3.14.1- High-pressure holders for the microfluidic device

Figure 52 shows a close-up view of high-pressure holders. The holder comprises two pieces made of 304 stainless steel at Department of Chemical engineering, University of Wyoming. As shown in Figure 52a, these plates feature an opening that accommodates the typical microfluidic devices built in the laboratory at the University of Wyoming. The two plates are connected via hex socket cap screws. Inlet-outlet lines are fixed in place via the threaded through-hole in each holder, which protects the ports from leaks mechanically by applying compressive force against the sandblasted hole in the device. As such, the holders also protect the microfluidic device from dislocation during high pressure injection without the need for adhesive-based sealants. The through-hole in the holder and the hex socket cap screws are shown in Figure 52b. The hex socket cap screws are spaced center-to-center 35 mm apart. The top plate (Figure 52b) is 43 mm x 150 mm x 12 mm thick, and the bottom plate is 43 mm x 150 mm x 5 mm thick. The housing for the microfluidic device is 112 mm x 25 mm deep x 5 mm high; it is formed in the top plate and reduces the thickness of the top plate to 7 mm.

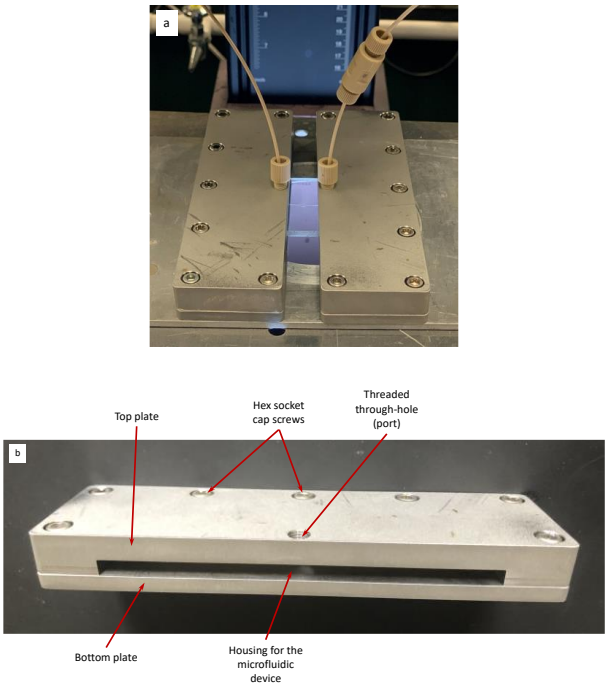

Figure 52. High-pressure holder for microfluidic devices; a) close-up view of the holders during a flow experiment, and b) close-up view of a single holder, reprinted with permission from [121] JOVE 2020

$scCO_2$ foam microscale texture, fracture transport, stability and loss properties are examined via a high-pressure foam flooding apparatus utilized with microchip module, high resolution Phase one camera system, illumination source and advanced computing image processing unit. The schematic of the system is presented in Figure 53.

Figure 53. (a) schematic of high-pressure CO_2 foam injection and visualization of microchip in laboratorial scale; the system is capable of scCO_2 foam generation as well as oil injection through the microchips. The simultaneous visualization is performed by high resolution camera and fast processing units. (b) The photo of the actual setup in the lab in Professor Saman Aryana's lab in Chemical Engineering Department, University of Wyoming, reprinted with permission from [121] JOVE 2020

Figure 54 reveals the main module containing the chip holder (Figure 54a) and visualization system (Figure 54b). Schematic of high-resolution visualization system is depicted in Figure 54b.

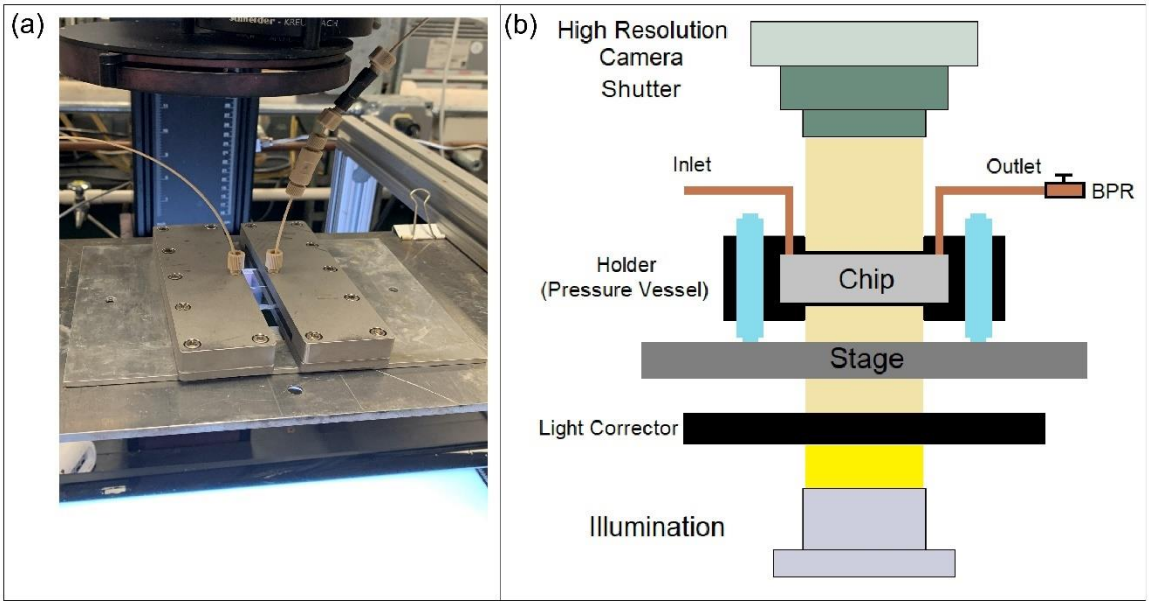

Figure 54. Microfluidic device placed inside a holder and the imaging system comprising a high-resolution camera and an illumination system. (a) A photograph of laboratory setup, and (b) schematic of a lab-on-a-chip under observation via the high-resolution camera and illumination system, reprinted with permission from [121] JOVE 2020

The CO_2 and high saline brine are compressed and co-injected at (40°C and ~ 8.6 MPa). The mixture of $scCO_2$ and pressurized high saline brine are mixed (through glass micro bead pack and Swagelok inline mixer with 7 μm and 15 μm pore size) and directed to the microchip held by pressure holders. The back pressure is applied at outlet to maintain the control on pressure of the injecting fluid. The initial flow rate is selected to achieve a range of foam qualities (FQ) including of FQ = 90% (5.4 ml/min $scCO_2$ and 0.6 ml/min brine containing surfactant/nanoparticle).After foam generation is detected at outlet, the flow rate is dropped 100 times and low flow rates are maintained up to 30 min to stabilize the flow inside the micromodel. For stability measurements, the flow is stopped, and inlet/outlet valves are closed instantly, so the multiphase fluid inside the chip is isolated and visual characterization is executed. The microscale observations are performed with

Phase One IQ260 Camera mounted on DT Versa capture station manufactured by DT Scientific and LED light box from the bottom provided the requires backlight luminance and image processing unit. The images are captured, processed and stored electronically via Capture One software running on computer with high power (INTEL® Xenon® CPU E5-2687W v2 @ 3.40GHz, 3.40GHz (dual processors)) and graphic capability (NVIDIA Tesla K20 Graphic Card - 706 MHz Core - 5 GB GDDR5 SDRAM - PCI Express 2.0 x16). At the end of observation, the valves are opened, heaters are turned off and depressurization to ambient condition is performed. The micromodel channels are flushed with DI water multiple times. In case of hydrocarbon injection, the microfluidic device must be thoroughly cleaned using a cleaning protocol in the following order: brine containing surfactant/nano particle to rinse the oil, DI water to rinse the surfactant/nanoparticle.

3.15. Image analysis and post processing

The obtained images with Phase one IQ260 camera are analysed with special dedicated software Capture One 12 to convert the obtained pictures to editable format (Tiff). Once the bubble dimension and scale are known, MATLAB image processing tool (the MathWorks, Inc. Natick MA, USA) coupled with a general image analysis tool ImageJ (ImageJ, an open-source Java image-processing program inspired by NIH image) are employed to enhance the quality of images including light, contrast and sharpness and to obtain the average bubble size and bubble size distributions for each foam microstructural images with known pixel/distance parameter. Figure 55 depicts the image processing steps in this work.

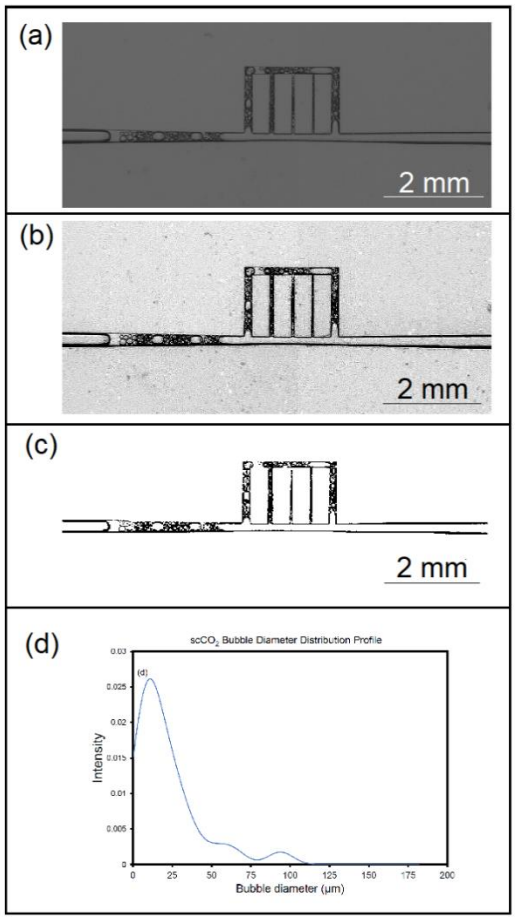

Figure 55. Image post processing steps after obtaining the image from injection/visualization unit. (a) Obtained image in original form (b) correction of light/contrast/sharpening by MATLAB (c) applying the black/white contrast to processed image (d) corresponding bubble size distribution measured by ImageJ, reprinted with permission from [121] JOVE 2020

The enhanced image with MATLAB is then processed through ImageJ for bubble size distribution analysis. The pore size distribution is obtained with the following protocol. First, the desired area of the picture is selected and duplicated. Then, the image is converted to gray scale (8-bit image type). The known distance obtained from optical/microCT observations is entered to ImageJ with 'Set Scale'. FFT Bandpass Filter command filters large structure down to 160 pixels. "Adjust Threshold" is employed to create the black and white contrast between two phases. By checking "over/under" the contrast is varied in a

green and black colored background and on B&W, the ultimate black and white contrast is set. Eventually, using analyze particles with size range 1 to infinity and selecting to show overlay, the summary of particles and particle size distribution is obtained. “Analyze particle” in ImageJ determines the bubble size distribution. Some larger bubbles with this method are ignored and more accurate analysis is required.

3.16. Micro-CT Analysis

Three-dimensional (3D) micro X-ray computer tomography (Xradia MicroXCT-400, Carl Zeiss Microscopy, LLC, Thornwood, New York) optimized for non-destructive imaging of complex internal structures was employed for identification of microchip internal structure. The instrument was equipped with 90 keV Microfocus X-ray source and 2K*2K CCD camera and an X-ray detector with a pixel resolution of about 0.3 mm and spatial resolution of less than 1 mm. The transmission X-ray imaging of the samples was performed using an X-ray tube with a tungsten anode setting of 50 kV at 8 W. The 3D images were constructed with the help of the software “XM Reconstructor 8.0” (Carl Zeiss Microscopy, LLC, Thornwood, New York), using 1600 images taken at 35 s and 40 s exposure time per image for microchip #1 and #2 respectively.

Chapter 4: Results and Discussion

4.1. Molecular complexation mechanism (Fracturing, EOR)

Complexation of surfactant and PECNPs were investigated for foam flow through fractures in tight shales (hydraulic fracturing) and foam flow through porous carbonate reservoirs (EOR application).

4.1.1. Complexation for foams in hydraulic fracturing

Aqueous mixtures of PECNP and Zwitterionic surfactants presented in section 2.1 were evaluated with light scattering techniques such DLS, TEM and Raman Spectroscopy.

4.1.1.1 Particle size and zeta potential measurements.

The particle size and zeta potential values for variety of PECNP to surfactant proportions (1:9, 2:8, 3:7 and 4:6) in 33.3 kppm and 66.7 kppm brine solutions are presented in Figure 56.

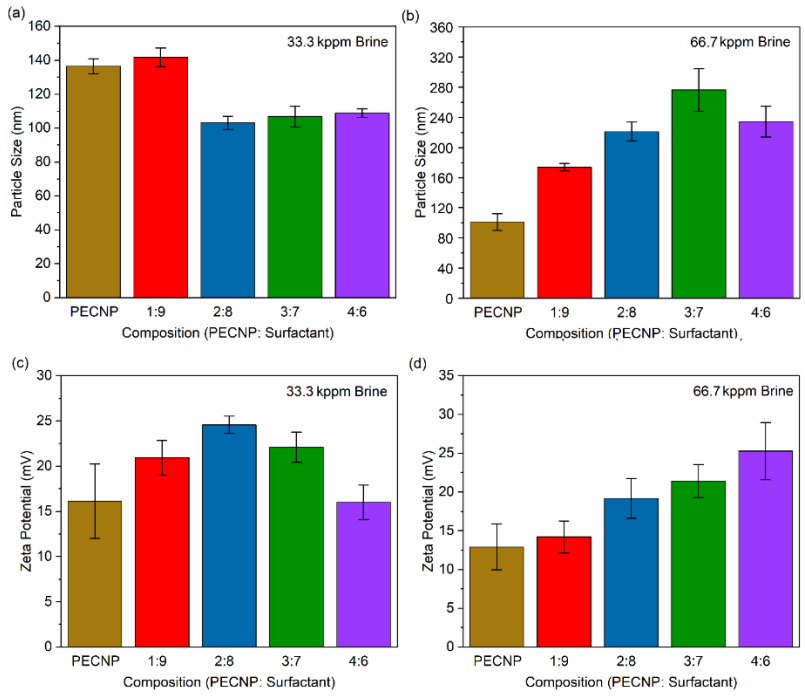

Figure 56. Particle size and zeta potential measurements for PECNP and different proportions of PECNP to surfactant in 33.3 kppm and 66.6 kppm brine systems, reprinted with permission from [28] ACS 2019

For 33.3 kppm brine system, PEI and DS form PECNPs within the size range of 132 to 140 nm with an average zeta potential of +16 mV (Figure 56a,c) due to an excess of amine functional groups on the outer layer of the nano-aggregates resulting in a positive charge (PEI:DS 3:1). Addition of nanoparticles with the lowest proportion (1:9) to the surfactant solution enhances the average particulate size, preventing the fluid loss of the final mixture by bridging the pores on the surface of the rock matrix [125]. Nevertheless, further addition of PECNP lowers the average particle size due to precipitation and charge instability [5,126] (Figure 56a). Accordingly, PECNP:surfactant with the 1:9, 2:8 and 3:7 ratios represent the highest positive zeta potential on the surface of nanoaggregates and no further stable charge accumulations were observed for higher proportion of PECNP in the 33.3 kppm brine system due to ionic and charge imbalances on the PECNP and surfactant coagulates, allowing electrostatic attractions of opposite charges and electrostatic instabilities. Considering the combined effect of particle size and charges, the 1:9 and 2:8 ratio for PECNP:Surfactant are the prime candidates to stabilize the CO_2 - water lamella and prevents the fluid loss in 33.3 kppm brine mixtures.

Particle size and potential for ionic mixtures at 66.7 kppm system are represented in Figure 56b, d. Addition of PECNP to WLMs directly enhances the particle size and positive potential. Higher salinity enhances the hydrophilicity of formed nanoparticles and it accelerates the aggregation of PECNPs, and PECNP-surfactant due to weakening of electrostatic repulsions and higher concentration of divalent ions [127]. As previously reported, the stronger adsorption of nanoparticles on the lamellae and formation of an electrostatic dense layer in the lamella results in particles with larger zeta potentials [61,128], therefore, ratios of 3:7 and 4:6 result in optimal size and surface charge in the 66.7 kppm high salinity brine and the stable quasi colloidal particles of PECNP and surfactants (WLMs) can withstand harsh condition of high salinity brine.

4.1.1.2 Transmission Electron Microscopy (TEM)

Morphological representations of nanoparticles and surfactants in high salinity brines agree with the light scattering and Raman spectroscopy observations presented in sections 4.1.1.3. Figure 57 shows the TEM images for PECNP, 1 wt% surfactants and PECNP-surfactant (with 1:9 ratio) prepared in 33.3 kppm high salinity brine. Formation of PECNPs as particles made by electrostatical interaction between PEI and DS is visible in Figure 57a, Figure 57b and Figure 57c. The size range of PECNPs is consistent with the predicted values of dynamic light scattering measurements (section 4.1.1.1). The 1 wt% surfactant solution in the high salinity brine exhibits the formation of WLMs as elongated rod-like surfactant aggregates (Figure 57d, e and f).

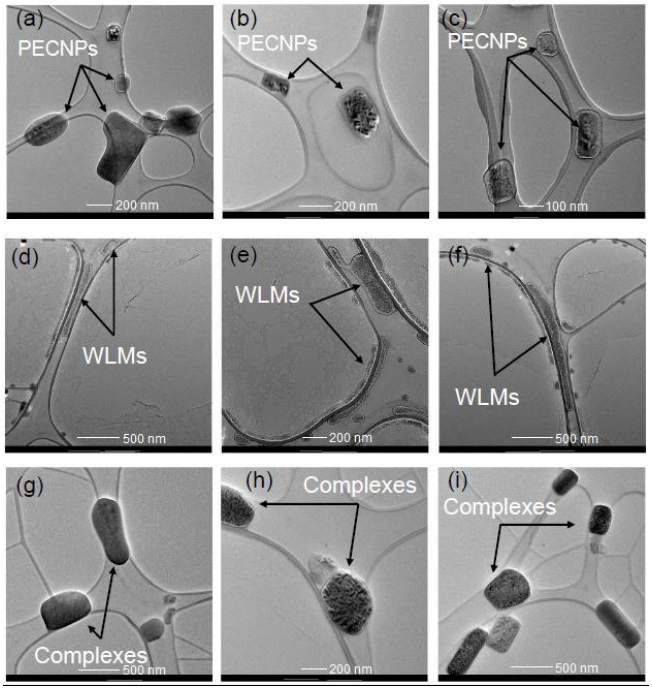

Figure 57. TEM images for PECNP nanoparticle (a, b and c), 1 wt% surfactant (d, e and f), and complexes of PECNP: Surfactant 1:9 (g, h and i) prepared in 33.3 kppm high salinity brine. The semi dried mixtures were examined on copper grid, reprinted with permission from [28] ACS 2019

Initially, nanoparticle agglomerates with WLMs form ring-like structures. WLMs are formed and coiled in the presence of nanoparticles starting to merge with the nanoparticle as they cover the outermost layer of a PECNP. Decoration of micelles on nanoparticle is derived through the redistribution and direct adsorption of micelles on nanoparticles due to electrostatic attractions between the amine and sulfonate groups, confirmed by Raman spectroscopy (section 4.1.1.3). With time, the PECNP helps to form an elastic layer at the interface to overcome the foam coarsening, as, accumulation of elastic and positively charged hydrophilic particles at the plateau border hinders liquid drainage. Formation of stable nanogels in the form of vesicular structures (sphere to rod transition) was previously shown and studied in molecular dynamic simulations in cetyltrimethylammonium chloride (CTAC)-functionalized NP self-assembly [54,129], where double layer coverage of WLMs on oppositely charged and spherical nanoparticle induces the self-assembly of nanoparticle- surfactant in an aqueous medium.

4.1.1.3. Raman spectroscopy

Figure 58 illustrates the identified characteristic bands in Raman spectra and corresponding functional groups for the mixtures of PECNP and 1 wt% surfactant prepared in 33.3 kppm brine.

(a)

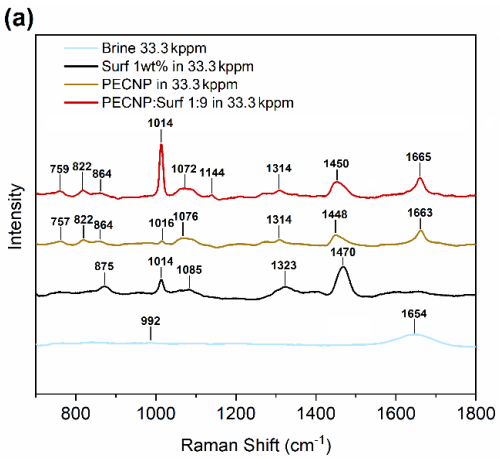

(b)

Raman shift (cm^{-1})	Vibrational mode/Assignment
992 (free, aqueous) 1014 (bound)	$\nu_1 SO_4$
600-1300	νC-C (aliphatic chain vibrations)
1200-1340	δN-H (Amide III) νC-N stretch
1400-1470	δCH_2, δCH_3 asym
1510-1580	νC-N, δN-H (Amide II)
1640	δH_2O
1680-1820	δN-H (Amide I) νC=O

Figure 58. The identified bands and corresponding assignments in Raman spectra for 33.3 kppm brine, surfactant, PECNP, and PECNP:surfactant (1:9) in brine (a) and identification of key Raman bands (b) corresponding groups based on the values reported in the literature [130,131], reprinted with permission from [28] ACS 2019

The PECNP and surfactant spectra share many of the same bands, corresponding to their backbones and other shared functional groups. Of special note are the 1014 cm^{-1} and 1665 cm^{-1} bands. The first represents a totally symmetric sulfate stretching mode associated with the surfactant (present to a very minor extent in the PECNP spectrum due to the dextran sulfate used to make the PECNP), while the second band represents the δN-H in plane bending generated by the nitrogen-hydrogen bonds and is unique to the polyehtyleneimine. A band around 1654 cm^{-1} is observed in the brine (and underlying some of the other spectra) that can be attributed to the remaining water present in the lyophilized samples [132,133]. The 33.3 kppm brine spectrum has a weak band for free sulfate (SO_4^{-2}) from Na_2SO_4 centered at 992 cm^{-1} [134]. The chemically bound sulfate band can be found at 1014 cm^{-1} in the three other spectra as that functional group is found in both the surfactant and the dextran sulfate used to make the PECNPs, although the relative intensity of this band varies significantly among the spectra. This observed shift is consistent with

previously reported findings by Wang and coworkers [135] about the noticeable band shift for SO_4^{2-} band from 992 to 1010 cm^{-1} in titanium hydroxide complexation with sulfate.

To better understand the changes in intensity of the sulfate signal, especially in the PECNP-surfactant spectrum, a simple model was developed. Using least-squares fitting, four PECNP:Surfactant 1:9 Raman spectra (collected from different locations within the lyophilized samples) were fit with average PECNP and surfactant spectra. The residual of corresponding fit indicates locations within the spectra where the PECNP:Surfactant spectrum is not completely explained by the sum of the components. If the PECNP:Surfactant spectrum represented a mixture, rather than a change in chemistry, then its residual should represent the noise in the data, however, this is clearly not the case, as shown in Figure 59. In each residual, the sulfate band at 1014 cm^{-1} stands out as significantly different, indicating that complexation between the PECNP and the surfactant occurs and that the complex itself has a unique Raman signature (possibly due to a change in chemical environment of the key functional groups). The strength of the sulfate band varies between samples, however, as the complexes are not homogenous, this should not be a surprise. There are other minor changes to peaks within the Raman spectrum, particularly at 1144 cm^{-1}, indicating that the changes due to complexation are not confined to the polyatomic anions.

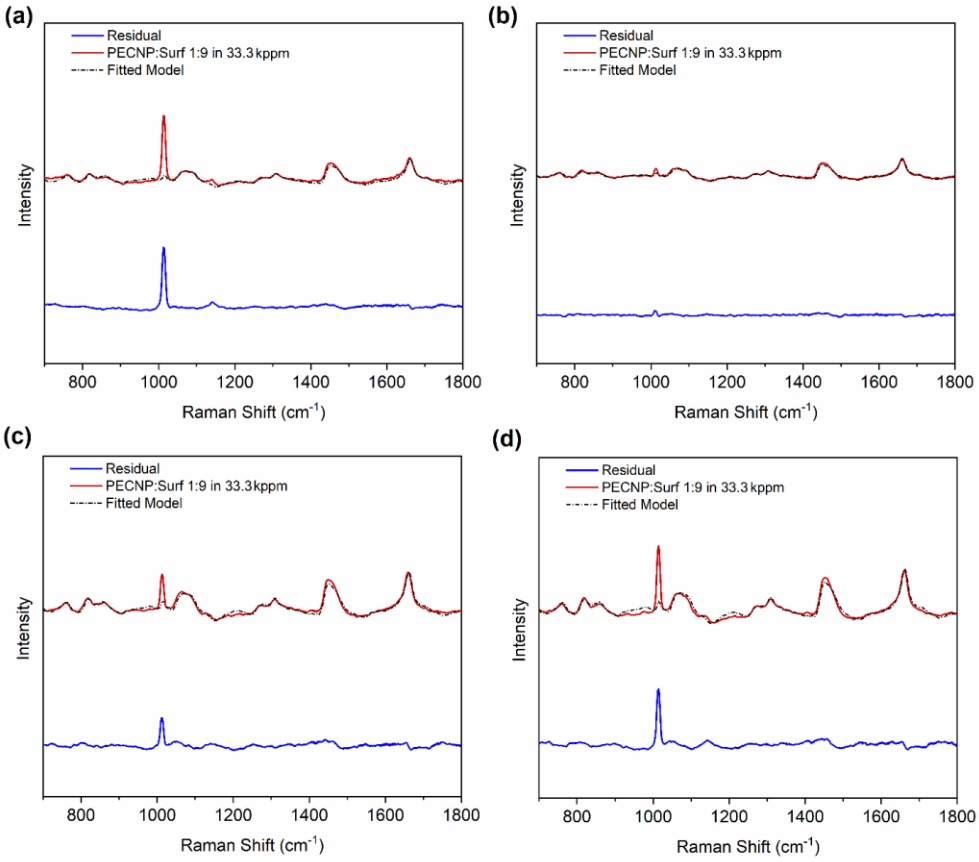

Figure 59. The Raman spectra of four PECNP:surfactant 1:9 samples (blue) fit with average PECNP and surfactant spectra for surfactant (red dots) and corresponding residual (black, offset) along with zero residual line (also black, offset), reprinted with permission from [28] ACS 2019

4.1.1.3.1. Raman spectroscopy 632.8 nm excitation wavelength post processing with MATLAB

The mixture of PECNP and surfactant was fit with the model basis spectra (consisting of average spectra of PECNP and surfactant) using the least-squares method described by Shafer-Peltier using MATLAB [116]. Pre-processing of the spectra included fitting with a fifth degree of polynomial using MATLAB's polyfit function. Vectors representing each fit were created using the polyval function and residuals of each fit were determined. An average of three to four spectra were then used (except in the case of the PECNP:Surf complex spectra) for further analysis. Cosmic rays were removed manually, and MATLAB's smoothing function was used to bin neighboring points to remove digital noise. The magnified region of interest was selected and

normalized to initial data points at 1000 cm^{-1} (lowering the curves with the magnitude of intensity at 1000 cm^{-1}). Figure 60 represents the normalized bands in magnified region 1000-1025 cm^{-1} for surfactant and PECNP in 33.3 kppm brine, clearly illustrating the intensifying the 1014 cm^{-1} band.

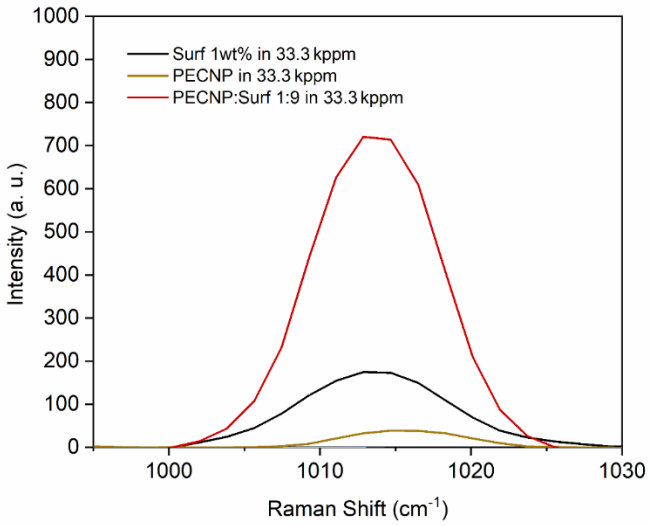

Figure 60. Normalized bands in magnified region 1000-1025 cm-1 for surfactant and PECNP in 33.3 kppm brine, reprinted with permission from [28] ACS 2019

4.1.1.4. FTIR

To analyze the surfactant behavior in detail, the zwitterionic surfactant was characterized with Fourier transform-Infrared spectroscopy (FT-IR) to identify the chemical functional groups. As Figure 61 illustrates there exist characteristic bands for the surfactant mixture between 970 to 1575 cm^{-1} as well as between 2800 to 3000 cm^{-1}, which were not present in water spectrum (blue curve). As the majority of surfactant is composed of water (60-70 w/w % , Table 2), water bands (1580 to 1680 cm^{-1}, 2000 to 2220 cm^{-1} and 3000 to 3700 cm^{-1}) dominate the surfactant spectrum.

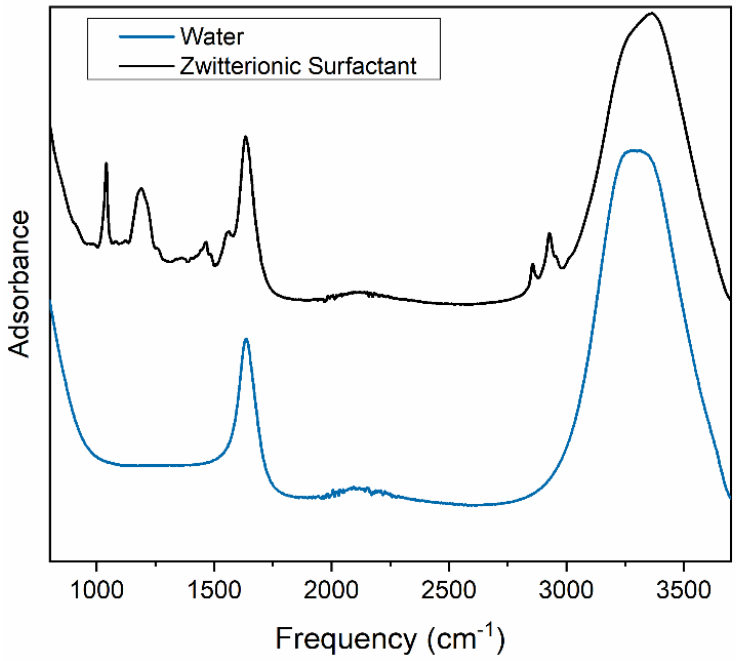

Figure 61. Fourier transform infrared spectra for water and Zwitterionic surfactant used in this study, reprinted with permission from [28] ACS 2019

Stretching vibrations for alkyl aryl ether (C-O) and sulfonate and sulfonamide (S=O) chemical bonds were observed at 1177 cm^{-1}. Medium bending for methyl group (C-H) was identified at 1457 cm^{-1} followed by medium to weak bending located at 1570 cm^{-1} for the amine group (N-H). Presence of other bending for amine, strong stretches for alkene, secondary amine and ketone are anticipated, however, coverage by H-O-H scissors in water overwhelmed the bands. Medium adsorptions at 2850 and 2924 cm^{-1} belong to C-H stretch in alkane and aldehyde (doublet). The down field bands such as expected surfactant amine stretches (N-H) and hydroxide (O-H) in the range of 3000 to 3700 cm^{-1} were covered by strong stretch resulted from the O-H bond from water molecules. The main functional groups are quaternary and secondary amines as well as pendant hydroxide groups, amide and sulfonate ($R\text{-}SO_3^-$). Combination of ammonium and

sulfonate offers a zwitterionic surfactant with both cationic and anionic charge head groups capable of conjunction with PECNP in $scCO_2$ lamella interface.

Taken together the IR spectra (Figure 61), Raman data the surfactant structure resembles the amidopropyl hydroxysultaine with a long hydrophobic tail, sulfonate and quaternary ammonium pendant groups. The main functional groups are quaternary and secondary amines as well as pendant hydroxide groups, amide and sulfonate ($R\text{-}SO_3^-$). Combination of ammonium and sulfonate offers a zwitterionic surfactant with both cationic and anionic charge head groups capable of conjunction with PECNP in $scCO_2$ lamella interface.

4.1.2. Complexation for foams in EOR

4.1.2.1 Transmission Electron Microscopy (TEM)

Morphological graphs of nanoparticles and surfactants in high salinity brines agree with the data obtained from previously reported light scattering results [63]. Figure 62 represents the TEM images for 0.1 wt.% surfactants, PECNP, and PECNP:surfactant (with 1:9 ratio) prepared in 33,667 ppm salinity brine. The 0.1 wt.% surfactant solution in the high salinity brine exhibits the formation of micellar domains with less than 100 nm dimensions (Figure 62a, b and c). Formation of PECNPs as soft matters made by electrostatic interaction between PEI and DS is illustrated in Figure 62d, e, and f. The elctrostatic bonding between the PEI-DS complex and the surfactant is illustrated in Figure 62g, h and i. The size range of PECNPs is consistent with the predicted values of dynamic light scattering measurements (~ 200 nm) [28].

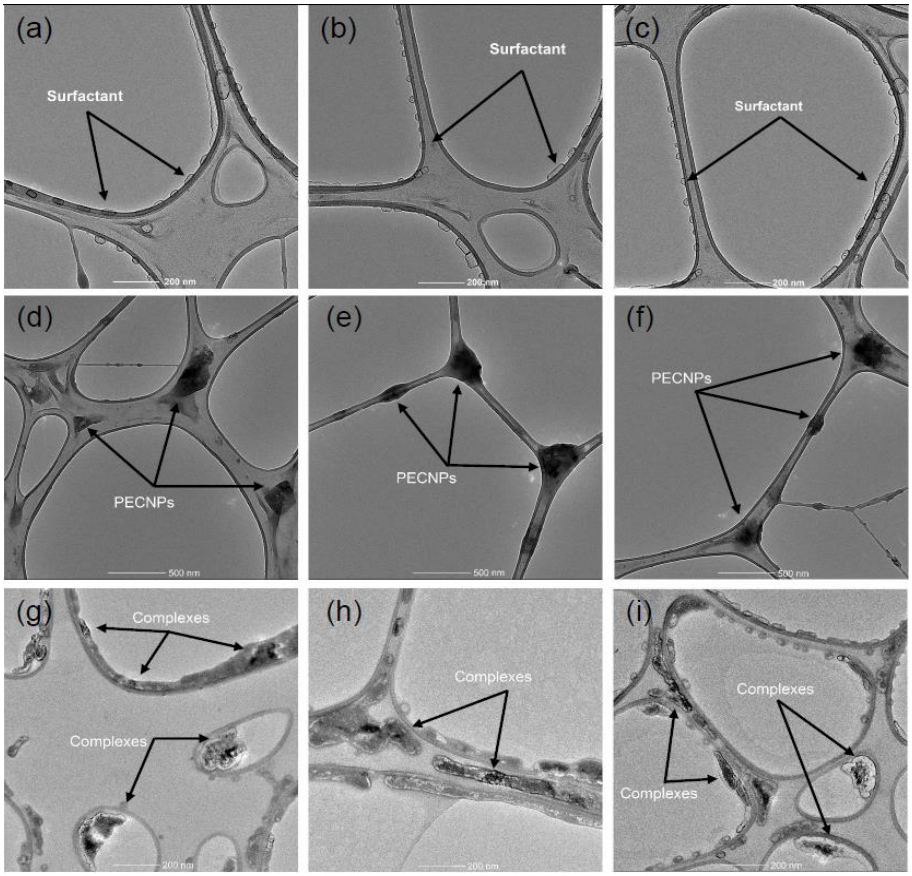

Figure 62. TEM images for 0.1 wt. % surfactant (a, b and c), PECNP (d, e and f), and complexes of PECNP: Surfactant 1:9 (g, h and i) prepared in 33,667 ppm salinity brine, reprinted with permission from [48] Elsevier 2020

Nanoparticle aggregation with N-120 micelles forms wormlike or vesicular structures comprising both nanoparticle and surfactant components electrostatically merged into each other. Figure 62f, g, and h illustrate the complexation of PECNP and N-120 micelles. Redistribution and direct bonding of micelles on nanoparticles is due to electrostatic attractions between the amine groups in PECNP and hydrated ether and hydroxide groups in N-120. The Raman spectroscopy data supports this interpretation. Accumulation of elastic and positively charged hydrophilic particles (complexes of PECNP-surfactant) at the plateau border and lamella interface hinders liquid drainage and foam coarsening.

4.1.2.2 Raman Spectroscopy

Figure 63 shows the Raman spectra and identified characteristic bands for lyophilized samples of brine, sulfate, 1 wt.% surfactant, PECNP and PECNP-surfactant prepared in 33,667 ppm salinity brine.

(a)

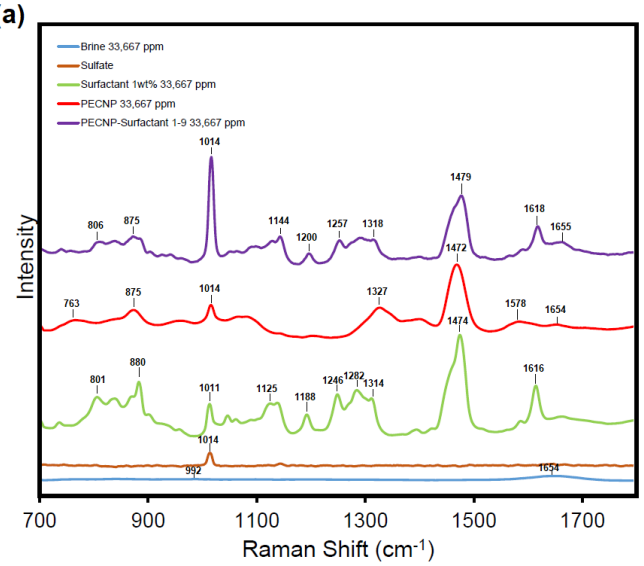

(b)

Raman shift (cm^{-1})	Functional Group/Vibration
992 (free, aqueous) 1014 (bound)	$\nu_1 SO_4$
600-1300	νC-C (aliphatic chain vibrations)
800-970	νC-O-C
990-1100	δ, ν aromatic ring
1200-1340	δNH, νC-N stretch
1400-1470	δCH_2, δCH_3 asym
1510-1580	νC-N, δN-H
1580, 1610	νC-C (aromatic chain vibrations)
1640	δH_2O
1680-1820	δNH, νC=O

Figure 63. The Raman spectra for ionic species comprising the CO_2-water lamella interface (b) Table of key Raman bands and corresponding groups based on reported values in the literature [131,137], reprinted with permission from [48] Elsevier 2020

The strong Raman band observed at 1014 cm^{-1} in the sulfate and PECNP spectra is characteristic of bound sulfate (Figure 63b). Its intensity varies greatly in lyophilized form, most likely due to orientation and potential concentration effects of the lyophilization process, and thus the sulfate contribution is being treated as a separate basis spectrum [138] (Figure 63a). The sulfate band overlaps with the aromatic ring vibrations present in the N-120 spectrum at 1011 cm^{-1} and therefore the band observed at 1014 cm^{-1} in the PECNP-surfactant spectrum is likely the result of contributions from both sulfate and aromatic ring vibrations. Free sulfate (SO_4^{-2}) from the Na_2SO_4 dissolved in the brine can be found at 992 cm^{-1}, in agreement with the literature [28,135]. Bands between 1011 cm^{-1} and 1474 cm^{-1} represent a combination of aliphatic C-C bond vibrations,

aromatic ring vibrations, and anti-asymmetric -CH_2,-CH_3 vibrational modes in the surfactant backbone, while the band 1613 cm^{-1} indicates further existence of the aromatic ring present in N-120 structure connecting the ethoxylated heads to the aliphatic tale (N-120 structure in Figure 28). The PECNP spectrum comprises the characteristic surface functional groups including sulfate and amine. The sulfate vibrational mode from dextran sulfate is located at 1014 cm^{-1}. The relative intensity of sulfate band varies significantly among the spectra of PECNP, surfactant and the mixture of PECNP-surfactant. This observation is consistent with our previously reported results for shift and intensification of SO_4^{2-} as a result of electrostatic complexation between zwitterionic surfactant and PECNPs [138]. Bands centered at 1327 cm^{-1} and 1578 cm^{-1} represent the δ_{N-H} stretch and in plane bending generated by the nitrogen-hydrogen bonds as unique feature of the polyethyleneimine [138]. The wide band centered at 1654 cm^{-1} in the brine is shared with other samples and can be attributed to the remaining water present in the lyophilized samples [28,132,133]. The PECNP-surfactant spectrum shares the features of both PECNP and surfactant solutions.

Variations in Raman scattering for the mixture of PECNP-surfactant solution in 33,667 ppm salinity brine can be predicted and modeled with least-square fitting approach [138]. A two-component model comprised of an average PECNP an average surfactant spectrum was created and used to fit four spectra collected from different locations within the lyophilized samples (Figure 64). The model was used to identify regions within the spectra where the PECNP-surfactant spectrum is not completely explained by the sum of the components, indicating a change in the chemical environment of the components when mixed. The residual when mostly noise is representative of a complete fit of the model to the mixture, whereas the presence of well-defined peaks is indicative of a change in chemical environment because of reactions between the individual components.

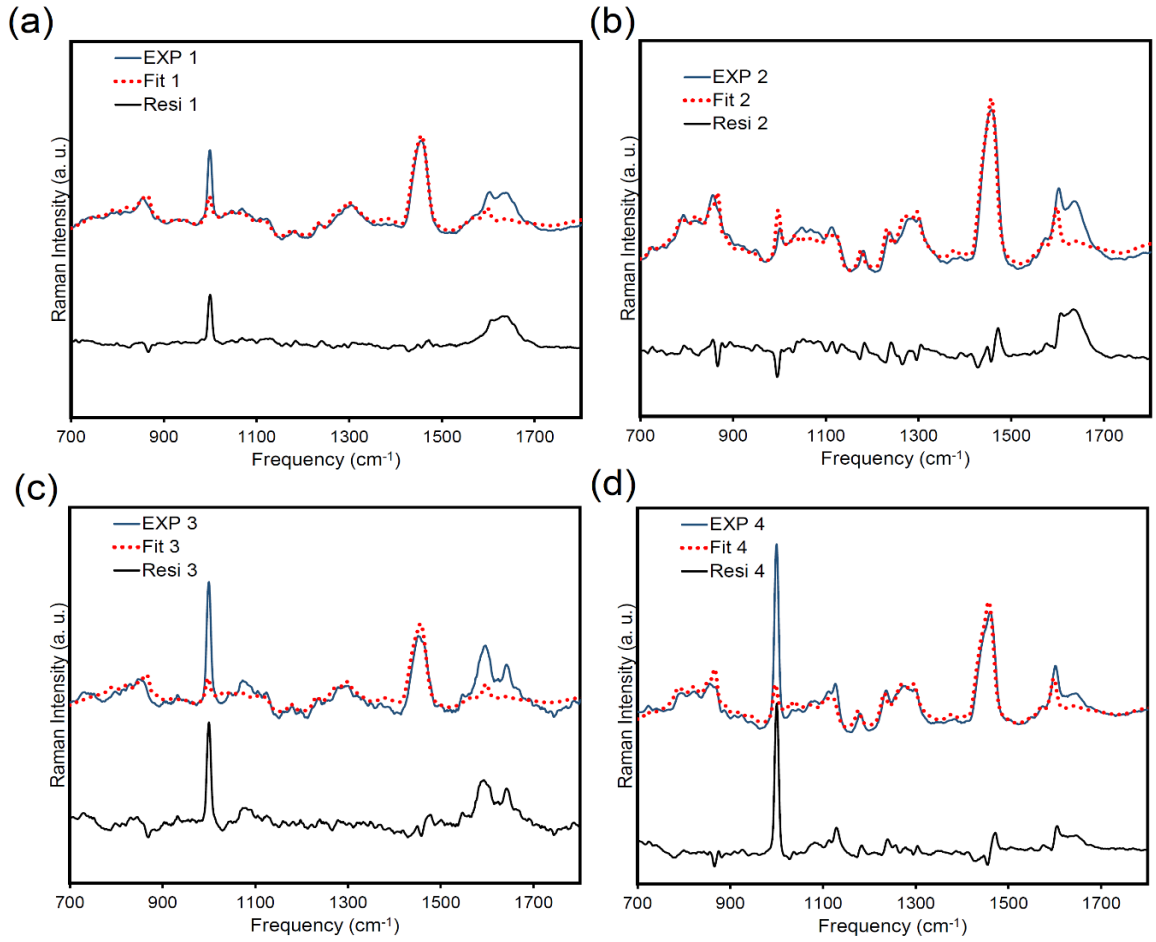

Figure 64. Raman spectra for four PECNP:Surfactant (1:9 ratio) samples shown with blue line were fitted with the average spectra for PECNP and surfactant and corresponding residual line, reprinted with permission from [48] Elsevier 2020

In each residual shown in Figure 64, the sulfate band at 1014 cm^{-1} represents a fingerprint residue and band regions between 1060 to 1100 cm^{-1} and 1615 to 1670 cm^{-1} are not explained with least-square model containing the features from PECNP and surfactant spectra. The sulfate intensification is due to change in chemical environment of key functional groups [138]. The residual peaks at 1060 to 1100 cm^{-1} and between 1615 and 1670 cm^{-1} are characteristic of aromatic and

aliphatic chain vibrational modes. The strength of the intensified regions varies between samples due to inhomogeneity of the lyophilized powders.

4.2. Complex fluid bulk and interfacial characterization

4.2.1. Bulk rheological properties

Hydraulic fracturing fluids experience high shear rates since fluid flows through the wellbore tubular and the shear rate drops significantly as the fluid gets into the fracture [54]. Therefore, shear rate sweep and static measurement studies help with understanding of the fluid behavior as fluid flow is mainly affected by flow geometry, time scale, foam microstructure and stability [20]. The rheology of dry CO_2 foam is widely regarded as non-Newtonian [20,21]. To characterize the non-Newtonian nature of $scCO_2$ foam created by the PECNP-surfactant mixture, first, the viscosity is measured at specific value of shear rate 2000 s^{-1} (Figure 65). The maximum apparent viscosity trend with time was observed for $scCO_2$ foam generated with PECNP:Surfactant systems with ratios of 1:9 and 4:6 prepared in 33.3 kppm and 66.7 kppm brines, respectively.

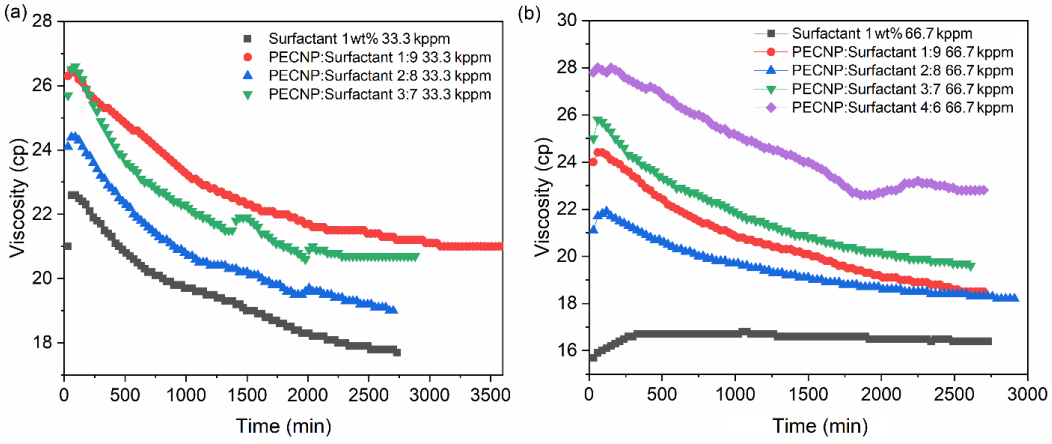

Figure 65. Viscosity with respect to time for 90% $scCO_2$ foam quality generated using 1:9, 2:8, 3:7 and 1:6 ratios of PECNP:Surfactant prepared in (a) 33.3 kppm and (b) 66.7 kppm brine. (Static constant shear measurement), reprinted with permission from [28] ACS 2019

It was previously noted that a high gas volume fraction above the volume fraction of bulk closed pack spheres can significantly increase the viscosity [139]. The bubble deformation at constant shear occurs with a slower rate for the most stable mixtures (1:9 and 4:6), as the surface tension of PECNP at the interface restores the bubble shape [20]. A higher apparent viscosity indicates the formation of smaller bubble sizes and a narrower size distribution [140], as a result of monodispersed ordered structures formed by the ionic PECNP/Surfactant stabilizers in the lamella [141]. Higher shear resistivity originates from the ability of lamella to reverse the deformations as well as energy storage capacity at the interface controlled by chemical components at CO_2-water interface [20].

The shear thinning behaviors of PECNP-surfactants were examined with the shear rate sweep test shown in Figure 66. Shear thinning for WLM at high concentrations entangled with flexible polymer chains on the nanoparticle surface was reported due to alignment of wormlike chains, which increases the viscoelasticity of the mixture [54]. Wanniarachchi et al presented the effect of very low and very high viscosity fracture propagation and proppant transport [142]. Although high viscosity foam carries the required amount of proppants to the fracture, it may not be able to penetrate through micro-fractures with tiny openings, so the moderate viscosity range (50-250 cP) is recommended [142,143].

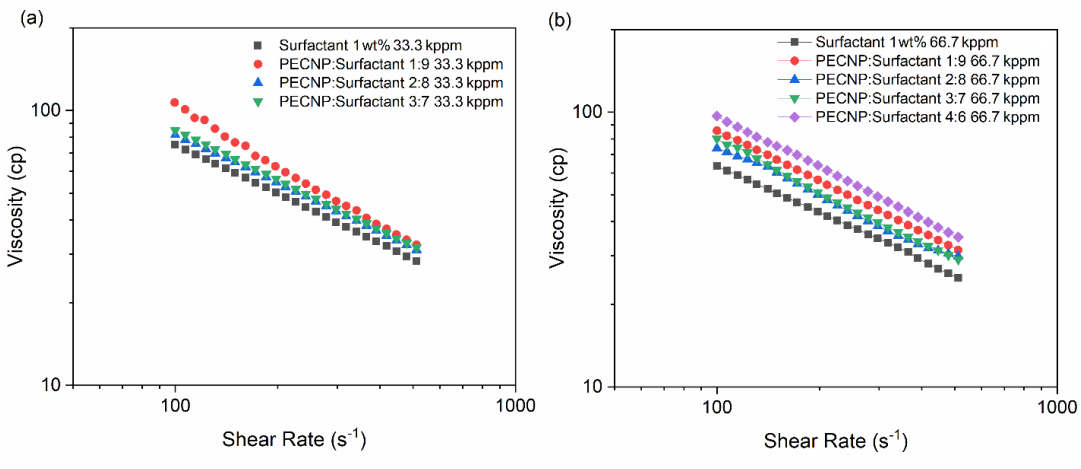

Figure 66. Viscosity with respect to shear rate of 90% $scCO_2$ foam quality systems prepared using 1:9, 2:8, 3:7 and 4:6 ratios of PECNP:Surfactant in (a) 33.3 kppm and (b) 66.7 kppm brine. (Static Shear Sweep Measurement), reprinted with permission from [28] ACS 2019

Shear thinning properties were evaluated through the laminar flow of incompressible $scCO_2$ foam through a Couette geometry rheometer and the results were matched by the power law model [20,144]. The apparent viscosity of the foam was reduced with increasing shear rate (shear softening with $n < 1$). Foam lamella drainage is at its lowest for the highest viscosities achieved with PECNP:Surfactant solutions with 1:9 ratio in 33.3 kppm and 4:6 in 66.7 kppm, respectively. Xue and coworkers demonstrated the viscous thick lamella's ability in 'CO_2- aqueous phase' to lower the rates of Ostwald ripening [55] which leads to generation of smaller bubbles [85]. The two PECNP-surfactant systems prepared in the 33.3 kppm and 66.7 kppm, respectively, offer higher apparent viscosity and flow consistency indices (Table 5) to enhance proppant transport and placement.

The flow consistency index depicts the highest value for optimal concentrations of PECNP and WLMs shown in Table 5.

Table 5. Flow consistency index (K) and flow behavior index (n) for variety of PECNP/Surfactant scCO2 foam systems. Reprinted with permission from [17] Copyright SPE 2018.

33.3 kppm System	K (Pa s^n)	n
Surfactant-$scCO_2$	1184.3	0.402
PECNP:Surfactant-$scCO_2$ (3:7)	1387.9	0.394
PECNP:Surfactant-$scCO_2$ (2:8)	1261.6	0.407
PECNP:Surfactant-$scCO_2$ (1:9)	2916.4	0.276
66.7 kppm System	K (Pa s^n)	n
Surfactant-$scCO_2$	1035.7	0.368
PECNP:Surfactant-$scCO_2$ (4:6)	1683.1	0.380
PECNP:Surfactant-$scCO_2$ (3:7)	1443	0.371
PECNP:Surfactant-$scCO_2$ (2:8)	1163.9	0.405
PECNP:Surfactant-$scCO_2$ (1:9)	1464.6	0.385

Plastic deformation in the bulk fluid shown in Figure 66 are the result of stress induced bubble slide, coalescence and coarsening, which are controlled by elastic deformation of film containing a network of the PECNP-WLMs nanoparticles in the solid like interface studied by dilatational elasticity measurements. The flow consistency index depicts the highest value for optimal concentrations of PECNP and WLMs (Table 5), therefore, pressure drops across the tubular wellbore and fractures reaches their highest level for optimal values [145].

The formation of PECNPs as a result of electrostatic complexation of PECNP with WLMs helps to stabilize the water-CO_2 lamella by enhancing the viscosity, rigidity and electrostatic repulsion among lamellae surfaces [56]. In addition to Ostwald ripening slow down caused by high packing fractions of WLMs [55], association of surfactant with nanoparticle enhances the stability and viscosity of foam lamella even further.

4.2.2. Interfacial tension analysis and CMC

Figure 67 reveals the CMC calculations for a variety of surfactant concentrations in 33.3 kppm and 66.7 kppm brine systems according to the analysis of interfacial tension measurements.

The determined CMCs are 0.059 wt% for 33.3 kppm brine and 0.055 wt% for 66.7 kppm brine. The presence of two charges on the surfactant molecule helps to form the micelles at lower concentrations [54]. Micellar solutions are formed above the CMC in both 33.3 kppm and 66.7 kppm high salinity brines. The zwitterionic surfactant micelles were found to aggregate into worm like micelles (WLM) with self-assembly of surfactant into the elongated structures [54], thus, WLMs are expected to exist at 1 wt% surfactant in high salinity brine. It was previously reported that salt ions would screen the electric double layer around the micelles and negatively affect the micellar assembly [115], however, the ionic activity of zwitterionic surfactant gives rise to the effective micellar volume fraction, therefore, CMC is still achieved at low concentrations.

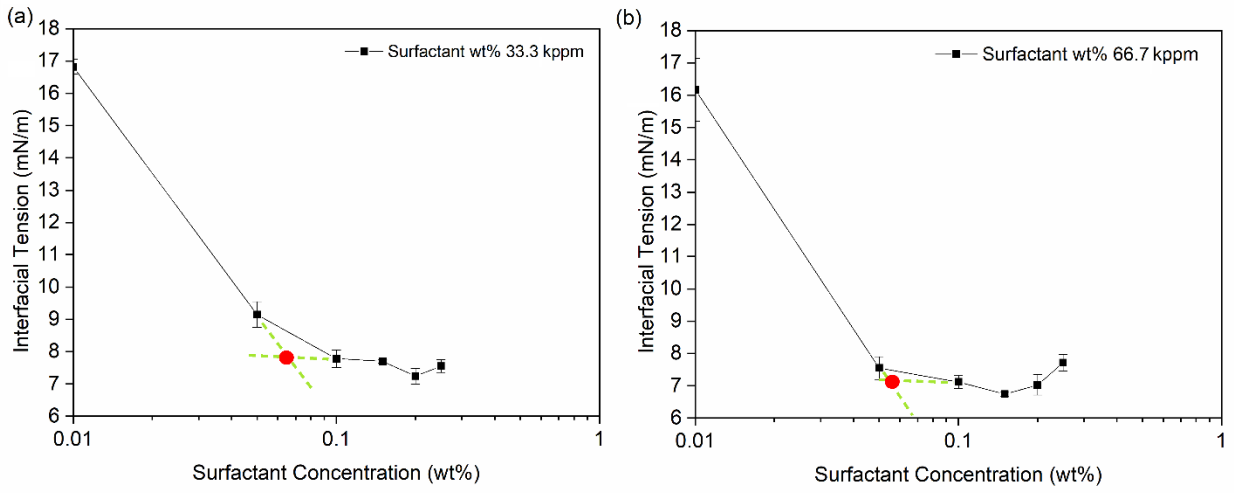

Figure 67. The critical micelle concentration for the viscoelastic surfactant at two different brine salinity of (a) 33.3 kppm, and (b) 66.7 kppm, reprinted with permission from [28] ACS 2019

Interfacial tension analysis results for $scCO_2$ bubbles formed in 1 wt% surfactant and PECNP in 33.3 kppm and 66.7 kppm brine systems suggest that the interfacial tension dramatically declines upon addition of surfactant and PECNP:Surfactant (Figure 68 a,b). The very low IFT values of 5.4 and 6.4 mN/mm were obtained after addition of 1 wt% surfactant and PECNP-surfactant, with 1:9 ratio, to 33.3 kppm brine due to interfacial stabilization of $scCO_2$-brine lamella

by improving repulsive forces created using ionic micelles, wormlike micellar self-assembly with PECNP and the network layer formed in the lamella. The IFT decline hits the minimum value (5.5 mN/mm) in lower concentration of ionic salts (33.3 kppm), whereas at higher concentrations (66.7 kppm), due to higher presence of ionic interactions and imbalanced forces, slightly a higher IFT value was detected. Addition of WLMs further stabilizes the $scCO_2$ lamella due to micellar branching and intra-aggregate attractions which lower the perturbations and imbalanced forces at the interface, as reported by Bouri and Tewes [114,146]. Polymeric nanoparticles present in the lamella in conjunction with WLMs form vesicular nano-capsules in which ionic aggregates reorient from the bulk phase to the lamella border and form arrays of stabilized PECNPs lining up on the interface between the supercritical phase and aqueous phase. While PECNPs do not necessarily reduce the IFT at the interface, one should note PECNP-surfactant nanoparticles are not a driving force for lamella instability and imbalanced forces at the interface, so the ionic compatibility and stability are preserved.

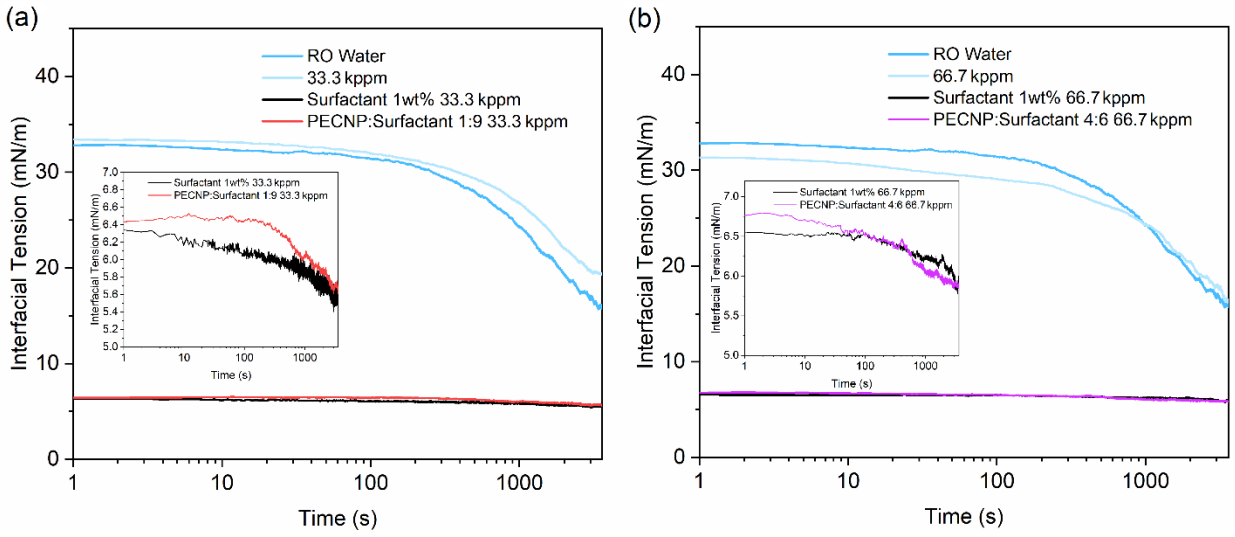

Figure 68. The interfacial tension measured for surfactant and PECNP in (a) 33.3 kppm and (b) 66.7 kppm brine, reprinted with permission from [28] ACS 2019

The dilatational elasticity was measured for RO water, surfactant and PECNP in (a) 33.3 kppm and (b) 66.7 kppm brine according to equation (1) using dynamic interfacial tension measurements with $scCO_2$ (Figure 69). Examples of calculations for ionic mixtures in 33.3 kppm and 66.7 kppm high salinity brine are shown in Table 6 and 7.

Table 6. Summary of elasticity calculations from interfacial tension analysis in 33.3 kppm systems, reprinted with permission from [28] ACS 2019

System	Initial π	Final π	Δπ(ne)	Δπ(e)	Initial A	Final A	ΔA	ΔA/Ai	Ee
RO-Water-$scCO_2$	32.21	24.91	7.3	24.91	18.87	14	4.87	0.26	96.52
33.3kppm-$scCO_2$	31.51	28.7	2.81	28.7	18.86	20.04	1.18	0.066	458.71
33.3kppm-Surf-$scCO_2$	5.95	5.59	0.36	5.59	7.41	3.79	3.62	0.49	11.44
33.3kppm-PECNP:Surf 1:9 $scCO_2$	6.27	5.76	0.51	5.76	5.25	4.39	0.86	0.16	35.16

Table 7. Summary of elasticity calculations from interfacial tension analysis in 66.7 kppm systems, reprinted with permission from [28] ACS 2019

System	Initial π	Final π	Δπ(ne)	Δπ(e)	Initial A	Final A	ΔA	ΔA/Ai	Ee
RO-Water-$scCO_2$	32.21	24.91	7.3	24.91	18.87	14	4.87	0.26	96.52
66.7kppm-$scCO_2$	29.93	27.14	2.79	27.14	20.9	21.9	1	0.05	567.23
66.7kppm-Surf-$scCO_2$	5.64	7.39	1.75	7.39	4.7	5.94	1.24	0.265	28.01
66.7kppm-PECNP:Surf 4:6 $scCO_2$	6.78	6.34	0.44	6.34	4.96	5.3	0.34	0.07	92.49

Dilatational elasticity represents the surface tension gradient which opposes the film drainage and provides a more stable film along the CO_2-water interface [115]. High values of surface elasticity does not guarantee the counterbalance of surfactant adsorption and surface diffusion to

surface tension gradient and velocity of film thinning [115], thus the surface tension variation at the interface with respect to area change needs to fall within the allowable range to oppose the destabilizing forces [146,147].

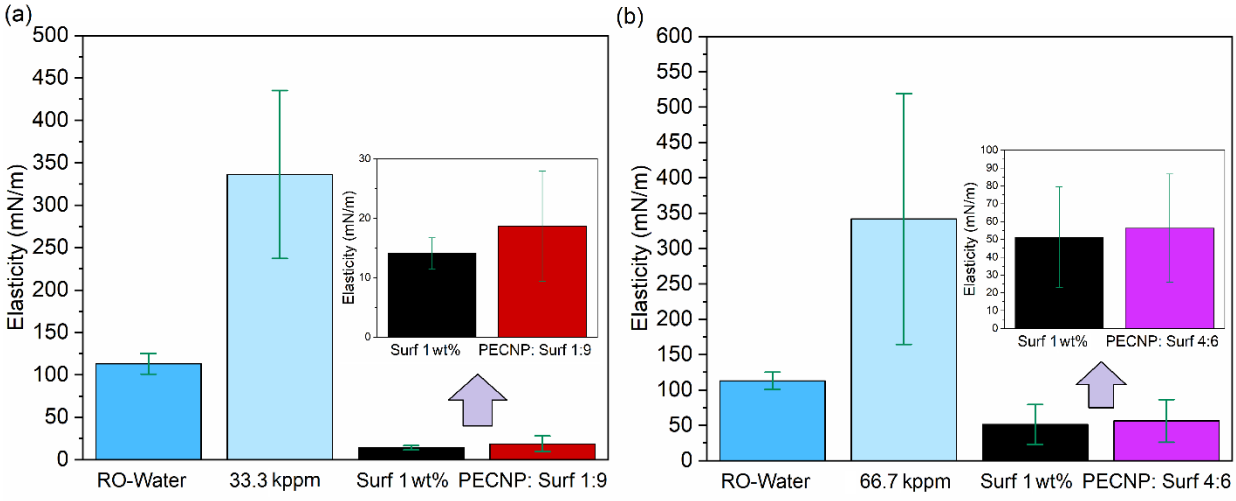

Figure 69. The dilatational elasticity measured for RO water and surfactant and PECNP in (a) 33.3 kppm and (b) 66.7 kppm brine according to interfacial tension analysis, reprinted with permission from [28] ACS 2019

Similar to IFT, the equilibrium surface dilatational elasticity is significantly lower than RO water and high salinity brines, when WLMs and PECNP-WLM mixtures exist in the CO_2-water interface (Figure 68). The difference between the elasticity obtained by WLMs and PECNP-WLM is not considerable, though addition of PECNP slightly increases the value as an indication of infinitesimal rigidity added to the interface, when PECNP-WLMs agglomerates form networks at the interface, giving rise to lamella elasticity and prolonging the bubble rupture time.

4.3. Macroscale foam stability measurements

For initial stage of stability measurements, the foaming mixture was mixed with air as shown in Figure 70. The foam height was measured with respect to time.

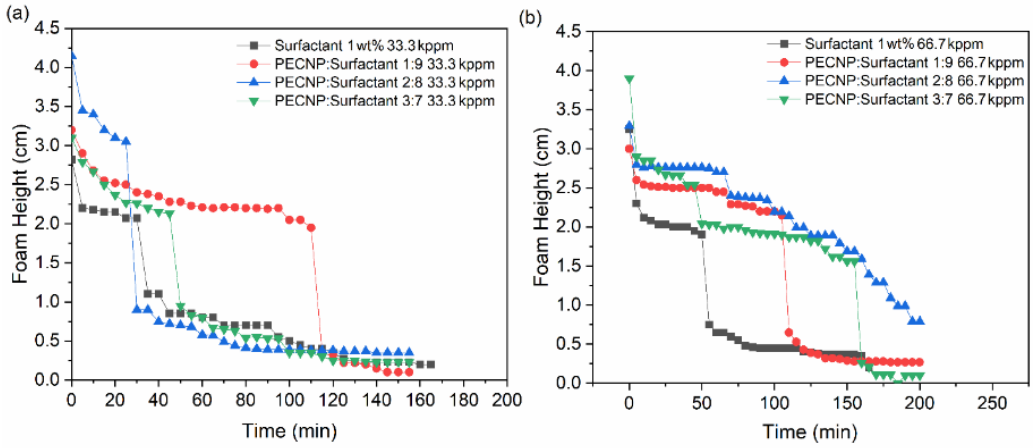

Figure 70. Preliminary foam stability test for different ratios of PECNP to Surfactant mixed with air for two different brine concentrations (a) 33.3 kppm and (b) 66.7 kppm, reprinted with permission from [28] ACS 2019

Zhang and coworkers reported adsorption and self-assembly of micelles above CMC at the air-water interface for ionic surfactants forming surface segregation with hydrophobic and hydrophilic regions so repartitioning around the gas-liquid interface [148]. Surfactant-water solubility and nanoparticle compatibility to the ionic interface helped to create relative stability as the resulting foam remains stable for at least 100 min when optimum concentrations of micelles and nanoparticles exist.

Actual foam stability measurement was performed on $scCO_2$ mixture with PECNP-surfactant in high salinity brines. Figure 71 illustrates the foam stability measurements and the actual foam formation and degradation inside the sapphire view cell (Figure 71c). Fine-textured and homogenous cellular structures with dominant microcellular texture (~200 to 300 µm) were formed with different ratios of PECNP to surfactant solution. Uniform bubble size and distribution was achieved with 1:9 and 4:6 portions of PECNP to surfactant (Figure 71d).

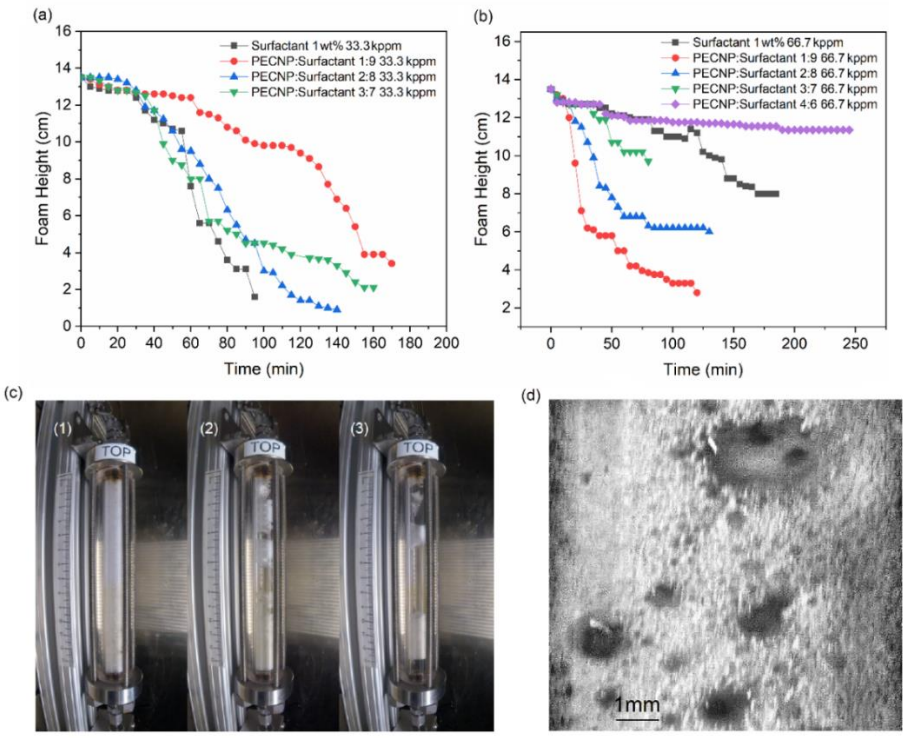

Figure 71. Foam stability measurements for $scCO_2$ foam made with variety of PECNP-surfactant mixtures in (a) 33.3 kppm brine solutions. (b) 66.7 kppm brine solutions (c-1) Foam generation and isolation in the view cell (c-2) foam drainage progress (c-3) Total foam Total foam disappearance and breakage (d) foam microstructural view inside the view cell for PECNP:Surfactant 1:9 in 33.3 kppm brine, reprinted with permission from [28] ACS 2019

Likewise, the longest-lived foam belongs to 1:9 and 4:6 ratios in the 33.3 kppm and the 66.7 kppm brines, respectively, as foam preserves the cellular structure for at least 2 h in the view cell in these scenarios. The foam half-decay time for different systems are presented in Table 8. The half-decay time for PECNP-surfactant (with 1:9 ratio in 33.3 kppm brine) is more than twice that of 1 wt% surfactant mixed with $scCO_2$. The half-life shortens when a higher portion of nanoparticle is used due to lower electrostatic repulsions as explained in section 3.1.1.1 In contrast, for 66.7 kppm brines, a higher proportion of nanoparticle to surfactant increases the half-life dramatically (PECNP: Surfactant 4:6 in 66.7 kppm). Recently, Al-Anssari and co-workers

reported that the increased surface tension caused by increasing salinity can eliminate the stabilizing influence of nanoparticles at CO_2-brine interface [149].

Table 8. Foam half decay time for variety of PECNP-Surfactant proportions (No half time: No recorded decay to half of the foam height due to stability of the foam system), reprinted with permission from [28] ACS 2019

33.3 kppm System	half decay time (min)
Surfactant-$scCO_2$	65
PECNP:Surfactant-$scCO_2$ (3:7)	70
PECNP:Surfactant-$scCO_2$ (2:8)	80
PECNP:Surfactant-$scCO_2$ (1:9)	140
66.7 kppm System	half decay time (min)
Surfactant-$scCO_2$	No half time
PECNP:Surfactant-$scCO_2$ (4:6)	No half time
PECNP:Surfactant-$scCO_2$ (3:7)	No half time
PECNP:Surfactant-$scCO_2$ (2:8)	60
PECNP:Surfactant-$scCO_2$ (1:9)	30

Bubble rupture and CO_2-water lamella drainage occur in a longer period with lower rate, when PECNP forms ionic complexes with WLMs resulting in stronger electrostatic interactions in the lamella, including the plateau border and lamella border wall. In 66.7 kppm salinity brine, addition of PECNP to surfactant deteriorates the foam stability to some extent due to excessive charge attractions destabilizing the lamella. However, increasing the PECNP-surfactant solution ratio (to PECNP of around 40 v/v %) provides a very stable lamella against lamella drainage, bubble coalescences and coarsening.

In foam fracturing, initial good film stability at initial stages is necessary, however, the generated foam needs to degrade when it comes to contact with oil, breaking, as fast during the flow back, leaving behind a fracture with high effective conductivity [17]. Therefore, an unstable lamella is required upon introduction of oil to foaming system. The foam stability measurements in the presence of oil are shown in Figure 72 where $scCO_2$ foam made in 33.3 kppm and 66.7 kppm

was exposed to MLP crude oil in a view cell and the foam height with respect to time is shown. The most stable foams presented in Figure 70a,b (with 1:9 and 4:6 PECNP:Surfactant ratios), are the least stable ones with fastest drainage when the oil is introduced to the view cell (Figure 72a, b).

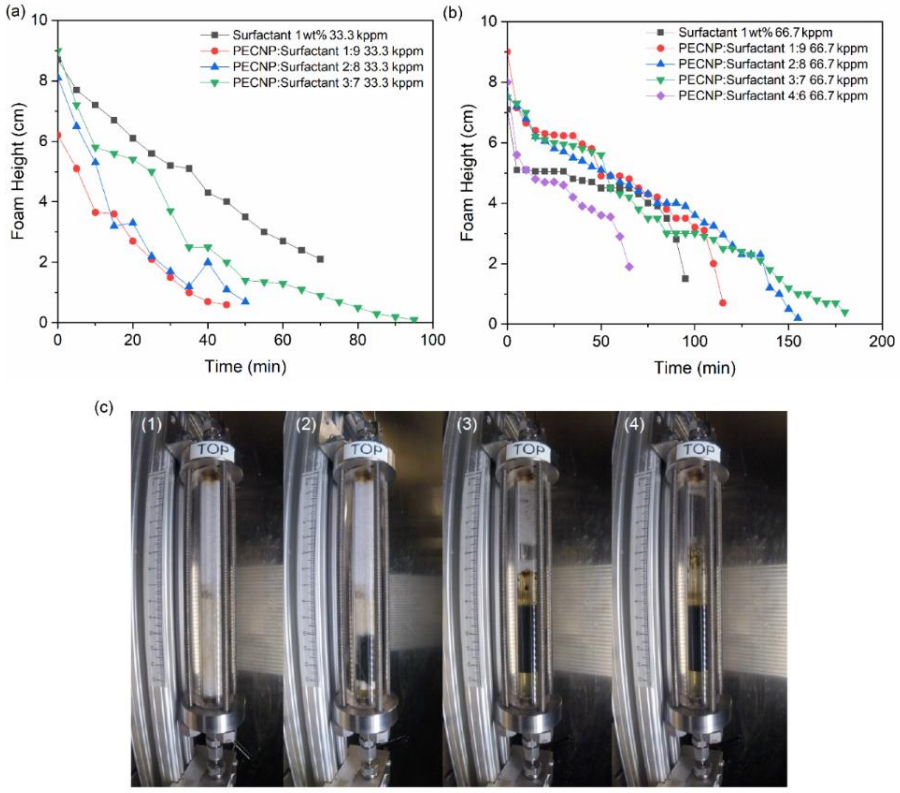

Figure 72. Foam stability measurements in the presence of crude oil for variety of PECNP-surfactant mixtures in 33.3 kppm brine solutions (b) 66.7 kppm brine solutions (c-1) Foam generation and isolation in the view cell (c-2) Introduction of the oil (c-3) Foam drainage in the presence of oil (c-4) Total foam disappearance and oil dominance**,** reprinted with permission from [28] ACS 2019

As it was previously noted, due to low interfacial tension between CO_2 and oil at high pressures, crude oil enters the original lamella, spreading and accelerating the thinning of lamella, coarsening the foam and causing gas bubble coalescence [150,151]. The time frame of the lamella

breakage depends heavily on the interaction of oil with the chemical components residing in the lamella, in this case, the PECNP-Surfactant complexes in lamella. As WLMs meet the oil molecules, the oil collapses into an emulsion [54]. The PECNP is also susceptible to degradations as carboxylic acid groups on MLP crude oil can trigger the secessions of coiled PEI-DS chains and electrostatic desorption of amine functional groups resulting in instability of the PECNP-WLMs in the lamella. Configuration of the oil at the gas-aqueous interface is another determining factor in oil instability, when pseudo-emulsion film formed between the oil and the gas is ruptured and oil spreads at the interface (bridge configuration) [115]. Accordingly, disintegration of the interface is anticipated due to positive entering and spreading coefficients previously reported by Xiao et al [22]. Table 9 summarizes the entering (E) and spreading (S) coefficients obtained by interfacial tension measurements as underlying equations for calculation are as following [152]:

(4-1) $$E = \sigma_{wg} + \sigma_{ow} - \sigma_{og}$$

(4-2) $$S = \sigma_{wg} - \sigma_{ow} - \sigma_{og}$$

Table 9. Entering and Spreading Coefficients for PECNP and Surfactant mixtures in the presence of $scCO_2$ and MLP crude oil, reprinted with permission from [28] ACS 2019

33.3 kppm System	σ_{wg}(mN/m)	σ_{ow}(mN/m)	E (mN/m)	S (mN/m)
Brine	33.42	11.47	44.89	21.95
Surfactant 1 wt%	6.35	0	6.35	6.35
PECNP	14.97	0.87	15.84	14.1
PECNP:Surfactant (1:9)	6.43	0	6.43	6.43
66.7 kppm System	σ_{wg}(mN/m)	σ_{ow}(mN/m)	E (mN/m)	S (mN/m)
Brine	31.45	9.97	41.42	21.48
Surfactant 1 wt%	6.55	0	6.55	6.55
PECNP	15.1	1.7	16.8	13.4
PECNP:Surfactant (4:6)	6.74	0	6.74	6.74

Surface tension between the oil and $scCO_2$ (σ_{og}) is considered a negligible value since the operating condition is above the minimum miscibility pressure of the MLP and $scCO_2$ (MMP~ 1200 psi). Considering the positive values of E and S, crude oil is capable of entering the gas-water interface and spreading on the liquid lamella, so the weakening of the disjoining pressure by disturbing the PECNP-Surfactant charge distribution and desorption to the lamella occurs spontaneously [22].

4.4. Hydraulic fracturing performance

4.4.1 Dynamic Fluid Loss

It is critical to control the leak off rate of fracturing fluids to reduce pumping cost and to ensure the mechanical integrity of the formation. Production from horizontal wells in tight reservoirs requires high internal fracture conductivity since conductivity provides a path to accommodate high velocity hydrocarbon flow [153]. Fluid loss coefficients were measured with the setup presented in Figure 36 for the $scCO_2$ foams prepared with highest apparent and dynamic viscosities (1:9 ratio and 4:6 ratio of PECNP- surfactant in 33.3 kppm and 66.7 kppm brine systems, respectively) and the results are shown in Figure 73.

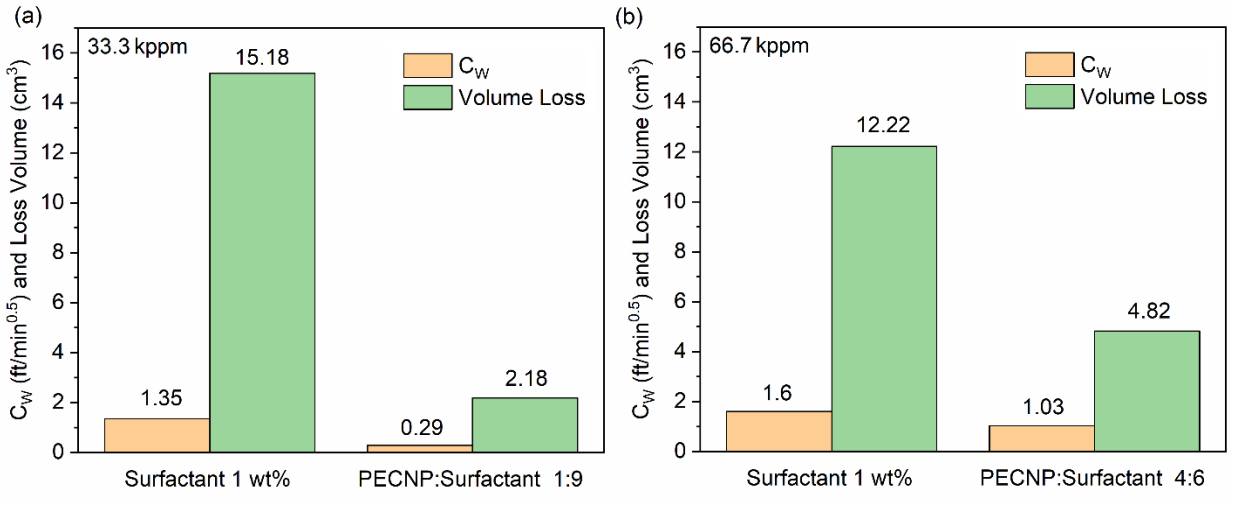

Figure 73. Total fluid loss (gas and liquid) and fluid loss coefficient for the mixtures prepared in (a) 33.3 kppm and (b) 66.7 kppm high salinity brines, reprinted with permission from [28] ACS 2019

The volume loss (gas and liquid) belong to the surfactant and PECNP:Surfactant systems penetrated through the Kentucky limestone core placed in the module (Figure 36) is shown in Figure 74.

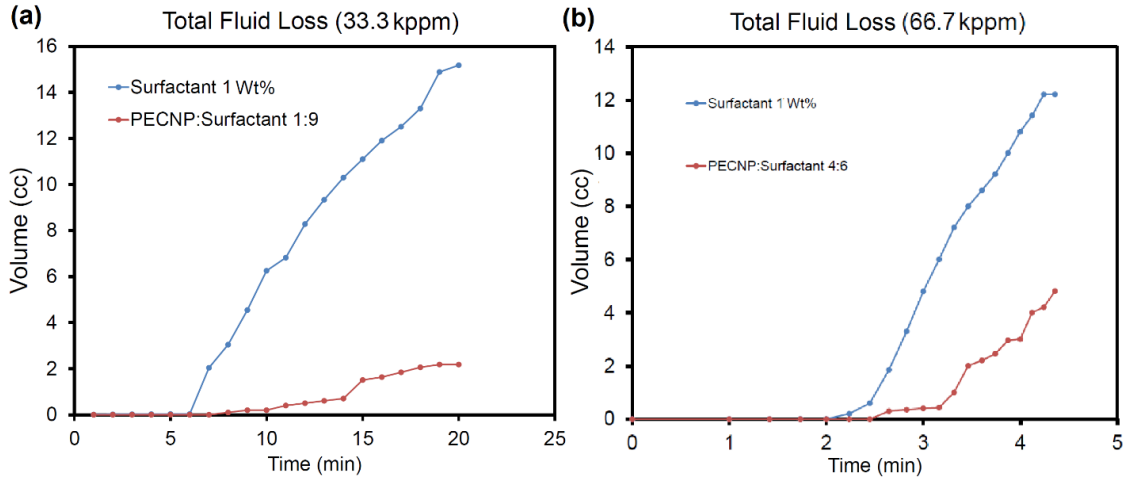

Figure 74. Volume of gas and liquid fluid loss for surfactant and PECNP:Surfactant mixtures in (a) 33.3kppm and (b) 66.7kppm high salinity brine, reprinted with permission from [28] ACS 2019

The Permeability of the core before and after the foam flood through the module was measured (Table 10) and the results indicated no significant change in the permeability of tight cores (varying between 0.18 to 0.23 mD). Here is the example of permeability measured before and after fluid loss experiment with surfactant 1 wt% and PECNP:Surf 4:6 in 66.7 kppm brine. The permeability was calculated for each individual core sample according to Darcy's law with the flow rate of 0.1, 0.3 and 1 mL/min.

Table 10. Summary of permeability calculations from core flood analysis on Kentucky Sandstone tight core in 66.7 kppm systems, reprinted with permission from [28] ACS 2019

Core	Fluid Loss Liquid	Slope	KA/μL	μ (cP)	A (cm^2)	L (cm)	K (D)	K(mD)
Kentucky	-	0.0005	0.0005	1.05	5.08	2.23	0.000231	0.23
Kentucky	Surf 1% 66.7kppm	0.0005	0.0005	1.05	5.08	2.23	0.000231	0.23
Kentucky	PECNP:Surf 4:6 66.7 kppm	0.0004	0.0004	1.05	5.08	2.23	0.000185	0.18

The initial and final permeability of a Kentucky sandstone tight core exposed to the flow of $scCO_2$ foam with PECNP-surfactant remained constant (0.18 mD) revealing minimal pore throat plugging and damage to the core as a result of core exposure to the fracturing fluid. The fluid loss volume and fluid loss coefficients were significantly lowered when PECNP-surfactant was used as the aqueous component of the foaming solution as compared to surfactant alone, resulting in a reduced leaked volume in the tight core and enhanced fracture properties. The fluid loss coefficient is a function of core permeability, surfactant/PECNP concentration and temperature [69]. Furthermore, it was previously reported that higher foam quality provides higher viscosity and reduced leak-off [154]. Efficient merge of WLMs to PECNPs resulted in the formation of nanoparticles performing as fluid loss additives during the injection of the foam solutions. The

results were consistent with rheological measurements where PECNP-surfactant systems prepared in 33.3 kppm and 66.7 kppm brine exhibited the highest viscosities over the shear thinning period. It was previously argued that osmotic pressure, which leads to foam tendency to retain water, prevents the water leak-off to the formation [155], thus, it can be concluded that PECNP-WLMs enhance the proppant carrying capability of $scCO_2$ foam while lowering the water usage.

4.4.2 Sand Pack Measurements

The detailed flooding scenarios and mobility features in the sand pack experiment are indicated in Table 11.

The sand pack experiment included a primary brine flood to measure the initial pack permeability, an oil flood for complete saturation, a foam flood for clean-up and a secondary brine flood for secondary packed bed permeability. The flood scenarios and apparent viscosities for different scenarios of flood in the sandpack is represented in Table 11.

Table 11. Flood scenarios and mobility features for surfactant, oil and $scCO_2$ foam floods in the sand pack, reprinted with permission from [28] ACS 2019

Sand pack scenarios	PV (cm^3)	Q (cm^3/s)	k (D)	ΔP (psi)	μ_{app} (cP)
33.3 kppm Brine Flood	7.58	0.1	169.94	0.38	0.93
Oil Flood	7.58	0.1	169.94	2.71	6.66
Surf 1 wt% $scCO_2$ Flood	7.58	0.1	169.94	6.00	14.75
Secondary Brine Flood	7.58	0.1	154.22	0.32	0.71
33.3 kppm Brine Flood	7.63	0.1	154.23	0.48	1.07
Oil Flood	7.63	0.1	154.23	2.42	5.4
PECNP:Surf 1:9 $scCO_2$ Flood	7.63	0.1	154.23	8.43	18.8
Secondary Brine Flood	7.63	0.1	157.77	0.35	0.8
66.7 kppm Brine Flood	7.41	0.1	155.14	0.56	1.26
Oil Flood	7.41	0.1	155.14	2.87	6.44
Surf 1 wt% $scCO_2$ Flood	7.41	0.1	155.14	4.02	9.02
Secondary Brine Flood	7.41	0.1	156.12	0.34	0.77
66.7 kppm Brine Flood	7.47	0.1	154.91	0.43	0.96
Oil Flood	7.47	0.1	154.91	2.66	5.96
PECNP:Surf 4:6 $scCO_2$ Flood	7.47	0.1	154.91	5.56	12.46
Secondary Brine Flood	7.47	0.1	143.87	0.36	0.75

The pressure drop profile for each condition is presented in Figure 75 to 78 for the cases where the 33.3 kppm brine is used. Primary brine flood pressure profile is represented in Figure 75 for different flow rates.

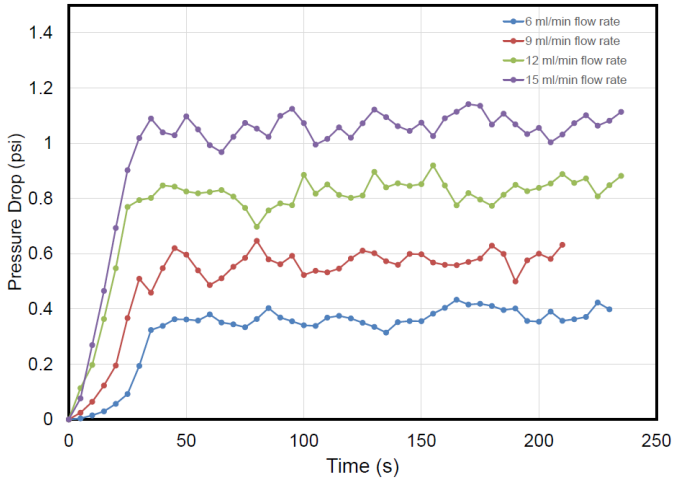

Figure 75. Primary brine flood in the proppant filled packed bed with 33.3 kppm high salinity brine, reprinted with permission from [28] ACS 2019

Oil flood is the second step of sandpack experiment, and the corresponding pressure profile is represented in Figure 76 (flow rate 6 ml/min).

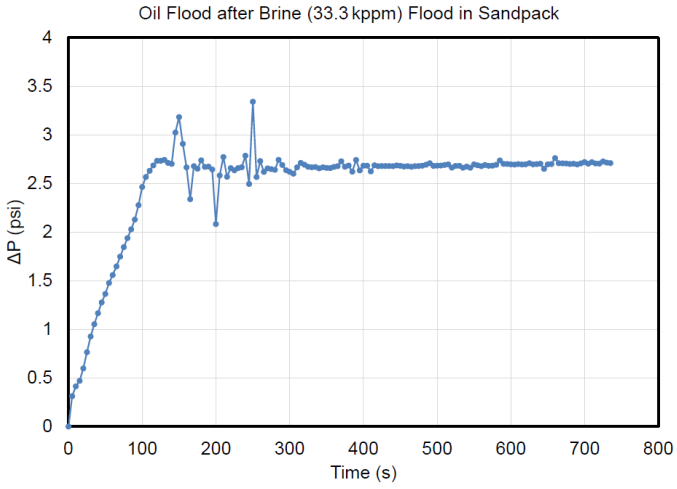

Figure 76. Oil Flood in the proppant filled packed bed saturated with 33.3 kppm high salinity brine, reprinted with permission from [28] ACS 2019

Foam flood is the third step of sandpack experiment, and the corresponding pressure profile is represented in Figure 77 (flow rate 6 ml/min).

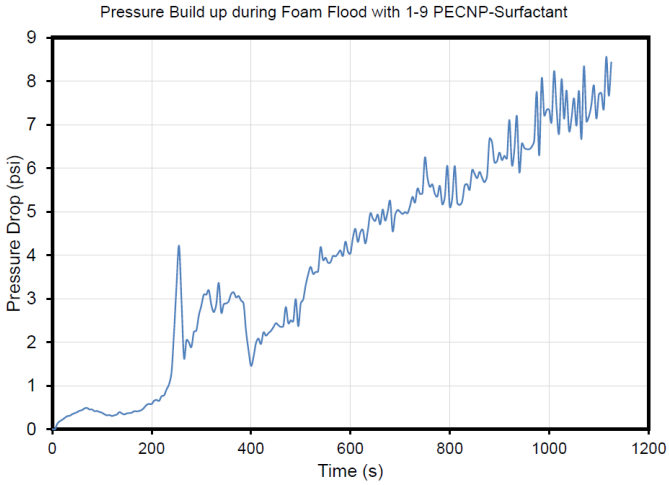

Figure 77. Foam Flood in the proppant filled packed bed saturated with MLP Crude Oil, reprinted with permission from [28] ACS 2019

Secondary brine flood is the last step of sandpack experiment, and the corresponding pressure profile is represented in Figure 78 for different flow rates.

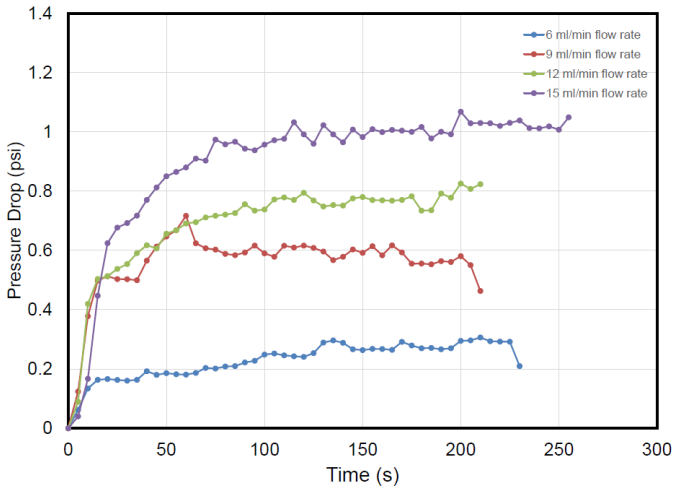

Figure 78. Secondary brine flood in the proppant filled packed bed, reprinted with permission from [28] ACS 2019

Also, no significant change in pack permeability was observed when the permeability of pack during primary and secondary brine flood were compared in this case. The results are summarized in Table 12.

Table 12. Summary of permeability calculations from sand pack analysis (primary and secondary brine flood), reprinted with permission from [28] ACS 2019

Stage	Slope	KA/μL	μ (cP)	A (cm^2)	L (cm)	K (D)	K(mD)
Primary Flood	3.07	3.07	1.02	0.55	25.93	147.30	147302
Secondary Flood	3.05	3.05	1.02	0.55	25.93	146.24	146237.2

The saturation of oil in the pack after oil and foam flood is measured and presented in Table 13.

Table 13. Summary of calculations related to oil saturation in the sand pack after oil and foam flood in 66.7 kppm high salinity brine systems, reprinted with permission from [28] ACS 2019

System	Pore Volume (mL)	Volume of Flooded Oil (mL)	Volume of Collected Oil (mL)	Oil Saturation after Oil Flood (%)	Volume of Flooded Foam (liquid) (mL)	Volume of Collected Oil (mL)	Oil Saturation after Foam Flood (%)
Surf 1wt% 66.7kppm	7.69	76.34	59.8	97.96	11.37	18.2	30.17
PECNP:Surf 4:6 66.7 kppm	7.58	75.01	59.6	84.47	11.36	18.1	17.02

The permeability of the pack after an initial brine flood with 33.3 kppm and 66.7 kppm brine varies between 144 to 170 D, based on Darcy's law, the value represents the high permeability porous pack. The apparent viscosity of fracturing fluid in the pack is calculated according to the Darcy's equation (equation 4-3):

(4-3) $$\mu_{app} = \frac{k.A.\Delta P.}{Q.L}$$

where k is permeability of the fluid inside the pack, ΔP is the pressure difference between the two ends of the pack, A is the cross section area of the pack, Q is the volumetric flow rate of fracturing fluid flow in the pack column and L is the pack length. Accordingly, the apparent viscosity is obtained, and the results are shown in Table 12. Upon oil saturation, 10 pore volumes of crude oil were flooded to completely saturate the pack. The efficiency of the oil flood varied between 84 to 100%. Consequently, the $scCO_2$ foam was flooded to clean up the oil saturated pack. Foam breakthrough occurred at 5.9 and 5.35 PV of foam flood for 33.3 kppm and 66.7 kppm brines, respectively, representing the better oil clean-up and sweep efficiency for 33.3 kppm salinity $scCO_2$ foams as a result of the foam half decay time and higher viscosity shown in Table 5 and Table 8.

The pressure drop is recorded during the propagation of oil or $scCO_2$ foam through the sand pack. Figure 79a, b exhibits the magnitude of the pressure drop with respect to time of foam flood. Relative stability, propagation, and performance of the $scCO_2$ foam in the pack helped to effectively mobilize and recover the crude oil in the fractured reservoirs. Accordingly, large effective viscosities and sufficient mobility control for PECNP-Surfactant enhanced $scCO_2$ foam are concluded.

The saturation of oil and water phase in the pack after the oil flood is calculated from the following sets of equations:

(4-4) $$S_{o1} = \frac{V_{oi} - V_{oc} - V_{P2} - V_{P1}}{PV} \text{ and}$$

(4-5) $$S_{w1} = 1 - S_{o1},$$

where S_{o1} is the oil saturation in the pack, V_{oi} is the injected volume of oil through the lines and pack, V_{oc} is the collected volume of oil in the outlet after the oil flood. V_{P1} and V_{P2} are purt volumes of inlet and outlet lines connected to the pack. S_{w1} is the remaining saturation of aqueous phase in the pack. PV is pore volume of ceramic proppants in the pack. Likewise, the saturation of oil and water phase in the pack after the foam flood is shown as:

(4-6) $$S_{o2} = S_{o1} - \frac{V_{ocf} - V_{P2} - V_{P1}}{PV} \text{ and}$$

(4-7) $$S_{w2} = 1 - S_{o2},$$

where S_{o2} and V_{ocf} are the oil saturation and collected oil volume.

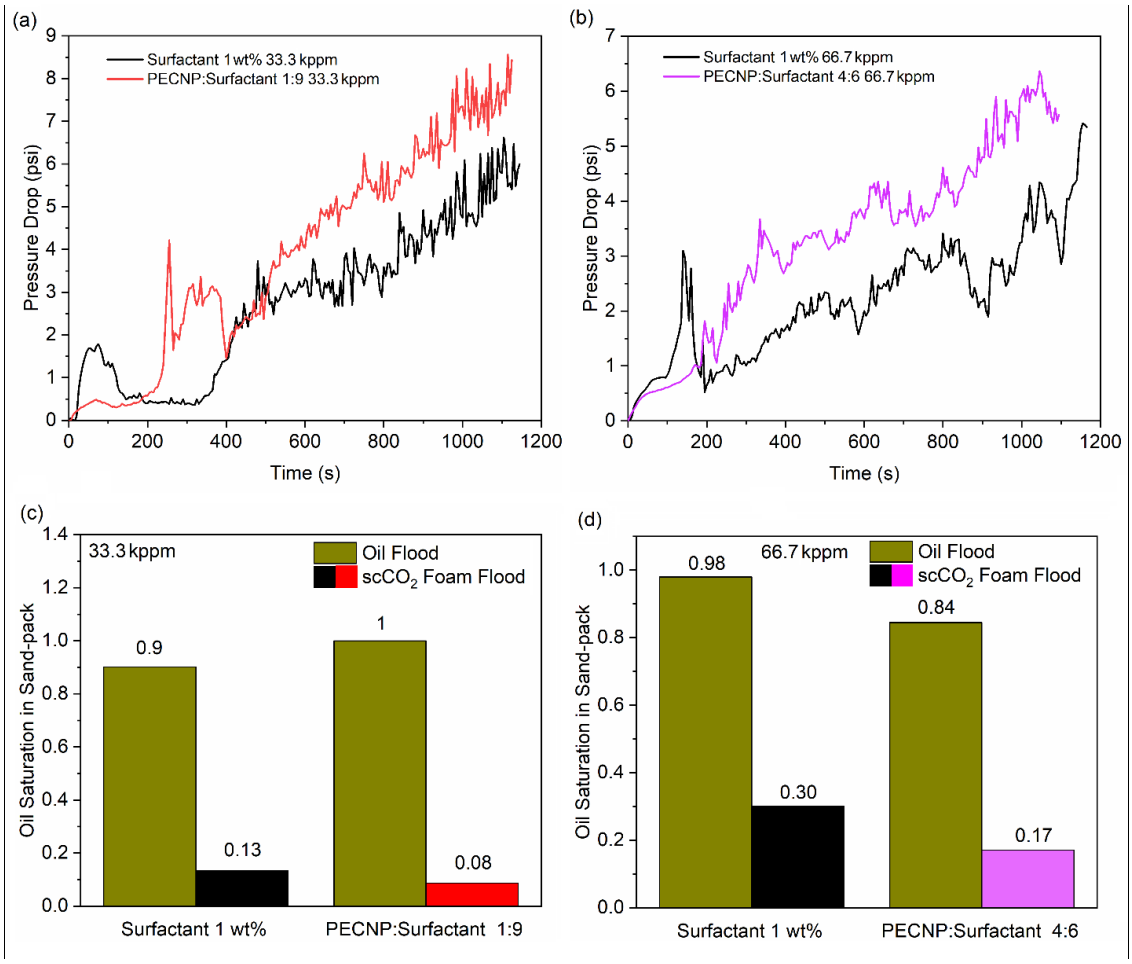

Figure 79. Foam pressures drop and saturation profile for $scCO_2$ foams generated by surfactant and PECNP-surfactants in high salinity brine. (a) Pressure drop profile for foam flood inside the oil saturated sand pack in 33.3 kppm brine (b) Pressure drop profile for foam flood inside the oil saturated sand pack in 66.7 kppm brine (c) Oil saturation in sand pack after oil flood and foam flood for clean-up in 33.3 kppm brine (d) Oil saturation in sand pack after oil flood and foam flood for clean-up, reprinted with permission from [28] ACS 2019

The oil saturation is measured before and after foam flood with 1 wt% surfactant and PECNP-surfactant enhanced $scCO_2$ foam is shown in Figure 79 c, d. The initial oil saturation varies between 0.84 to 1 depending on the available pore volume and packing efficiency. The secondary oil saturation drops to lower values after performing the surfactant foam flood indicating capability of the foam to clean-up the pack. Efficiency of the clean-up improves with 1:9 and 4:6 PECNP-

surfactant $scCO_2$ foam as oil saturation drops 85 % to 92 % reduction in 33.3 kppm systems (Figure 79c) and 69 % to 86 % in 66.7 kppm systems (Figure 79d). The results are consistent with the apparent and shear viscosities presented in Figure 65 and Figure 66 where 1:9 and 4:6 ratios exhibit the capacity for clean-up and oil improvement of sweep efficiency. It is concluded that enhanced viscosity as a result of bulk foam stability using PECNP-surfactant improves the dynamics of foam flow in porous media.

4.5. Macroscale visualization

4.5.1. Analysis of diverging entrance flow-Foam entrance from inline tube to view cell

To capture the foam rheological characteristics in fracture and porous media, motion of bubbles in capillary tubes and large tubes at small Reynolds number are studied [156]. The $scCO_2$ foam stabilized with surfactant and PECNP:Surfactant complexes was generated through physical mixing of $scCO_2$ and foaming solution in inline mixer and it entered the vertical view cell from upper inline tube (see Figures 37 and 38). The generated foam in view cell was isolated and immediately examined and initial moment of isolation/examination was called “t = 0 min”. The diameters of feeding tube and vertical view cell are 1.15 mm and 28.82 mm, respectively. The upper and middle part of view cell was visualized with camera and topography of the generated foam at time zero was examined. The lower part of view cell was not examined in case of isolation of foam due to dense accumulation of drained bubbles/liquids at bottom of view cell. Figure 80 reveals the bubble micrograph analysis results in terms of bubble size and size distribution.

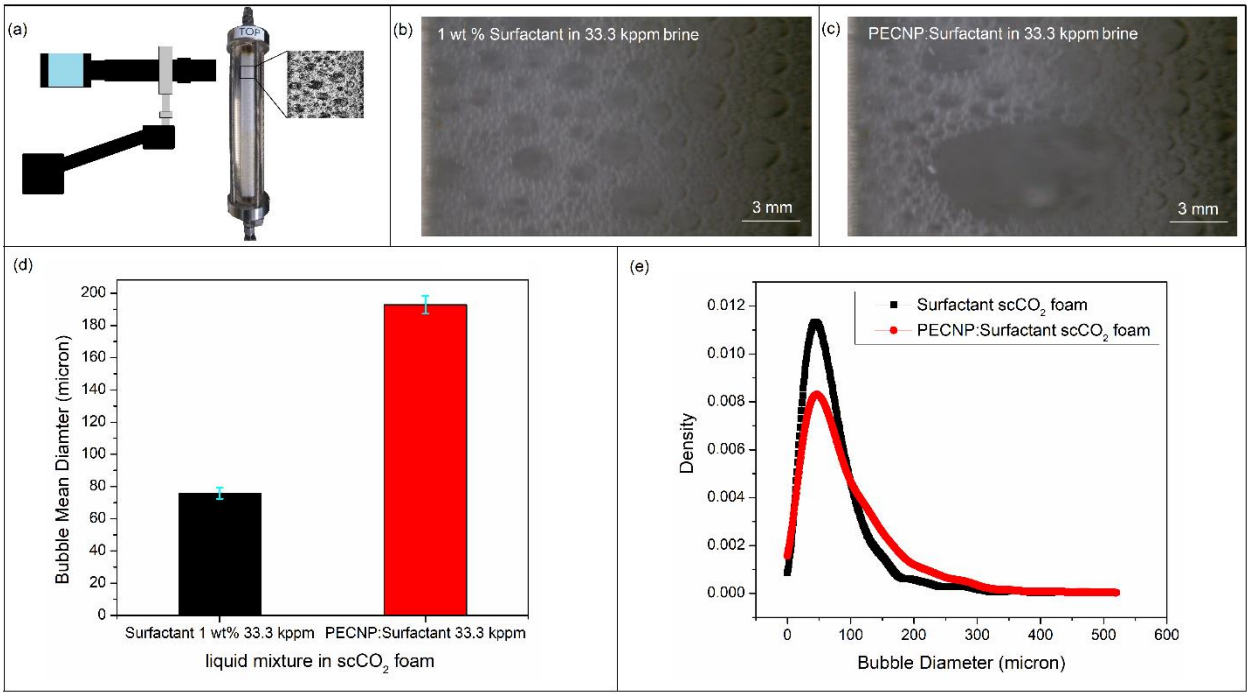

Figure 80. Foam bubble micrographs and texture properties for variety of stabilizers (a) camera configuration and position with respect to view cell (upper level) (b) foam micrograph for $scCO_2$ foam in 1 wt % surfactant and (c) foam micrographs for PECNP:Surfactant in 33.3 kppm brine at t = 0 min upon instant generation and isolation of $scCO_2$ foam in view cell apparatus (d) average bubble size and (e) diameter distribution for variety of mixtures in 33.3 kppm in upper part of view cell at time = 0 min (super large and millimetric bubbles were not included/detected in computational analysis)

More regular dispersion of $scCO_2$ bubbles with average size 75.84 μ are seen in Figure 80b for foams stabilized with surfactant (with WLMs at concentrations above CMC [28]). Millimetric bubbles (up to 2 mm in diameter size) were evenly distributed and distanced in a pool of micrometric bubbles. The surfactant $scCO_2$ foam monograph pattern is more closely resembling monodisperse array of millimetric and micrometric bubbles than the monograph observed for PECNP:Surfactant generated $scCO_2$ foams (Figure 80c). For foams made with PECNP:Surfactant liquid, entrapment of super large $scCO_2$ bubbles in upper part of view cell with (up to 10 mm diameter size) is seen. The bubble size distribution was affected and broader range of bubble

diameter was detected for PECNP:Surfactant $scCO_2$ foam entrapped at top level of view cell (Figure 80d). General pattern of foam isolation in vertical view cell is illustrated in Figure 81a.

The phenomenon was likely originated from inline transition of multiphase from upper feeding tube to view cell (Figure 81a). The foam generally experiences pressure drops upon entering the view cell from feeding tube with lower diameter as it was previously stated channel divergence tends to have destabilizing influence on interfacial disturbance [157]. The pressure drop in breakup location leads to bubble expansion, however, contrary to our expectation, this expansion was noticeable for PECNP:Surfactant generated foams with super large bubbles (Figure 80c and Figure 81a) as PECNP suppresses snap-off due to higher dilatational elasticity.

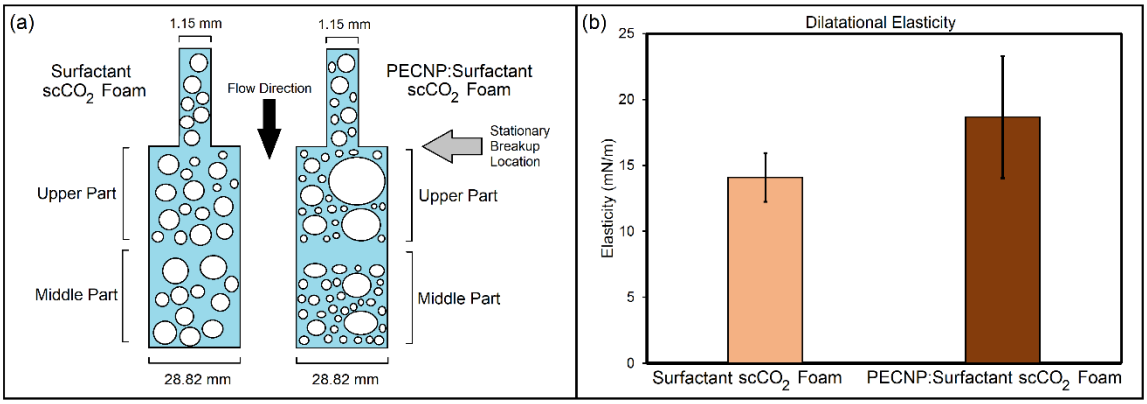

Figure 81. (a) schematics of foam transport across the height of view cell and isolation at time = 0 min (b) dilatational elasticity values obtained from interfacial tension analysis from our previous work [28]

Widening flow in upper part of view cell was affected by confinement ratio of tube and view cell. The compressed foam thread in the feeding tube became increasingly unstable in stationary breakup location along the vertical pathway shown in Figure 81a. This eventually leads to formation of less uniform droplets in PECNP:Surfatcant $scCO_2$ foam. Recently, Badve and co-workers adapted the texture/elasticity tensor and local plastic rearrangement of lamella (T1 event) concept to measure the elastic strain for pattern of deformed bubbles in narrow constricted

channels [158]. Figure 82 depicts the T1 event between four neighboring bubbles resulting in lamella plastic deformation [158].

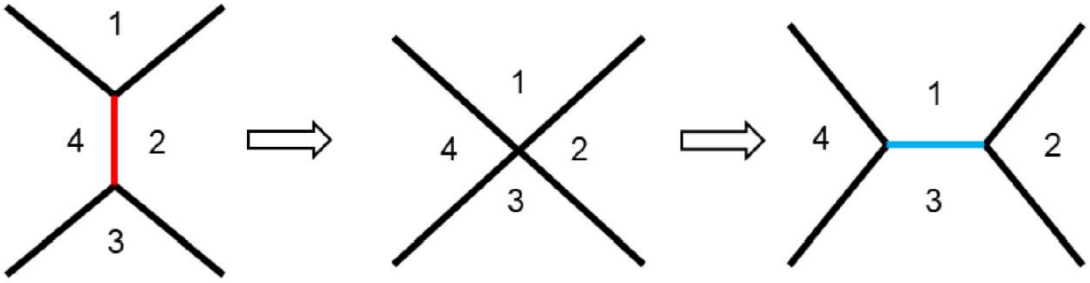

Figure 82. Local plastic rearrangement between the bubbles in which one of the soap films between the bubbles vanishes and the lamella is formed [158], reprinted with permission from [158] Elsevier 2020

The distribution and frequency of T1 events provide a local measure of plasticity for foam flowing through 2D narrow channels, thus, highlighting regions where foam is likely to undergo plastic deformation and elucidating how flow dynamics and flow geometry can affect its plasticity [158] and these regions are constrictions where compressibility and bubble elasticity are responsible for undershoot of velocity and morphological deformations [158].

The value of elasticity tensor which signifies the total extensional strain and distribution of T1 events are concentrated in the vicinity of constriction and outset of diverging flow highlighting the high plastic deformation of lamella and high pressure drop at this location. It was also argued high degree of elastic deformation and compressibility of bubbles lead to bubble elongation and velocity gradients upon decompression when foam leaves the constriction (stationary breakup point) [158]. Figure 83 represents the simulation of foam flow velocity field before, through and after constriction. The corresponding dynamic perturbations affect the bubble morphology.

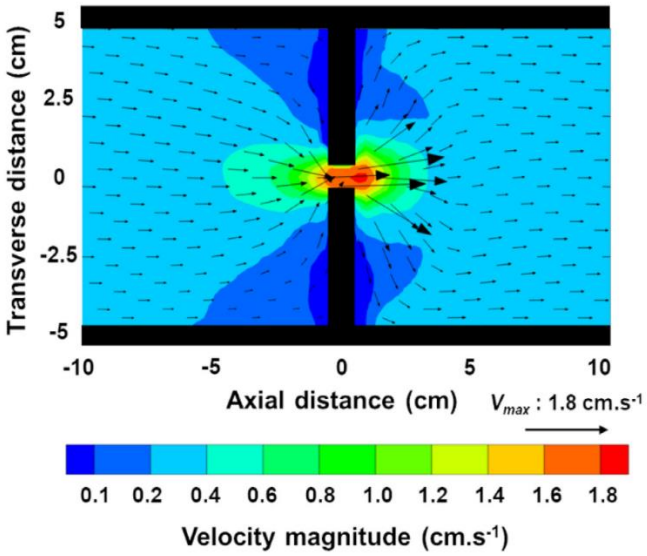

Figure 83. Simulation of foam flow velocity field before, through and after constriction [158], reprinted with permission from [158] Elsevier 2020

Nguyen and coworkers also concluded the surface elasticity and surface viscosity give rise to lamella pressure gradients and asymmetric shape transition of bubbles in diverging flow [159]. Here, it was presumed excessive lamella breakup occurs in widening flow with faster pace for PECNP:Surfatcant $scCO_2$ foam. This observation was attributed to elastoplastic properties of interface [160] originated by presence of branched PEI chains in PECNP mixture (assembled or freely moving branches). Previously, the dilatational elasticity for foaming liquids from ramp-type perturbation approach was determined and reported by Tewes and coworkers [114] from interfacial analysis results (Figure 81b) [28]. Dilatational elasticity is a representative value for the variation of interfacial pressure as a result of compression of lamella which is then correlated to lamella surface area variation [28]. The higher value of dilatational elasticity for PECNP:Surfatcant complexes may lead to plastic deformation of lamella under shear induced perturbations at stationary breakup location. Elasticity and elongation properties of PEI chains in aqueous solution of lamella affects the pressure characteristics of PECNP:Surfactant $scCO_2$ foam flow which eventually affects the

foam front pressure drop after the flow leaves the constriction in diverging flow and thus local lamella breakage occurs in PECNP:Surfactant $scCO_2$ foams, while bubble volume is preserved for surfactant generated $scCO_2$ foams. The breakup is either delayed or happens to fewer portion of lamella in Surfactant $scCO_2$ foams.

4.5.2. Foam travel from upper part to middle part of view cell

After the diverging flow is generated on top of the view cell, the flow traveled to the middle part and alternate morphology was developed (Figure 84a, middle part). The stability of $scCO_2$ foam was evaluated through the onset of filling the middle part view cell and subsequent isolation (t = 0 min) to the time of total breakage/drainage in the field of view. Figure 84 represents the micrograph of pictures taken upon isolation of middle part of view cell module (t = 0 min) from the $scCO_2$ foam generated by zwitterionic surfactant and PECNP:Surfactant 1:9 in 33.3 kppm salinity brine.

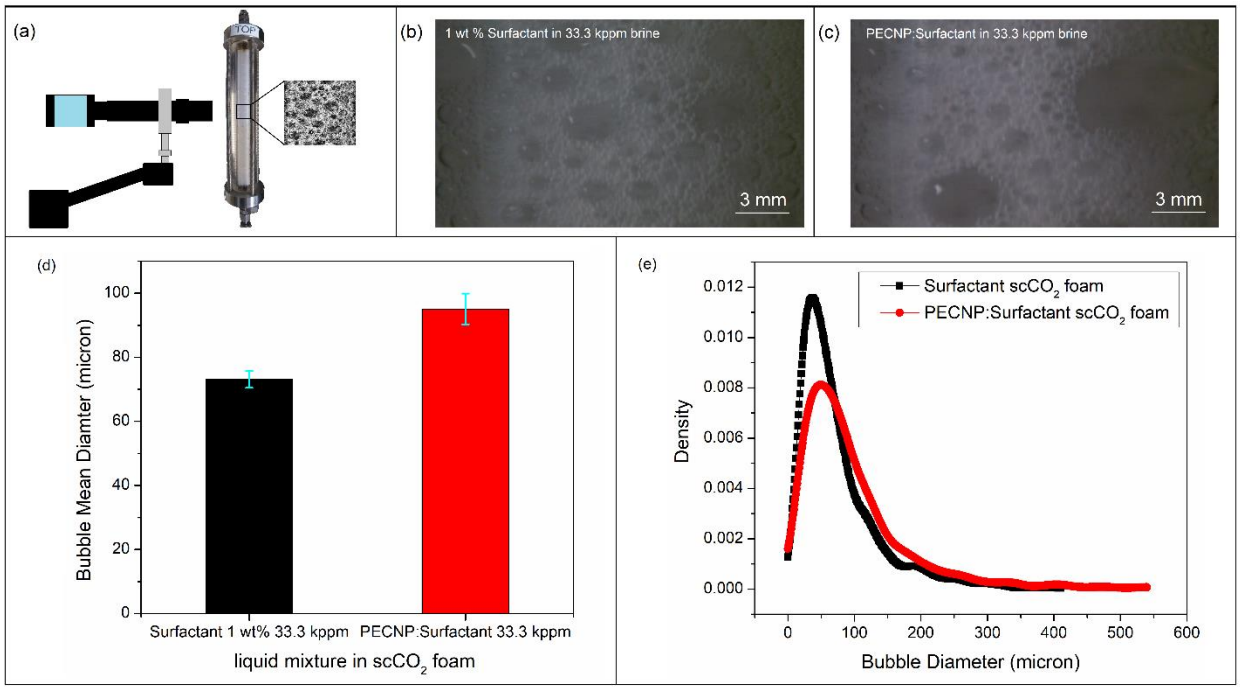

Figure 84. Foam bubble methodology and micrographs for variety of stabilizers (a) camera configuration and position with respect to view cell (middle level) (b) foam micrograph for $scCO_2$ foam in 1 wt % surfactant and (c) foam micrographs for PECNP:Surfactant in 33.3 kppm brine at t = 0 min upon instant generation and isolation of $scCO_2$ foam in view cell apparatus (d) average bubble size and (e) diameter distribution for variety of mixtures in 33.3 kppm in middle part of view cell at time = 0 min (super large and millimetric bubbles were not included/detected in computational analysis)

More uniform bubble sizes were observed in 1 wt% surfactant $scCO_2$ foam with observable size range (~ 70 µm – 3.4 mm) while in PECNP:Surfactant 1:9 $scCO_2$ foam noticeably larger population of smaller bubbles (~ 100 to 300 µm) as well as seldom dispersion of very large $scCO_2$ bubbles (up to 9 mm) were detected. Upon foam view cell filling and isolation (t= 0 min), the super large $scCO_2$ bubbles (5 to 9 mm) are trapped in a medium of electrostatically stabilized highly concentrated electrolytes with ionic complexes. Compared to micrographs of upper part of view cell, most bubbles were preserved the initial size in surfactant generated $scCO_2$ foam (~ 80µm), whereas, supper large bubbles in PECNP:Surfatcant were shrunken in size (down to average 100

μm) due to pressure drop across the view cell height and gravity drainage affecting the instability of super large bubble. The uniformity of bubble sizes was affected by travel across the view cell height, even at early stages of isolation. The morphological parameters of as -obtained pictures were quantified with the method presented in section 3.11. Bubble mean diameter and average bubble size distribution for initial stage of foam isolation at middle part of view cell (t = 0 min) are illustrated in Figure 84d, e.

Figure 84d confirms the average mean bubble diameter of 73.07 μm to 95.09 μm for surfactant and complex generated $scCO_2$ foams, respectively. The mean diameter of trapped $scCO_2$ is up to 30 % larger for lamella stabilized by surfactant and nanoparticle complexes compared to sole presence of zwitterionic micelles in CO_2 - water interface. The bubble size distributions (BSD) of mixtures were estimated by MATLAB distribution fitter tool with non-parametric fitting method. The average of three BSD for each foam are shown in figure 84e. The BSD for zwitterionic surfactant $scCO_2$ foam is narrow with larger population of smaller bubbles, whereas the higher population of larger bubbles are observed in wider distribution of complex generated $scCO_2$ foam.

4.5.3. Long term stability of isolated foams in view cell

The long-term foam stability in hydraulic fracturing is vital to carry the proppants from the wellbore to the fracture [28], however, the foam needs to degrade when it meets the hydrocarbons [28]. The long run stability observation for $scCO_2$ within the field of view (upper and middle part of view cell) is illustrated in Figure 85. One should note there is a continuous lamella/gravity drainage from the top part of the view cell to the middle part and middle part to lower part which affects the stability of foam in middle part in long term. Our previous work has shown the thin layer lamella separating the $scCO_2$ and concentrated electrolyte is stabilized with ionic complexation of PECNP

and zwitterionic surfactant which prevents the lamella drainage and coalescence and improves the stability and rheological properties of final $scCO_2$ foam [28]. Thus, variety of bubble sizes in PECNP:Surfatcant generated $scCO_2$ foam are stabilized and hypothetically break in longer time and long term observation will shed light on stability behavior of emulsified $scCO_2$ bubbles.

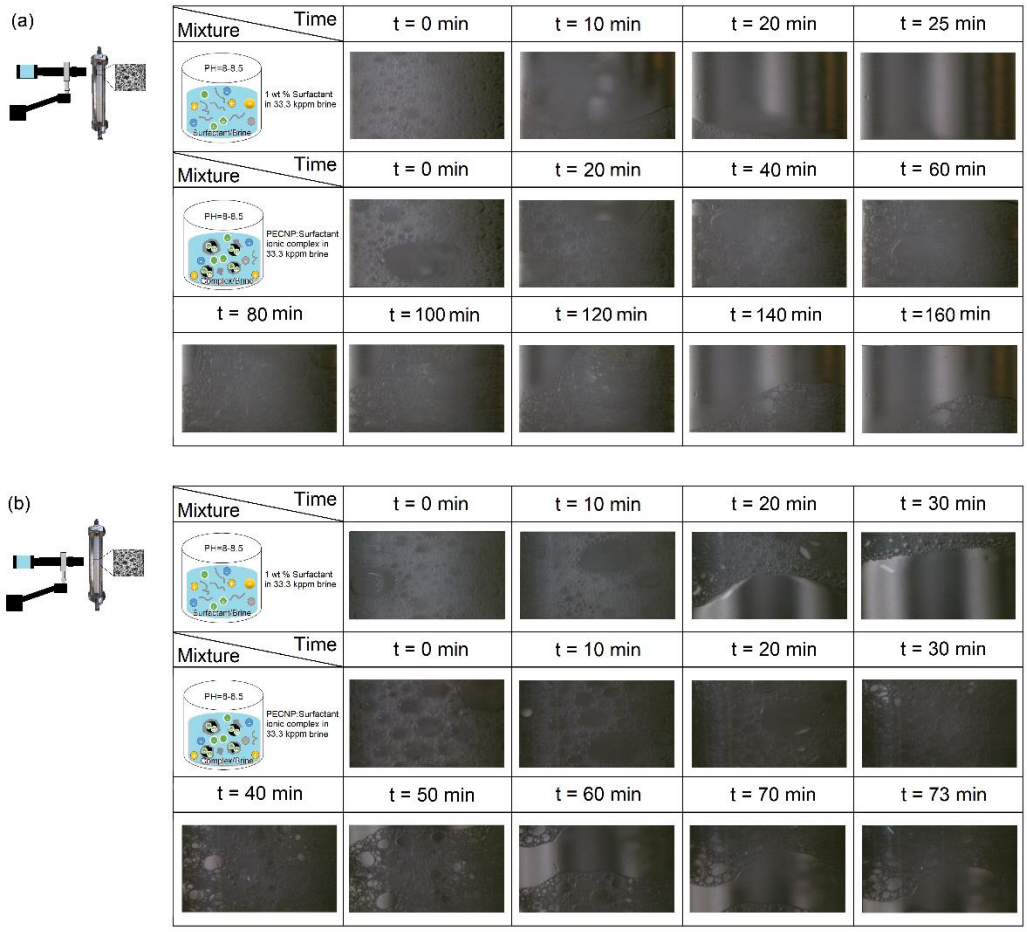

Figure 85. Summary of foam microstructural stability in field of view for $scCO_2$ foam generated in the solution of surfactant and nanoparticle/surfactant in 33.3 kppm brine (a) upper part (b) middle part of view cell

The end of drainage is defined by the time the movable portion of the foam (majority) leaves the field of view and minor stagnant phase remains in place. The foam drainage as a result of bubble rupture and coalescence occurs at significantly longer time and the foam preserves the

cellular structure up to 160 min in field of view (Figure 85a) with ionic stabilization of lamella (in case of Figure 85b, up to 73 min). The zwitterionic surfactant in form of wormlike micelles (WLMs) fails to offer long standing lamella against the gravity drainage and so the resulting foam lasts only for couple of minutes in the field of view (Figure 85).

The drainage time is measured through the field of view (Figures 80 and 84) is quantified and shown in Figure 86. PECNP:Surfactant $scCO_2$ foams outperforms ZS enhanced $scCO_2$ foam in terms of time scale required for foam to degrade and leave the field of view in both height gradients of view cell (upper and middle parts).

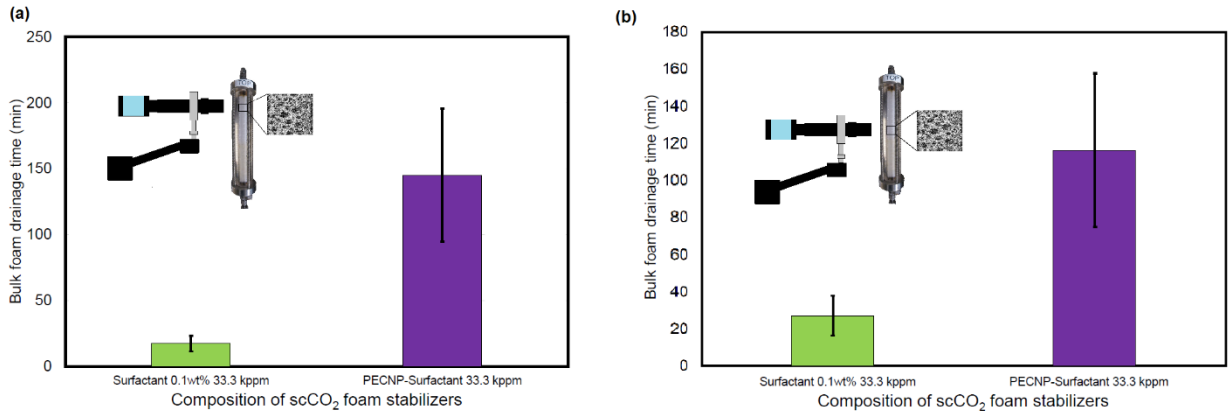

Figure 86. The bulk foam drainage time for $scCO_2$ foam generated in the solution of surfactant and nanoparticle/surfactant in 33.3 kppm brine (a) upper part (b) middle part of view cell

The long-term stability observations are consistent with our previously reported foam height measurements with respect to time in entire view cell column [28]. The stability of the same mixtures in entire view cell column (13 cm view cell height compared to 1.12 cm field of view width) followed the similar trend as ionic complexes in foaming mixture enhance the foam half-life and stability in entire column height up to 115 % [28]. Table 14 presents the foam half decay time for zwitterionic surfactant and PECNP-Surfactant enhanced $scCO_2$ foams in entire view cells column shown in Figure 34.

Table 14. Foam half decay time for zwitterionic surfactant and PECNP-Surfactant enhanced $scCO_2$ foams in entire view cells column shown in Figure 84a

33.3 kppm System	half decay time (min)
Surfactant-$scCO_2$	65
PECNP:Surfactant-$scCO_2$ (1:9)	140

In terms of bubble geometry, shape of the bubbles remains elliptical during the time and bubble drainage and coalescence would not affect the bubble morphology. The stability of bubble shape is likely due to stability of lamella borders and plateau with electrostatic repulsions of WLMs, PECNPs and complexes and as mentioned in section 3.2, external constraints and constrictions may change the morphology depending of elasticity of lamella constituents.

4.5.4. Size and distribution over time

Bubble diameter and diameter distribution for $scCO_2$ foams produced in high salinity brine containing surfactant and PECNP:Surfactant were measured and quantified over the time and the results were presented in Figure 87. The bubble size distribution is narrow at time of isolation (t = 0 min) and broadens over the time for both ZS and ZS:PECNP enhanced $scCO_2$ foams. The bubble size growth and drainage accelerate over the time, illustrating the higher degree of CO_2-water lamella instability in ZS generated $scCO_2$ foams. The diameter of bubbles for ZS foams reaches to 250 μm in 30 min (Figure 87b), whereas in rakes up to 80 min for ZS-PECNP foams to develop bubbles with similar sizes (Figure 87d) in the first hour of stability measurement the bubble size remains in a near to constant size range with less noticeable fluctuations (100-130 μm) in ZS-PECNP foams (Figure 87d). Smaller bubble size will slow down the Oswald ripening and coalescence and so more uniform bubble size and distribution will result in reduction Oswald ripening. Furthermore, another reason for slow drainage in CO_2-water lamella would be higher

viscosity and density of lamella [161]. Mean bubble area (MBA) change during foam life is proven to be dependent on physical and chemical properties of the gas and also lamella composition might be an influential factor, as moderate increase in MBA or lower variation of MBA with time might also result in higher foam stability [161]. Also, a homogenous bubble size distribution (monodisperse) reduces the disproportion and thereby leads to an increased foam stability [161].

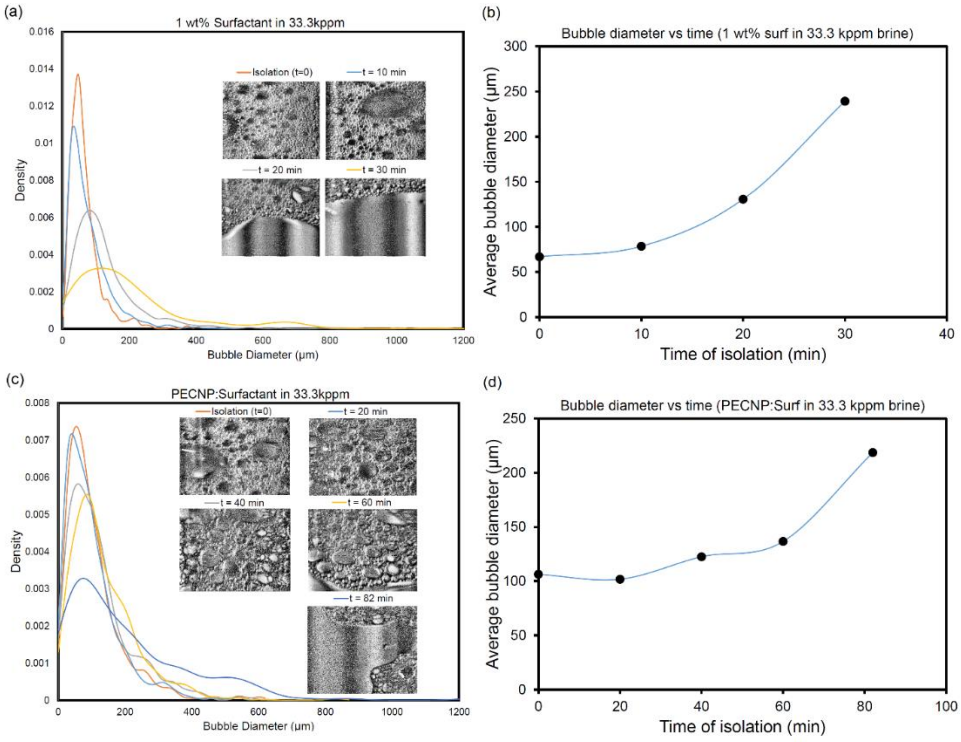

Figure 87. Bubble diameter and diameter distribution for $scCO_2$ foams produced in high saline brine containing surfactant and PECNP:Surfactant (a, b) bubble diameter distribution trend and bubble diameter with respect to time for 1 wt% surfactant $scCO_2$ foam (c, d) bubble diameter distribution trend and bubble diameter with respect to time for PECNP:surfactant $scCO_2$ foam

4.5.5. Morphological changes over time

Micrographs obtained from variety of stabilizing mixtures enhancing $scCO_2$ foams were carefully examined in terms of bubble breakage and coalescence. Figure 88 reveals the detection of this disrupting incidents in foam stability.

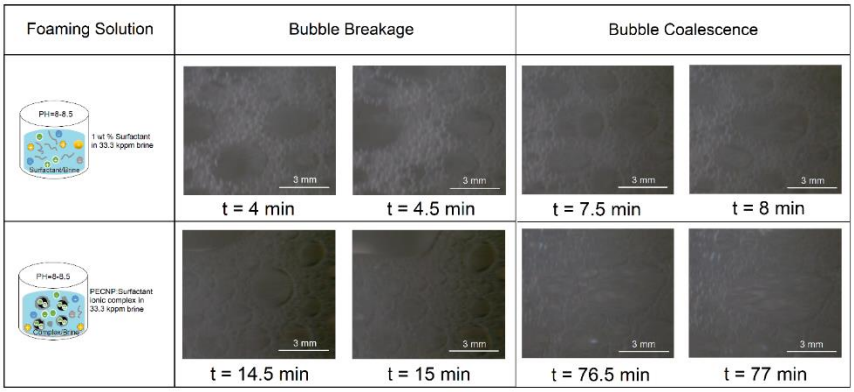

Figure 88. Long term phenomena observed in timely manner for micrographs obtained from variety of stabilizing mixtures enhancing $scCO_2$ foams

The bubble breakage is visually detected for the first time between t = 4 min to 4.5 min for surfactant generated $scCO_2$ foam, whereas the same phenomenon is observed between time = 14.5 and 15 min for PECNP:Surfactant $scCO_2$ foams. Bubble coalescence as other stabilizing effect in bubble rupture happens in a longer time for PECNP:Surfactant generated foam (Figure 88).

4.6. Microscale visualization

4.6.1. Fracture network properties

The main model for fracture/micro-crack emulation used in this work consists of a main fracture and regular pattern of micro-crack with determined apertures illustrated by optical/laser microscopy in Figure 89a. The design could also include main fracture connected to array of circular pins to increase the flow resistance and to resemble the fluid loss to tight shale formation as shown in Figure 89b.

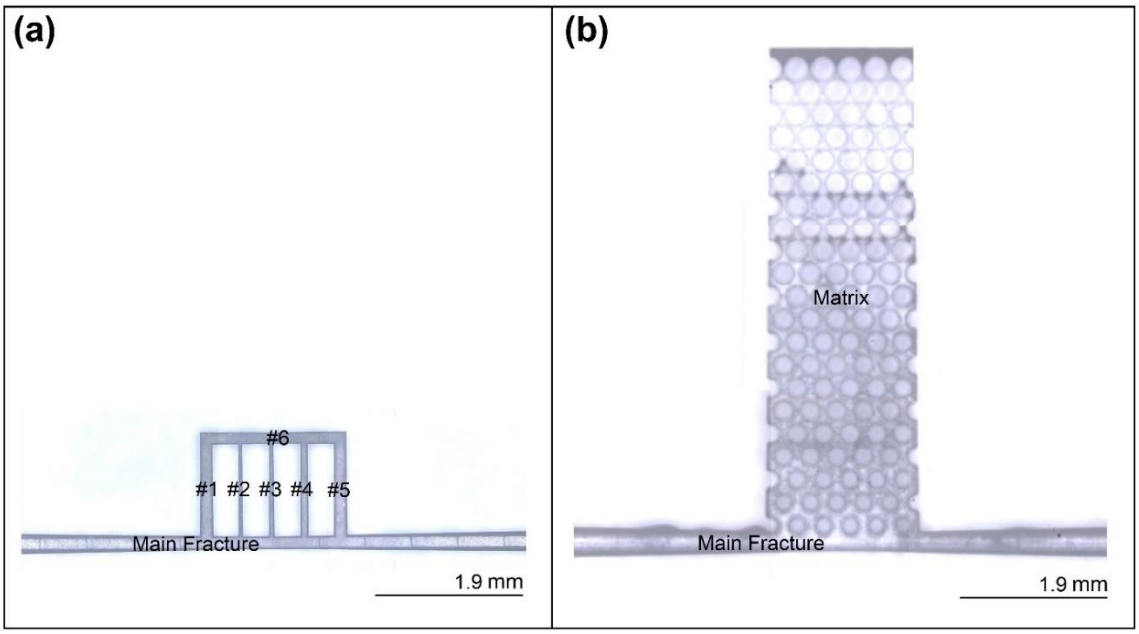

Figure 89. Close view of superimposed optical micrographs for (a) pseudo fractured network (b) fracture/matrix etched with SLE technique on fused silica

In fracture network design #1 (Figure 89a), largest aperture belongs to the main fracture (173.23 μm) which allows the multiphase flow travel and propagation through the array of micro-crackmicro-cracks with lower apertures (down to 45.26 μm). For fracture/matrix design #2 main fracture aperture is 178.49 μm wide connected to pinned matrix with grains with average diameter of 202.66 μm. Table 15 lists the fracture/matrix network dimensional properties for two microchip designs.

Table 15. Physical and dimensional properties of pseudo-fracture network (design #1) and fracture/matrix (design #2) on glass micromodel. The measurements were made by optical microscopy and micro-CT analysis.

Feature in Network (Design #1)	L (μm)	H (μm)	W (μm)	K (mD)	d_H
Main Fracture (limited length in field of view as shown in Figure 6a)	6509.18	297.1	173.23	8048.07	66.09
Micro-crack #1	1166.24	282.67	168.3	-	-
Micro-crack #2	1189.98	282.67	45.26	-	-
Micro-crack #3	1189.98	282.67	60.86	-	-
Micro-crack #4	1178.08	282.67	96.93	-	-
Micro-crack #5	1189.98	282.67	167.53	-	-
Micro-crack #6	1880.20	282.67	150.9	-	-
Fracture/Matrix (Design #2)	L	H	W	K (mD)	d_H
Main Fracture (limited length in Figure 6b)	6842.38	336.9	178.49	306.86	66.75
Matrix (pinned area)	6271.18	342.67	1832.564	-	-
Matrix (pore throat)	-	342.68	135.1	--	-
Matrix (grain)	202.66	342.66	202.66		-

Micro-CT validated the accuracy of reactive etching for SLE fabrication with negligible degree of error. Calculated lengths on 2D projections and 3D tomograms are shown in Figure 90 and 91.

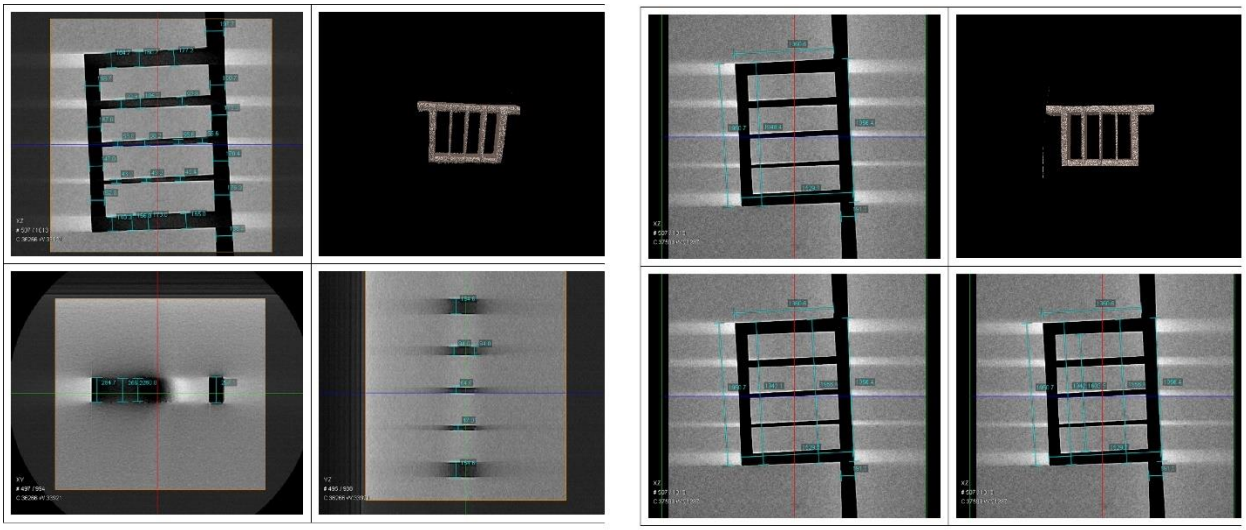

Figure 90. Dimensional analysis for Chip #1 via Micro CT scanning

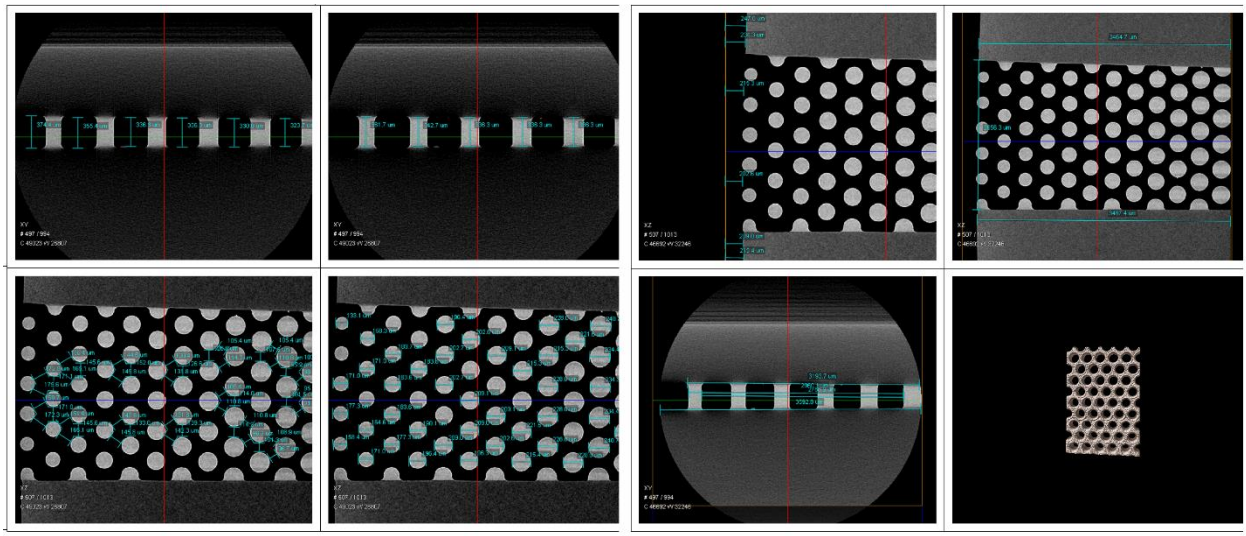

Figure 91. Dimensional analysis for Chip #2 via Micro CT scanning

Hydraulic aperture was measured by injection of DI water and recording of the injecting pressure, according to the formula previously introduced for flow rate- pressure dependency in a single fracture [162,163]:

(4-8) $$Q = \frac{1}{12}\frac{|\nabla P| w d_H^3}{\mu}$$

Where Q denotes to volumetric flow rate, |∇P| represents the pressure-gradient, w is fracture width and d_H and μ are hydraulic aperture and viscosity of fracturing fluid, respectively. The pseudo-linear relation between fluid pressure and flow rate is illustrated in Figure 92.

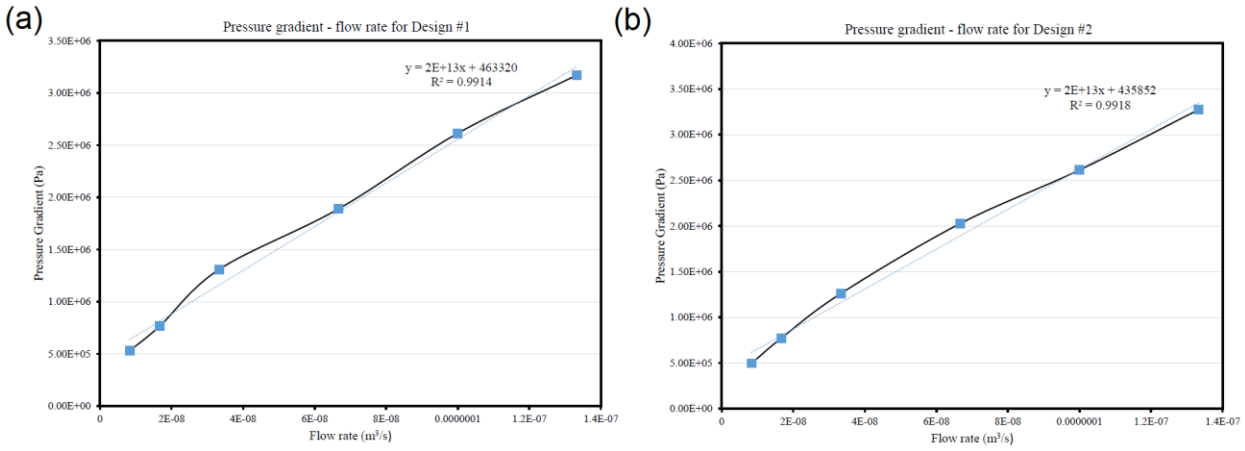

Figure 92. Pressure gradient – flow rate relationship for chip designs #1 and 2

As it was previously reported, perfectly linear relation between pressure and flow rate points at negligibility of the inertial force and aperture variations [162]. A slight deviation from the linearity indicates minor changes in aperture during the flow due to presence of main features (micro-crack/matrix) etched at the center of microchip. The aperture was slightly widened for Design #2 (66.75) indicating the presence of matrix in fracture flow pathway. The permeability of each fracture/macro-crack/matrix pathway was calculated according to Darcy's equations [138]:

(4-9) $$K = \frac{\mu.Q.L}{A.\Delta P}$$

where K is permeability of the fluid inside the etched feature (mD), μ is the viscosity of complex fluid (cp), Q is the volumetric flow rate of $scCO_2$ foam (ml/s), L is the feature length, ΔP is the pressure gradient of fluid injection on injecting pump (atm) and A is the cross section

area of the fluid pathway through the channels of fracture/micro-crack/matrix (cm^2). Calculated permeabilities for two designs were obtained and reported in Table 15 (details are found in Table 16).

Table 16. Detailed parameters for calculation of permeability in microchip #1 and #2

Main Fracture	ΔP (atm)	μ (cp)	A (cm^2)	L (cm)	K (D)	K (mD)
ZS $scCO_2$ foam	84.73	1.02	0.0006	4.02	8.04	8048.073
ZS-PECNP $scCO_2$ foam	84.52	1.11	0.0006	4.02	8.77	8779.336
Matrix	ΔP (atm)	μ (cp)	A (cm^2)	L (cm)	K (D)	K (mD)
ZS $scCO_2$ foam	84.73	1.02	0.0024	0.62	0.30	306.86
ZS-PECNP $scCO_2$ foam	84.52	1.11	0.0024	0.62	0.33	334.74

The value of matrix permeability is not within the range of tight shale formations (0.15 mD [138]), however, it is significantly lower than the permeability of main pathway (fracture) and the ratio of matrix permeability over fracture is almost 0.03 which is dramatic permeability decline and flow resistance build up for the flow entering the pinned area. Fracture conductivity (F_c) was obtained from equation (3) by finding the product of fracture permeability and fracture width:

$$F_c = K.W \quad (4\text{-}10)$$

F_c was obtained for the main fracture (4.02 mD.ft) and the amount varies for variety of channel width in the network. Aspect ratio is a critical factor in etching as height of the channel (H) to width (W) and it has to be more than one ($\alpha = H/W$) [164]. The overall size range agrees with stimulated hydraulic fractures reported in the literature. Recently, Li et al employed $scCO_2$ to induce hydraulic fractures on homogenous and layered tight sandstones in laboratory triaxial fracturing experiment and stimulated shattered zone up to 348 μm wide and micro-cracks width ranging 0.2 to 92 μm [165].

4.6.2. CO_2 foam in micro-models fabricated by UV-lithography and SLE

Geothermal and CCUS operations employing hydraulic fracturing include high pressure pumping from the wellbore, fluid flow at subsurface environment, fluid loss through the tight shale and flow back to the wellbore [10,138], all dependent on development of micromodel materials and fabrication technique consistent with harsh reservoir condition [97]. Lithography technique (photo and soft) has been a common tool to etch and fabricate glass and PDMS micromodels [105,166]. The ability of UV-etched borosilicate (borofloat) chip to emulate CO_2 foam transport in the fracture was compared to selective laser-induced etching (SLE) method in Figure 93. Figure 93a, b represent difference in optical micrograph of etched area by variety of etching techniques on borofoat and fused silica glass.

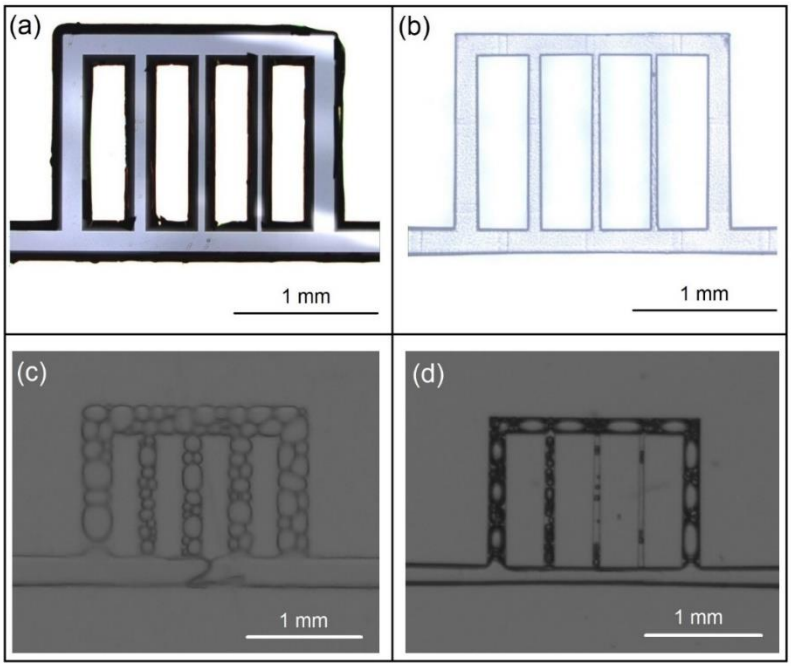

Figure 93. Comparison of topography of features and multiphase flow in microchips etched by UV-lithophany on borofloat glass at 0.055 m/s superficial velocity and SLE on silica glass at 0.019 m/s superficial velocity for ZS-generated CO_2 foam in 33.3 kppm high saline brine (~ 4.13 MPa) (a) Optical micro graph for

UV-etched microchip (b) Optical micro graph for SLE glass microchip (c) ZS generated foam flow at ~ 4.13 MPa in UV-etched microchip (d) ZS generated foam flow at ~ 4.13 MPa in SLE fabricated chip

The fluid pressure (4.13 MPa) was almost half the required pressure to reach CO_2 super-critical state (8.6 MPa) and total superficial velocities for UV and laser etched microchips were 0.055 m/s and 0.019 m/s, respectively. For both chips, CO_2 foam lamella was not formed in the main fracture and the micro-crack network helped to form the CO_2-brine lamella. Chips made with lithography offer shallow channel depth (~ 80 μm – depending on etching time- in this case 14 days) and wider channels (Figure 93c, Table 17) which led to formation of more visible lamella, larger bubbles and better wettability (gas-covered ability) of borofloat by CO_2 bubbles, indicating more lyophobic nature of borofloat [167], whereas, smaller CO_2 bubbles with more uniform texture and lower CO_2 affinity to fused silica were observed in CO_2 foam transport in SLE chip (Figure 93d), where the channel is up to 2.71X deeper and down to 0.25X narrower (Table 17). Comparison of accuracy of SLE printing and UV etching CAD design is illustrated in Table 17. The dimensions of SLE fabricated chips are significantly closer to determined values in CAD, illustrating a better accuracy of SLE printing technique to achieve targeted design and geometries. Moreover, some flaws and channel distortions were observed on UV-etched chips (Figure 93c). Figure 93d reveals more uniform and sharpened edges of channel network etched by SLE technique.

Table 17. Main fracture dimensional error in comparison of initial CAD and resulted SLE and UV lithography chips (measurement obtained by optical microscopy and micro-CT)

Feature/method	CAD (μm) intended	SLE fabricated chip (μm)	Standard error of SLE from CAD design (%)	UV-Lithography (μm)	Standard error of UV lithography from CAD design (%)

Channel width	127	173.23	36.4	231.10	81.90
Channel depth	254	297.10	16.96	80	68
Channel length (confined in micro-crack network)	1905	1948.40	2.28	1979.47	3.91

The chip made by UV-lithography technique was inconsistent in handling the fluid pressures higher than 6.2 MPa and split of two thermally bonded layers led to the chip mechanical failure during multiphase fluid injection, in contrast, the SLE fabricated chip successfully handled $scCO_2$ pressure and beyond (9.65 MPa), thanks to bulk integrity and fused silica high bending and tension strength (Table 18).

Table 18. Fused silica physical and mechanical properties, information provided by SIEGERT WAFER GmbH

Glass Material	Manufacturer	Density (g/cm^3)	Melting method	Softening Point (°C)	Compression resistance Strength (MPa)	Bending resistance Strength (MPa)	Tension resistance Strength (MPa)	Poisson's Ratio
Fused Silica	SIEGERT WAFER GmbH	2.2	Synthetic CVD	1680	1100	67	48	0.14-0.17

SLE fabricated microchip offers high modulus and transparency and it is able to sustain high deformation rate [164], complex fluid pressure and operational temperature suited for harsh conditions of tight shale formations [97] and thus the SLE approach was preferred for $scCO_2$ foam injection, nevertheless, optical lithography is a robust technique in terms of complexity of design [124] and low-cost manufacturing [168] specific to mid-range pressure applications such as CO_2 storage and sequestration in saline aquifer [169] and carbon utilization in EOR [170].

4.6.3. Dry $scCO_2$ foam generation

Pumping a particle-laden fluid into the perforated rock with low permeability exerts a shear force on the fluid not comparable (much lower shear rate [171]) to shear history fluid experiences while pumped through the wellbore tubular [10,138], thus, injection of $scCO_2$ foam components inside the fracture (pre-generation) and real-time monitoring of multiphase flow formation would picture a realistic capability of complex fluid for fracture transport, shear resistivity, stability and proppant release capability. $scCO_2$ foam pre-generation involves the transition of single to multiphase flow while propagating inside the main fracture and micro channels. Figure 94 illustrates multiple stages of $scCO_2$ foam pre-generation conduced in high flow rates and 90% foam quality (FQ) within the SLE glass microchip.

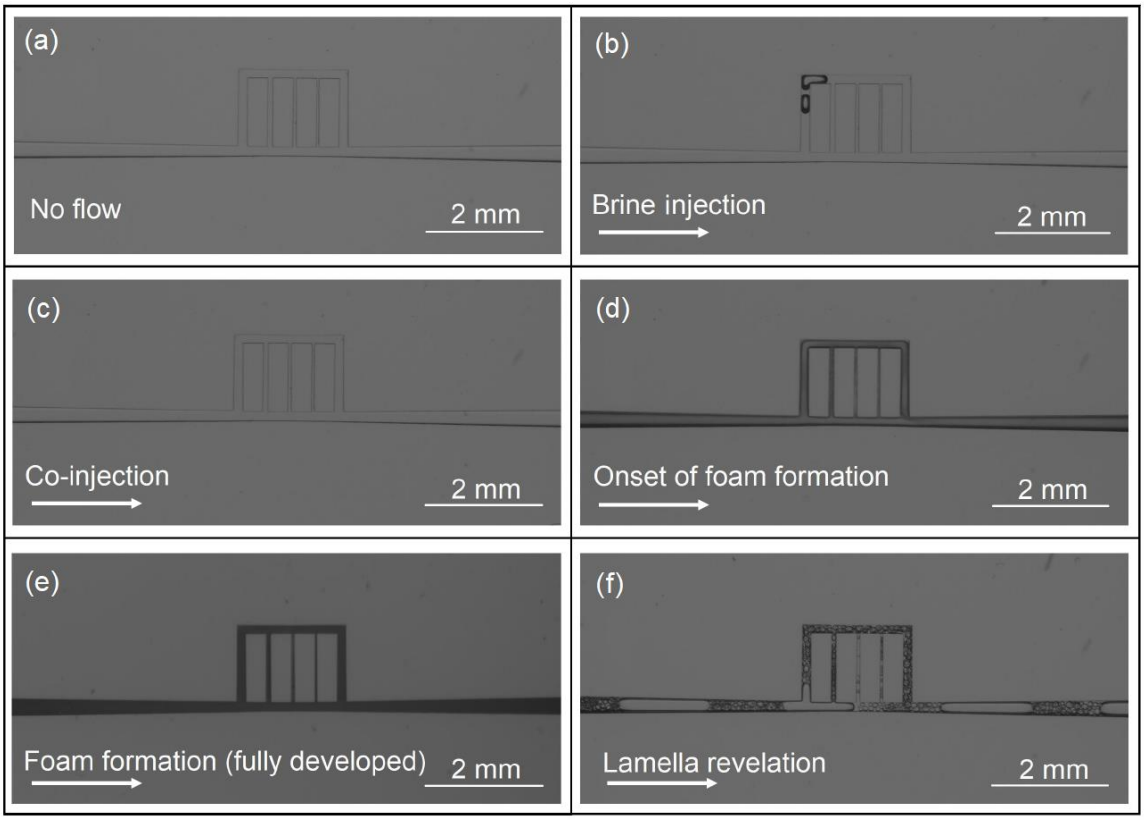

Figure 94. schematic of ZS enhanced $scCO_2$ foam pre-generation in the SLE micromodel: (a) Ambient condition with no flow through the micro-channels (b) Injection of brine containing surfactant into channel moves the air bubbles within the pattern (Ambient condition) (c) co-injection of CO_2 and aqueous phase (containing surfactant or nanoparticle) at supercritical condition with 1.94 m/s total superficial velocity (7.72 MPa and 40 ˚C) (d) onset of $scCO_2$ foam generation 5 min after the start of co-injection (8.35 MPa and 40 ˚C) (e) fully developed scCO2 foam at high flow rates, 6 min after start of co-injection (8.41 MPa and 40 ˚C) (f) lowering the total superficial velocity (0.019 m/s) helps to reveal dispersed scCO2 bubbles separated by lamella in aqueous phase (8.41 MPa and 40 ˚C)

The 2D geometrical pattern with no direct flow inside is shown at ambient condition in Figure 94a and can be considered as background. Subsequently, ZS containing high salinity brine (33.3 kppm) was introduced to the channel at ambient condition (with visibly moving air bubbles) and liquid pressurization started (Figure 94b). Immediate brine and $scCO_2$ co-injection at 7.72 MPa and 40 ˚C made no visual difference in background since

a recognizable multiphase flow was not formed at this moment (Figure 94c). 5 min after inline mixing of the two phases (at inline filters, Swagelok with 15 and 7 μm pore size placed before the microchip inlet), the grey phase was detected within the flow pathway (Figure 94d) as gas-liquid lamella were starting to form at this moment. The grey phase turned to dark as mixing of two phases continued to create more lamella and uniform and homogenous multiphase (Figure 94e). The fully developed foam was observed at micromodel outlet at this stage (6 min from onset of co-injection). Fast fluid transport (1.94 m/s) was required at initial stages to create and stabilize the high internal phase emulsion and once the homogeneity was achieved, the superficial velocity was reduced by 100 times (0.019 m/s) to detect the dispersed phase confined with lamella (Figure 94f). Therefore, the dispersed $scCO_2$ bubbles and continuous electrolyte phase containing ionic stabilizers (ZS) were recognizable within the simplified fracture pattern.

4.6.4. $scCO_2$ volume fraction effect on fracture transport

Minimal fresh water use and produced water disposal are core pillars of environmentally friendly hydraulic fracturing [172,173]. Therefore, establishing a sustainable water-less process highlights the effect of gas/liquid phase volume ratio on foam stability and transport in subsurface formation [174]. It is commonly known that foam viscosity and texture are controlled by foam quality as behavior of wet and dry foams differ in terms of bubble dispersion, interaction and frictions [175]. In our previous study with foams formed near ultra-dry limit (90 v/v% $scCO_2$ phase), the highest viscosity and fluid loss reduction were achieved in macro scale fluid transport [138,176]. For variety of practical foam qualities of $scCO_2$ foam, significant change in flow pattern and bubble size with alternation of $scCO_2$ volume fraction upon injection was evident in micrographs presented in Figure 95. Varying

superficial velocities of $scCO_2$ and stabilizing solution resulted in foam with different qualities and textures.

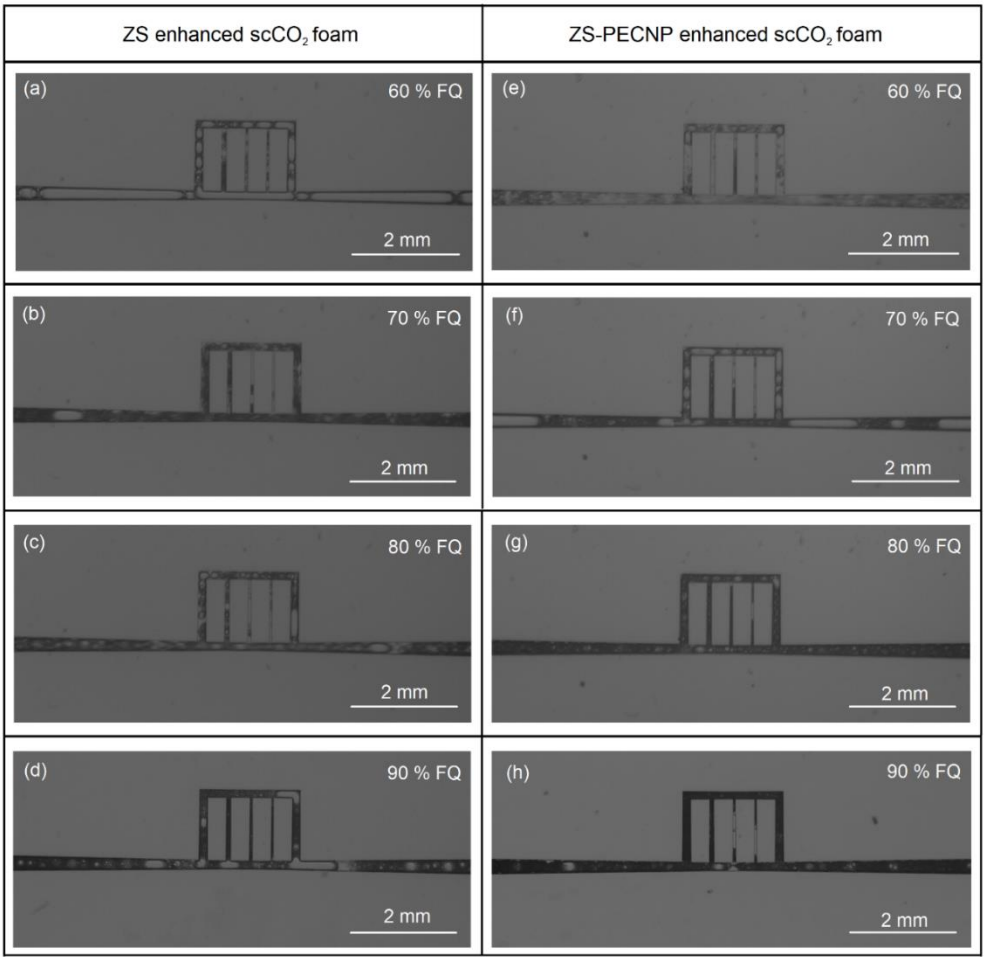

Figure 95. Foam quality comparison at fixed injection velocities for variety of $scCO_2$ foams generated in the fractured network (a-d) ZS containing $scCO_2$ lamella in 33.3 kppm brine (e-h) ZS-PECNP containing $scCO_2$ lamella in 33.3 kppm brine

The flow was not characterized as segregated for all tested FQs due to homogeneity of dispersion and mixing and shear resistive properties approved by rheological measurements [138] and partly because of absence of gravity segregations in microchip observations, however, the foam flow regime may divide into free gas threads and foam slugs with respect to lamella stability, foam quality and viscosity [177]. For all FQs, bubble

shape remained round and didn't turn to polygonal, since FQ of ultra-dry foams ($\varphi > 90\%$) was not tested [29]. Achieving a complex fluid with single uniform phase would be an ideal case for fracture opening and optimum proppant distribution [138]. Injection of lower quantity of internal phase (60 v/v%) led to formation of millimetric bubbles in form of free gas threads in ZS stabilized foam (Figure 95a) as oppose to nearly phase inverted foam with the similar FQ containing ZS-PECNP enforced lamella (Figure 95e). Changing the FQ to higher volume fractions of injected $scCO_2$ phase (FQ=70%) led to development of more portion of wetted foam stabilized with ZS (Figure 95b) and dryer foam with large bubbles stabilized with PECNP-ZS (Figure 95f). Subsequent increase in portion of internal phase (FQ = 80%) led to entrapment and condensation of $scCO_2$ bubbles in highly concentrated electrolyte (Figure 95c, g). Formation of more CO_2-water lamella with smaller bubbles was observed for ZS-PECNP stabilized $scCO_2$ foam (Figure 95g). This is in line with our previous bulk studies indicating that the addition of PECNP resulted in a more viscous and more stable foam [48,138]. Plug flow with fully developed texture foam is observable in Figure 95g, h for ZS-PECNP stabilized $scCO_2$ foam, while ZS generated $scCO_2$ foam with high foam qualities (figure 95c, d) represented the repetition of fine-textured foam and noticeably large bubbles. Condensation of $scCO_2$ bubbles was frequent upon raise in FQ for both ionically stabilized mixtures. The increase in amount of liquid film per unit length is a result of formation of multiple electrostatically stabilized lamellas and is directly responsible for apparent viscosity rise [29]. It's been reported the foam elasticity improves with high FQ (dry foam) as contributing factor to capability of proppant transport [20]. It was shown recently improved viscoelasticity is achieved with more solid- like gas-water interface stabilized by nanoparticle and surfactant complexes in shear thinning study for

laminar flow of incompressible $scCO_2$ foam through a Couette geometry rheometer [138] Furthermore, Harris and co-workers reported that higher foam quality would lead to higher viscosity and reduced fluid loss to the matrix [69] (section 3.6.8). One can easily conclude that the closely packed monodispersed array of bubbles in ZS-PECNP $scCO_2$ with 90 v/v% gas volume fraction is an ideal candidate to optimize the fracture transport, proppant carrying capability and distribution.

4.6.5. Dry $scCO_2$ foam fracture transport

Characteristics of foam flow in fractures is of importance for tight and low permeability reservoirs, since the fracture is the main flow pathway of complex fluid [29]. Figure 96a, b reveals the $scCO_2$ foam produced with ZS and ZS-PECNP complexes dissolved in 33.3 kppm high saline brine upon reaching to slow momentum with low superficial velocities (0.017 m/s for $scCO_2$, 0.002 m/s for aqueous phase). FQ equal to 90% was selected for comparative analysis, due to optimal texture (Figure 96d, h).

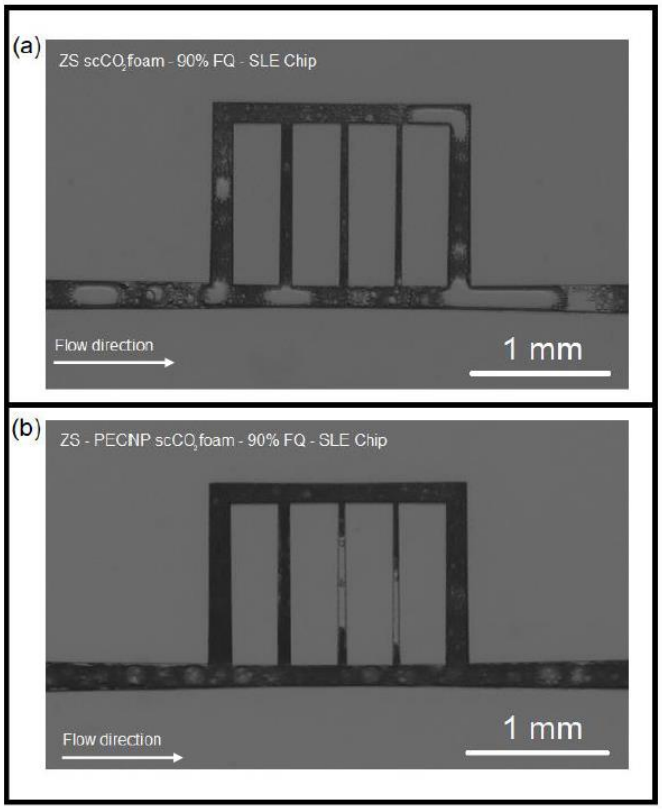

Figure 96. Dry $scCO_2$ foam (90% foam quality) generated within the main fracture and micro-crack after the flow with low flow rates reaches to pseudo laminar stage (a) bubble lamella stabilized with ZS in 33.3 kppm brine (b) bubble lamella stabilized with ZS-PECNP in 33.3 kppm

Larger bubbles are formed within the ZS generated foam with average 40.74 μm and largest size 1028.27 μm and as a result, near to coarse texture was observed, whereas, the largest detectable bubble sizes during coherent and stable flow of ZS-PECNP stabilized $scCO_2$ foam are 137.85 μm, with detectable average bubble size 35.42 μm representing a fine textured foam. Table 19 lists the microstructural quantification of two flow regimes in pseudo-fractured media.

Table 19. Microstructural quantification of complex fluids flowing through the fracture and micro crack network (analysis was performed on detectable phases)

Foam mixture	Mean bubble size (μm)	Largest bubble size (μm)	$scCO_2$ bubble morphology	Polydispersity Index (PDI)
ZS $scCO_2$ foam	40.74	1028.27	Near to coarse	7.87 (highly polydisperse)
ZS-PECNP $scCO_2$ foam	35.42 (detectable)	137.85	Fine	2.00 (near uniform)

The bubble population in ZS-PECNP generated foam is the result of excessive lamella formation and supreme stability of electrostatically enhanced foam system. The instability of ZS-lamella upon foam generation and isolation of $scCO_2$ bubbles led to more bubble coalescence and lamella drainage and formation of larger bubbles upon onset of mixing (Figure 96a), while ZS-PECNP generated $scCO_2$ foam exhibits condensed and populated array of smaller and monodispersed bubbles with barely recognizable midrange bubbles were detected being dragged through the smallest micro channels (Figure 96b). Fast inter-bubble diffusion/compression (no collusion) regulates the bubble size in ZS-PECNP $scCO_2$ foam propagated through the fracture, according to the bubble dynamic that was introduced and investigated as influencing factor on bubble geometry in the literature [162].

Previously, it was reported that the electrostatic complexation of ZS and PECNP improves the lamella disjoining pressure and repulsive forces over the capillary pressure and van der Waals motivated mechanisms responsible for bubble degradation and expansions [138,178]. Ostwald ripening rate is slowed down by high packing efficiency of WLMs [179] and the effect is improved by PECNP conjugation to WLM [138]. The improvement of ionic strength for aqueous polyelectrolytes is responsible for appearance of more populated array of smaller $scCO_2$ bubbles indicating more lamellas were formed in ZS-

PECNP generated $scCO_2$ foam and a larger volume of foam was generated with better foamability achieved using ZS-PECNP complexations with constant concentration of surfactant.

Both mixtures successfully entered the micro-cracks as wide as 45 μm, which illustrates the high efficiency of multiphase fluid propagation and fracture invasion capability to maintain pathway conductivity and resistance against pressure gradient in confined geometries when hydrofracture size varies [180]. The foam was successfully diverted in cross flow from high permeability to low permeability area and withstood the high-pressure build-up upon entering the micro-crack region. For ZS generated $scCO_2$ foams, the dispersed phase size was controlled by the width of the flow pathway and with maintaining the constant flow (0.019 m/s) the stability of bubbles was not affected moving from fracture to micro-cracks for both stabilizing mixtures (Figure 96). ZS generated $scCO_2$ foam successfully filled the smallest channel sizes (45 μm channel width for micro-crack #2), however, the ZS-PECNP generated $scCO_2$ foam was unable to entirely fill the channels #2 and #3 with 45, 60 μm width. High frequency of lamella formation resulting in lower bubble size with higher internal pressure established the higher momentum of transport and rate of diffusion for ZS-PECNP $scCO_2$ foam and negatively affected micro-crack storage capacity and foam propagation into short-range micro-cracks (Figure 96b), however, when broken foam (elongated bubble) invaded the smallest microcrakcs, the opportunity for diverting the fluid by CO_2 to the fracture and eventually surface arises.

Less momentum and energy of transport for ZS generated $scCO_2$ foam allowed us to trace the movement of singular bubbles in the network. On this matter, Terry and co-workers made an interesting analogy for energy loss during multiphase flow changing

direction to race car travel around the track [181]. If the flow carries high momentum, the energy is lost in turns and morphology and integrity are affected. Figure 97 reveals the bubble flow direction through the fracture and channel network for lamella stabilized with ZS. Bubble in plug flow broke upon meeting the first T-junction and fed the smaller bubbles to the micro-crack network as foam propagated through and filled the smaller channels. Bubble travel from tiny channels to larger ones could be studied in terms of stability of multiphases when the flow experiences the pressure drop in a cross flow to increase the fracture conductivity as crack width widens.

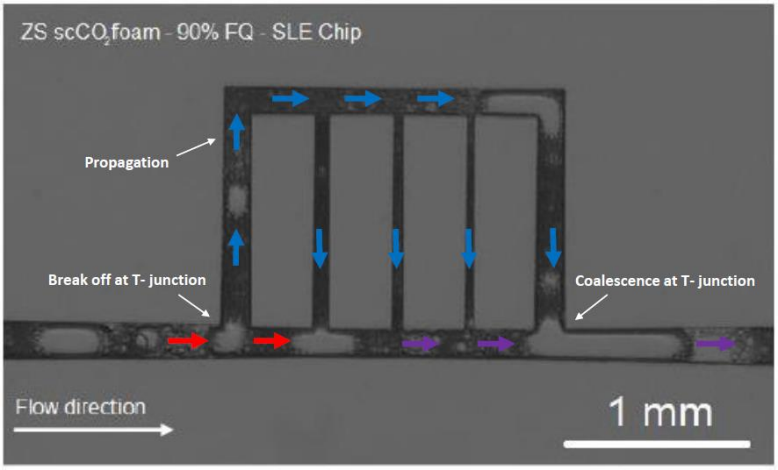

Figure 97. $scCO_2$ bubble direction through the fracture and channel network for ZS $scCO_2$ foam flow in SLE microchip

The morphology and integrity of ZS-PECNP generated $scCO_2$ was not affected by flow divergence from micro-crack to fracture, whereas the bubble growth and coalescence at T-junction was observed for ZS generated $scCO_2$ foam (Figure 97) indicating the $scCO_2$ lamella instability on sharp edges when lamella was only filled with WLMs and the foam was obstructed or decelerated by T-junctions or 90° constriction. Conversely, confinement and flow divergence did not induce deformation to bubbles and breakup of fluid interface

comprising ZS-PECNP complexes was not observed. 1D (fracture) and 2D (network) flow of ZS-PECNP foams remained stable for a longer period (Figure 98). Inability to fully examine the texture of ZS-PECNP $scCO_2$ foam due to excessive lamella formation and high degree of monodispersity of droplets led to inaccuracy of analysis for bubble population, so foam at macroscale was generated and complementary observations were performed in view cell. To characterize the dynamics of $scCO_2$ foam bubbles, dimensionless parameters containing important information about the microstructure, shear condition and relative density were defined [20]. Reynolds, Peclet, Stokes and Capillary numbers are critical parameters to explain the foam hydrodynamic dependence on microstructure (Table 20).

Table 20. Hydrodynamic and flow parameters for $scCO_2$ foam characterization in microchips

Hydrodynamic Value	Formula	Description	Parameters
Reynolds	$Re = \frac{\rho_m R_b^2 \dot{\gamma}}{\mu_m}$	$\frac{\text{Inertial Forces}}{\text{Viscouse Forces}}$	ρ_m and μ_m are the ambient fluid density and shear viscosity, respectively and $\dot{\gamma}$ denotes the applied shear rate and R_b is the bubble radius.
Peclet	$Pe = \frac{6\pi\mu_m R_b^3 \dot{\gamma}}{K_B T}$	$\frac{\text{Hydrodynamic Forces}}{\text{Brownian Forces}}$	T is absolute temperature and K_B is Boltzman constant
stocks	$Stk = \frac{\rho_b}{\rho_m} R_b \varsigma Re$	$\frac{\text{Bubble response time}}{\text{Fluid response time}}$	ρ_b is bubble density and ς is a shape factor.
Capillary	$Ca = \frac{\mu_m \dot{\gamma} R_b}{\sigma}$	$\frac{\text{Viscouse forces}}{\text{Surface tension forces}}$	μ_m is shear viscosity, $\dot{\gamma}$ is shear rate, R_b is the bubble radius and σ is surface tension
Deformation of bubble	$D_R \cong Ca$	$\frac{R_{max} - R_{min}}{R_{max} + R_{min}}$	Where R_{max} and R_{min} are maximum and minimum axis lengths of an ellipsoid bubble under shear.

To calculate basic hydrodynamic parameters, results from macro scale observations were considered (section 3.5, Table 21).

Table 21. Dimensionless parameters to characterize the dynamics of bubbles in $scCO_2$ foam (T=40 °C, 313.15 °K, K_b = 1.38064852 × 10-23 m^2 kg s^{-2} K^{-1}, ς = 1) FQ = 90 %

33.3 kppm System	R_b(μm)	$\mu_m(cp)$	$\dot{\gamma}$(1/s)	ρ_m (gr/cm^3)	ρ_b (gr/cm^3)	σ (mN/m)	*Re*	*Pe*	*Stk*	*Ca*
ZS $scCO_2$ foam	144.76	1	26.30	1.0217	0.526	6.355	56.32	3.48E+8	0.0042	0.0006
ZS-PECNP $scCO_2$ foam	102.62	1.05	31.74	1.0221	0.526	6.43	32.54	1.57 E+8	0.0017	0.00053

The macro scale observation was performed on visualized flow of $scCO_2$ foam generated in standard 1/8 inches stainless steel pipes. The shear rate was calculated according to velocity distribution profile for power-law flow in circular pipe [182]. More details are found in Table 22 and 23.

Equation 1 expresses the shear rate obtained for fluid flow governed by power law model in circular pipe [182]:

(4-11) $$\dot{\gamma} = \frac{Q}{\pi r^3} * \left[3 + \frac{1}{n}\right]$$

The characteristic indexes of power-law fluid (n, K) were previously obtained by rheological measurement [138] and listed in Table 22.

Table 22. Flow consistency index (K) and flow behavior index (n) for variety of PECNP/Surfactant $scCO_2$ foam systems

33.3 kppm System	K (Pa s^n)	n
ZS generated $scCO_2$	1184.3	0.402
ZS-PECNP generated $scCO_2$ (1:9)	2916.4	0.276

Accordingly, the shear rate was calculated and listed in Table S6.

Table 23. Shear rate for variety of macroscale flow in circular pipe

33.3 kppm System	n	(3+(1/n))	Q (m3/s)	R (m)	$\dot{\gamma}$
ZS generated $scCO_2$	0.402	5.48	0.0000001	0.0019	26.30
ZS-PECNP generated $scCO_2$ (1:9)	0.276	6.62	0.0000001	0.0019	31.49

Table 21 represents the corresponding values for introduced dimensionless parameters using the average bubble diameter obtained from macro visualization experiments. Reynolds is defined as ratio of inertial force to viscose forces. The flow regime for all the stabilizing mixtures was laminar (Re<2300) which illustrates the homogenous phase dispersions and lack of eddies at moderate flow rates in small tubes [183]. Peclet number is representative of bubble dynamics and high value of Peclet indicates slow bubble movement overcome Brownian movements and hydrodynamic interaction was prevalent. Low Stokes value ($Stk \ll 1$) showed no phase segregation occurred in $scCO_2$ foams (FQ = 90%) with variety of introduced stabilizers [20]. Capillary number was defined to determine the equilibrium shape of bubble [20]. This value is a measure of bubble deformity, as at early stages of deformation, at low capillary number, the emulsion is isotropic, [20]. Capillary number value is in correlation with bubble deformation under shear, so it represents destabilizing forces in the lamella as well as the magnitude of opposite forces to disjoining pressure. One should note in case of ordered foams, the packing structure of the bubbles is dictated by capillary pressure and surface energy minimization [20], as such, improvements in disjoining pressure through electrostatic interactions balances the forces in CO_2-water interface, and the capillary value decreases for ZS-PECNP generated $scCO_2$ foam (Table 21).

The $scCO_2$ foam propagation schemes in chronological order for both ZS and ZS-PECNP mixtures were shown in Figure 98.

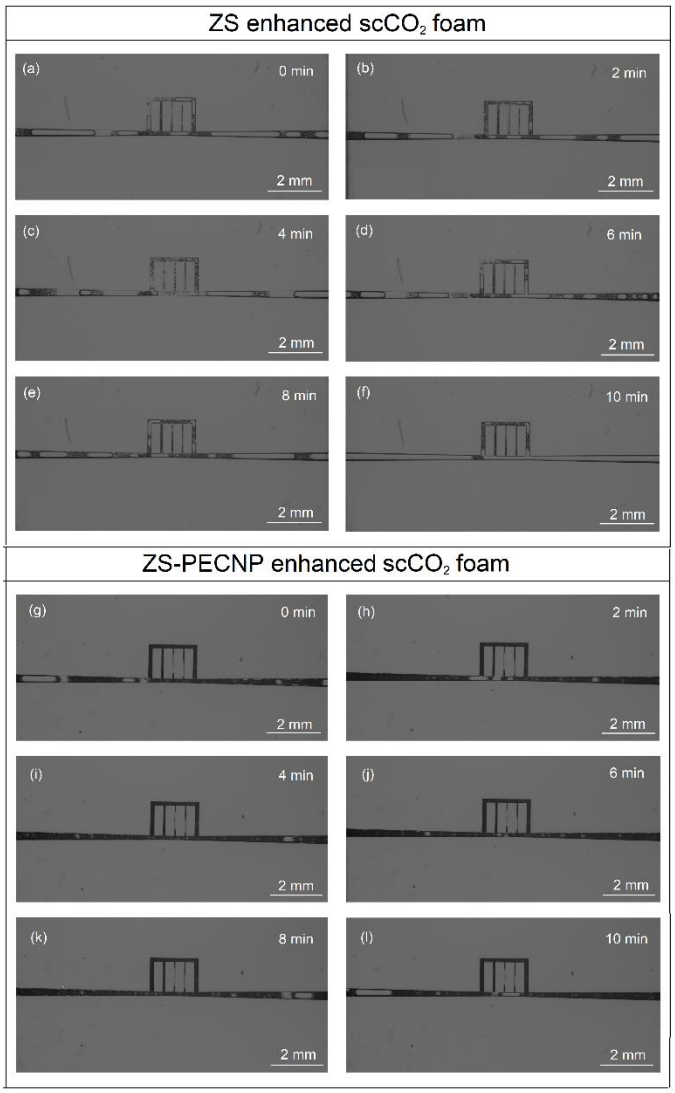

Figure 98. $scCO_2$ foam propagation schemes in chronological order for $scCO_2$ bubble in highly saline brine containing (a-f) ZS and (g-l) ZS-PECNP mixtures

The transport of $scCO_2$ foam through the fracture slit is shown for variety of stabilizing mixtures. The fluid total superficial velocity was 0.019 m/s. The ZS-generated $scCO_2$ foam represented discrete movement of super large bubbles of $scCO_2$ surrounded by interconnected arrays of smaller $scCO_2$ bubbles dispersed in highly saline brine (Figure 98a). At early stages of transport (Figure 98b, t = 2 min), the multiphase was discretized at main fracture, despite the fact that flow was homogenous at micro-crack network for ZS-

generated $scCO_2$ foam, then when time elapsed, the foam flow began to discretized (Figure 98c to 98e) and eventually a singular $scCO_2$ bubble grew to fill the main channel (Figure 98f, 10 min) due to instability of CO_2-water lamella leading to bubble growth, coalescence and ultimate instability of multiphase transport. Bubble growth and coalescence directly affect proppant settling rate and triggers fast sedimentation [80]. Zhu et al argued that for unstable lamella the plateau border is unable to provide the drag force against the gravity in shale formation due to reduction of bubble pressure [184], therefore, the proppant settlement deficiency is expected for ZS generated $scCO_2$ foam. Coherent multiphase was observed for ZS-PECNP generated $scCO_2$ foam (Figure 98 g to 98 l). The slugs of $scCO_2$ were noticeably within the smaller size range (detectable up to 35μm), though as mentioned the channel filling (micro crack network) was not as effective as the foam generated with WLMs (channel filling efficiency), negatively affected by high shear rate at lower width micro-cracks [20]. The multiphase system with supercharged ionic complexes in aqueous phase was coherent and integrated during the time frame of expansion through the micro-cracks (10 min) and pressure gradient through the micro channel network didn't affect the bubble size and stability of phases. Micro-cracks with lower dimensions than fracture (Table 15, up to 0.26 times lower) exert higher pressure and local strain on fracturing fluid where flow experiences sudden contraction, shear and extensional stress with risk of doubling the topological changes [158]. It was previously reported that the ZS-PECNP $scCO_2$ foam offers higher viscosity than ZS foam in entire shear rate range from wellbore to fracture [138], as higher shear resistivity leads to formation of smaller bubble size and narrower size distribution [140], due to ability of ionic complexes to improve storage capacity of interface against the deformations [20]. The observations are consistent with previously

measured flow consistency index K= 2916.4 Pa.s^n for ZS-PECNP generated foams over K=1184.3 Pa.s^n for ZS based $scCO_2$ foams verifying improved complex fluid capability for proppant transport and placement [138] and to resist against pressure drop across the fracture [145] and elastic deformations in constrictions [158].

4.6.6. $scCO_2$ bubble stability in main fracture

Selection of proper fracturing fluid poses a direct impact on fracture width, fluid loss reduction, fracture conductivity and fracture clean-up process[138,185]. Failure to maintain the foam stability results in inhomogeneous distribution of proppants in the fracture [10]. $scCO_2$ foam stability in the fracture was affected by high temperature conditions, high shear rate while pumping and low shear rates while fracture is closing [10]. Stability of ZS and ZS-PECNP generated $scCO_2$ foam was compared over the course of 120 min from the point the multiphase flow was stopped, and the microchip was isolated. The micrographs are illustrated in Figure 99.

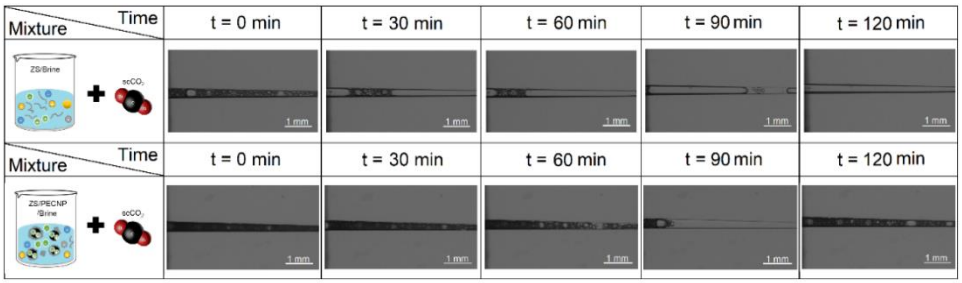

Figure 99. Foam stability comparison in the main fracture. The flow was stopped, and microchip was isolated

The stability of $scCO_2$ foam generated using ZS along the main fracture was drastically affected by bubble coalescence and lamella breakage during the first 30 min of stabilization. The lamella was not stable enough to separate the $scCO_2$ phases from each other in electrolyte solution. For ZS-PECNP generated $scCO_2$ foam, extremely small and

monodisperse droplets were largely stable in fracture slit for entire time frame except some instable movements observed at t = 90 min due to inertia effect. The gradual bubble growth was observed but not significant to destabilize the stream. The ZS-PECNP $scCO_2$ remains stable for entire time frame of isolation (up to 7 hr – Figure 100).

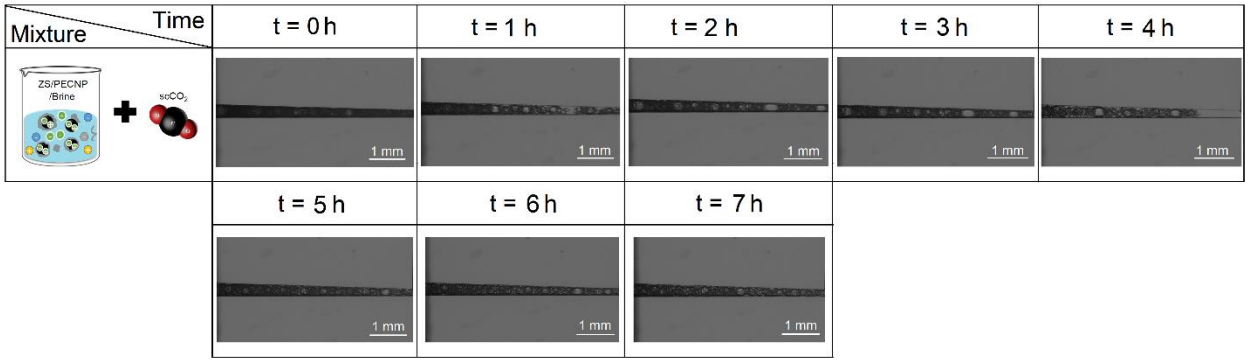

Figure 100. Long term fracture stability for ZS-PECNP $scCO_2$ foams

4.6.7. $scCO_2$ bubble stability in micro-cracks

Figure 101 illustrates the level of stability for $scCO_2$ bubbles in micro-crack networks. The main foaming solution fed the micro-crack from the main channel (lower edge on squared network).

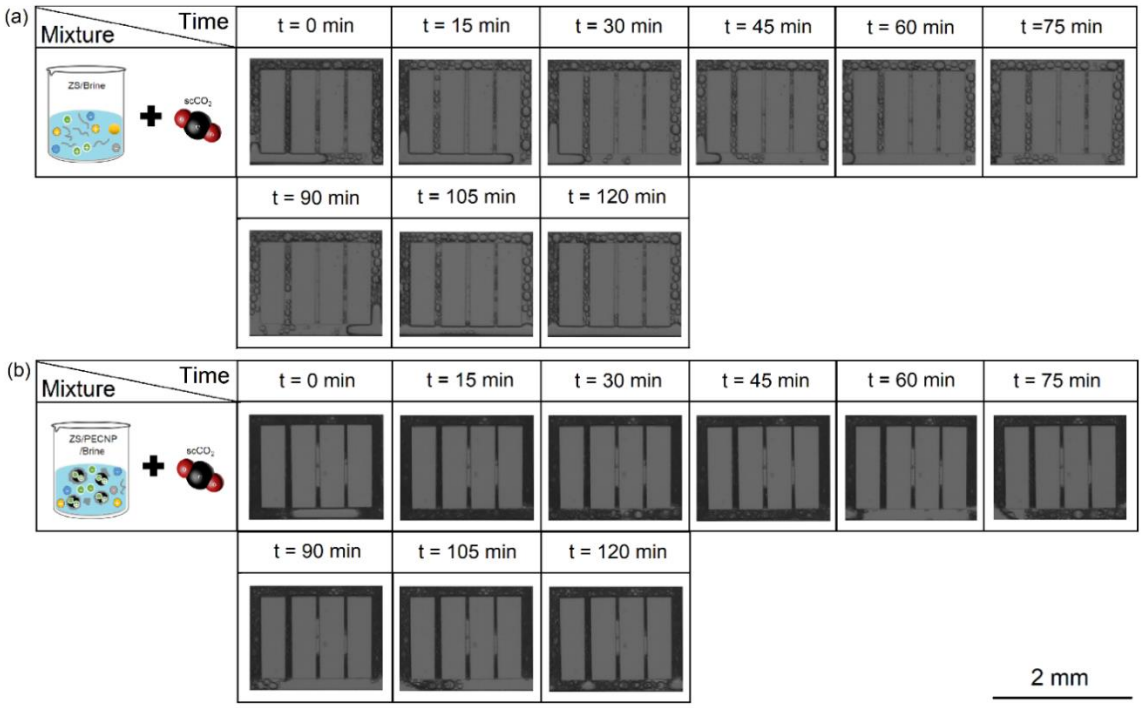

Figure 101. Stability of foaming mixtures in micro-crack network for $scCO_2$ bubble stabilized in high saline electrolyte containing (a) ZS (b) ZS-PECNP in every 15 min after foam isolation in SLE microchip

Discreet movements of bubbles were visible in ZS generated foams (Figure 101a). Initially the feeding main bubble diffused through varying size micro-crack and broke into smaller bubbles confined with the micro cracks aperture, the foam within the micro-crack was stable enough through the entire timeframe (t = 2 h) with local variations in bubble size, however, the bubbles traveled and collided into the one millimetric bubble and foam breaks eventually in the main fracture (Figure 101a, after t = 105 min). It is worth noting that despite isolation of microchip from inlet/outlet, the low inertia in the channel, prompts the bubble movement and relocation. Highly monodispersed and emulsified $scCO_2$ foam with lamella containing ZS-PECNP complexes successfully maintained the stability and offered proper channel occupancy (Figure 101b). The mixture remained stable for entire time frame of isolation (up to 7 hr – Figure 102) mainly due to surfactant-brine solubility

and nanoparticle compatibility to the WLMs and concentrated electrolytic interface, needless to mention the synergistic effect was previously introduced as influencing factor for improved foam stability in macroscale observations for foam height measurements [138].

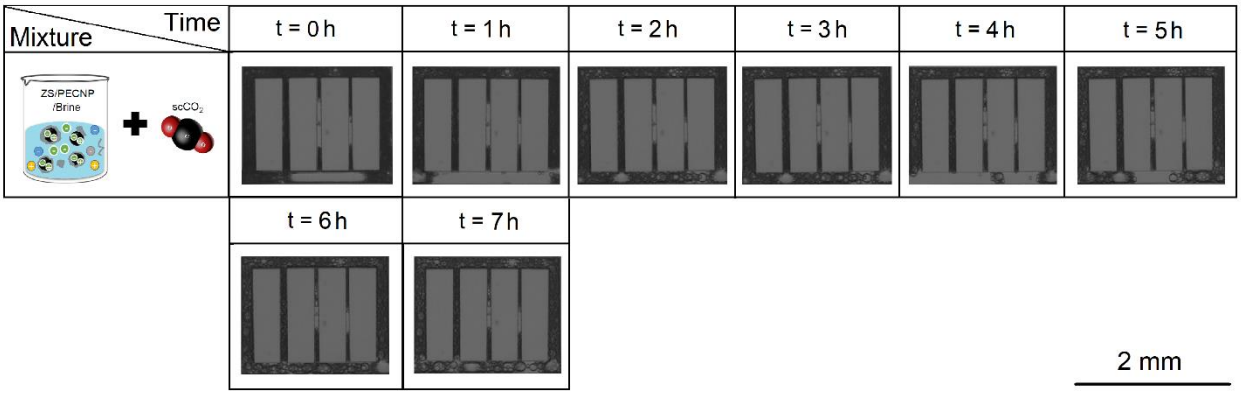

Figure 102. Long term stability of ZS-PECNP $scCO_2$ foam in microcrack network

4.6.8 Fluid loss assessment in fracture/matrix pattern

High internal fracture conductivity and control of leak-off rate to formation reduce the pumping cost and ensures the mechanical integrity of formation in an environmentally friendly oil recovery process [138]. Limiting the leak-off, extends the fracture length in practical operation due to higher viscosity [186]. The tight shale formation damage can be evaluated in simplified problem of two-dimensional (2D) Cartesian complex flow in matrix domain. The schematic of this design is shown in Figure 89b and dimensional analysis is provided in Table 15. The fluid loss assessment was performed for flow of $scCO_2$ foam in fracture/matrix (design #2) with high superficial velocities (total = 1.66 m/s) to distinguish the fluid pattern and to highlight the colour contrast in tight shale during visualization. Figure 103 represents the fluid loss micrographs for ZS and ZS-PECNP generated $scCO_2$ foam from main fracture to tight shale matrix (microchip design #2) with average 135.10 μm pore throat (see Table 15) within the first 2.5 min after foam generation. The efficient

electrostatic conjugation of ZS and PECNP introduces a reliability of nanoparticle additive to control the formation damage in micro-scale.

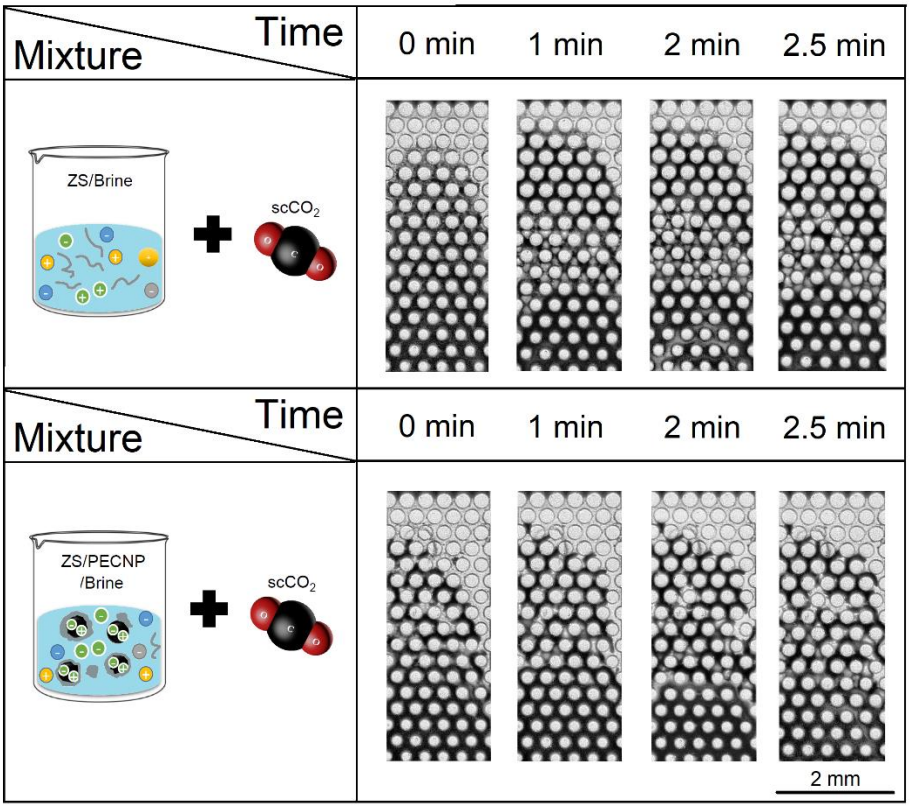

Figure 103. Fluid loss pattern representing the leak off from the fracture to the matrix on SLE microchip design #2 (a) flow of ZS and (b) flow of ZS-PECNP stabilized $scCO_2$ foams with 90% FQ at high superficial velocities (total 1.66 m/s)

Less volume of fluid leaked to the matrix from the fracture in flow of $scCO_2$ foam stabilized with ZS-PECNP (Table 24). It was previously reported larger magnitude of compressibility and higher apparent and dynamic viscosities prevents the fluid to penetrate through the pore throats of tight shale and so high internal fracture conductivity is maintained [138,153]. The volumes of lost fluids to the matrix in the chip design #2 with respect to the recording time of the micrograph and corresponding fluid loss coefficients were measured from the following equation [117]:

(4-12) $$V_L = C_w\sqrt{t} + S_P$$

where V_L is the total fluid loss volume, C_W is the fluid loss coefficient for multiphase flow in chip design #2 and S_P is volume leaked off before filter cake formation, which was neglected for microchip test due to lack of filter cake formations for foams. Thus, the following form was selected for assessment.

(4-13) $$V_L = C_w\sqrt{t}$$

Table 24 illustrates the matrix storage capacity (portion of filled area in the matrix) and estimated volume loss to the matrix (schematic provided in Figure 104).

Table 24. Matrix storage capacity (portion of filled area in the matrix) and estimated volume loss for the flow into the glass microchip with area resembling the tight shale formation

Time (min)	Percentage of matrix filled with ZS $scCO_2$ foam (%)	Volume loss for ZS (ft^3)	Percentage of matrix filled with ZS-PECNP $scCO_2$ foam (%)	Volume loss for ZS-PECNP (ft^3)
0	80.55	1.51e-8	72.97	1.41e-8
1	88.8	1.73e-8	78.16	1.71e-8
2	88.19	1.74e-8	79.87	1.68e-8
2.5	88.49	2.04e-8	81.82	1.81e-8

Table 25 represents the fluid loss coefficient for the flow into the glass microchip with area resembling the tight shale formation and for the flow through Kentucky sandstone tight core previously measured by our group [138]. (0.18 mD permeability for Kentucky sandstone). Table 25 verifies the dramatic decline of fluid loss coefficient was observed in microscale observations.

Table 25. Fluid loss coefficients for measured volumes of fluid penetrated through tight formation in macro and micro scale observations

Stabilizing mixture	Volume loss slope (microfluidic) ($ft^3/min^{0.5}$)	C_W ($ft/min^{0.5}$) (Micro scale observation)
ZS generated $scCO_2$ foam	2.00E-08	2.39E-02
ZS-PECNP generated $scCO_2$ foam	8.00E-09	9.57E-03

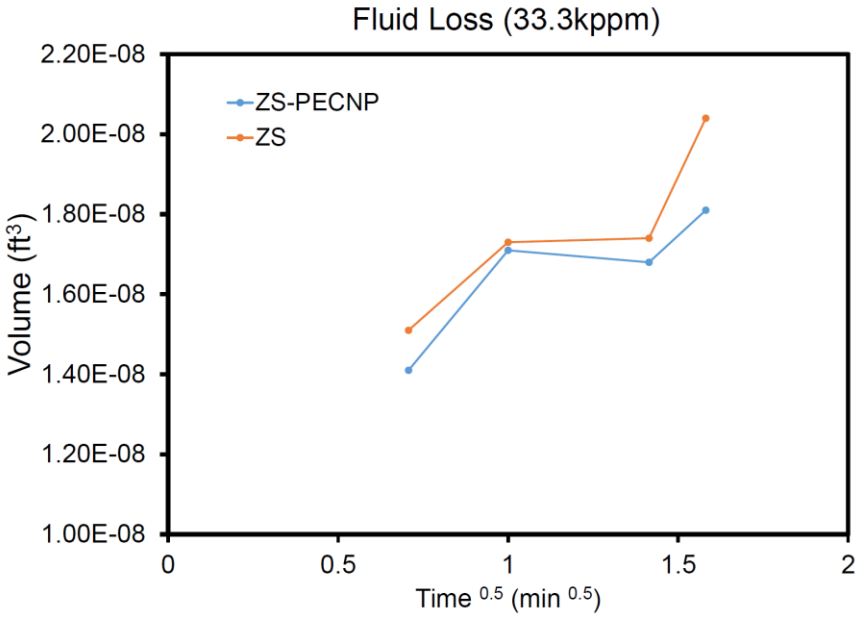

Figure 104. Volume loss with respect to time in chip micromodel #2

The fluid loss coefficient is a function of foam quality [186] matrix permeability, surfactant/nanoparticle concentration and temperature [69] and so at constant FQ (90%), temperature (40°C) and permeability of matrix (Table 15), the stabilizing mixture determines the foam tendency to retain water by improving the viscosity and osmotic pressure [138]. Imbibition of shale matrix by fracturing fluid is also influenced by

compressibility of the rock, fracture/rock conductivity and permeability [187]. Here, compressibility of complex fluid and capillary pressure in the pore level controlled the amount the fluid penetrated through the pore throats of matrix and PECNP/Surfactant $scCO_2$ foam offered less pore throat plugging and damage demonstrating yet another environmentally friendly aspect of waterless fracturing fluids enhanced with supercharged complexes.

Chapter 5: Conclusions

5.1. Molecular complexation, complex fluid development and hydraulic fracturing performance

Herein, results are reported for a responsive $scCO_2$ foam which combines improved viscosity and stability, to better carry proppants, as well as instability in the presence of the oil phase, resulting in rapid degradation upon contact. A novel mixture containing PECNP-surfactant in high salinity brine was successfully prepared to enhance $scCO_2$ foam, reduce formation damage and improve clean-up properties during the hydraulic fracturing process. The major conclusions can be summarized as follows:

1. The presented mixture overcomes the traditional issues of water-based foam liquids such as foam instability at high temperature and pressure, and formation damage due to high water content. It offers a compatibility of $scCO_2$ with high salinity produced waters (including divalent ions) up to 67 kppm TDS (higher than sea level) to minimize fresh water use and produced water disposal in the hydraulic fracturing process, helping to create a more sustainable process of oil recovery from tight shale formations and to store large volumes of CO_2 from the atmosphere.

2. Minimum polyelectrolyte and surfactant concentrations are required for effective performance with the recommended PECNP-surfactant mixture. A zwitterionic surfactant resistant

to high temperatures, compatible with high salinity brine and charged nanoparticles was employed to interact with PECNPs electrostatically. The mixture lowers the surface tension of $scCO_2$ bubbles up to 74% in 33.3 kppm and 93% in 66.7 kppm high salinity brines.

3. The formation of vesicular complexes as a result of electrostatic complexation of PECNP with WLMs was visually identified with TEM images and confirmed with Raman and spectroscopy. The ionic complexes are capable of stabilizing the water-CO_2 lamella by enhancing the viscosity (rheometry), rigidity (dilatational elasticity), and electrostatic repulsion (zeta potential measurements) among lamellae surfaces. A least-squares fitting algorithm as a morphological model indicated the synergistic complexation between PECNP and surfactant based on fitting analysis on acquired Raman spectra from ionic mixtures. The underlying mechanism was identified as electrostatic rearrangement of WLMs along the structure of PECNP to form electrostatically bound layers with nanoparticles and create a stable complex.

4. A novel ionic complex containing PECNP and N-120 ethoxylated surfactant is capable of enhancing interfacial interactions and disjoining pressure of the thin film of high salinity brine formed between $scCO_2$ bubbles, and can improve DLVO forces in aqueous polyelectrolytes for carbonate surfaces (EOR application). TEM imaging and Raman spectroscopy analysis confirm the PECNP's electrosteric interaction with N-120 micelles as wormlike or vesicular structures comprising both nanoparticle and surfactant components. These ionic nano-structures offer noticeable IFT reduction and also provide improvements in rigidity of lamella against the surface tension variations at the interface, opposing the lamella drainage and bubble coalescence. Raman spectroscopy results were used to understand the chemical interaction between N-120 oligomers and the PECNPs. A two-component model comprising an average PECNP and an average surfactant was fit to Raman spectra of lyophilized PECNP:surfactant solution with 1:9 ratio. The

model enabled identification of three major spectral regions not explained by the N-120 and PECNP spectra alone, indicating a change in chemical environment of the key functional groups as a result of ionic complexation and reorganization of the aromatic and aliphatic chain components.

5. The stability of $scCO_2$ bubbles is improved through the formation of electrostatically enhanced bubbles containing the aggregates of PECNP-surfactant. The foam stability drastically improved in view cell test as optimum mixtures presented longer foam life time. PECNP-surfactant mixtures represent a new prospect for stabilizing the bubble film in a high salinity environment, and for tailoring the lamella repulsive forces through addition of different ratios of PECNP to surfactant to overcome the lamella drainage and film thinning.

6. Fluid loss commonly occurs in fracturing process, but can be controlled using the presented PECNP-surfactant $scCO_2$ foam. Fluid loss volume and fluid loss coefficients for CO_2 and water were lowered up to 86 and 78%, respectively, by employing PECNP-surfactant, resulting in lower formation damage.

7. Rapid and easy clean-up is offered by PECNP-surfactant $scCO_2$ foam, as evidenced by the high pressure drop and decline in oil saturation detected in sand-pack tests.

5.2. Macroscale (millimetric) visualization of foam flow at reservoir condition

Macroscale observation of $scCO_2$ foam generation and stability in vertical view cell led to the following conclusions.

1. Macroscale visualization enabled access to complex fluid morphological and geometrical features, quantification of bubble frequency and measurement of hydrodynamic parameters influencing underground fluid transport and stability.

2. Widening flow in upper part of view cell was affected by confinement ratio of tube and view cell. The compressed foam thread in the feeding tube became increasingly unstable in stationary breakup location along the vertical pathway, which eventually led to formation of less uniform droplets in PECNP:Surfatcant $scCO_2$ foam. Local plastic rearrangement of lamella happens with stronger magnitude for PECNP:Surfactant $scCO_2$ foam, and a pattern of deformed bubbles exiting narrow constricted channels was observed for this mixture. The incident ultimately led to formation of asymmetric shape transition of bubbles in diverging flow. Excessive lamella breakup occurs in widening flow with faster pace for PECNP:Surfatcant $scCO_2$ foam. This observation was attributed to elastoplastic properties of interface originated by presence of branched PEI chains in PECNP mixture.

3. Instability mechanisms, such as coalescence, and bubble drainage were evaluated, and it was determined the destabilizing incidents happen with faster rates for ZS $scCO_2$ foams.

4. The comparative stability performance of $scCO_2$ foams generated in high salinity produced water containing Zwitterionic Surfactants and PECNPs was demonstrated by macroscale observation of the long foam life for ZS:PECNP $scCO_2$ foams.

5. Morphology and structural parameters of foam bubbles including size, size distribution as well as film drainage and rate of deformation were quantified via visualization techniques and it was discovered PECNP:Surfactant $scCO_2$ foam with larger initial bubble size preserves the size over the time compared to ZS $scCO_2$ foam with smaller initial bubble size and ascending size trend throughout the time.

5.3. Microchip fabrication for foam flow in harsh reservoir condition

This section presented a protocol related to a fabrication platform to create robust, high-pressure glass microfluidic devices. The protocol presented in this work alleviates the need for a

cleanroom by performing several of the final fabrication steps inside a glovebox. The use of a cleanroom, if available, is recommended to minimize the potential for contamination.

1. This work is concerned with microfluidic platforms that enable direct, in situ visualization of transport of complex fluids in complex permeable media that faithfully represent the complex structures of subsurface media of interest. As such, this work used a buffered etchant that enables the study of mass transfer and transport in surrogate media resembling geologic permeable media.

2. UV lithography technique in this work employs a positive photoresist. As a result, the areas in the design that correspond to features that are intended to be etched on the substrate are optically transparent and the other areas obstruct the transmission of light (collimated UV light). In the case of a negative photoresists, the situation would be the opposite. The areas in the design that correspond to the features that are intended to be etched on the substrate shall be optically non-transparent. UV light source the patterns are transferred to the photoresist by altering its solubility as a result of its exposure to UV light. A full-spectrum, mercury-vapor lamp may serve as the UV source. The use of a collimated, narrow-band UV source, however, improves the quality and precision of the fabrication significantly. The UV source is a developed in-house and offers a low maintenance, low-divergence, collimated UV light source for lithography. The UV source consists of a square array of nine high-power LEDs with a target peak emission wavelength of 365 nm at 25 °C (3.45 mm x 3.45 mm UV LED with Ceramic substrate). A light-collecting UV lens (LED).

3. This work also presents a step by step roadmap for high-pressure foam injection in fabricated glass microfluidic devices using a high-resolution camera and an illumination source. Examples of CO_2 and $scCO_2$ foam microstructure and transport in microfluidic devices are also

presented with relevance to fractured tight and ultra-tight formations. Direct observation of transport in these subsurface media is a challenging task. As such, the devices described in this work provide an enabling platform to study transport in permeable media under temperature and pressure conditions that are relevant to subsurface applications such as fractured media, EOR processes and aquifer remediation. Devices used in this work are fabricated using two different techniques, namely photolithography/wet-etching/thermal-bonding and SLE. The photolithography/wet-etching/thermal-bonding technique comprises a relatively low-cost etching process using a low-maintenance, collimated UV light-source. SLE is executed using a femto-second laser source followed by removal of modified glass from the glass bulk via wet-etching.

4. The main steps involved in the developed photolithography/wet-etching/thermal-bonding technique include printing the design on polyester based transparency film or a glass substrate and transferring the pattern on to a chrome/photoresist coated borosilicate substrate followed by removal of exposed area by photo developer and chrome etchant solutions and etching the patterned area of the borosilicate substrate to the desired depth, ultimately, thermal bonding of the etched substrate and the cover plate.

5. In contrast, SLE employs a two-step process: (i) selective laser-induced printing in a transparent fused silica substrate, and (ii) selective removal of the modified materials via wet chemical etching leading to the development of three-dimensional features in the fused silica substrate. Both SLE and UV-lithography techniques result in devices that are chemically and physically resistant and tolerant of high pressure and temperature conditions that correspond to subsurface systems of interest. Both techniques provide pathways to create high-precision etched micro-channels and capable lab-on-a-chip devices. The photolithography/wet-etching/thermal-bonding technique is robust in terms of the geometry of the channels and may be used to etch

complex channel networks, whereas SLE is limited to relatively simple networks due to practical reasons. On the other hand, devices made with photolithography/wet-etching/thermal-bonding may be more vulnerable to breakage due to bonding imperfections, residual thermal stresses from fast heating/cooling rates during thermal bonding and structural flaws from the wet-etching process. In contrast to photolithography, SLE devices appear more resilient under high pressures (tested up to 9.65 MPa). Regardless of the fabrication technique, rapid pressure buildup rates may increase the chance of mechanical failures in microfluidic devices.

5.4. Multiphase fracture flow in harsh reservoir condition

Herein, synergistic stabilization of $scCO_2$ in highly concentrated electrolytes was reported and corresponding fracture/matrix multiphase flow visualization in SLE fabricated fused silica glass microchips for CCUS and environmentally and sustainable oil recovery. In the comparative study between microchip fabrication techniques, different ionic stabilizers and mixing phase ratios were introduced to find the optimum complex fluid composition and lab-on-a-chip (LOC) platform for sustainable and waterless multiphase flow in tight shale formation. The major conclusions can be summarized as follows:

1. The high-pressure complex fluid injection into LOC was evaluated and it was revealed that fused silica glass microchips fabricated with selective laser-induced etching (SLE) outperformed photo lithography fabricated borofloat glass microchips in terms of mechanical integrity, pressure resistivity, accuracy of printing and ease of visualization. Accordingly, SLE was introduced as an ideal candidate for subsurface emulation on LOC.

2. In order to emulate a recyclable and sustainable water-less fracturing process on LOC, a zwitterionic surfactant compatible with concentrated electrolytes and charged nanoparticles was employed to interact with PECNPs electrostatically in high salinity brine (33.3 kppm) and the

mixture was co-injected with $scCO_2$ into SLE chip micromodel. Pre-generation of $scCO_2$ foam coupled with in-situ observation of SLE micromodel helped to identify the optimized foam quality and superficial velocities to achieve the formation of HIP with near to coarse texture and larger bubbles within the ZS generated foam, whereas, the largest detectable bubble sizes during the coherent and stable flow of ZS-PECNP stabilized $scCO_2$ foam were roughly 0.13x smaller, with fine texture topography. The morphology and integrity of ZS-PECNP generated $scCO_2$ was not affected by geometrical constraints and pressure drop induced by flow divergence from micro-crack to fracture, whereas destabilizing effects such as the bubble growth and coalescence at T-junction were observed for ZS generated $scCO_2$ foam.

3. To characterize the dynamics of $scCO_2$ foam bubbles, dimensionless parameters containing important information about the microstructure, shear condition and relative density were calculated from macroscale observations. Laminar flow and homogenous phase dispersion were verified by Reynolds number. Existence of hydrodynamic interaction were revealed by Peclet number, and low Stokes value ($Stk \ll 1$) indicated the phase segregation did not occurred in $scCO_2$ foams (FQ = 90%) with variety of introduced stabilizers. Improvements in disjoining pressure through electrostatic interactions balances the forces in CO_2-water interface, verified by decline of capillary number for ZS-PECNP generated $scCO_2$ foam,

4. Fracture transport of $scCO_2$ foam enhanced with ZS and ZS-PECNP complexes was tracked in chronological order. Bubble population of unknown frequency was observed for ZS-PECNP generated foam because of excessive lamella formation and supreme stability of electrostatically enhanced bubbles. The instability of ZS-lamella upon foam generation and isolation of $scCO_2$ bubbles leads to more bubble coalescence and lamella drainage and formation of larger bubbles upon onset of mixing, while ZS-PECNP generated $scCO_2$ foam

exhibits condensed and populated array of smaller and monodispersed bubbles with barely recognizable midrange bubbles with sizes as big as the main fracture.

5. Fracture/micro-crack stability was evaluated for variety of stabilizing mixtures. ZS generated $scCO_2$ foam stability along the main fracture was negatively affected by bubble coalescence and lamella breakage. The lamella was not stable enough to separate the $scCO_2$ bubbles from each other in electrolyte solution, whereas in ZS-PECNP generated $scCO_2$ foam, extremely small and monodisperse droplets were largely stable in fracture slit for entire time frame. The fracture stability of $scCO_2$ bubbles was improved through the formation of electrostatically enhanced bubbles containing the aggregates of PECNP-surfactant. ZS generated $scCO_2$ foam breaks into smaller bubbles confined with the micro-crack aperture, the foam within the micro-crack is stable enough through the entire timeframe (t = 2 h) with local variations in bubble size, however, the bubbles traveled and collided into the one millimetric bubble and eventually foam broke in the main fracture. Highly monodispersed and emulsified $scCO_2$ foam with lamella containing ZS-PECNP complexes successfully maintained the stability and offers proper channel filling due to the surfactant-brine solubility and nanoparticle compatibility to the WLMs and concentrated electrolytic interface.

6. An alternative design containing simplified problem of two-dimensional (2D) Cartesian complex flow in matrix domain was evaluated to measure the formation damage. The formation of vesicular complexes originated from electrostatic complexation of PECNP with WLMs leads to stabilizing the water-CO_2 lamella by enhancing the viscosity and osmotic pressure. The chronological binary graphs of emulated tight matrix exhibited the effective reduction of the

fluid loss volume and fluid loss coefficients for PECNP:Surfactant mixtures down to 11% and 60% respectively, by employing PECNP: surfactant which results in lower formation damage.

Bibliography

1. Roser, H. R. M. Fossil Fuels. *OurWorldInData.org* https://ourworldindata.org/fossil-fuels (date accessed: 12/16/2020).
2. Cséfalvay, E. Horváth, I. T. Sustainability Assessment of Renewable Energy in the United States, Canada, the European Union, China, and the Russian Federation. *ACS Sustain. Chem. Eng.* **6**, 8868–8874 (2018).
3. Lifton, V. A. Microfluidics: An enabling screening technology for enhanced oil recovery (EOR). *Lab Chip* **16**, 1777–1796 (2016).
4. Rezaei, F. *et al.* MOF-74 and UTSA-16 film growth on monolithic structures and their CO2 adsorption performance. *Chem. Eng. J.* **313**, 1346–1353 (2017).
5. H. Hosseini, J.S. Tsau, E. Peltier, R.B. Ghahfarokhi, Highly stable scCO2-high salinity brine interface for waterless fracturing using polyelectrolyte complex nanoparticles, in: Abstr. Pap. Am. Chem. Soc., AMER CHEMICAL SOC, DC 20036 USA, 2018.
6. Wang, L. *et al.* Advances in improved / enhanced oil recovery technologies for tight and shale reservoirs Energy Information Administration of the United States. *Fuel* **210**, 425–445 (2017).
7. Hyman, J. D. *et al.* Understanding hydraulic fracturing: a multi-scale problem. *Philos. Trans. A. Math. Phys. Eng. Sci.* **374**, (2016).
8. Smith, M.B., Montgomety, C. T. *Hydraulic Fracturing. Reference Module in Chemistry, Molecular Sciences and Chemical Engineering* (2015). doi:10.1016/B978-0-12-409547-2.11013-3.
9. Pangilinan, K. D., De Leon, A. C. C. & Advincula, R. C. Polymers for proppants used in hydraulic fracturing. *J. Pet. Sci. Eng.* **145**, 154–160 (2016).
10. Barati, R., Liang. J.T. A review of fracturing fluid systems used for hydraulic fracturing of oil and gas wells, **131**, 16 (2014).
11. Barbati, A. C., Desroches, J., Robisson, A. & McKinley, G. H. Complex Fluids and Hydraulic Fracturing. *Annu. Rev. Chem. Biomol. Eng.* **7**, 415–453 (2016).
12. Al-muntasheri, G. A., Houston, C. & Aramco, S. A Critical Review of Hydraulic-Fracturing Fluids for Moderate- to Ultralow- Permeability Formations Over the Last Decade. 16–18 (2014).
13. Yekeen, N., Padmanabhan, E. & Kamal, A. Journal of Industrial and Engineering Chemistry A review of recent advances in foam-based fracturing fl uid application in unconventional reservoirs. *J. Ind. Eng. Chem.* **66**, 45–71 (2018).
14. Middleton, R. S. *et al.* Shale gas and non-aqueous fracturing fluids: Opportunities and challenges for supercritical CO_2. *Appl. Energy* **147**, 500–509 (2015).
15. Yekeen, N., Padmanabhan, E. & Idris, A. K. A review of recent advances in foam-based fracturing fluid application in unconventional reservoirs. *J. Ind. Eng. Chem.* **66**, 45–71 (2018).

16. Ellsworth, W. L. Injection-Induced Earthquakes. **341**, 1–8 (2013).

17. Hosseini, H., Tsau, J. & Barati, R. SPE-189555-MS Lowering Fresh Water Usage in Hydraulic Fracturing by Stabilizing scCO$_2$ Foam with Polyelectrolyte Complex Nanoparticles Prepared in High Salinity Produced Water. (2018).

18. Amirmoshiri, M. *et al.* Probing the Effect of Oil Type and Saturation on Foam Flow in Porous Media: Core-Flooding and Nuclear Magnetic Resonance (NMR) Imaging. *Energy & Fuels* acs.energyfuels.8b02157 (2018) doi:10.1021/acs.energyfuels.8b02157.

19. Dreiss, C. A. & Feng, Y. *(RSC soft matter series 6) Wormlike micelles_advances in systems, characterisation and applications-Royal Society of Chemistry (2017).*

20. Faroughi, S. A., Pruvot, A. J. C. J. & McAndrew, J. The rheological behavior of energized fluids and foams with application to hydraulic fracturing: Review. *J. Pet. Sci. Eng.* **163**, 243–263 (2018).

21. Xiao, C., Balasubramanian, S. N. & Clapp, L. W. Rheology of Viscous CO $_2$ Foams Stabilized by Nanoparticles under High Pressure. *Ind. Eng. Chem. Res.* **56**, 8340–8348 (2017).

22. Xiao, S. *et al.* Destabilization , Propagation , and Generation of Surfactant- Stabilized Foam during Crude Oil Displacement in Heterogeneous Model Porous Media. (2018) doi:10.1021/acs.langmuir.7b02766.

23. Wang, Y. & Shahvali, M. Discrete fracture modeling using Centroidal Voronoi grid for simulation of shale gas plays with coupled nonlinear physics. *FUEL*, **163**, 65–73 (2016).

24. Yekeen, N., Padmanabhan, E. & Idris, A. K. A review of recent advances in foam-based fracturing fluid application in unconventional reservoirs. *J. Ind. Eng. Chem.* (2018) doi:10.1016/j.jiec.2018.05.039.

25. Liang, F., Sayed, M., Al-muntasheri, G. A. & Chang, F. F. Review article A comprehensive review on proppant technologies. *Petroleum*, **2**, 26–39 (2016).

26. Burke, L. H., Eng, P. & Energy, R. P. S. Improved Hydraulic Fracture Performance with Energized Fluids : A Montney Example. 1–6 (2011).

27. Tong, S., Singh, R. & Mohanty, K. K. SPE-187376-MS Proppant Transport in Fractures with Foam-Based Fracturing Fluids. **0**, 9–11 (2017).

28. H. Hosseini, J.S. Tsau, K. Shafer-Peltier, C. Marshall, Q. Ye, R. Barati Ghahfarokhi, Experimental and mechanistic study of stabilized dry CO_2 foam using polyelectrolyte complex nanoparticles compatible with produced water to improve hydraulic fracturing performance, Ind. Eng. Chem. Res. 58 (2019) 9431–9449.

29. Chen, L., Huang, M., Li, Z., Liu, D. & Li, B. Journal of Petroleum Science and Engineering Experimental study on the characteristics of foam flow in fractures. *J. Pet. Sci. Eng.* **185**, 106663 (2020).

30. H. Hosseini, J. Tsau, E. Peltier, R. Barati, Lowering Fresh Water Usage in Hydraulic Fracturing by Stabilizing scCO$_2$ Foam with Polyelectrolyte Complex Nanoparticles Prepared in High Salinity Produced Water, SPE Int. Conf. Exhib. Form. Damage Control. (2018). https://doi.org/10.2118/189555-MS.

31. Fe, C. N. O. D.- *et al.* Development of Nanoparticle-Stabilized Foams to Improve Performance of Water-less Hydraulic Fracturing Original Project Period : 1 Oct 2013 – 30 Sept 2016 Prepared by Department of Petroleum and Geosystems Engineering The University of Texas at Austin and.

(2017).

32. Anandan, R., Johnson, S. & Barati, R. SPE-187489-MS Polyelectrolyte Complex Stabilized CO 2 Foam Systems for Hydraulic Fracturing Application. 1–19 (2017).

33. Keith, D. W. Why Capture CO2 from the Atmosphere? *Science (80-.).* **325**, 1654–1655 (2009).

34. Rownaghi, A. A. *et al.* Aminosilane-Grafted Zirconia – Titiania – Silica Nanoparticles / Torlon Hollow Fiber Composites for CO 2 Capture. 1–13 (2016) doi:10.1002/cssc.201600082.

35. Moodie, N. *et al.* Impacts of relative permeability formulation on forecasts of CO 2 phase behavior , phase distribution , and trapping mechanisms in a. **258**, 241–258 (2017).

36. Jun, Y., Zhang, L., Min, Y. & Li, Q. Nanoscale Chemical Processes A ff ecting Storage Capacities and Seals during Geologic CO 2 Sequestration Published as part of the Accounts of Chemical Research special issue " Chemistry of Geologic Carbon Storage " . (2017) doi:10.1021/acs.accounts.6b00654.

37. Allam, R. J., Bredesen, R. & Drioli, E. *CO2 Separation Technologies*. *Carbon Dioxide Recovery and Utilization* (2003).

38. Polzot, A., Gullo, P. & Cortella, G. Id : 339 Water Storage To Improve the Efficiency of Co 2 Commercial Refrigeration Systems. (2015).

39. Tomasko, D. L. *et al.* A review of CO(2) applications in the processing of polymers. *Ind. Eng. Chem. Res.* **42**, 6431–6456 (2003).

40. Lin, F. *et al.* Recent progress in heavy metal extraction by supercritical CO2 fluids. *Ind. Eng. Chem. Res.* **53**, 1866–1877 (2014).

41. Dzyuba, S. V. & Bartsch, R. A. Recent advances in applications of room-temperature ionic liquid/supercritical CO2 systems. *Angew. Chemie - Int. Ed.* **42**, 148–150 (2003).

42. Verma, M. K. Fundamentals of Carbon Dioxide-Enhanced Oil Recovery (CO 2 -EOR)—A Supporting Document of the Assessment Methodology for Hydrocarbon Recovery Using CO 2 - EOR Associated with Carbon Sequestration. *U.S. Geol. Surv. Open-File Rep.* 19 (2015) doi:https://dx.doi.org/10.3133/ofr20151071.

43. Middleton, R., Viswanathan, H., Currier, R. & Gupta, R. CO2as a fracturing fluid: Potential for commercial-scale shale gas production and CO2sequestration. *Energy Procedia* **63**, 7780–7784 (2014).

44. Aroonsri, A. *et al.* Conditions for Generating Nanoparticle-Stabilized CO_2 Foams in Fracture and Matrix Flow. *Spe* **2**, 1–19 (2013).

45. Barati, R. & Liang, J. T. A review of fracturing fluid systems used for hydraulic fracturing of oil and gas wells. *J. Appl. Polym. Sci.* **131**, 1–11 (2014).

46. Gandossi, L. *An overview of hydraulic fracturing and other formation stimulation technologies for shale gas production. JRC Technical Reports* (2013). doi:10.2790/99937.

47. Nguyen, V. H., Kang, C., Roh, C. & Shim, J.-J. Supercritical CO_2 -Mediated Synthesis of CNT@Co_3O_4 Nanocomposite and Its Application for Energy Storage. *Ind. Eng. Chem. Res.* **55**, 7338–7343 (2016).

48. Negar Nazari; Hooman Hosseini; Jyun-Syung Tsau; Karen Shafer-Peltier; Craig Marshall; Qiang

Ye; Reza Gh. Barati. Development of Highly Stable Lamella Using Polyelectrolyte Complex Nanoparticles: An Environmentally Friendly scCO$_2$ Foam Injection Method for CO$_2$ Utilization Using EOR. *Fuel* (2019).

49. Worthen, A. J. *et al.* Journal of Colloid and Interface Science Nanoparticle-stabilized carbon dioxide-in-water foams with fine texture. *J. Colloid Interface Sci.* **391**, 142–151 (2013).

50. Dreiss, C. A. & Feng, Y. *(RSC soft matter series 6) Wormlike micelles_advances in systems, characterisation and applications-Royal Society of Chemistry (2017).pdf*. (2017).

51. Peach, J. & Eastoe, J. Supercritical carbon dioxide: A solvent like no other. *Beilstein J. Org. Chem.* **10**, 1878–1895 (2014).

52. Breward, C. J. W. & Howell, P. D. The drainage of a foam lamella. *J. Fluid Mech.* **458**, 379–406 (2002).

53. Osei-Bonsu, K., Shokri, N. & Grassia, P. Foam stability in the presence and absence of hydrocarbons: From bubble- to bulk-scale. *Colloids Surfaces A Physicochem. Eng. Asp.* **481**, 514–526 (2015).

54. Dreiss, C. A. & Feng, Y. *Wormlike Micelles*. (The Royal Society of Chemistry, 2017). doi:10.1039/9781782629788.

55. Xue, Z. *et al.* Ultradry Carbon Dioxide-in-Water Foams with Viscoelastic Aqueous Phases. *Langmuir* **32**, 28–37 (2016).

56. Al-muntasheri, G. A., Advanced, E. & Aramco, S. Nanoparticle-Enhanced Hydraulic-Fracturing Fluids : A Review. *SPE Prod. Oper. Conf. Exhib.* **32**, 187–195 (2017).

57. William, J. K. M., Ponmani, S., Samuel, R., Nagarajan, R. & Sangwai, J. S. Effect of CuO and ZnO nanofluids in xanthan gum on thermal, electrical and high pressure rheology of water-based drilling fluids. *J. Pet. Sci. Eng.* **117**, 15–27 (2014).

58. Vryzas, Z., Mahmoud, O., Nasr-El-Din, H. A. & Kelessidis, V. C. Development and Testing of Novel Drilling Fluids Using Fe_2O_3 and SiO_2 Nanoparticles for Enhanced Drilling Operations. *Int. Pet. Technol. Conf.* (2015) doi:10.2523/IPTC-18381-MS.

59. Cai, J., Chenevert, M. E., Sharma, M. M. & Friedheim, J. E. Decreasing Water Invasion Into Atoka Shale Using Nonmodified Silica Nanoparticles. *SPE Drill. Complet.* **27**, 103–112 (2012).

60. Haroun, M. *et al.* Smart Nano-EOR Process for Abu Dhabi Carbonate Reservoirs. *Abu Dhabi Int. Pet. Exhib. Conf.* 1–13 (2012) doi:10.2118/162386-MS.

61. Wang, J. *et al.* Interaction between surfactants and SiO2nanoparticles in multiphase foam and its plugging ability. *Energy and Fuels* **31**, 408–417 (2017).

62. Qajar, A. *et al.* Modeling fracture propagation and cleanup for dry nanoparticle-stabilized-foam fracturing fluids. *J. Pet. Sci. Eng.* **146**, 210–221 (2016).

63. Nazari, N., Tsau, J.-S. & Barati, R. CO2 Foam Stability Improvement Using Polyelectrolyte Complex Nanoparticles Prepared in Produced Water. *Energies* **10**, 516 (2017).

64. Kalyanaraman, N., Arnold, C., Gupta, A., Tsau, J. S. & Ghahfarokhi, R. B. Stability improvement of CO2 foam for enhanced oil-recovery applications using polyelectrolytes and polyelectrolyte complex nanoparticles. *J. Appl. Polym. Sci.* **134**, 1–15 (2017).

65. Veisi, M. *et al.* Application of polyelectrolyte complex nanoparticles to increase the lifetime of poly vinyl sulfonate scale inhibitor. *Proc. - SPE Int. Symp. Form. Damage Control* **2018-Febru**, (2018).

66. Veisi, M. *et al.* Controlled release of poly(vinyl sulfonate) scale inhibitor to extend reservoir treatment lifetime. *J. Appl. Polym. Sci.* **47225**, 1–11 (2018).

67. Zeng, S. *et al.* Ionic-Liquid-Based CO_2 Capture Systems: Structure, Interaction and Process. *Chem. Rev.* **117**, 9625–9673 (2017).

68. Hosseini, H., Dornbusch, D. A. & Suppes, G. J. Improved Electrochemical Performance of Alkaline Batteries Using Quaternary Ammonia Polysulfone-Functionalized Separators. *Ind. Eng. Chem. Res.* **55**, 8557–8566 (2016).

69. Harris, P. C. Dynamic Fluid-Loss Characteristics of CO2-Foam Fracturing Fluids. *SPE Prod. Eng.* 89–94 (1987).

70. Barati, R. *et al.* Polyelectrolyte Complex Nanoparticles for Protection and Delayed Release of Enzymes in Alkaline pH and at Elevated Temperature During Hydraulic Fracturing of Oil Wells. (2012) doi:10.1002/app.

71. Barati, R. *et al.* Fracturing fluid cleanup by controlled release of enzymes from polyelectrolyte complex nanoparticles. *J. Appl. Polym. Sci.* **121**, 1292–1298 (2011).

72. Ghahfarokhi, R. B. Stability improvement of co2 foam for enhanced oil recovery applications using polyelectrolytes and polyelectrolyte complex nanoparticles. (2017).

73. Tiyaboonchai W., Woiszwillo J., M. C. . Formulation and characterization of DNA – polyethylenimine – dextran sulfate nanoparticles. **19**, 191–202 (2003).

74. Johnson, S. *et al.* Polyelectrolyte complex nanoparticles to entrap enzymes for hydraulic fracturing fluid cleanup. **56**, 15–16 (2011).

75. Mark, H. F. Gene-Delivery Polymers. *Encyclopedia of Polymer Science and Technology* 329–337 (1996).

76. Ashenhurst, J. Primary, Secondary, Tertiary, Quaternary In Organic Chemistry. (2019).

77. University of Calgary, department of C. University of Calgary online chemistry courses, chapter 22: Amines.

78. By, A. & Crisp, J. ACTI171TY COEFFICIENTS OF THE n-PRIMARY , SECONDARY AND TERTIARY ALIPHATIC AMINES.

79. Farzaneh, S. A. & Sohrabi, M. SPE 164917 A Review of the Status of Foam Applications in Enhanced Oil Recovery. (2013).

80. Fei, Y., Pokalai, K., Johnson, R., Gonzalez, M. & Haghighi, M. Experimental and simulation study of foam stability and the effects on hydraulic fracture proppant placement. *J. Nat. Gas Sci. Eng.* **46**, 544–554 (2017).

81. Lv, Q., Li, Z., Li, B., Li, S. & Sun, Q. Study of Nanoparticle − Surfactant-Stabilized Foam as a Fracturing Fluid. (2015) doi:10.1021/acs.iecr.5b02197.

82. Tong, M., Cole, K. & Neethling, S. J. Colloids and Surfaces A : Physicochemical and Engineering Aspects Drainage and stability of 2D foams : Foam behaviour in vertical Hele-Shaw cells.

Colloids Surfaces A Physicochem. Eng. Asp. **382**, 42–49 (2011).

83. Transactions, T. & Techniczne, C. RHEOLOGY OF THE WET SURFACTANT FOAMS AND BIOFOMAS – A REVIEW WŁAŚCIWOŚCI REOLOGICZNE PIAN CIEKŁYCH WYTWARZANYCH NA BAZIE SYNTETYCZNYCH SURFAKTANTÓW ORAZ BIOSURFAKTANTÓW – PRZEGLĄD. (2013).

84. Caps, H., Vandewalle, N. & Broze, G. Foaming dynamics in Hele-Shaw cells. 5–8 (2006) doi:10.1103/PhysRevE.73.065301.

85. Szabries, M., Jaeger, P. & Amro, M. M. Foam Analysis at Elevated Pressures for Enhanced Oil Recovery Applications. *Energy & Fuels* acs.energyfuels.8b03088 (2019) doi:10.1021/acs.energyfuels.8b03088.

86. Sinton, D. Energy: The microfluidic frontier. *Lab Chip* **14**, 3127–3134 (2014).

87. Hemling, M. *et al.* Micro fl uidics for High School Chemistry Students. (2014) doi:10.1021/ed4003018.

88. Ren, K., Zhou, J. & Wu, H. Materials for microfluidic chip fabrication. *Acc. Chem. Res.* **46**, 2396–2406 (2013).

89. Prakash, S. & Yeom, J. *Nanofluidics and Microfluidics*. *Nanofluidics and Microfluidics* (2014). doi:10.1016/B978-1-4377-4469-9.00006-8.

90. Karadimitriou, N. K. & Hassanizadeh, S. M. A Review of Micromodels and Their Use in Two-Phase Flow Studies. (2012) doi:10.2136/vzj2011.0072.

91. Dupas, A., Hénaut, I., Argillier, J., Aubry, T. & Degradation, M. Mechanical Degradation Onset of Polyethylene Oxide Used as a Hydrosoluble Model Polymer for Enhanced Oil Recovery HAL Id : hal-00815882 Mechanical Degradation Onset of Polyethylene Oxide Used as a Hydrosoluble Model Polymer for Enhanced Oil Recovery. (2013).

92. Howe, A. M., Clarke, A. & Giernalczyk, D. Soft Matter Flow of concentrated viscoelastic polymer solutions in porous media : effect of M W and concentration on elastic turbulence onset in various geometries. 6419–6431 (2015) doi:10.1039/c5sm01042j.

93. Scopus data base link for fracture Microfluidics.

94. Er, V., Babadagli, T., Xu, Z. & Tg, A. Pore-Scale Investigation of the Matrix - Fracture Interaction During CO 2 Injection in Naturally Fractured Oil Reservoirs. **23**, 1421–1430 (2010).

95. Jiménez-martínez, J., Porter, M. L., Hyman, J. D., Carey, J. W. & Viswanathan, H. S. Mixing in a three-phase system : Enhanced production of oil-wet reservoirs by CO 2 injection. 196–205 (2016) doi:10.1002/2015GL066787.Abstract.

96. Jiménez-Martínez, J. *et al.* Pore-scale mechanisms for the enhancement of mixing in unsaturated porous media and implications for chemical reactions. *Geophys. Res. Lett.* **42**, 5316–5324 (2015).

97. Porter, M. L. *et al.* Lab on a Chip Geo-material microfluidics at reservoir conditions for subsurface energy resource applications. 4044–4053 (2015) doi:10.1039/c5lc00704f.

98. Carey, J. W., Lei, Z., Rougier, E., Mori, H. & Viswanathan, H. Fracture-permeability behavior of shale. *J. Unconv. Oil Gas Resour.* **11**, 27–43 (2015).

99. Iliescu, C., Taylor, H., Avram, M., Miao, J. & Franssila, S. A practical guide for the fabrication of

microfluidic devices using glass and silicon. *Biomicrofluidics* **6**, 1–16 (2012).

100. Hassanizadeh, S. M. A Review of Micromodels and Their Use in Two-Phase Flow Studies. (2012) doi:10.2136/vzj2011.0072.

101. Wang, Z. B. *et al.* Laser micro / nano fabrication in glass with tunable-focus particle lens array. **16**, 19706–19711 (2008).

102. Formation of through holes in glass substrates by laser-assisted etching.PDF.

103. N.F. Borrelli, J.F. Schroeder, C.M. Smith, A. Streltsov, Direct writing of optical devices in silica-based glass using femtosecond pulse lasers, (2005).

104. Yonemura, M., Kato, S., Hasegawa, K. & Takahashi, H. Formation of through holes in glass substrates by laser-assisted etching. *J. Laser Micro Nanoeng.* **11**, 143–146 (2016).

105. Gerami, A. *et al.* Microfluidics for Porous Systems : Fabrication , Microscopy and Applications. *Transp. Porous Media* (2018) doi:10.1007/s11242-018-1202-3.

106. SPE. Reservoir-on-a-Chip Technology Opens a New Window Into Oilfield Chemistry. https://pubs.spe.org/en/print-article/?art=4900.

107. Tiggelaar, R. M. *et al.* Fabrication , mechanical testing and application of high-pressure glass microreactor chips. **i**, 163–170 (2007).

108. Paydar, O. H. *et al.* Sensors and Actuators A : Physical Characterization of 3D-printed microfluidic chip interconnects with integrated O-rings. *Sensors Actuators A. Phys.* **205**, 199–203 (2014).

109. Rognmo, A. U., Fredriksen, S. B. & Alcorn, Z. P. Pore-to-Core EOR Upscaling for CO 2 Foam for CCUS. 11–14 (2019).

110. Negar Nazari, Hooman Hosseini, Jyun-Syung Tsau, Karen Shafer-Peltier, Craig. P. Marshall, R. B. Development of Highly Stable Lamella Using Polyelectrolyte Complex Nanoparticles: An Environmentally Friendly scCO2 Foam Injection Method for Greenhouse Gas Management. in *MIT Applied Energy A+B* (2019).

111. Mclendon, W. J. *et al.* Journal of Petroleum Science and Engineering Assessment of CO 2 -soluble non-ionic surfactants for mobility reduction using mobility measurements and CT imaging. *J. Pet. Sci. Eng.* **119**, 196–209 (2014).

112. Huntsman Technical Bulletin: SURFONIC® N-120 Surfactant.

113. L.L., S. *Surfactants: Fundamentals and Applications in the Petroleum Industry*. (Cambridge University Press, 2000).

114. Tewes, F., Pierre, M. & Boury, F. Dynamical and Rheological Properties of Fluorinated Surfactant Films Adsorbed at the Pressurized CO 2 À H 2 O Interface. 8144–8152 (2011).

115. Schramm, L. L. *Foams: Fundamentals and Applications in the Petroleum Industry*. (American Chemical Society, 1994). doi:10.1021/ba-1994-0242.

116. Shafer-Peltier, K. E. *et al.* Raman microspectroscopic model of human breast tissue: Implications for breast cancer diagnosis in vivo. *J. Raman Spectrosc.* **33**, 552–563 (2002).

117. Howard, G. C. & Fast, C. R. Optimum Fluid Characteristics for Fracture Extension. *Drilling and Production Practice* (1957).

118. CARBO Ceramics Inc, CARBOECONOPROP low density ceramic proppant. https://www.carboceramics.com/Oil-gas/Fracture-technologies/ceramic-proppant/carboeconoprop-low-density.

119. Drenckhan, W. & Saint-jalmes, A. The science of foaming. *Adv. Colloid Interface Sci.* **222**, 228–259 (2015).

120. Rabbani, A., Jamshidi, S. & Salehi, S. Journal of Petroleum Science and Engineering An automated simple algorithm for realistic pore network extraction from micro-tomography images. *J. Pet. Sci. Eng.* **123**, 164–171 (2014).

121. Hosseini, H., Guo, F., Ghahfarokhi, R. B. & Aryana, S. A. Microfluidic fabrication techniques for high-pressure testing of microscale supercritical CO2 foam transport in fractured unconventional reservoirs. *J. Vis. Exp.* **2020**, 1–29 (2020).

122. Erickstad, M., Gutierrez, E. & Groisman, A. Lab on a Chip lithography light source based on. *Lab Chip* **15**, 57–61 (2015).

123. Guo, F., Aryana, S. A., Wang, Y., Mclaughlin, J. F. & Coddington, K. International Journal of Greenhouse Gas Control Enhancement of storage capacity of CO 2 in megaporous saline aquifers using nanoparticle-stabilized CO 2 foam. *Int. J. Greenh. Gas Control* **87**, 134–141 (2019).

124. Guo, F. & Aryana, S. A. An Experimental Investigation of Flow Regimes in Imbibition and Drainage Using a Microfluidic Platform. 1–13 (2019) doi:10.3390/en12071390.

125. Whitfill, D. Lost Circulation Material Selection, Particle Size Distribution and Fracture Modeling with Fracture Simulation Software. *IADC/SPE Asia Pacific Drill. Technol. Conf. Exhib.* 1–12 (2008) doi:10.2118/115039-MS.

126. Mahajan, S. *Encyclopedia of Materials: Science and Technology*. (Pergamon, 2001).

127. Agista, M. N. & Guo, K. applied sciences A State-of-the-Art Review of Nanoparticles Application in Petroleum with a Focus on Enhanced Oil Recovery. doi:10.3390/app8060871.

128. Denkov, N. D., Ivanov, I. B., Kralchevsky, P. A. & Wasan, D. T. A possible mechanism of stabilization of emulsions by solid particles. *J. Colloid Interface Sci.* **150**, 589–593 (1992).

129. Sambasivam, A., Sangwai, A. V. & Sureshkumar, R. Self-Assembly of Nanoparticle-Surfactant Complexes with Rodlike Micelles: A Molecular Dynamics Study. *Langmuir* **32**, 1214–1219 (2016).

130. Long, D. A. *Infrared and Raman characteristic group frequencies. Tables and chartsGeorge Socrates John Wiley and Sons, Ltd, Chichester, Third Edition*. *Journal of Raman Spectroscopy* vol. 35 (2004).

131. Yvon, H. J. Raman Data and Analysis - Raman Bands. **2012**, 2–3 (2012).

132. Roessl, U., Leitgeb, S., Pieters, S., De Beer, T. & Nidetzky, B. In situ protein secondary structure determination in ice: Raman spectroscopy-based process analytical tool for frozen storage of biopharmaceuticals. *J. Pharm. Sci.* **103**, 2287–2295 (2014).

133. Kumar, S. *et al.* Raman and infra-red microspectroscopy: Towards quantitative evaluation for clinical research by ratiometric analysis. *Chem. Soc. Rev.* **45**, 1879–1900 (2016).

134. Ben Mabrouk, K., Kauffmann, T. H., Aroui, H. & Fontana, M. D. Raman study of cation effect on sulfate vibration modes in solid state and in aqueous solutions. *J. Raman Spectrosc.* **44**, 1603–

1608 (2013).

135. Wang, W. *et al.* Mechanism and kinetics of titanium hydrolysis in concentrated titanyl sulfate solution based on infrared and Raman spectra. *Chem. Eng. Sci.* **134**, 196–204 (2015).

136. Hosseini, H. *et al.* Experimental and Mechanistic Study of Stabilized Dry CO_2 Foam Using Polyelectrolyte Complex Nanoparticles Compatible with Produced Water To Improve Hydraulic Fracturing Performance. *Ind. Eng. Chem. Res.* **58**, 9431–9449 (2019).

137. DA, L. *Infrared and Raman characteristic group frequencies*. (2004). doi:doi:10.1002/jrs.1238.

138. Hosseini, H. *et al.* Experimental and Mechanistic Study of Stabilized Dry CO_2 Foam Using Polyelectrolyte Complex Nanoparticles Compatible with 3 Produced Water To Improve Hydraulic Fracturing Performance. (2019) doi:10.1021/acs.iecr.9b01390.

139. Alzobaidi, S., Lotfollahi, M., Kim, I., Johnston, K. P. & Dicarlo, D. A. Carbon Dioxide-in-Brine Foams at High Temperatures and Extreme Salinities Stabilized with Silica Nanoparticles. 10680–10690 (2017) doi:10.1021/acs.energyfuels.7b01814.

140. Stevenson, P. *Foam Engineering, Fundamentals and Applications;* (Wiley: Hoboken, 2012).

141. Denkov, N. D., Tcholakova, S., Golemanov, K., Ananthpadmanabhan, K. P. & Lips, A. The role of surfactant type and bubble surface mobility in foam rheology. 3389–3408 (2009) doi:10.1039/b903586a.

142. Wanniarachchi, W. A. M. *et al.* Current opinions on foam-based hydro-fracturing in deep geological reservoirs. *Geomech. Geophys. Geo-Energy Geo-Resources* **1**, 121–134 (2015).

143. Zhang, J. *Chemical Engineering III*. (London: CRC Press., 2014).

144. Lauridsen, J., Twardos, M. & Dennin, M. Shear-Induced Stress Relaxation in a Two-Dimensional Wet Foam. *Phys. Rev. Lett.* **89**, 1–4 (2002).

145. Dlugogorski, B. Z., Schaefer, T. H. & Kennedy, E. M. Verifying Consistency of Effective-Viscosity and Pressure- Loss Data for Designing Foam Proportioning Systems. *Natl. Inst. Stand. Technol.* **3**, (2005).

146. F. Boury, T. Ivanova, I. Panaieotov, J. E. Proust, A. Bois, and J. R. Dilatational Properties of Adsorbed Poly(D,L-lactide) and Bovine Serum Albumin Monolayers at the Dichloromethane/Water Interface. *Langmuir* **11**, 1636–1644 (1995).

147. Georgieva, D., Cagna, A. & Langevin, D. Link between surface elasticity and foam stability. *Soft Matter* **5**, 2063–2071 (2009).

148. Zhang, X. L. *et al.* Adsorption behavior of hydrophobin and hydrophobin/surfactant mixtures at the air-water interface. *Langmuir* **27**, 11316–11323 (2011).

149. Al-anssari, S., Barifcani, A., Keshavarz, A. & Iglauer, S. Impact of nanoparticles on the CO2 - brine interfacial tension at high pressure and temperature. *J. Colloid Interface Sci.* **532**, 136–142 (2018).

150. Lau, H. & O'Brien, S. Effects of spreading and nonspreading oils on foam propagation through porous media. *SPE Reserv. Eng.* 893–896 (1988) doi:10.2118/15668-PA.

151. Kuhlman, M. Visualizing the Effect of Light Oil in CO2 Foams. *J. Pet. Technol.* **42**, (1990).

152. Ross, S. Inhibition of Foaming. II1,2A Mechanism for the Rupture of Liquid Films by

Antifoaming Agents. *J. Phys. Colloid Chem.* **54**, 429–436 (1950).

153. Saldungaray, P. & Palisch, T. Hydraulic fracture optimization in unconventional reservoirs. *World Oil* 7–13 (2012).

154. Fei, Y., Johnson, R. L., Gonzalez, M., Haghighi, M. & Pokalai, K. Experimental and numerical investigation into nano-stabilized foams in low permeability reservoir hydraulic fracturing applications. *Fuel* **213**, 133–143 (2018).

155. Ribeiro, L. H. & Sharma, M. M. Multiphase Fluid-Loss Properties and Return Permeability of Energized Fracturing Fluids. *Spe Prod. Oper.* **27**, 265–277 (2012).

156. Du, D., Li, Y., Chao, K., Wang, C. & Wang, D. Laboratory study of the Non-Newtonian behavior of supercritical CO2 foam flow in a straight tube. *J. Pet. Sci. Eng.* **164**, 390–399 (2018).

157. Khomami, B. & Wilson, G. M. An experimental investigation of interfacial instability in superposed flow of viscoelastic fluids in a converging/diverging channel geometry. *J. Nonnewton. Fluid Mech.* **58**, 47–65 (1995).

158. Badve, M. & Barigou, M. Local description of foam flow, deformation and pressure drop in narrow constricted channels. *Int. J. Multiph. Flow* 103279 (2020) doi:10.1016/j.ijmultiphaseflow.2020.103279.

159. Nguyen, Q. P., Currie, P. K. & Zitha, P. L. J. Motion of foam films in diverging-converging channels. *J. Colloid Interface Sci.* **271**, 473–484 (2004).

160. Dollet, B. & Bocher, C. Flow of foam through a convergent channel. *Eur. Phys. J. E* **38**, 1–11 (2015).

161. Szabries, M., Jaeger, P. & Amro, M. M. Foam Analysis at Elevated Pressures for Enhanced Oil Recovery Applications. *Energy and Fuels*, **33**, 3743–3752 (2019).

162. AlQuaimi, B. I. & Rossen, W. R. Study of foam generation and propagation in fully characterized physical-model fracture. *J. Pet. Sci. Eng.* 1–13 (2018) doi:10.1016/j.petrol.2018.06.025.

163. Fernø, M. A., Gauteplass, J., Pancharoen, M., Haugen, A. & Graue, A. Experimental Study of Foam Generation , Sweep Efficiency , and Flow in a Fracture Network. (2016).

164. Burshtein, N., Chan, S. T., Toda-peters, K., Shen, A. Q. & Haward, S. J. ScienceDirect 3D-printed glass microfluidics for fluid dynamics and rheology. *Curr. Opin. Colloid Interface Sci.* **43**, 1–14 (2019).

165. Li, S. *et al.* Hydraulic Fractures Induced by Water- / Carbon Dioxide-Based Fluids in Tight Sandstones. *Rock Mech. Rock Eng.* **52**, 3323–3340 (2019).

166. Lin, C. H., Lee, G. Bin, Lin, Y. H. & Chang, G. L. A fast prototyping process for fabrication of microfluidic systems on soda-lime glass. *J. Micromechanics Microengineering* **11**, 726–732 (2001).

167. Guancheng, J. *et al.* Evaluation of gas wettability and its effects. *Petroleum Science*, 10, 515–527 (2013) doi:10.1007/s12182-013-0303-4.

168. Nguyen, H., Thach, H., Roy, E. & Huynh, K. Low-Cost , Accessible Fabrication Methods for Microfluidics Research in Low-Resource Settings. 1–10 (2018) doi:10.3390/mi9090461.

169. Guo, F., Aryana, S. A., Wang, Y., Mclaughlin, J. F. & Coddington, K. International Journal of

Greenhouse Gas Control Enhancement of storage capacity of CO_2 in megaporous saline aquifers using nanoparticle-stabilized CO_2 foam. *Int. J. Greenh. Gas Control* **87**, 134–141 (2019).

170. Guo, F., He, J., Johnson, A. & Aryana, S. A. Sustainable Energy & Fuels and recyclable iron oxide nanoparticles to improve. 814–822 (2017) doi:10.1039/c7se00098g.

171. Wu, X. *et al.* Journal of Petroleum Science and Engineering A smart recyclable VES fluid for high temperature and high pressure fracturing. *J. Pet. Sci. Eng.* **190**, 107097 (2020).

172. Hosseini, H., Tsau, J., Peltier, E. & Barati, R. Lowering Fresh Water Usage in Hydraulic Fracturing by Stabilizing scCO2 Foam with Polyelectrolyte Complex Nanoparticles Prepared in High Salinity Produced Water. *SPE Int. Conf. Exhib. Form. Damage Control* (2018) doi:10.2118/189555-MS.

173. H Hosseini, J Syung Tsau, K Shafer-Peltier, C Marshall, Q Ye, R. B. Environmentally friendly waterless fracturing with supercritical CO_2 foam prepared in produced water: Mechanistic study. in *Abstr. Pap. Am. Chem. Soc. 2019, 258* (2019).

174. Espinosa, D., Caldelas, F., Johnston, K., Bryant, S. L. & Huh, C. SPE 129925 Nanoparticle-Stabilized Supercritical CO_2 Foams for Potential Mobility Control Applications. 1–13 (2010).

175. Edrisi, A. R. & Kam, S. I. SPE 162709 A New Foam Rheology Model for Shale-Gas Foam Fracturing Applications. **2009**, 1–19 (2012).

176. Anandan, R., Barati, R. & Johnson, S. SPE-191424-18IHFT-MS Polyelectrolyte Complex Stabilized CO_2 Foam Systems for Improved Fracture Conductivity and Reduced Fluid Loss. (2018).

177. Gajbhiye, R. N. & Kam, S. I. Characterization of foam flow in horizontal pipes by using two-flow-regime concept. *Chem. Eng. Sci.* **66**, 1536–1549 (2011).

178. Zhou, J., Ranjith, P. G. & Wanniarachchi, W. A. M. Different strategies of foam stabilization in the use of foam as a fracturing fluid. *Adv. Colloid Interface Sci.* 102104 (2020) doi:10.1016/j.cis.2020.102104.

179. Xue, Z. *et al.* Ultradry Carbon Dioxide-in-Water Foams with Viscoelastic Aqueous Phases. *Langmuir* **32**, 28–37 (2016).

180. Green, S., Walsh, J., Mclennan, J. & Forbes, B. ARMA 17-555 Hydraulic Fracture Propagation in Steps Considering Different Fracture Fluids. 1–11 (2017).

181. Palisch, T., Duenckel, R., Bazan, L. & Heidt, H. J. SPE 106301 Determining Realistic Fracture Conductivity and Understanding Its Impact on Well Performance — Theory and Field Examples.

182. R. Byron Bird, Warren E. Stewart, E. N. L. *Transport Phenomena, Revised*. (Wiley-VCH Verlag GmbH & Co., 2006).

183. Hanselmanna, W. & Windhabh, E. Flow Characteristics and Modelling of Foam Generation in a Continuous Rotor / Stator Mixer. **38**, 393–405 (1999).

184. Zhu, J. *et al.* Journal of Petroleum Science and Engineering Settling behavior of the proppants in viscoelastic foams on the bubble scale. *J. Pet. Sci. Eng.* **181**, 106216 (2019).

185. Anandan, R., Johnson, S. & Barati, R. Polyelectrolyte Complex Stabilized CO_2Foam Systems for Hydraulic Fracturing Application. *SPE Liq. Basins Conf. - North Am.* 1–19 (2017) doi:10.2118/187489-MS.

186. Wang, J. & Elsworth, D. Journal of Natural Gas Science and Engineering Fracture penetration and proppant transport in gas- and foam-fracturing. *J. Nat. Gas Sci. Eng.* **77**, 103269 (2020).

187. Gehne, S. & Benson, P. M. Permeability enhancement through hydraulic fracturing : laboratory measurements combining a 3D printed jacket and pore fluid over-pressure. *Sci. Rep.* 1–11 (2019) doi:10.1038/s41598-019-49093-1.